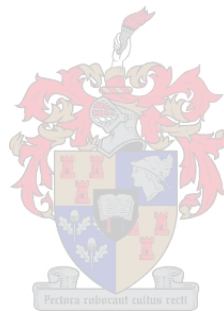


Development of a Low Phase Noise Microwave Voltage Controlled Oscillator

Elrien Vermaak

*Thesis presented in partial fulfilment of the requirements
for the degree of
MASTER OF SCIENCE IN ENGINEERING*



Department of Electrical & Electronic Engineering
Faculty of Engineering
Stellenbosch University

Supervisors:

Prof. J.B. de Swardt & Prof. P.W. van der Walt

December 2008

DECLARATION

By submitting this thesis electronically, I declare that the entirety of the work contained therein is my own, original work, that I am the owner of the copyright thereof (unless to the extent explicitly otherwise stated) and that I have not previously in its entirety or in part submitted it for obtaining any qualification.

Date: 10 December 2008

Copyright © 2008 Stellenbosch University
All rights reserved

ABSTRACT

The topic for this project entailed the development of a '*Low Phase Noise – Microwave – Voltage Controlled Oscillator*' for use in radar applications.

First of all, a *low phase noise oscillator* was designed. In order to minimise the phase noise of the oscillator, a high-Q, transmission line – cavity resonator was developed. By derivation it was confirmed that an optimal point for minimum phase noise does exist. The latter was done by evaluating the equation for the output power spectral density of the oscillator phase noise (as defined by Leeson's Phase Noise Model) at its minimum point. Subsequently, the amount of power that needed to be dissipated inside the resonator could be compared to that dissipated in the source and the load. This identified the amount of coupling to the resonator allowed, assuring minimum phase noise. Since a specific amount of coupling to the resonator was sought after, it had to be practically feasible. Therefore several coupling techniques were investigated to ensure the most user-friendly way of tuning the amount of coupling to the resonator, and hence easily reaching the optimum point of minimum phase noise.

After successful completion of the low phase noise oscillator design, it was modified for *voltage controlled oscillator (VCO)* use by means of variable tuning diodes. These varactor diodes were situated inside the cavity of the resonator. Again the most suitable position to place the diodes had to be determined. The latter was done through considerably detailed transmission line theory; where the *loaded Q*, the *tuning bandwidth* (amount of change in frequency reached) and the amount of *power dissipated* inside the resonator were measured against each other.

By means of the necessary phase noise measurements, it was confirmed that in order to keep the phase noise to a minimum, the tuning bandwidth had to be kept small and the amount of power dissipated inside the resonator maximised; so as to keep the overall loaded Q-value of the circuit as high as possible.

OPSOMMING

Die omvang van hierdie projek behels die ontwerp en bou van 'n '*Lae Faseruis – Mikrogolf – Spanning Beheerde Ossillator*' vir gebruik in radar toepassings.

Eerstens is 'n *lae faseruis ossillator* ontwerp. Met die doel om die faseruis van die ossillator te minimeer, is 'n hoë-Q transmissielyn – holte resoneerder ontwerp. Deur middel van wiskundige afleiding is dit bevestig dat daar 'n optimum punt van minimum faseruis bestaan. Die afleiding het plaasgevind deur die vergelyking van die uittree drywingsdigtheid spektrum van die ossillator faseruis (soos gedefinieer deur Leeson se Faseruis Model) te evalueer by sy minimum punt. Vervolgens kon die nodige hoeveelheid drywing wat binne in die resoneerder verkwis moet word, vergelyk word met die hoeveelheid drywing verkwis in die bron en die las. D.m.v. laasgenoemde kon die hoeveelheid toegelate koppeling aan die resoneerder identifiseer word, om sodoende minimum faseruis te verseker. Aangesien die koppeling aan die resoneerder 'n spesifieke hoeveelheid behels, was dit belangrik dat die fisiese koppeling prakties uitvoerbaar moes wees. Daarom is verskeie koppelingstegnieke ondersoek om sodoende die mees gebruikersvriendelike manier te vind, om die koppeling aan die resoneerder te kon verstel tot die optimum punt van minimum faseruis.

Nadat die ossillator ontwerp suksesvol afgehandel is, is dit aangepas vir *spanning beheerde ossillator* gebruik. Laasgenoemde is gedoen d.m.v. varaktor diodes, wat binne in die holte van die resoneerder geposisioneer is. Die mees geskikte posisie om die diodes te plaas is vasgestel deur middel van transmissielyn teorie; waar die *belaste Q*, die *verstelling bandwydte* (verandering in frekwensie) en die hoeveelheid *drywing verkwis* binne in die resoneerder met mekaar vergelyk is.

Deur middel van die nodige faseruis metings, is bevestig dat dit belangrik is om die verstelling bandwydte te minimeer, terwyl die aantal drywing verkwis in die resoneerder gemaksimeer word. Dit verseker dat die totale belaste Q-waarde van die stroombaan so hoog as moontlik is en dus bly die faseruis op 'n minimum.

ACKNOWLEDGEMENTS

First and foremost, I would like to thank our **Heavenly Father** for the strength, courage and endurance He created in me. I humbly thank Him for all the guidance given to be able to complete this task successfully.

On completion of this research, I would also like to convey my sincere and deepest gratitude to every single person involved in completing this project, as well as to the relevant institutions for their contribution:

To my supervisors, **Prof. J.B. de Swardt** and **Prof. P.W. van der Walt**. Thank you for every single piece of advice given, and for the unbelievable opportunity to be able to work alongside such amazing talents as yourselves! I honestly enjoyed working on this project with you. Thank you, Prof. De Swardt for all your guidance and encouragement. Prof. Van der Walt, thank you for your remarkable insight into every challenge we came across.

I would also like to show my sincere gratitude towards **Reutech Radar Systems (RRS)** in Technopark, Stellenbosch; for the financial support without which this project would not have been possible.

To the technical staff in the electronic workshop at Stellenbosch University - especially **Mr. Wessel Croukamp**, Chief Electrician; I would like to thank you for your thorough and precise work in manufacturing the resonator for my project, and for your patience in making all of the necessary adjustments.

Mr. Martin Siebers, RF (Microwave and Antenna Measurement) Laboratory Manager at Stellenbosch University; thank you for your friendly advice provided whenever needed.

The **University of Stellenbosch** is also thanked for making the necessary measurement equipment and laboratories available to complete this project successfully.

And then, thank you to ***my family and friends*** for their daily encouragement and advice. To my parents, thank you Mom and Dad for all the financial support through the years, for all of your devoted love and commitment. To my sister, thank you for just being there with me; encouraging me to keep on going. I would also like to thank my friend, Dirk Mouton for all his prayers and loyal support.

CONTENTS

DECLARATION	i
ABSTRACT	ii
OPSOMMING	iii
ACKNOWLEDGEMENTS	iv
LIST OF FIGURES	xii
LIST OF TABLES	xxi
LIST OF TERMS AND ABBREVIATIONS	xxiii
LIST OF APPENDICES	xxvi
CHAPTER 1 – INTRODUCTION AND MOTIVATION	1
1.1 INTRODUCTION	1
1.2 MOTIVATION	2
1.3 PROPOSED SOLUTION	3
1.4 THESIS ORGANISATION	4
CHAPTER 2 – LITERATURE REVIEW : OSCILLATORS	6
2.1 THEORETICAL LAYOUT	6
2.1.1 Classical Feedback System	6
2.1.2 General Analysis of Transistor Oscillator Circuits	8
2.1.2.1 Circuit Parameters	9
2.1.2.2 Derivation of the Input Impedance	15
2.1.2.3 Strategies for Proper Oscillator Design	17

2.2 SIMULATION EXAMPLE	18
2.2.1 Linear Analysis (<i>MWO</i>)	19
2.2.1.1 Port Impedances	19
2.2.1.2 Oscillator Analysis Probe	21
2.2.2 Nonlinear Analysis (<i>Orcad PSPICE</i>)	23
2.2.2.1 Voltage Probe	23
2.2.2.2 Fourier Transform	24
2.3 PHASE NOISE THEORY	26
2.3.1 Types of Noise	26
2.3.1.1 Noise in The Circuit	26
2.3.1.2 Noise in Oscillators	35
2.3.2 What is Phase Noise?	37
2.3.3 Review of Angle Modulation	41
2.3.3.1 Phase Modulation (PM) Review	42
2.3.3.2 Frequency Modulation (FM) Review	46
2.3.3.3 Narrowband Phase & Frequency Modulation Approximations	51
2.3.4 Representation of Phase Noise	54
2.3.4.1 Definition of Single Sideband Phase Noise	54
2.3.5 Leeson's Phase Noise Model	60
2.3.6 Why is Low Phase Noise Important?	67
2.3.7 Requirements for Low Noise Oscillators	69
2.3.7.1 Ways to Minimise Oscillator Phase Noise	74

2.3.8 Voltage Controlled Oscillator (VCO) Noise	76
CHAPTER 3 – SYSTEM : OSCILLATOR	80
3.1 RESONATOR	80
3.1.1 Derivation Of The Optimum Point For Minimum Phase Noise	81
3.1.2 Resonator Design	88
3.1.2.1 Technical Specifications	88
3.1.2.2 The Incremental-Inductance Rule	92
3.1.2.3 Q calculation by means of the Susceptance Slope Parameter	99
3.1.2.4 Transmission Line Theory	101
3.1.2.5 Coupling Techniques Considered	109
3.1.2.6 Microwave Tuning Element	111
3.1.3 Simulation Results	113
3.1.3.3 MATLAB	113
3.1.3.1 MICROWAVE OFFICE	117
3.1.3.2 CST	119
3.1.4 Measurements and Results	127
3.1.4.1 S-Parameters at Resonance – Network Analyser	127
3.1.4.2 Unloaded Q-value	129
3.1.4.3 Loaded Q-value	129
3.1.5 Resonator Results Compared	129
3.2 ACTIVE COMPONENT : AMPLIFIER (ZX60-2522M+)	132
3.2.1 Technical Data	132

3.2.2	Measurements and Results	132
3.2.2.1	Noise Figure, NF_{dB}	132
3.2.2.2	S-Parameters – Network Analyser	133
3.3	OPEN-LOOP OSCILLATOR ELEMENTS	134
3.3.1	Power Splitter: 3 dB Coupler (ZSFC-2-5-S+)	134
3.3.2	Attenuators (VAT-X+)	135
3.3.3	Phase Shifter	136
3.3.4	Measurements and Results	138
3.4	CLOSED LOOP – OSCILLATOR	141
3.4.1	Element Block Diagram	141
3.4.2	Measurements and Results	141
3.4.2.1	Expected Power Levels	141
3.4.2.2	Oscillation	142
3.4.2.3	Phase Shifter	143
3.5	OSCILLATOR PHASE NOISE	144
3.5.1	Theoretical Prediction by Leeson’s Phase Noise Model	144
3.5.1.1	Implementation in MATLAB	145
3.5.2	Measurements and Results	147
3.5.2.1	Spectrum Analyser	147
	Confirmation of the Oscillation	147
	Single-sideband Phase Noise Representation	148
	Oscillator Noise Floor Measurement	149

3.5.2.2 PN9000B – Automatic Phase Noise Test System	152
Theory of Operation (<i>Reference Phase Locking Method</i>)	152
Setup for the Oscillator Phase Noise Measurement	154
Measured Results	156
CHAPTER 4 – SYSTEM : VOLTAGE CONTROLLED OSCILLATOR	161
4.1 VARIABLE TUNING DIODES	161
4.1.1 What Diodes were used?	162
4.1.2 How many Diodes would be sufficient?	164
4.1.3 Where these Diodes should be connected?	168
4.1.4 Bypass Capacitors for the Varactor Diodes	177
4.1.5 The PCB layout Design	183
4.2 MEASUREMENTS AND RESULTS	186
4.2.1 SA Confirmation of Oscillation	186
4.2.2 Loaded and unloaded Q-values	187
4.2.3 Tuning Bandwidth, f	189
4.2.4 PN9000B – Automatic Phase Noise Test System	192
Theory of Operation (<i>Delay Line FM Discrimination Method</i>)	192
Setup for the VCO Phase Noise Measurement	193
Measured Results	194
4.2.5 ‘Destructive’ Measurements	200
4.2.6 Theoretical Explanation for the adverse effect of the PCB on the Q- value	201

4.3 ADDITIONAL CST SIMULATIONS	207
CHAPTER 5 – SUMMATION OF THE OSCILLATOR VS. VCO RESULTS	211
5.1 SUMMARY OF ALL RELEVANT OUTCOMES	211
5.2 COMPARED SSB PHASE NOISE MEASUREMENT	211
CHAPTER 6 – CONCLUSIONS AND RECOMMENDATIONS	213
LITERATURE REFERENCES	216
APPENDICES	220

LIST OF FIGURES

		Page
Figure 2.1	: Classical feedback system of an oscillator	6
Figure 2.2	: Voltage divider of the Colpitts oscillator	8
Figure 2.3	: (a) Common-emitter npn BJT and (b) a simplified small-signal hybrid- π equivalent circuit for the npn transistor ..	9
Figure 2.4	: Expanded hybrid- π equivalent circuit of Fig. 2.3(b)	12
Figure 2.5	: The h -parameter model of the common-emitter BJT	12
Figure 2.6	: Expanded hybrid- π equivalent circuit with the output short-circuited	13
Figure 2.7	: Expanded hybrid- π equivalent circuit with the input open-circuited	14
Figure 2.8	: Equivalent small-signal circuit of Fig. 2.2	15
Figure 2.9	: The complete Colpitts oscillator. Test circuit for simulation purposes	20
Figure 2.10	: $\text{Im}[Z_{\text{Resonator}}]$ and $\text{Im}[Z_{\text{Active}}]$ versus frequency	20
Figure 2.11	: $\text{Re}[Z_{\text{Active}}]$ versus frequency	21
Figure 2.12	: The Colpitts oscillator and the use of the <i>OSCAPROBE</i> in <i>MWO</i>	22
Figure 2.13	: Illustration of the oscillation frequency	22
Figure 2.14	: Time domain analysis of the Colpitts oscillator in <i>PSPICE</i>	23
Figure 2.15	: Output, emitter voltage v_E , in the time domain	23
Figure 2.16	: Closer look at the emitter voltage $v_E(t)$	24
Figure 2.17	: Spectrum of the voltage signal $v_E(t)$	24
Figure 2.18	: (a) A resistor at temperature T produces the noise voltage $v_n(t)$. (b) The random noise voltage generated by a resistor at temperature T	27
Figure 2.19	: (a) The Thevenin equivalent circuit for a noisy resistor. (b) Maximum power transfer of noise power from a noisy resistor to a load over bandwidth B	28
Figure 2.20	: SSB PSD of thermal noise	30

	Page
Figure 2.21 : Circuits for noise calculation. (a) Resistor network. (b) Noise equivalent circuit	30
Figure 2.22 : PSD of flicker noise	33
Figure 2.23 : Spectral density of the noise in electronic circuits	34
Figure 2.24 : Oscillator model illustrating noise	35
Figure 2.25 : Amplitude spectra for the signal $V_0 \cos[\omega_0 t]$. (a) Single-sided. (b) Double-sided	37
Figure 2.26 : Phase spectra for the signal $V_0 \cos[\omega_0 t]$. (a) Single-sided. (b) Double-sided	38
Figure 2.27 : Noise Phasor Diagram. (a) Amplitude fluctuations taken into account. (b) Resultant signal phase, represented by $\omega_0 t + \text{phase noise } \theta(t)$	39
Figure 2.28 : <i>Timing Jitter</i> . Phase noise illustration in the time domain	40
Figure 2.29 : Output spectrum of a typical oscillator	40
Figure 2.30 : Time domain waveforms illustrating phase modulation. (a) Unmodulated carrier $V_0 \cdot \cos(2\pi f_0 t)$. (b) Message signal $\theta_{pk} \cdot \sin(2\pi f_m t)$. (c) Output of phase modulator with the unmodulated carrier. (d) Output of phase modulator with the message signal	43
Figure 2.31 : Amplitude spectra of the waveform, illustrating phase modulation. (a) Spectra of the unmodulated carrier signal (in red) and the message signal (in green). (b) Phase modulated carrier signal	45
Figure 2.32 : Time domain waveforms illustrating frequency modulation. (a) Unmodulated carrier $V_0 \cdot \cos(2\pi f_0 t)$. (b) Message signal $\beta \cdot \cos(2\pi f_m t)$, with the modulation index β , varied according to the peak frequency deviation	48
Figure 2.33 : Time domain waveforms illustrating the varying modulation index, β . <i>Left</i> : FM output with the message signal. <i>Right</i> : FM output with the unmodulated carrier. For (a) $\beta = 0.1$, (b) $\beta = 1.0$, and (c) $\beta = 2.5$	49

	Page
Figure 2.34 : Amplitude spectra of the unmodulated carrier signal (in black) and the message signal $m(t)$. $m(t)$ is illustrated for three different values of the modulation index β . For $\beta = 0.1$ in red; $\beta = 1.0$ in blue, and $\beta = 2.5$ in green	50
Figure 2.35 : Amplitude spectra of the FM signal for different values of the modulation index β . (a) $\beta = 0.1$ and (b) $\beta = 1.0$	50
Figure 2.36 : Amplitude spectrum of the FM signal for $\beta = 2.5$	51
Figure 2.37 : DSB Amplitude spectrum illustrating Narrowband Phase Modulation where $\theta_{pk} \ll 1$	53
Figure 2.38 : Phase Noise specification of a typical signal source	55
Figure 2.39 : Single-sideband phase noise to carrier ratio representation	57
Figure 2.40 : Spectrum analyser display of the VCO noise power, with a 10 kHz frequency per division	59
Figure 2.41 : Feedback amplifier model for characterising oscillator phase noise	60
Figure 2.42 : Amplifier noise power for an input signal at f_0	62
Figure 2.43 : Input PSD of the oscillator	63
Figure 2.44 : PSD of the output phase noise of an oscillator according to Leeson's Model. (a) Low-Q response ($f_c < f_h$). (b) High-Q response ($f_h < f_c$)	66
Figure 2.45 : A simplified bipolar transistor noise model	71
Figure 2.46 : Adding negative feedback can reduce the amount of AM-to-PM modulation of the carrier by the transistor's flicker noise	73

	Page
Figure 3.1 : The designed Transmission-line, Cavity Resonator	80
Figure 3.2 : Top view of the Resonator, showing the coupling loops ...	80
Figure 3.3 : Block diagram representation of an oscillator	81
Figure 3.4 : Circuit element representation of Fig. 2.47. (a) Coupling represented by transformers. (b) Transformed resistance values. (c) 'Dissipation' circuit, with the corresponding conductance values	83
Figure 3.5 : Schematic representation of the proposed Cavity Resonator	89
Figure 3.6 : Transmission line representation of Fig. 3.3	89
Figure 3.7 : Transmission line resonator with the relevant values	91
Figure 3.8 : Representation of an incremental length of transmission line. (a) Illustration of the current and voltage on the line. (b) The Lumped-element equivalent circuit	92
Figure 3.9 : Transmission line parameters for a Coaxial Line	94
Figure 3.10 : Coaxial Transmission line – illustrating the skin effect	95
Figure 3.11 : Resonator Dimensions as determined by Wheeler	97
Figure 3.12 : Illustrating the input admittance at different locations along the transmission line	100
Figure 3.13 : Illustration of how B_{in} and G_{in} varies, at different locations along the transmission line	100
Figure 3.14 : Coaxial Transmission Line Configuration	101
Figure 3.15 : Different Coupling Techniques. (a) Coupling to the Electric Field. (b) Coupling to the Magnetic Field	109
Figure 3.16 : Image of the utilised coupling loop	110
Figure 3.17 : Illustration of Z_{02} versus d_2	114
Figure 3.18 : Illustration of Z_{01} versus d_1	114
Figure 3.19 : Magnitude of the Resonator's Input Impedance	115
Figure 3.20 : Resonator's Input Conductance, G_{in}	115
Figure 3.21 : Calculating the Slope of the Input Susceptance Curve, B_{in}	116
Figure 3.22 : Unloaded Q-value, Q_u of the designed Resonator	116

	Page
Figure 3.23 : Resonator Circuits as simulated in <i>MWO</i> , illustrating different parameters specified. (a) Line Impedance. (b) Coaxial Diameters	117
Figure 3.24 : Input Admittance, illustrating G_{in} and the calculation of b_n	118
Figure 3.25 : Unloaded Q-value as calculated in <i>MWO</i>	118
Figure 3.26 : Top- and Side View of the Electric Field inside the cavity of the Resonator	119
Figure 3.27 : Top- and Side View of the Magnetic Field inside the cavity of the Resonator	120
Figure 3.28 : <i>CST</i> representation of the cavity resonator at 900 MHz ...	121
Figure 3.29 : <i>CST</i> representation of the cavity resonator at 1 GHz	122
Figure 3.30 : The Final Resonator Design and its Coupling Loops	124
Figure 3.31 : The <i>CST</i> simulated S-parameters of the Resonator	125
Figure 3.32 : Illustration of the Resonator 3 dB Bandwidth	126
Figure 3.33 : S-parameters of the Cavity Resonator	127
Figure 3.34 : S-parameters of the Resonator, illustrating the 3 dB Bandwidth	127
Figure 3.35 : Photograph of the Rohde & Schwarz ZVB 8 – Vector Network Analyser	128
Figure 3.36 : Photograph of the ZX60 Amplifier	132
Figure 3.37 : S-parameters of the Mini-Circuits ZX60-2522M+ Amplifier	133
Figure 3.38 : S_{21} of the ZX60-2522M+ Amplifier	133
Figure 3.39 : Open-loop Oscillator Block Diagram	134
Figure 3.40 : Photograph of the 3 dB Coupler	134
Figure 3.41 : The 2 dB Attenuator	135
Figure 3.42 : Illustration of the 1 dB Compression Point for an Amplifier	135
Figure 3.43 : Typical piece of Transmission Line used	137
Figure 3.44 : Phase Shifter	138
Figure 3.45 : Effect of the circuit elements on S_{21} of the open-loop Oscillator	138

	Page
Figure 3.46 : Effect of the circuit elements on the phase of the open-loop Oscillator	139
Figure 3.47 : S_{21} of the open-loop Oscillator with the Phase Shifter	140
Figure 3.48 : Effect of the Phase Shifter on the phase of the open-loop Oscillator	140
Figure 3.49 : Block Diagram of the closed-loop Oscillator	141
Figure 3.50 : Spectrum Analyser Output of the closed-loop Oscillator ..	142
Figure 3.51 : Phase Shifter at its Minimum and Maximum settings	143
Figure 3.52 : Frequency Response of the Phase Shifter – tuning it from its maximum to its minimum setting	143
Figure 3.53 : Noise Contributions to the Oscillator SSB Phase Noise relative to the Carrier	145
Figure 3.54 : Phase Noise of the Oscillator as predicted by Leeson's Phase Noise Model	146
Figure 3.55 : Spectrum Analyser Output, illustrating the offset frequencies	147
Figure 3.56 : Illustration of the SSB phase noise of the measurement in Fig. 3.55	148
Figure 3.57 : Block diagram of the setup to measure the oscillator noise floor	149
Figure 3.58 : Measured S-parameters of the ERA-51SM+	150
Figure 3.59 : SA Oscillator Noise Floor Measurement	151
Figure 3.60 : Simplified block diagram of the PN9000B system	152
Figure 3.61 : Photograph of the Aeroflex Phase Noise Measurement System	153
Figure 3.62 : Block diagram of the Oscillator measurement setup in Fig. 3.61	154
Figure 3.63 : Measured SSB Phase Noise of the Oscillator, comparing the effect of a 5V power supply to that of a 5V battery	156
Figure 3.64 : Measured SSB Phase Noise of the Oscillator, comparing the effect of different attenuators in the feedback loop	157

	Page
Figure 3.65 : Comparison of the Oscillator Phase Noise as predicted by Leeson's Phase Noise Model to that measured on the PN9000B Phase Noise Test System	159
Figure 4.1 : Photograph of the Voltage Controlled Oscillator System as a whole	161
Figure 4.2 : (a) Case Style and (b) photograph of the MA46H201 Varactor Diode	162
Figure 4.3 : C_{Tot} vs. $V_{Reverse}$	163
Figure 4.4 : Equivalent Circuit for the packaged Tuning Varactor.	163
Figure 4.5 : Transmission line representation of the resonator, showing the coupling of the varactor diodes along line 2 .	164
Figure 4.6 : Q-value and f against the coupling position L, for 1 diode connected	165
Figure 4.7 : Q-value and f against the coupling position L, for 2 diodes connected	166
Figure 4.8 : Q-value and f against the coupling position L, for 4 diodes connected	167
Figure 4.9 : The Q-value and Tuning Bandwidth f , against the coupling position L, at f_0	171
Figure 4.10 : The Q-value and Tuning Bandwidth f , against the coupling position L, at f_0	173
Figure 4.11 : Power dissipated in the Resonator versus the input Voltage, V_{in}	175
Figure 4.12 : Line Voltage, V_{line2} versus the resonator input Voltage, V_{in}	175
Figure 4.13 : Power dissipated in the Resonator versus the Coupling position, L	176
Figure 4.14 : Line Voltage, V_{line2} versus the Coupling position, L	176
Figure 4.15 : Typical Bypass Capacitor parallel bank	177
Figure 4.16 : Frequency response of a capacitor	178
Figure 4.17 : Equivalent model of a surface mount capacitor	178

	Page
Figure 4.18 : (a) $ S_{11} $ in dB, and (b) $\text{Re}\{S_{11}\}$ and $\text{Im}\{S_{11}\}$, all versus frequency	180
Figure 4.19 : Smith Chart representations of (a) S_{11} , and (b) Z_{eq} of the 27 pF capacitor	181
Figure 4.20 : Representation of Z_{11} , the Impedance of the 27 pF capacitor, at port 1	181
Figure 4.21 : Equivalent Impedance Z_{eq} of the 27 pF capacitor, plotted against f	182
Figure 4.22 : Capacitance versus frequency for $L_S = 800$ pH	182
Figure 4.23 : Proposed Varactor Diode and Bypass Capacitor layout, with (a) the Resonator, and (b) the PCB	183
Figure 4.24 : Layout Topologies for the Varactor Diode and its Bypass Capacitor (a) illustrating the problems experienced, and (b) giving the proposed solution	184
Figure 4.25 : Photograph of the designed Printed Circuit Board	185
Figure 4.26 : Photographs of the Varactor Diodes and their Bypass Capacitors soldered onto the PCB. (a) Illustrate the problems experienced, while (b) demonstrate the proposed solutions	185
Figure 4.27 : Photograph of the HP Spectrum Analyser at RRS	186
Figure 4.28 : Confirmed oscillation of the VCO system before its PN measurement	187
Figure 4.29 : S-parameters of the Resonator loaded by the Varactor Diodes	188
Figure 4.30 : S-parameters of the unloaded Resonator	188
Figure 4.31 : Wide-band plot of the S-parameters of the unloaded Resonator	189
Figure 4.32 : Tuning bandwidth f measured on the Spectrum Analyser	190
Figure 4.33 : Tuning bandwidth f measured on the Vector Network Analyser	190
Figure 4.34 : Tuning bandwidth f measured on the HP SA at RRS ...	191

	Page
Figure 4.35 : Block diagram of the VCO measurement setup in Fig. 4.36	193
Figure 4.36 : Photograph of the cabling done on the Aeroflex Phase Noise Measurement System, for the VCO phase noise measurement setup	194
Figure 4.37 : Delay Line Measurement of the SSB Phase Noise, comparing the 1 dB to the 6 dB Attenuation, while $\tau = 20$ ns	196
Figure 4.38 : Delay Line Measurement of the SSB Phase Noise, comparing the 1 dB to the 6 dB Attenuation, while $\tau = 100$ ns	197
Figure 4.39 : Delay Line Measurement of the SSB Phase Noise with a 1 dB Attenuator in the feedback loop	198
Figure 4.40 : Delay Line Measurement of the SSB Phase Noise with a 6 dB Attenuator in the feedback loop	199
Figure 4.41 : Two equipotential surfaces shown	203
Figure 4.42 : Representation of the designed PCB, situated inside the cavity of the resonator	204
Figure 4.43 : Electric Field distribution for the PCB (a) without Cu-tracks, and (b) with Cu-tracks	205
Figure 4.44 : A piece of the FR-4 PCB, illustrating the Electric Field present	206
Figure 4.45 : Simulations done on the Resonator for different PCB solutions	208
Figure 5.1 : Comparison between the SSB phase noise measurements for the Oscillator and the VCO Systems ..	512

LIST OF TABLES

	Page
Table 2.1 : Collector Current for a Typical Bipolar Transistor vs. the Flicker Corner Frequency	70
Table 3.1 : Starting values for the resonator's dimensions	98
Table 3.2 : Formulas for the Coaxial Transmission Line Configuration	102
Table 3.3 : General Transmission Line Formulas	103
Table 3.4 : Characteristics of the Shorted Transmission Line (Line 2)	105
Table 3.5 : γ_2 , Z_{in2} and Y_{in2} of the Shorted Transmission Line (Line 2)	106
Table 3.6 : Characteristics of the Open Transmission Line (Line 1) ...	107
Table 3.7 : γ_1 , Z_{in1} and Y_{in1} of the Open Transmission Line (Line 1)	108
Table 3.8 : b_n and Q_u calculated for the Resonator	108
Table 3.9 : Resonator Dimensions at $f_0 = 900$ MHz	121
Table 3.10 : Resonator Dimensions at $f_0 = 1$ GHz	122
Table 3.11 : Comparing the different CST Simulations	123
Table 3.12 : The Simulated- versus the Measured Q-values of the Resonator	130
Table 3.13 : Amplifier, Noise Figure (NF) measurements	132
Table 3.14 : Measured Power Levels along the oscillator circuit in Fig. 3.49	142
Table 3.15 : Compared SSB Phase Noise Values	149
Table 4.1 : Proposed Q-value and f for different number of diodes coupled	168
Table 4.2 : Q-values when no diodes are coupled. Taken from Fig. 4.9, p.171	172
Table 4.3 : Summary of the expected (calculated) values for the VCO system	174
Table 4.4 : Measured Q-values for the VCO system	187

	Page
Table 4.5 : Summary of the Tuning Bandwidth (f) measurements ..	189
Table 4.6 : Comparison of the Expected values to that Measured for Q_U , Q_L and f	191
Table 4.7 : Q-values measured during the ‘Destructive’ Measurements	200
Table 4.8 : Resonator S-parameters and Q-values obtained for different PCB solutions simulated	209
Table 5.1 : Summation of the Oscillator vs. VCO results	211
Table 5.2 : SSB phase noise values for the measurement in Fig. 5.1	211

LIST OF TERMS AND ABBREVIATIONS

AC	:	alternating current
α_F	:	common-base current gain, always slightly < 1
AGC	:	Automatic Gain Control
AO	:	<i>Analog Office</i>
AWR	:	<i>Applied Wave Research</i>
β	:	Modulation Index = $\theta_{pk} = f_{pk} / f_m$
BJT	:	bipolar junction transistor
BW	:	Frequency Bandwidth
CST	:	<i>Computer Simulation Technology, Germany</i>
DC	:	direct current
DSB	:	Double-sideband
F	:	Noise Factor (absolute terms)
FET	:	Field Effect Transistor
FM	:	Frequency Modulation
f_0	:	resonant frequency, [hertz]
f_h	:	$f_0/2Q_L$, half-power 3 dB BW of the resonator, [hertz]
GaAs FET	:	Gallium Arsenide [GaAs], FET
g_m	:	Transistor transconductance = I_{CQ}/V_T
h_{fe}	:	small-signal current gain = $g_m r_\pi = \beta$
h_{ie}	:	small-signal input resistance = $(r_b + r_\pi \parallel r_\mu) \approx r_\pi$
h_{oe}	:	small-signal output admittance = $[(1 + \beta)/r_\mu + 1/r_o] \approx 1/r_o$
HEMT	:	High Electron Mobility Transistor - is also called heterostructure FET (HFET) or modulation-doped FET (MODFET). It is a FET incorporating a junction between two materials with different band gaps.
IEEE	:	<i>Institute of Electrical and Electronics Engineers, Inc.</i>
IF	:	Intermediate frequency, Mixer product
I_S	:	contains electrical parameters of the transistor's B-E junction

JFET	:	Junction Gate FET (also JUGFET). The simplest type of FET. Can be used as an electronically-controlled switch. It is also used as a voltage controlled resistance. Electric current flows from the source to the drain; while the gate determines the amount of current that flows. A negative bias voltage at the gate can in effect switch the transistor off.
KCL	:	Kirchoff current law, summation of the currents at a node
KVL	:	Kirchoff voltage law, summation of the voltages around a loop
$L(f_m)$:	SSB phase noise (absolute terms)
$L(f_m)_{[\text{dBc/Hz}]}$:	SSB phase noise (logarithmic terms), $L(f_m)_{[\text{dBc/Hz}]} = 10 \log_{10}(L(f_m))$
MATLAB	:	<i>The Language of Technical Computing</i> , Ver. 7.0.1, The MathWorks, Inc.
MWO	:	<i>Microwave Office</i>
NF	:	Noise Figure (logarithmic terms), $NF_{\text{dB}} = 10 \cdot \log_{10}(F)$
npn	:	transistor structure, thin p-region between two n-regions
ω_0	:	resonant frequency, $[\text{rad} \cdot \text{s}^{-1}]$
PCB	:	Printed Circuit Board
PF	:	Loss Power Factor, Incremental-Inductance Rule
PM	:	Phase Modulation
PSD	:	Power Spectral Density, a frequency domain representation of the phase noise power density of an oscillator
PSK	:	Phase-shift keying, a digital modulation technique
Q	:	Quality factor, a figure of merit often used in describing the sharpness of a tuned circuit response. A high-Q circuit has a sharper response, and vice versa. In resonant systems, the Q is a measurement of the effect of resistance to oscillation.
Q-point	:	Quiescent parameters, intersection of the load line and the device characteristic curve
QAM	:	Quadrature Amplitude Modulation. It is a modulation technique in which data is conveyed by means of modulating (changing) the amplitude of two carrier waves. These two waves are called quadrature carriers, since they are 90° out of phase and are usually sinusoids.
Q_U	:	Unloaded Q-value of the resonator
Q_L	:	$Q_U/2 = f_0/(3 \text{ dB BW})$, Loaded Q-value of the resonator

$Q_{R\&D}$:	Q-value predicted by theory (equation 4.1) and simulation (CST)
$Q_{R\&D\&C}$:	Loaded Q of the system including the effect of the R esonator, the V aractor D iodes and the SMA C onnectors
RADAR	:	Radio Detection and Ranging
RBW	:	Resolution Bandwidth, Spectrum Analyser. The width of the resolution bandwidth (IF) filter of a SA. The ability of a SA to separate closely spaced spectral components and display them individually.
RF	:	radio frequency
rms	:	Root Mean Square = (Peak Value)/ 2
r_{π}	:	diffusion resistance or base-emitter input resistance = V_T/I_{BQ} , typically in the kilohm range
r_o	:	small-signal transistor output resistance = V_A/I_{CQ}
r_b	:	series resistance of the semiconductor material at the transistor base, typically, a few tens of ohms $\ll r_{\pi}$
r_{μ}	:	Reverse-biased diffusion resistance of the base-collector junction, typically in the order of megohms $\gg r_{\pi}$
SA	:	<i>Rohde & Schwarz</i> – Spectrum Analyser – FSEK 30 (20Hz - 40GHz)
SPAN	:	Measurement frequency range
SSB	:	Single-sideband
SUT	:	Source Under Test
$S_{\theta}(f_m)$:	PSD of the phase noise power at the input of an oscillator, at an offset frequency f_m , from the carrier f_0
$S_{\phi}(f_m)$:	PSD of the phase noise power at the output of an oscillator, at an offset frequency f_m , from the carrier f_0
TEM	:	Transverse Electromagnetic, wave propagation on transmission lines
θ_{pk}	:	Peak Phase Deviation, in [radians]
θ_{rms}	:	Root Mean Square (rms) value = $\theta_{pk}/\sqrt{2}$
VBW	:	Video Bandwidth, Spectrum Analyser. Usually set to a factor of 10 less than the RBW. It smoothes the displayed noise.
VNA	:	<i>Rohde & Schwarz</i> – Vector Network Analyser – ZVB 8 (300kHz - 8GHz)
V_T	:	thermal voltage, $V_T = 0.026$ [volt], at room temperature, $T = 300^{\circ}\text{K}$
V_A	:	early voltage, $50 < V_A < 300$ [volt]

LIST OF APPENDICES

- A : Incremental-Inductance Rule
- B : Susceptance Slope Parameter
- C : Resonator – Measured S-parameters
- D : Amplifier ZX60-2522M – Datasheets and Measured S-parameters
- E : Power Splitter ZFSC-2-5 – Datasheet
- F : Fixed Attenuator VAT-2 – Datasheet
- G : Leeson's Phase Noise Model – Oscillator Phase Noise Prediction
- H : Spectrum Analyser Phase Noise Measurement of the Oscillator and ERA-51SM Datasheet
- I : Spectrum Analyser – FSEK30 – Specifications (only relevant pages)
- J : Aeroflex PN9000 Phase Noise Test System Manual – Oscillator Measurement
- K : Oscillator Phase Noise Measurements – PN9000B
- L : M/A-COM Surface Mount Tuning Varactors - MA46H201
- M : Aeroflex PN9000 Phase Noise Test System Manual - VCO Measurement

CHAPTER 1

INTRODUCTION AND MOTIVATION

1.1 INTRODUCTION

Robert Buderer describes RADAR as “*The Invention That Changed the World*”.

It all started in the frantic summer of 1940. England was under attack by Germany’s Luftwaffe bombers. The only way the British imagined surviving that German invasion was to ship about all of their secret military inventions to the United States. This was a desperate attempt to get the necessary weapons manufactured by the Americans, in order for Britain to win the war.

More or less by accident, only a few months earlier, the British invented one special secret. At the time the concept wasn’t properly understood, not even by its designers. The secret invented was a “*resonant cavity magnetron*”, which was responsible for producing radio energy. But the difference was that it produced radio energy at a level far beyond that of any other existing source at the time, operating at useful wavelengths. This “*resonant cavity magnetron*” laid the foundation for the American and British radar systems; the key to building high power short-wavelength radars.

Buderer ended his input by saying that while the atomic bomb ended the Second World War, radar won it...

One of the foremost applications seen in electronics and electromagnetics is the development of radar. Quite a long list of modern technologies developed from the existence of radar. The radar has for the most part been encouraged by the military; to satisfy the need for surveillance, navigation and weapon control. But radar is also largely employed in civilian applications.

Radar is seen on almost all the major ship transports of the world, as well as on many pleasure boats. Looking at air-traffic, modern commercial air travel is highly dependant on radar for navigation. This includes navigation onboard the aircraft, as well as the air-traffic control done from the ground-base. Radar is making air travel a whole lot safer than travelling by road.

Used as a remote sensor, radar can investigate targets from only a few tens of feet away, for instance traffic speed-meters. It can also investigate up to ranges of hundreds of millions of miles away, for instance large radars probing the universe. For example, the ability to map the contours of far-off planets has been realised using radar.

Today, images of internal organs are clearly visible to physicians and rain fall in distant places is easily measured by meteorologists using radar. Even in modern communication, using long-distance telephone calls provide a much cheaper way than postage. Computers have become omnipresent and today, one can even prepare your dinner during the advertisement break, while watching television [1, 2].

1.2 MOTIVATION

Oscillators play a major role in a radar system. When the radar is in transmit mode, the oscillator is responsible for the up conversion of the message signal to a suitable frequency, associated with the antenna. On the other hand, for the radar in receive mode, the oscillator down converts the received signal to an intermediate frequency, where it gets filtered and then further down converted to baseband for the necessary signal analysis to take place.

One of the most important considerations when evaluating the performance of wireless systems is the *effect of noise*. This is true because, the threshold for the minimum signal level that can reliably be detected by a receiver is ultimately determined by the amount of noise present in the system. This is **very** important in radar applications. For instance, a transmitter can cause significant interference to

other services even if minute amounts of phase noise is present on a transmitter signal. In the case of a receiver, phase noise seriously degrades the receiver's selectivity by causing *reciprocal mixing*, which is directly associated with the local oscillators involved.

Determining the *phase noise* present in a signal gives a clear indication of the limit it sets on the dynamic/operating range of a system. A few systems that are negatively influenced by *phase noise* are for instance, radar's operating range and its ability to detect different targets at the same time; the quality of television images; the precision of satellite positioning and the quality of data transmission.

By keeping all of the above said in mind, it becomes clear why the design of ***low phase noise oscillators*** is a critical factor in the development of a reliable radar system.

1.3 PROPOSED SOLUTION

In this project, the goal was pursued to bring about the design of a ***low phase noise oscillator***. Once the former was accomplished, the design was altered to also obtain a *low phase noise voltage controlled oscillator* (VCO).

In order to achieve low phase noise, one of the techniques applied was to make use of a high-Q resonator. In this project it was decided to design a *transmission line – cavity resonator*, since both types demonstrate reasonably higher Q-values than the usual lumped element resonators. Cavity resonators are also more appropriate at higher frequencies, for instance 1 GHz which was the design frequency for this project.

In designing the resonator, it was confirmed by derivation that an optimal point for *minimum phase noise* does exist. This was recognised by comparing the amount of power dissipated inside the resonator to that dissipated in the source and

the load. Following the latter, the allowed amount of coupling to the resonator was identified, assuring minimum phase noise. Since a specific amount of coupling to the resonator was sought after, it had to be practically feasible. Therefore several coupling techniques were investigated to ensure the most user-friendly way of tuning the amount of coupling to the resonator and hence easily reaching the optimum point of minimum phase noise.

Once the oscillator design was completed and successfully measured, it was modified for VCO use by means of variable tuning diodes. These variable tuning diodes, also called varactor diodes, were positioned inside the cavity of the resonator. Again, the most suitable position to place the diodes had to be determined. This specific location was determined through considerably detailed transmission line theory; where the *loaded Q-value*, the *tuning bandwidth* (amount of change in frequency reached) and the amount of *power dissipated inside the resonator* were measured against each other.

By means of the necessary phase noise measurements, it was confirmed that in order to keep the phase noise to a minimum, the tuning bandwidth had to be kept small and the amount of power dissipated inside the resonator maximised so as to keep the overall loaded Q-value of the circuit as high as possible.

1.4 THESIS ORGANISATION

Although it is in the intent to give a detailed description of every aspect covering the theory and design of low phase noise oscillators, no single volume, including this one, can ever be complete. All of the *necessary* theory and explanations are covered in order to provide a *useful guide in designing low phase noise oscillators*. At the end of the thesis a list of all references used is provided for those readers desiring additional information.

The first chapter serves as a *brief history behind the development of radar*, as well as motivation for this project, the proposed solution and lastly an overview of the thesis.

Chapter 2 provides a detailed description on the *theoretical design of oscillators*. This comprises the general analysis of a transistor oscillator, followed by typical simulation results one could obtain. Also included in Chapter 2 is a comprehensive account on the theory behind noise, and specifically phase noise in oscillator systems. All of the necessary mathematical equations used to describe an oscillator system are also shown, for example the derivation of *Leeson's Phase Noise Model*. Advice is given on ways to minimise phase noise in oscillators, as well as in VCOs.

Chapter 3 starts by showing the derivation of the optimum point for minimum phase noise in oscillators. It further describes the *various parts constituting an oscillator system* as a whole. Firstly, the resonator is discussed. The discussion involves all calculations regarding the theoretical design of the resonator, the simulation results obtained from several software packages, all measurements done and the important results obtained. The active component and all of the other feedback-loop elements, for example the attenuators and the coupler used are also described. Lastly, a theoretical prediction of the oscillator phase noise is given before the measured phase noise results are shown.

Chapter 4 describes the *VCO system* as a whole. Firstly, the use of variable tuning diodes is discussed. The section consists of all the necessary design theory involved in obtaining the optimum point to connect the varactor diodes inside the resonator. All necessary simulation and measurement results for the VCO system are shown. Chapter 4 also includes all measured phase noise results for the VCO, as obtained from the *Aeroflex Automatic Phase Noise Test System*.

Chapter 5 gives a summation of all the relevant results of both the Oscillator and the Voltage Controlled Oscillator systems.

Chapter 6 ends the thesis by adding valuable conclusions and some future recommendations.

CHAPTER 2

LITERATURE REVIEW: OSCILLATORS

2.1 THEORETICAL LAYOUT

2.1.1 Classical Feedback System

A microwave oscillator is one of the most basic and an essential component in a microwave system, considering it converts DC power into RF power. In the development of a communication system, an oscillator is usually the first circuit needed, since it is used as a signal source. An energy source is used to produce a periodic waveform. The key is for the oscillator to be self-sustaining, and the basic criteria for such oscillations are:

- Initial signal needed
- Active element with gain at ω_0
- Frequency selective element
- In-phase, positive feedback (system loop gain = 1) [3].

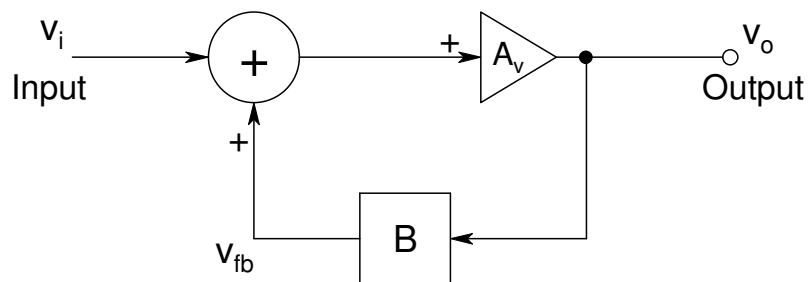


Figure 2.1: Classical feedback system of an oscillator.

The noise present in the actual oscillator circuit serves as the initial signal needed to start the oscillation seeing that the latter will never begin spontaneously. Since the oscillator circuit itself dissipates energy, it overcomes its losses by applying energy into the resonant device, at the resonant frequency. An active element is needed to provide the necessary energy. To initiate and sustain the

steady-state oscillations, the gain of the active element should exceed the loss of the resonant device. The frequency of the oscillator is controlled by the resonant device.

For the oscillator to reach a stable oscillation stage, the feedback system has to answer to the *Barkhausen criteria* [3], namely:

- At the loop closure point the feedback signal must be exactly in phase with the original input signal. In other words, the total phase shift through the active element and resonant device must be a multiple of 360° .
- Taken as a whole, the steady-state gain around the feedback loop must exactly be equal to unity. Stated mathematically, $A_v B = 1$.

The overall *system* gain A_{fb} can be derived from Fig. 2.1, by noting the following:

$$v_{fb} = Bv_o \quad (2.1)$$

$$v_o = (v_i + v_{fb})A_v \quad (2.2)$$

Eliminate v_{fb} by substituting (2.1) into (2.2), which will yield the following equation:

$$A_{fb} = \frac{v_o}{v_i} = \frac{A_v}{1 - A_v B} \quad (2.3)$$

where

v_i = original input signal

v_o = output signal

v_{fb} = feedback signal

A_v = forward system gain

B = fraction of the output fed back to the input (*feedback factor*)

A_{fb} = overall *system* gain with feedback.

The difference between an amplifier and an oscillator is negative- vs. positive feedback respectively. For the former, stability is crucial, and therefore the loop gain $A_v B$ must experience a phase inversion. Hence, for systems with negative feedback, $A_{fb} = A_v / (1 + A_v B)$. On the other hand, from (2.3) it is clear that when the

Barkhausen criteria are met and $A_v B = 1$, the overall feedback gain goes to infinity and the system becomes unstable, so that,

$$A_{fb} = A_v / (1 - 1) \rightarrow \infty.$$

This behaviour is essential for oscillators, while it is undesirable in negative feedback systems. When sufficient energy is coupled back from the amplifier output to the amplifier input it becomes unstable and starts oscillating. For that reason an oscillator is often referred to as an unstable amplifier. Once oscillation is established, it is possible to achieve a nonzero output for a zero input voltage, forming an oscillator.

Also, from (2.3) it can be seen that for the loop gain $A_v B > 1$, the overall system gain A_{fb} will become negative (representing a 180-degree phase shift, for example, $A_{fb} = -100 = +100 \angle 180^\circ$), making the oscillator serve as an inverter. The system will be in saturation and the operation will be non-linear. This consequently will increase the system's phase noise.

For the case in which the loop gain $A_v B < 1$, A_{fb} will decrease as $A_v B$ gets smaller. The oscillation becomes unstable when not enough energy gets fed back to the amplifier input; in which case the oscillation could die out at any moment.

2.1.2 General Analysis of Transistor Oscillator Circuits

(The text contained from this section up to before 2.3, is only submitted as an example to understand oscillator design in-depth, even though it was not the focus of this Master study)

There are several possible configurations for oscillator design. A popular one for up to very high frequencies is the Colpitts oscillator circuit.

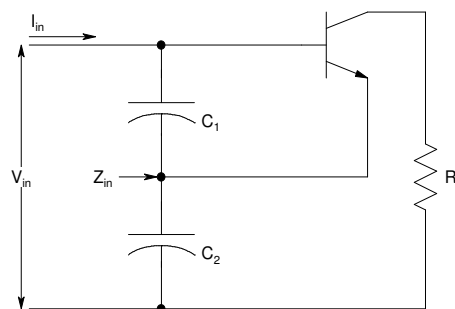


Figure 2.2: Voltage divider of the Colpitts oscillator.

The rule of operation for the feedback loop in the circuit illustrated in Fig. 2.2 is that it generates a negative impedance, which compensates for all the losses present.

The following analysis will demonstrate the calculations needed to determine the necessary conditions for oscillation. Looking at an ideal tuned circuit ($Q \rightarrow \infty$), with no resistance element present to dissipate the energy, it is clear that once excited, the circuit will oscillate infinitely. On the other hand, because of the energy dissipated due to the resistance present in an actual resonant device (finite Q), all oscillations will die out. To be able to maintain the oscillations, it is the function of the amplifier to supply sufficient energy, equal to the quantity dissipated. The energy supplied by the amplifier can be seen as a negative resistor (supplying energy instead of dissipating it), in series with the resonant circuit. The oscillation amplitude will increase if the total circuit resistance is negative, but will die out for a positive resistance. For oscillation to continue, it is desired that the two resistors (liable for the dissipated- and supplied energy respectively) be of equal magnitude [4].

By deriving the input impedance of the circuit in Fig. 2.2, it will be shown how the negative resistance is realized.

2.1.2.1 Circuit Parameters

First, consider the AC equivalent circuit for that in Fig. 2.2. The small-signal equivalent circuit for the bipolar transistor can be represented by the **hybrid- π** model, as follows:

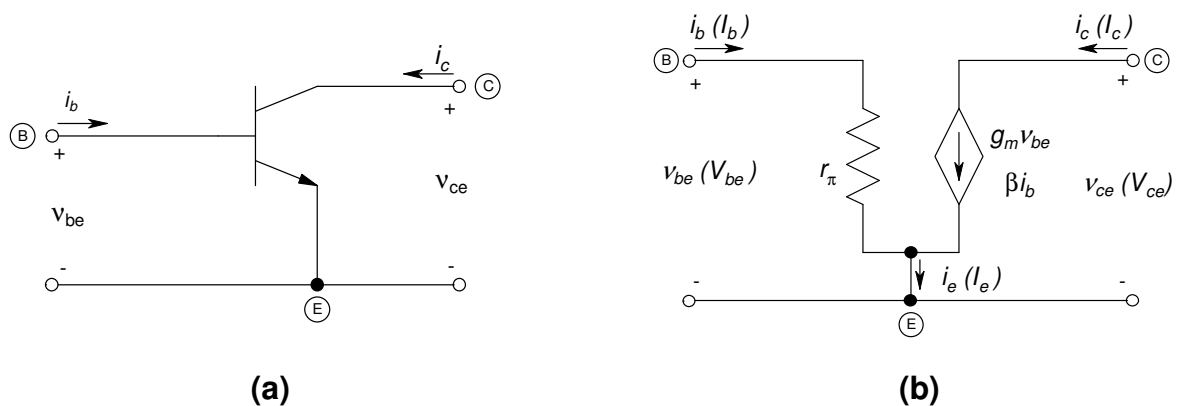


Figure 2.3: (a) Common-emitter npn BJT and (b) a simplified small-signal hybrid- π equivalent circuit for the npn transistor.

In Fig. 2.3 different notations are visible. The latter is necessary, since both time-varying as well as dc currents and voltages are being dealt with. The instantaneous *ac signal* values are presented by a lowercase letter with a lowercase subscript, such as i_b or v_{be} , whereas an uppercase letter with a lowercase subscript, such as I_b or V_{be} , indicates *phasor quantities*.

The resistance r_π is the base-emitter input resistance. Also called the **diffusion resistance**; it is a function of the *Q-point* (quiescent) parameters.

$$r_\pi = \left. \frac{\partial v_{BE}}{\partial i_B} \right|_{Q-pt} = \frac{v_{be}}{i_b} = \frac{V_T}{I_{BQ}}. \quad (2.4)$$

The parameter g_m is called the **transconductance**, since it relates a current in the collector (output), to a voltage in the base-emitter (input) circuit, and is written as

$$g_m = \left. \frac{\partial i_C}{\partial v_{BE}} \right|_{Q-pt} = \frac{i_c}{v_{be}} = \frac{I_{CQ}}{V_T}. \quad (2.5)$$

β is called an **incremental** or **ac common-emitter current gain**, and illustrates the relation between the small-signal collector current and the small-signal base current, as demonstrated in the following equation,

$$i_c = \left. \frac{\partial i_C}{\partial i_B} \right|_{Q-pt} \cdot i_b \equiv \beta \cdot i_b \Rightarrow \beta \cong \frac{i_c}{i_b}. \quad (2.6)$$

Consequently the relation between r_π and g_m is derived as,

$$r_\pi g_m = \left(\frac{\beta_F V_T}{I_{CQ}} \right) \left(\frac{I_{CQ}}{V_T} \right) = \beta_F. \quad (2.7)$$

The difference between β_F and β , is that β_F indicates the ratio between the dc collector- and dc base current (including all possible existing leakage currents); while β indicates the ratio between the incremental change in both the collector and base currents. It is said that $\beta_F \equiv \beta$ in an ideal BJT when all leakage currents are being neglected and the assumption is followed that β_F is independent of collector current.

However, it is important to keep in mind that β does vary with collector current and that β may differ from one device to another.

Notice that the collector current $i_C = \alpha_F I_S (e^{v_{BE}/V_T}) \cdot (1 + v_{CE}/V_A)$, varies with the collector-emitter voltage v_{CE} in the forward active region for different constant values of the base-emitter voltage v_{BE} ; it indicates that the slope is nonzero and therefore the resistance looking into the collector is finite. This is called the *Early Effect* and can be taken into account by adding an extra resistor r_o to the small-signal circuit in Fig. 2.3(b). The Early effect is that collector-emitter voltage, where $i_C = 0$.

The ***small-signal, transistor output resistance*** r_o looking back into the collector, is

$$\frac{1}{r_o} = \left. \frac{\partial i_C}{\partial v_{CE}} \right|_{v_{BE}=\text{const.}} \Rightarrow r_o \cong \frac{V_A}{I_{CQ}} \quad (2.8)$$

where

V_A = Early voltage, $50 < V_A < 300$ [V]

I_{CQ} = quiescent collector current when v_{BE} is a constant, and v_{CE} is small compared to V_A

I_S, α_F = assumed constant.

Two additional resistances, r_b and r_μ can also be added to Fig. 2.3(b). The ***series resistance*** of the transistor, semiconductor material between the external base terminal B and some ideal internal base region B' (see Fig. 2.4, below), is represented by the parameter r_b . In general r_b is usually insignificant at low frequencies since r_b is much smaller than r_π , only a few tens of ohms. On the other hand, r_b should definitely be taken into consideration when working at higher frequencies, since the input impedance becomes capacitive.

Another resistance called the ***reverse-biased diffusion resistance*** of the base-collector junction is represented by the parameter r_μ . This resistance presents some feedback between the output and input of the transistor circuit, which means

that the base current is a slight function of the collector-emitter voltage. In general, r_μ can be neglected (open circuit) since it is typically in the order of megohms.

The following circuit (Fig. 2.4) summarizes the preceding discussion:

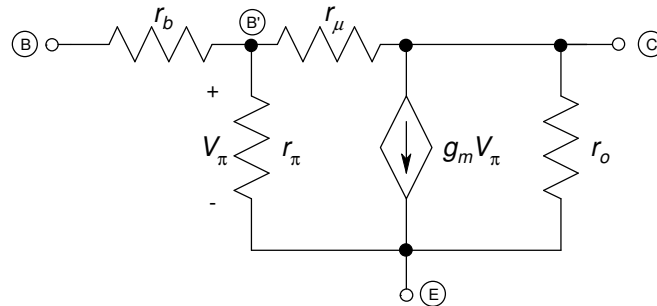


Figure 2.4: Expanded hybrid – π equivalent circuit of Fig. 2.3(b).

Another way of relating the small-signal, terminal currents and voltages of a two-port network, is by using the h – **parameters**. The latter are usually obtained from the bipolar transistor data sheets, and easily characterize an equivalent circuit model for the BJT, as shown in the following figure.

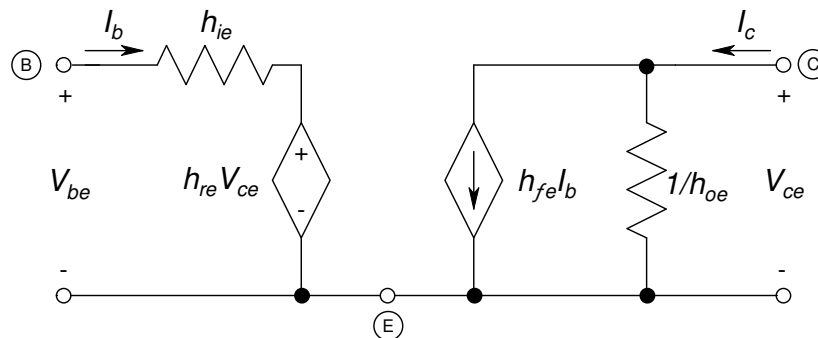


Figure 2.5: The h -parameter model of the common-emitter BJT.

By making use of Fig. 2.5 and Kirchoff's current- and voltage laws, the following linear, small-signal voltage-current relationships are obtained,

$$V_{be} = h_{ie} I_b + h_{re} V_{ce} \quad (2.9)$$

$$I_c = h_{fe} I_b + h_{oe} V_{ce} \quad (2.10)$$

Note the different subscripts used: i for input, r for reverse, f for forward, o for output, and e for common emitter.

The relation between the **hybrid**– π model and the **h –parameters** is shown by making use of the equivalent circuit shown in Fig. 2.4. *First*, the parameters h_{ie} and h_{fe} are determined by short-circuiting the output, thus making $V_{ce} = 0$. Therefore, Fig. 2.4 is transformed to the following circuit:

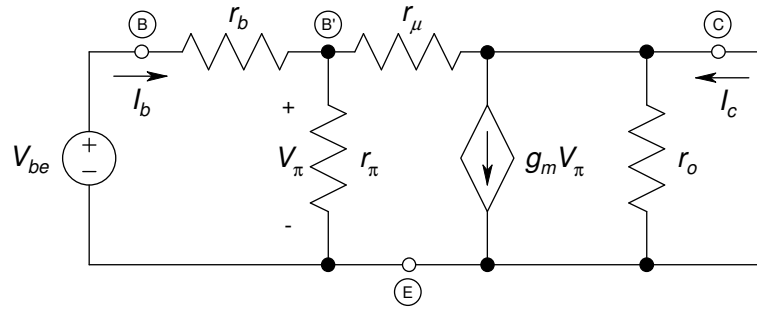


Figure 2.6: Expanded hybrid– π equivalent circuit with the output short-circuited.

Consequently, from (2.9), the **small-signal input resistance** h_{ie} , can be written as

$$h_{ie} = \left. \frac{V_{be}}{I_b} \right|_{V_{ce}=0} \quad (2.11)$$

and following from (2.11) and Fig. 2.6,

$$h_{ie} = r_b + r_\pi \parallel r_\mu \cong r_\pi \quad (2.12)$$

for the case in which r_b is very small and r_μ is very large.

From (2.10), the **small-signal current gain** parameter h_{fe} , can be written as

$$h_{fe} = \left. \frac{I_c}{I_b} \right|_{V_{ce}=0} . \quad (2.13)$$

Since the short-circuit collector current (from Fig. 2.6) is $I_c = g_m V_\pi$, and the voltage V_π is given as $V_\pi = I_b r_\pi$ (for a very small r_b and a very large r_μ), the current gain can be written from (2.6) and (2.7) as

$$h_{fe} = \left. \frac{I_c}{I_b} \right|_{V_{ce}=0} = g_m r_\pi = \beta . \quad (2.14)$$

In most situations, at low frequency, h_{fe} is essentially equal to β .

Secondly, the parameters h_{re} and h_{oe} are determined by defining the input signal base current as zero, thus making $I_b = 0$. Therefore, Fig. 2.4 is transformed to the following circuit:

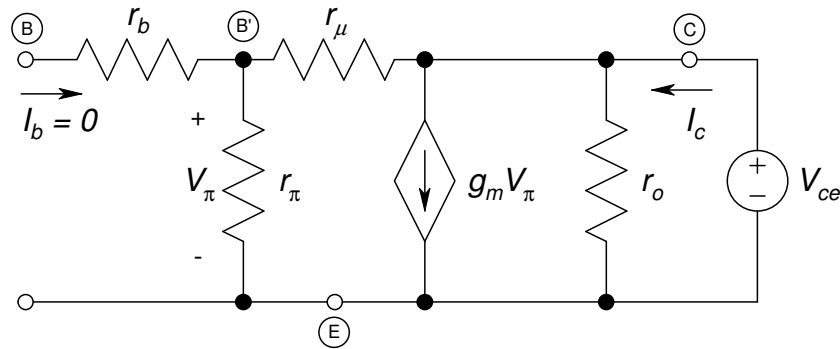


Figure 2.7: Expanded hybrid- π equivalent circuit with the input open-circuited.

From Fig. 2.7 it is clear that since I_b is defined as zero, the associated voltages are

$$V_{be} = V_{\pi} = \left(\frac{r_{\pi}}{r_{\pi} + r_{\mu}} \right) \cdot V_{ce}. \quad (2.15)$$

The **voltage feedback ratio**, indicated by the *third* parameter h_{re} , can be written as

$$h_{re} = \left. \frac{V_{be}}{V_{ce}} \right|_{I_b=0} \quad (2.16)$$

and therefore, from (2.15),

$$h_{re} = \left. \frac{V_{be}}{V_{ce}} \right|_{I_b=0} = \frac{r_{\pi}}{r_{\pi} + r_{\mu}} \cong \frac{r_{\pi}}{r_{\mu}}. \quad (2.17)$$

Since $r_{\pi} \ll r_{\mu}$ the value of h_{re} is very small, and can therefore usually be ignored.

The last and *fourth* h -parameter is the **small-signal output admittance** h_{oe} . From (2.10), it can be written that

$$h_{oe} = \left. \frac{I_c}{V_{ce}} \right|_{I_b=0}. \quad (2.18)$$

Looking at the output node of Fig. 2.7 with $I_b = 0$, a KCL equation produces,

$$I_c = g_m V_\pi + \frac{V_{ce}}{r_o} + \frac{V_{ce}}{r_\pi + r_\mu}. \quad (2.19)$$

From equations (2.14), (2.15) and (2.19), h_{oe} can be written as

$$\begin{aligned} h_{oe} &= \left. \frac{I_c}{V_{ce}} \right|_{I_b=0} \\ &= \left(g_m \left(\frac{r_\pi}{r_\pi + r_\mu} \right) V_{ce} + \frac{V_{ce}}{r_\pi + r_\mu} + \frac{V_{ce}}{r_o} \right) / V_{ce} \\ &= \frac{1 + \beta}{r_\mu} + \frac{1}{r_o} \\ &\cong \frac{1}{r_o} \end{aligned} \quad (2.20)$$

for $r_\pi \ll r_\mu$, since $r_\mu \rightarrow \infty$ in the ideal case [5].

2.1.2.2 Derivation of the Input Impedance

Now that it is clear where all the circuit parameters come from, Fig. 2.2 can be transformed to Fig. 2.8, from which the input impedance can easily be derived.

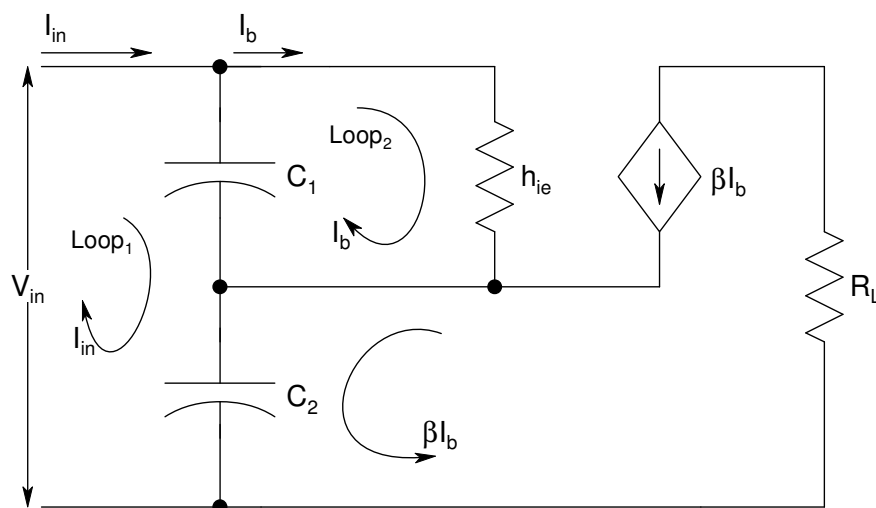


Figure 2.8: Equivalent small-signal circuit of Fig. 2.2.

By applying Kirchoff's voltage law, summing the voltages along a closed loop, the following equations are derived.

Loop 1:

$$V_{in} = I_{in}(Z_{C1} + Z_{C2}) - I_b(Z_{C1} - \beta Z_{C2}). \quad (2.21)$$

Loop 2:

$$0 = -I_{in}(Z_{C1}) + I_b(Z_{C1} + h_{ie}). \quad (2.22)$$

From (2.22) an equation for I_b is obtained as,

$$I_b = I_{in} \left(\frac{Z_{C1}}{Z_{C1} + h_{ie}} \right). \quad (2.23)$$

Substitute (2.23) into (2.21), so that

$$V_{in} = I_{in}(Z_{C1} + Z_{C2}) - I_{in} \left(\frac{Z_{C1}}{Z_{C1} + h_{ie}} \right) (Z_{C1} - \beta Z_{C2}).$$

Thus, from the previous equation, the input impedance Z_{in} is:

$$Z_{in} = \frac{V_{in}}{I_{in}} = \frac{(1 + \beta)Z_{C1}Z_{C2} + h_{ie}(Z_{C1} + Z_{C2})}{Z_{C1} + h_{ie}}. \quad (2.24)$$

In case $X_{C1} \ll h_{ie}$, it can be written from (2.24) that

$$Z_{in} \approx \frac{1 + \beta}{h_{ie}} Z_{C1}Z_{C2} + (Z_{C1} + Z_{C2}). \quad (2.25)$$

Since,

$$Z_{in} = (R_{in} - jX_{in}) = R_{in} - j \left(\frac{1}{\omega C_{in}} \right),$$

$\beta = g_m r_\pi$ and $h_{ie} \cong r_\pi$; (2.25) can be written as:

$$Z_{in} \approx \left(\frac{-g_m}{\omega^2 C_1 C_2} \right) - j \left(\frac{1}{\omega [C_1 C_2 / (C_1 + C_2)]} \right). \quad (2.26)$$

Consequently, from (2.26) it is clear that the input impedance of the circuit shown in Fig. 2.8 has a negative resistance,

$$R_{in} = \frac{-g_m}{\omega^2 C_1 C_2}; \quad (2.27)$$

in series with a capacitive reactance, with

$$C_{in} = \frac{C_1 C_2}{C_1 + C_2}, \quad (2.28)$$

the series combination of C_1 and C_2 . The ratio C_1/C_2 can be selected greater than 1, so that the circuit has sufficient loop gain for the start up condition at the lowest operation temperature. In other words, greater feedback occurs when $C_1 > C_2$.

The condition for sustained oscillation is a positive, series resistance R_s , and is obtained by connecting an inductor L across the input, so that with the inductor's equivalent resistance $R_L = R_s$, it can be written that

$$R_s = +R_{in} = \frac{g_m}{\omega^2 C_1 C_2}. \quad (2.29)$$

The frequency of oscillation is given by $\omega = 1/\sqrt{LC}$, therefore

$$f_o = \frac{1}{2\pi\sqrt{LC_{in}}}. \quad (2.30)$$

2.1.2.3 Strategies for Proper Oscillator Design

Following from the above analysis are a few important strategies for the proper design of an oscillator. Firstly consider the feedback capacitors. In order for the transistor's internal base-to-emitter and collector-to-emitter capacitances to have an insignificant effect on the oscillator circuit's performance, it is important to choose the value of the feedback capacitors C_1 and C_2 as large as possible. Since the equivalent impedance of a capacitor is given by $Z_C = 1/j\omega C$, it can be said that for C_1 as large as possible it is obtained that $X_{C1} \ll h_{ie}$, and for C_2 also large it follows that, $X_{C2} \ll 1/h_{oe}$.

It is important to notice that there is a definite limit to how large the capacitances can be made. In other words, how small the input reactance is allowed to become, since $X_{in} = 1/\omega C_{in}$. As the capacitance increases, the magnitude of R_{in} gets smaller and at some stage will no longer be large enough to compensate the losses. As mentioned earlier, there is a tuned circuit connected in series with the negative resistance. When for example the tuned circuit consists of an inductor with resistance r_L , then for oscillation to be maintained, it is said that the energy E ,

($E_{\text{Dissipated, resonant device}} \leq E_{\text{Delivered, active element}}$), thus

$$r_L \leq \frac{g_m}{\omega^2 C_1 C_2}. \quad (2.31)$$

When the transistor's maximum transconductance is presented by $G = \max(g_m)$ and the product of series capacitances C_1 and C_2 is a maximum when $C_1 = C_2 = C_m$, it can be written that,

$$r_L \leq \frac{G}{\omega^2 C_m^2} \Rightarrow \sqrt{\frac{r_L}{G}} < \frac{1}{\omega C_m}. \quad (2.32)$$

Thus, for sustained oscillations, it is clear from equation (2.32) that the minimum acceptable reactance X_m is greatly determined by the inductor's series resistance r_L , as well as the transconductance of the transistor $g_m = \beta/r_\pi$ [4].

2.2 SIMULATION EXAMPLE

Oscillators can be analysed in both the frequency domain as well as in the time domain. For the former, the harmonic balance technique is being used, while for the latter a transient simulator such as *SPICE* is applied. Since RF/Microwave engineers are mostly interested in the steady-state condition and not the transient process (start-up) of the oscillator, the harmonic balance approach would be the analysis of choice, since the latter computes the steady-state directly. Although frequency domain analysis is the actual choice for the analysis of oscillators, in

particular those that operate at high frequencies, difficulties do arise from the mathematical implications. This happens especially in high-Q circuits, because of the lack of knowledge of the fundamental oscillation frequency.

AWR Microwave Office (MWO) addressed the last mentioned challenge, when analysing an oscillator in the frequency domain, by implementing a special device called the '*Oscillator Analysis Probe*', or *OSCAPROBE*. This built in probe initiates a large-signal oscillator simulation. It is an ideal source in series with an ideal impedance element. The impedance presents an open circuit at all frequencies other than the fundamental frequency of oscillation. Since a lack of knowledge towards the fundamental oscillation frequency exists, it is necessary to define two fundamental parameters for the oscillator probe, namely F_{start} and F_{end} . These two parameters indicate the range in which to search for the start-up frequency. Choosing roughly $\pm 25\%$ of the resonator's centre frequency is sufficient in most cases [6].

2.2.1 Linear Analysis (*MWO*)

The following linear analysis will demonstrate the simulation of a typical Colpitts oscillator [7] in *AWR Microwave Office (MWO)*. There are two ways in which *MWO* can determine the oscillation frequency. The first is to look at the port impedances, and the second by using the previously mentioned *OSCAPROBE*.

2.2.1.1 Port Impedances

Firstly, as mentioned before, for an oscillation to start and be maintained, it is essential that the dissipated energy in the resonant circuit is at most, equal to the energy delivered by the active element. In other words, the reactance looking back into the resonant device $\text{Im}[Z_{\text{Resonator}}]$, and the reactance looking into the active element $\text{Im}[Z_{\text{Active}}]$, should sum to zero. The frequency at which the following equation holds true, gives an estimate of the oscillation frequency,

$$\text{Im}[Z_{\text{Active}}] + \text{Im}[Z_{\text{Resonator}}] = 0. \quad (2.33)$$

To illustrate equation (2.33), the following simulation was done:

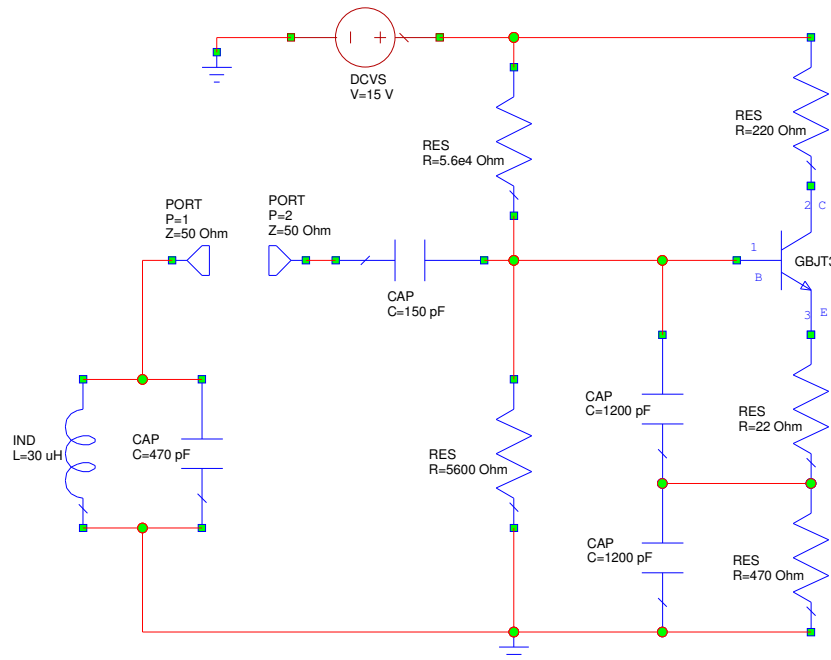


Figure 2.9: The complete Colpitts oscillator. Test circuit for simulation purposes.

In Fig. 2.9 port 1 indicates the impedance looking back into the resonant device; whereas port 2 indicates the impedance looking into the active element. In *MWO*, the following output equations were used to plot the different reactances to illustrate equation (2.33),

$$\begin{aligned} \text{Reactance_Resonator} &= \text{Oscillator:Im}(Z(1,1)) \\ \text{Reactance_ActiveElement} &= \text{Oscillator:Im}(Z(2,2)) \\ \text{Negative} &= -(\text{Reactance_ActiveElement}) \end{aligned}$$

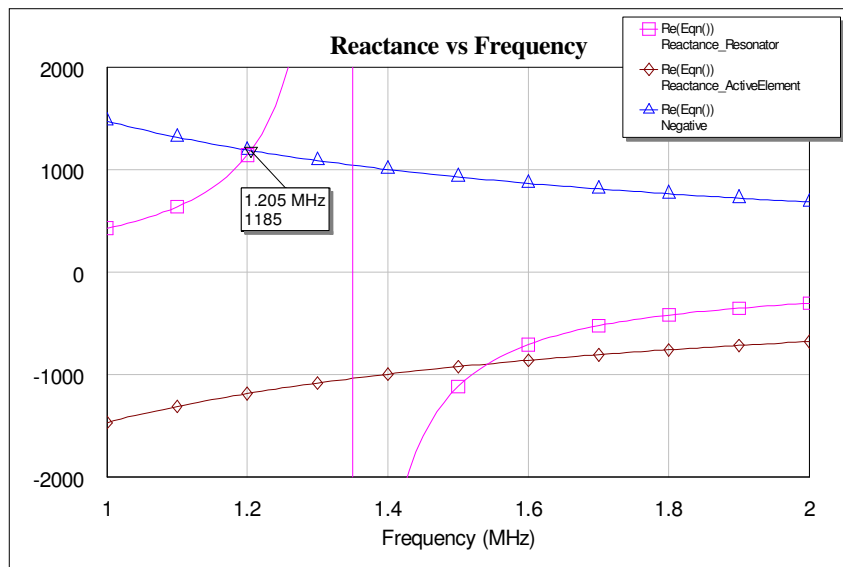


Figure 2.10: $\text{Im}[Z_{\text{Resonator}}]$ and $\text{Im}[Z_{\text{Active}}]$ versus frequency.

Fig. 2.10 is showing the imaginary parts of impedances $Z_{\text{Resonator}}$ and Z_{Active} versus frequency. The oscillation frequency is indicated by the crossover point between the reactance of the resonant device and the negative, of the reactance of the active element. Thus, where $X_{\text{Resonator}} = -X_{\text{Active}}$, from (2.33).

As mentioned earlier, the input impedance of the active element should have a negative resistance. The following output equation was used to plot the latter,

$$\text{Negative_Resistance} = \text{Oscillator:Re}(Z(2,2))$$

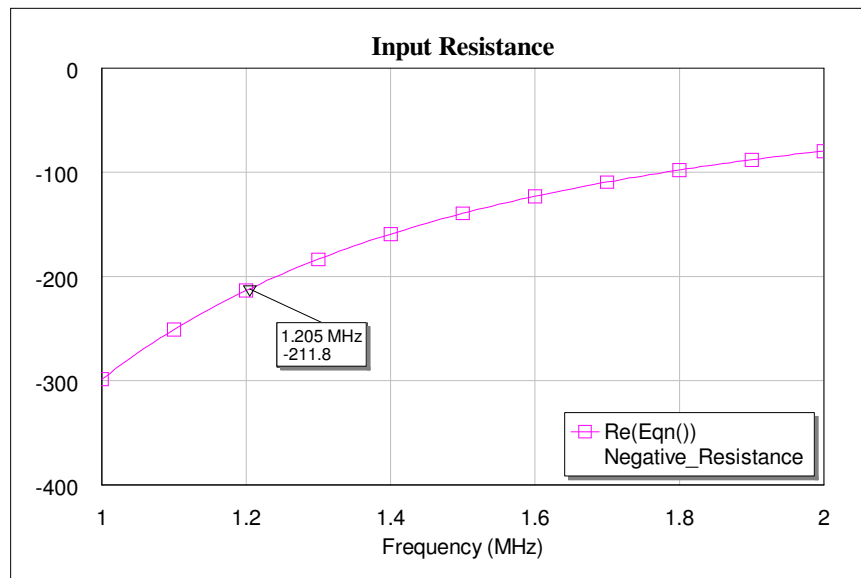


Figure 2.11: $\text{Re}[Z_{\text{Active}}]$ versus frequency.

From Fig. 2.11 it is clear that the input resistance of the active element is negative. It is important that the resistance is sufficiently large to compensate for all of the resonator losses (equation (2.31)). The magnitude of the resistance is controlled by the size of the feedback capacitances, as indicated by equation (2.27).

2.2.1.2 Oscillator Analysis Probe

Secondly illustrated is the use of the *OSCAPROBE* element in *MWO*. It is used for the linear analysis of the oscillator circuit in the frequency domain. Since it makes use of the Harmonic Balance Simulator Method, a solution is estimated and a frequency region specified; in which the simulator then iteratively will determine the specific oscillation frequency at hand.

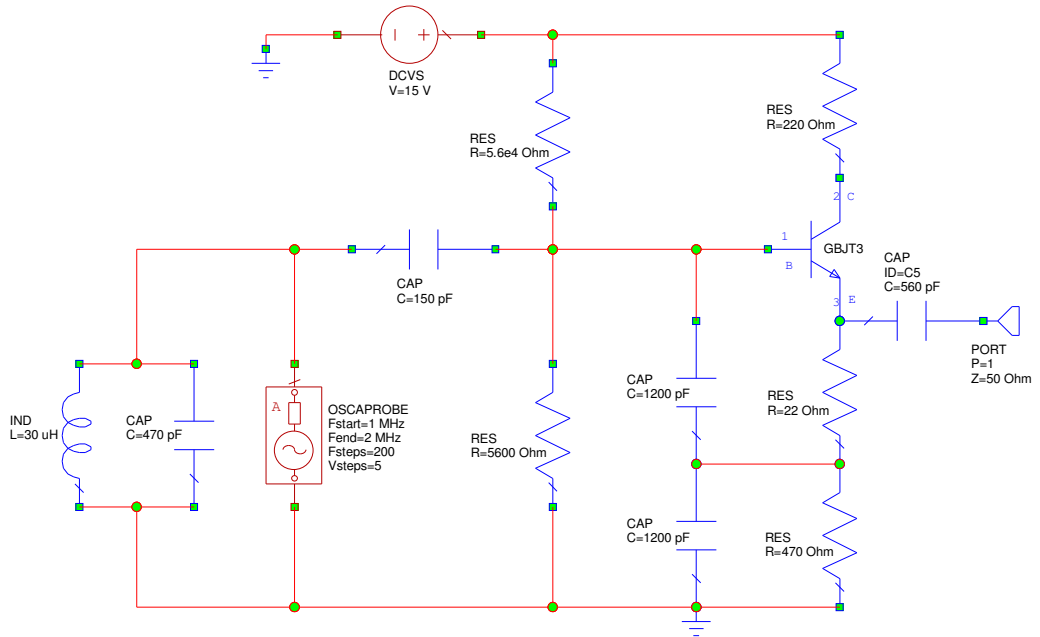


Figure 2.12: The Colpitts oscillator and the use of the *OSCAPROBE* in *MWO*.

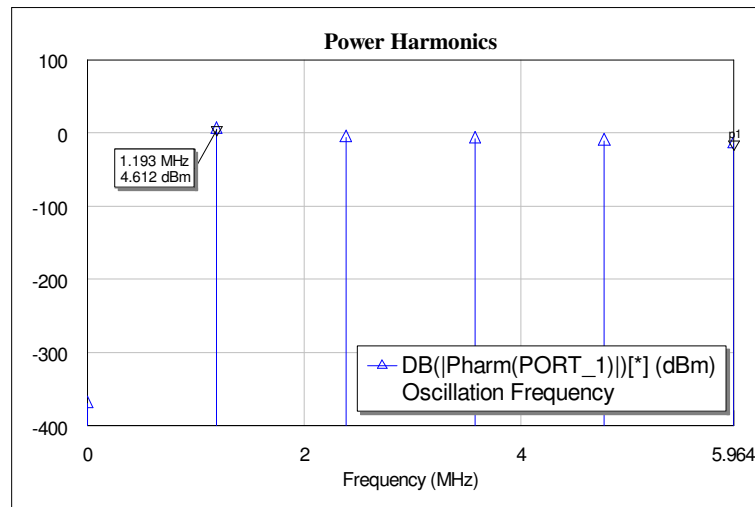


Figure 2.13: Illustration of the oscillation frequency.

Fig. 2.12 gives an illustration of the use of the *OSCAPROBE* in *MWO*. It is customary to place the oscillator probe between the resonant device and the active element in order for it to correctly determine the oscillation frequency. From Fig. 2.13 the associated power harmonics are visible for the circuit in Fig. 2.12. The first fundamental harmonic gives an indication of the oscillation frequency.

2.2.2 Non-linear Analysis (*Orcad PSPICE*)

As mentioned earlier, an oscillator can also be analysed in the time domain. This is a non-linear analysis done by means of a transient solver such as *SPICE*, which makes use of a large-signal *SPICE* model for each of the individual oscillator components.

2.2.2.1 Voltage Probe

Following in Fig. 2.14 is a typical time domain simulation done in *Orcad Capture PSpice* of the same Colpitts oscillator circuit, previously illustrated in Fig. 2.9.

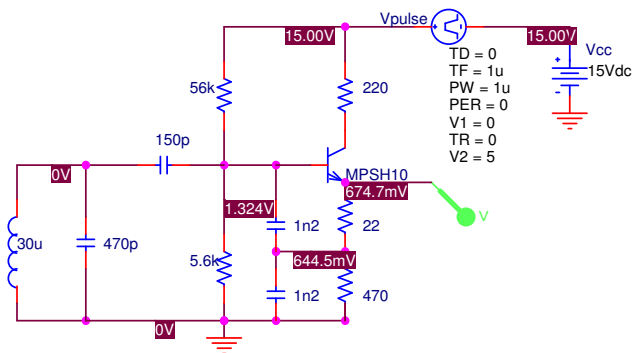


Figure 2.14: Time domain analysis of the Colpitts oscillator in *PSPICE*.

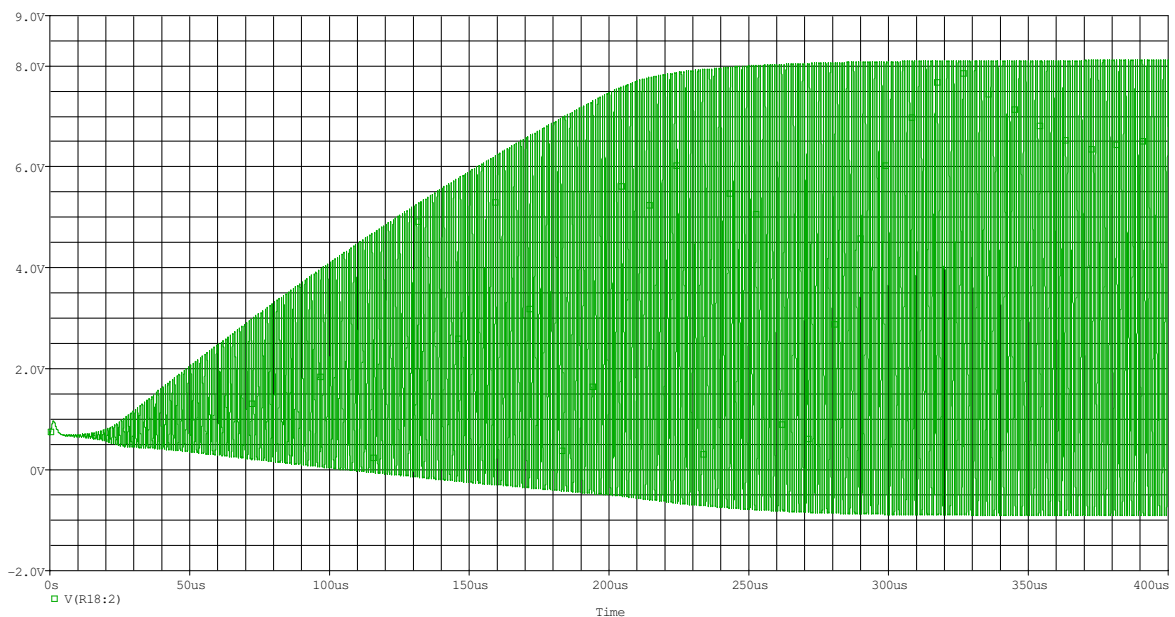


Figure 2.15: Output, emitter voltage v_E , in the time domain.

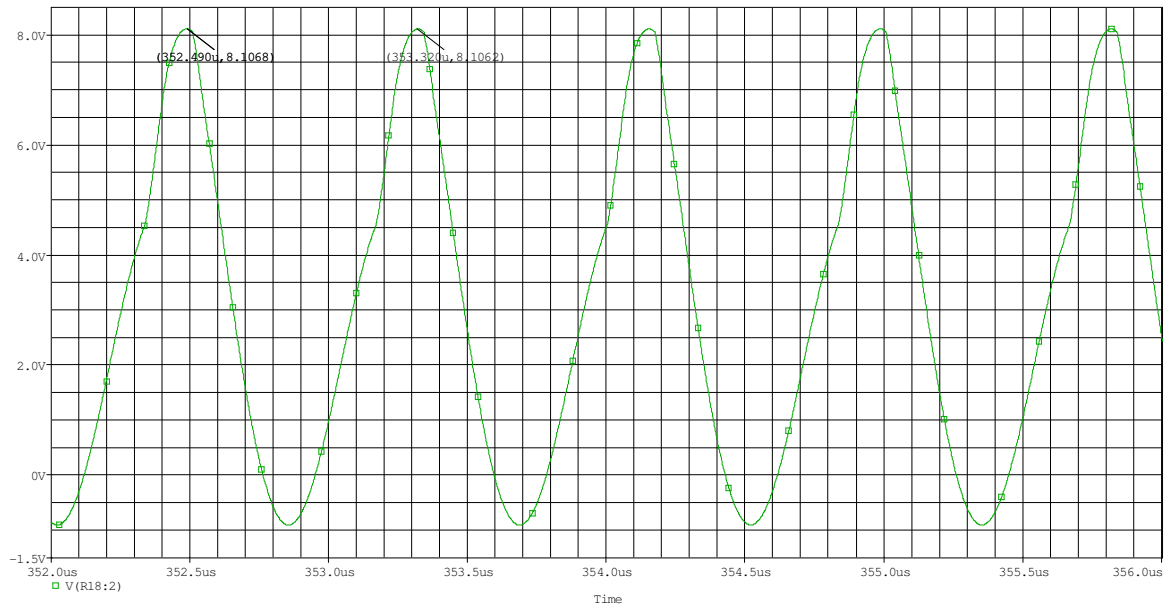


Figure 2.16: Closer look at the emitter voltage $v_E(t)$.

From both Fig. 2.15 and Fig. 2.16 a stable oscillation is visible. By noting the two peak values labelled in Fig. 2.16, the oscillation period can be determined as

$$T_0 = (353.320 - 352.490)\mu\text{s} = 830 \text{ ns},$$

from which the oscillation frequency is given as, $f_0 = \frac{1}{T_0} = 1.2048 \text{ MHz}$.

2.2.2.2 Fourier Transform

One way to confirm the above frequency is to apply the *Fourier Transform* (FFT) to the output, voltage-time signal:

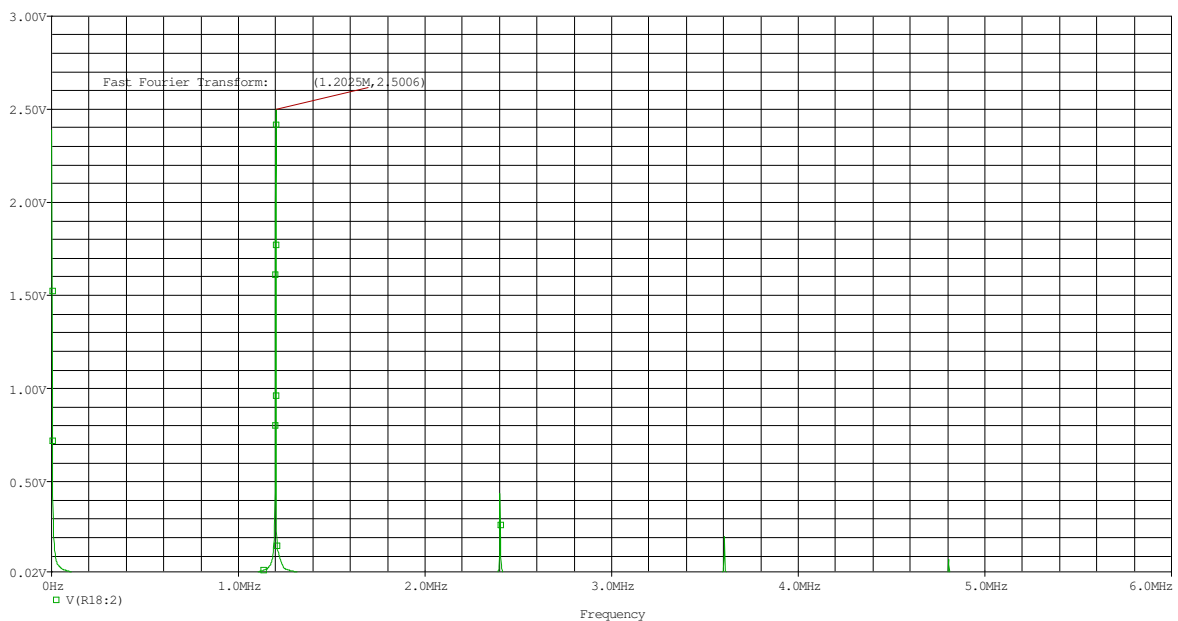


Figure 2.17: Spectrum of the voltage signal $v_E(t)$.

Fig. 2.17 illustrates the predicted output spectrum for the Colpitts oscillator operating at around 1.2 MHz. The resonator serves as a filter, assisting in cleaning up the unwanted harmonics. To achieve an acceptable level of harmonic suppression, the resonator's operating Q must be reasonably high.

Fourier Transforms are used to examine the spectrum of the output of non-linear circuits. Illustrated in Fig. 2.17 is the Fourier transform $V_E(f)$ versus frequency f , which is called the spectrum of the signal $v_E(t)$. Since the spectrum is defined for all frequencies, it is said to be continuous. Mathematically stated,

$$V_E(f) = \int_{-\infty}^{\infty} v_E(t) \cdot \exp(-j2\pi ft) \cdot dt \quad (2.34)$$

In general the Fourier transform $V_E(f)$ is a complex function of the frequency. It may therefore be expressed in the following form

$$V_E(f) = |V_E(f)| \cdot \exp[j \cdot \theta(f)] \quad (2.35)$$

where

$|V_E(f)|$ = amplitude spectrum of $v_E(t)$

$\theta(f)$ = phase spectrum of $v_E(t)$ [8].

All of the above analyses fundamentally achieve the same result for the oscillation frequency. This illustrates that both the linear as well as the non-linear simulation are reliable in giving accurate results.

2.3 PHASE NOISE THEORY

Since phase noise is perhaps the most vital parameter in many oscillators, it should be discussed in-depth; on what it is, how it sways a system's performance and how it can be minimised in an oscillator design. But firstly, a brief discussion will be given on noise theory in general.

2.3.1 Types of Noise

Noise, as defined by the *IEEE*, is any unwanted disturbances superimposed upon a useful signal, which tend to obscure its information content. Random noise is part of the noise that is unpredictable, except in a statistical sense [9].

Noise is inherent to all electrical systems and is a random process related to a variety of sources. Its primary characteristic is its randomness, and this is due to the physical mechanisms which generate it. For example, noise is being generated by RF components and devices as thermal noise, while atmospheric attenuation and man-made interference also generate noise. Noise from the external environment gets introduced to RF and microwave systems by means of the receive antenna. Internally, the receiver circuitry also generates additional noise. The system noise is then represented by both the externally coupled, as well as the internally generated noise [10].

2.3.1.1 Noise in The Circuit

Depending on its origin, noise is presented by two categories, ultimate noise or excess noise.

- *Ultimate noise*
 - This is noise that is only dependant on the physics of materials. It can never be suppressed; but one can optimise its action. This kind of noise is also mathematically expressible and is referred to as ultimate noise, since it sets a lower limit to the system's noise performance.
 - For example: Thermal Noise and Shot Noise.

- *Excess noise*
 - Excess noise is classified as noise dependant on the quality of the components; often on the cleanness of the component surfaces. It is possible that components with very different noise levels are produced by exactly the same manufacturing process. No mathematical expression exists to describe this type of noise.
 - For example: Flicker Noise and Popcorn Noise [11].

- **Thermal Noise**

Thermal noise is the most common type of noise encountered in RF and microwave systems. It is also known as *Nyquist* or *Johnson* noise. Any passive element that contains loss will generate thermal noise due to the random motion of charge carriers, i.e. thermal fluctuations of electrons in the object. Examples of lossy components are resistors or lossy transmission lines.

Thermal noise is modelled as a power source by means of a resistor of value R at temperature T degrees Kelvin [K]. In any object with electrical resistance, the thermal fluctuations of the electrons in the object will generate noise. This happens since the electrons in the resistor exert a kinetic energy proportional to temperature T ; given that they are in random motion. Because of these random motions, small random voltage fluctuations are being produced across the terminals of the resistor.

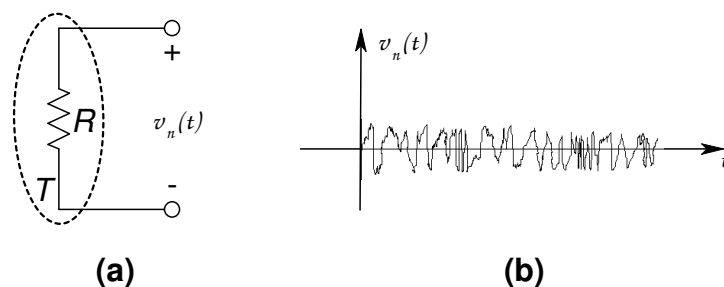


**Figure 2.18: (a) A resistor at temperature T produces the noise voltage $v_n(t)$.
 (b) The random noise voltage generated by a resistor at temperature T .**

From Fig. 2.18(b) the mean value of the noise voltage is zero, while the *root mean square* (rms) value in a narrow frequency bandwidth B is given by the following

Rayleigh-Jeans approximation. Equation (2.36) is valid for frequencies up through the microwave band.

$$V_n = \sqrt{4kTB}, \quad (2.36)$$

where

$k = 1.380 \times 10^{-23}$ [J/K], is Boltzmann's constant

T = the temperature, in degrees Kelvin [K]

B = the bandwidth, in [Hz]

R = the resistance, in [Ω].

Another way to model the noisy resistor is by means of a Thevenin equivalent circuit. In the latter, the resistor is seen as ideal (noiseless) while a voltage generator supplies the rms noise voltage, $v_n(t)$.

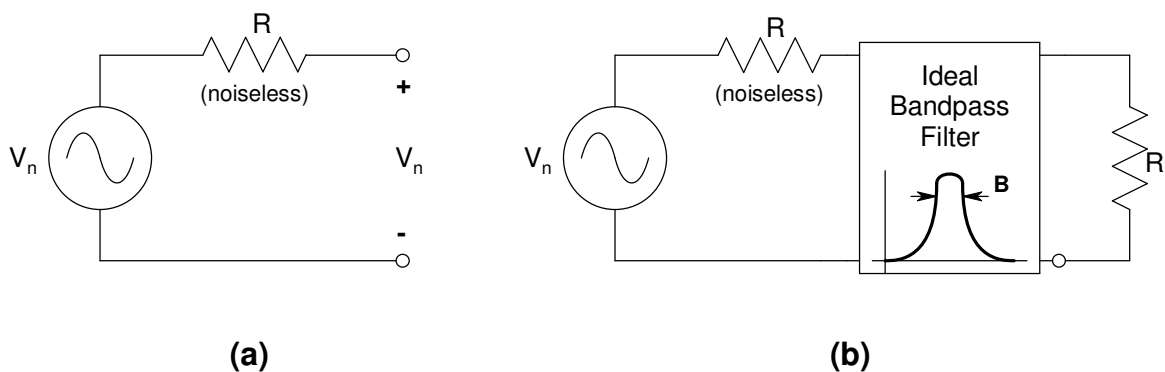


Figure 2.19: (a) The Thevenin equivalent circuit for a noisy resistor. (b) Maximum power transfer of noise power from a noisy resistor to a load over bandwidth B .

In Fig. 2.19(b) a load is connected to the Thevenin equivalent circuit illustrated in Fig. 2.19(a). The maximum power that can be delivered from the Thevenin equivalent circuit to the load resistor is called the **available noise power** and is only possible when the load is conjugately matched to the source. The noise power transmitted to the load is then calculated as

$$P_{an} = \left(\frac{V_n}{2}\right)^2 \frac{1}{R} = \frac{V_n^2}{4R} = kTB, \quad [\text{W}] \quad (2.37)$$

where

V_n = rms noise voltage of the resistor

$\frac{1}{2}$, is due to voltage division between the source and load resistances.

It is important to notice that the *noise power produced* by a resistor R , is given by $P_n = V_n^2 / R$. While the *available noise power delivered* to a load that is matched to the source (resistor, R), is represented by P_{an} . Thus for $R = R_L$ it is obtained that $P_{an} = P_n / 2$, due to the power P_n being split evenly between the source and load resistances.

Equation (2.37) gives wonderful insight into a wide variety of problems involving noise. There are three important conclusions that can be made from (2.37):

- Less noise power is collected if the system has a smaller bandwidth; since P_{an} decreases as B decreases.
- Noise effects generated internally can significantly be reduced by cooling the system down. This is possible since P_{an} decreases as T decreases.
- From (2.37) it is clear that P_{an} only depends on the absolute bandwidth of the system and not on its centre frequency. The spectral density of thermal noise is flat with frequency and therefore it is often referred to as white noise. Thermal noise got its nickname due to the analogy with white light which is composed of all other visible light frequencies.

From equation (2.37) the available noise power from a resistor at temperature $T = 290$ K, in a 1 Hz bandwidth, is calculated as,

$$\begin{aligned} 10\log_{10}(kTB) &= 10\log_{10}[(1.38 \times 10^{-23})(290)(1)] \\ &= -203.98 \text{ dB/Hz} \\ &= -173.98 \text{ dBm/Hz.} \end{aligned} \tag{2.38}$$

The result in (2.38) is often referred to as the **thermal noise floor** of an electric system or the **input thermal noise power** [10].

Another way to represent the noise power is by means of the **power spectral density** (PSD). The latter symbolises the density of the noise power in the spectral (frequency) domain for a given noise voltage. Since the noise power in (2.37) is constant in relation to the frequency, the same can be said for the PSD. The *single-sideband* (SSB) power spectral density of thermal noise is represented by the mean-squared noise voltage, expressed in per unit bandwidth as follows

$$S_m(f) = \frac{V_n^2}{B} = 4kTR \quad [V^2/\text{Hz}]. \quad (2.39)$$

Equation (2.39) is depicted in Fig. 2.20 over a bandwidth B [11].

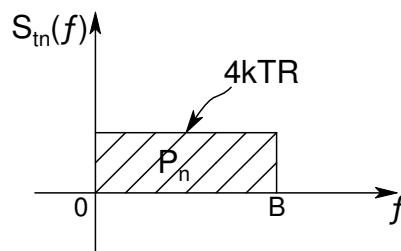


Figure 2.20: SSB PSD of thermal noise.

Following is an example of typical noise computations, involving several noisy resistors.

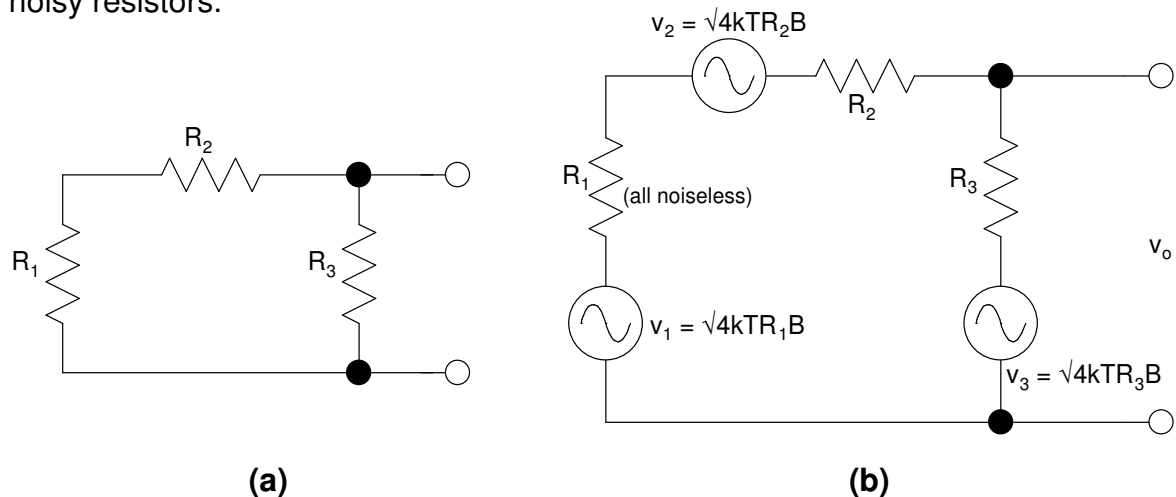


Figure 2.21: Circuits for noise calculation. (a) Resistor network. (b) Noise equivalent circuit.

When the resistor network in Fig. 2.21(a) is considered, the noise voltage due to each resistor across the output terminals is in question. Then by summing the square of the voltages due to each resistor, the square of the rms output voltage v_o is calculated. This can be done since the powers due to independent sources can be

added. By taking the square root of the latter, the rms voltage will be obtained. The calculation yields

$$v_o^2 = v_{o1}^2 + v_{o2}^2 + v_{o3}^2, \quad (2.40)$$

where

$$v_{o1} = \sqrt{4kTR_1B} \left(\frac{R_3}{R_1 + R_2 + R_3} \right),$$

$$v_{o2} = \sqrt{4kTR_2B} \left(\frac{R_3}{R_1 + R_2 + R_3} \right),$$

$$v_{o3} = \sqrt{4kTR_3B} \left(\frac{R_1 + R_2}{R_1 + R_2 + R_3} \right). \quad (2.41)$$

The rms voltage across resistor R_i , is represented by $\sqrt{4kTR_iB}$. By substituting all of (2.41) into (2.40), the voltage in question is obtained.

From the previous example, exceedingly long computations arise if many resistors are involved. The computations can be simplified by making use of *Nyquist's formula* which states that, for any one-port network that contains only resistors, capacitors and inductors, the mean-square noise voltage produced at the output terminals in a 1 Hz bandwidth, is given by

$$v_n^2(t) = 2kT \int_{-\infty}^{\infty} R(f) df \quad (2.42)$$

where

$R(f)$ = the $\text{Re}[Z_{in}(f)]$, and

$Z_{in}(f)$ = the complex impedance seen looking back into the terminals.

If only resistors is presented in the network, the mean-square noise voltage in a bandwidth B is given by,

$$v_n^2 = 4kTR_{eq}B \quad [V^2] \quad (2.43)$$

where

R_{eq} = is the Thevenin equivalent resistance of the network.

Equation (2.43) agrees with (2.36) [12].

- **Shot Noise**

As soon as a potential barrier is present in an electronic device, for instance a diode or a transistor, **shot noise** can be expected. The latter occurs due to the random motion of charge carriers, i.e. the discrete nature of current flow across a potential barrier. For example, consider electron flow in a diode. An average current flow I occurs due to the sum total of electrons emitted from the cathode to the anode. Thus, providing a randomly fluctuating noise power of mean-square value,

$$i_{sn}^2 = 2qIB, \quad (2.44)$$

where

$q = 1.602 \times 10^{-19}$ [C], the charge of an electron

$I =$ the DC current, in [A]

$B =$ the measuring bandwidth, in [Hz].

Equation (2.44) is known as *Schottky's theorem*.

Therefore, the spectral density can be presented as the noise power per bandwidth, B .

$$S_{sn}(f) = \frac{i_{sn}^2}{B} = 2qI \quad [\text{A}^2/\text{Hz}]. \quad (2.45)$$

From (2.45) it is clear that the power spectral density is independent of frequency, as is the case with thermal noise [12, 13].

- **Flicker Noise**

As previously mentioned, flicker noise is classified as a typical excess noise dependent on the quality of the component, for example on the cleanness of its surface. It appears to come from the macroscopic defects of materials. Flicker noise is mostly found in vacuum tubes or steady-state devices such as diodes, transistors and even resistors. At present, still no physical theory is available to describe the mechanism that gives rise to flicker noise. However in general, flicker noise is characterised by its power spectral density, which is illustrated in the following figure.

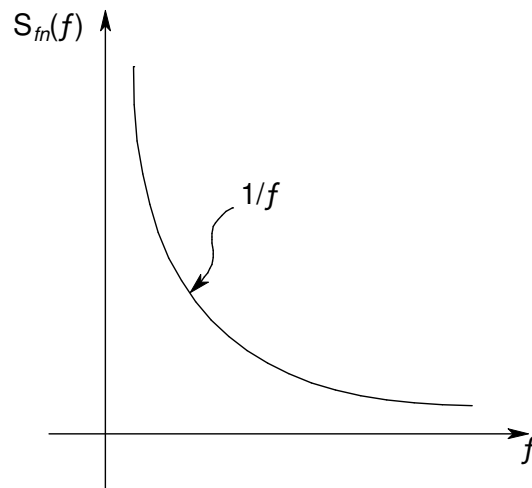


Figure 2.22: PSD of flicker noise.

The following equation for the PSD of flicker noise is depicted in Fig. 2.22.

$$S_{fn}(f) = \frac{const}{f^\alpha} \quad (2.46)$$

where

const = constant

f = frequency, in [Hz]

α = power, close to unity; $0.8 \leq \alpha \leq 1.5$.

Flicker noise is sometimes referred to as $1/f$ noise, since the PSD is often found to be proportional to the inverse first power ($\alpha = 1$) of the frequency [13, 14].

- **Popcorn Noise**

Popcorn noise generates a very-low-frequency spectral density due to its variance in time through random quantified jumps. This type of noise indicates a major defect in any component and it would be advisable to eliminate the component or reduce the problem by testing and selection [11].

▪ Total Noise Estimation of a Circuit

By adding (in power or spectral density) all the noise sources previously discussed, an estimation can be made of the *total noise of a circuit*. As previously shown, the different spectral densities per unit bandwidth are,

$$\text{Thermal noise: } S_m(f) = 4kTR \quad \text{Equation (2.39)}$$

$$\text{Shot noise: } S_{sn}(f) = 2qI \quad \text{Equation (2.45)}$$

$$\text{Flicker noise: } S_{fn}(f) = \text{const}/f. \quad \text{Equation (2.46)}$$

Thus, for example,

$$S_{total}(f) = 4kT(R_1 + R_2 + \dots) + 2q(I_1 + I_2 + \dots) + \frac{K_1}{f} + \frac{K_2}{f} + \dots \quad (2.47)$$

As shown in equation (2.48) and Fig. 2.23, the spectral density will have a general appearance of white noise and flicker noise, if the noise level has not been filtered.

$$S(f) = K_1 + \frac{K_2}{f} \quad (2.48)$$

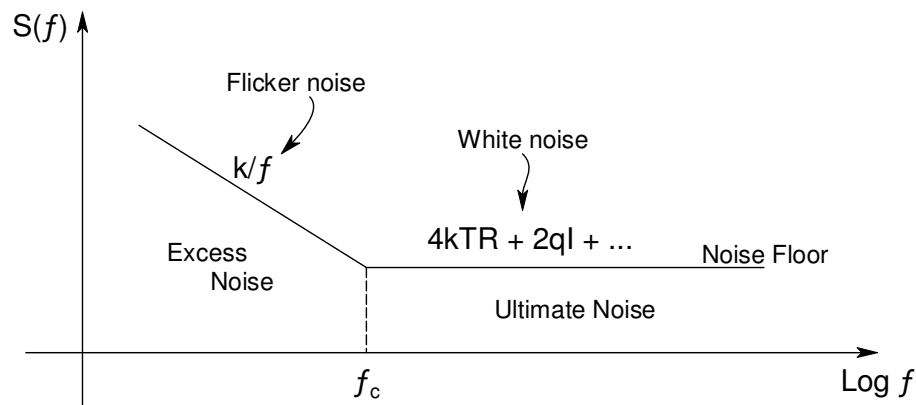


Figure 2.23: Spectral density of the noise in electronic circuits.

In Fig. 2.23 a cut-off frequency f_c is visible. This frequency is called the “flicker” cut-off frequency and can be defined as,

$$S(f) = K \left[1 + \left(\frac{f_c}{f} \right) \right]. \quad (2.49)$$

The flicker, cut-off frequency values are different for the various kinds of transistor technology. Typical values are mentioned in section 2.3.5, reporting on *Leeson’s Phase Noise Model* [11].

2.3.1.2 Noise in Oscillators

In an oscillator there are essentially three types of noise that will disturb the signal. As mentioned at the beginning of this chapter, an oscillator can be modelled as an amplifier with a band-pass filter (the resonant device) in the feedback loop.

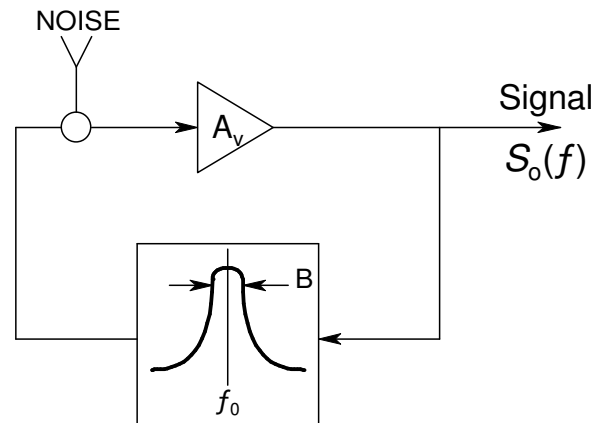


Figure 2.24: Oscillator model illustrating noise.

The noise illustrated in Fig. 2.24 represents the different noise sources considered in the following discussion. The band-pass filter's bandwidth B , is defined by its centre frequency f_0 and its loaded quality factor Q_L as follows

$$B = \frac{f_0}{Q_L}, \quad [\text{Hz}] \quad (2.50)$$

The following three factors contribute to noise in an oscillator:

- ✓ Amplifier
- ✓ Resonator
- ✓ External, frequency control input.

▪ Noise Generated by the Amplifier

Phase noise $\phi(t)$, is being generated by the amplifier's noise sources. In the previous section it was shown that the spectral density of circuit noise sources, comprising of white noise and flicker noise, can be presented by

$$S_{\text{circuit}}(f) = K \left[1 + \left(\frac{f_c}{f} \right) \right] \quad [\text{V}^2/\text{Hz}]. \quad (2.51)$$

As the signal is going through the amplifier, the signal's phase is being modulated by the circuit noise. Consequently, the generated phase noise depends on the level (A) of the signal, so that

$$S_{\phi}(f) = \left(\frac{K}{2A^2} \right) \left[1 + \frac{f_c}{f} \right] \quad [\text{radian}^2/\text{Hz}]. \quad (2.52)$$

- **Parametric Noise**

Varying a parameter that defines the value of the centre frequency f_0 , specifies **parametric noise**. Since f_0 is defined by the resonator, this means that the parametric noise modulates the oscillator by generating a **frequency noise**,

$$f_0(t) = f_0 + \Delta f(t). \quad (2.53)$$

- **Oscillator Control Noise**

If the external input to an oscillator is a noise signal used to control the frequency of the oscillator; this input will modulate the oscillator's frequency and consequently be generating **frequency noise** [11].

2.3.2 What is Phase Noise?

Phase noise represents the short term frequency stability of the oscillator. In other words, when a signal experience random frequency fluctuations it causes phase fluctuations (i.e. the signal will appear different over the same time instance). The term **phase noise** is used to describe these phase fluctuations. Phase noise can be caused by a number of conditions, but is mostly affected by an oscillator's frequency stability. The latter is described by the degree to which an oscillator can keep its frequency constant over a given time. Since small FM deviations are difficult to measure, it is recommended to measure single sideband phase noise for characterising short term stability of a signal. (Single sideband phase noise will be discussed in paragraph 2.3.4.1) [12].

A perfect sinusoidal oscillator produces an ideal cosine wave output, referred to as a *deterministic* signal (a completely specified function of time), where the amplitude of the signal V_0 and the oscillation frequency $f_0 = \omega_0 / 2\pi$ are constants.

As an example,

$$v_0(t) = V_0 \cos[\omega_0 t]. \quad (2.54)$$

In the frequency domain (2.54) is illustrated as a single impulse function with amplitude V_0 at frequency f_0 . In the double-sided amplitude spectrum, two discrete impulse functions with amplitude $V_0/2$ exist at frequencies $+f_0$ and $-f_0$. See illustration below [13].

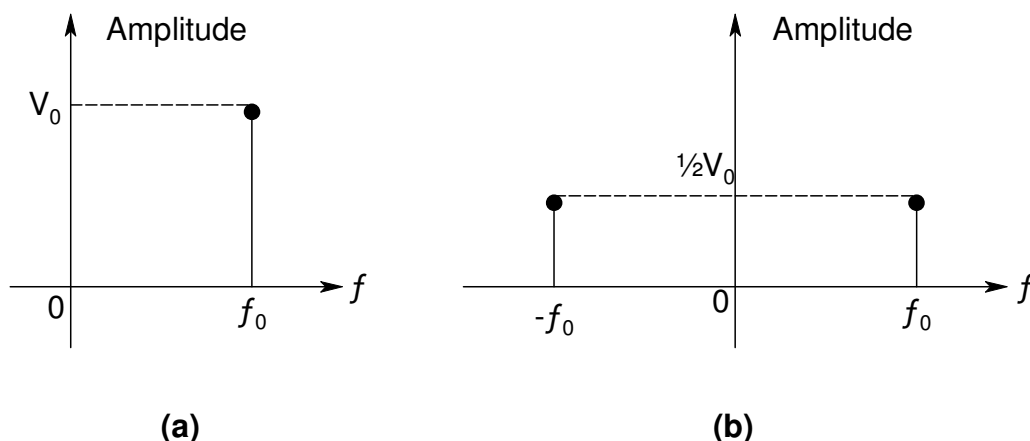


Figure 2.25: Amplitude spectra for the signal $V_0 \cos[\omega_0 t]$. (a) Single-sided. (b) Double-sided.

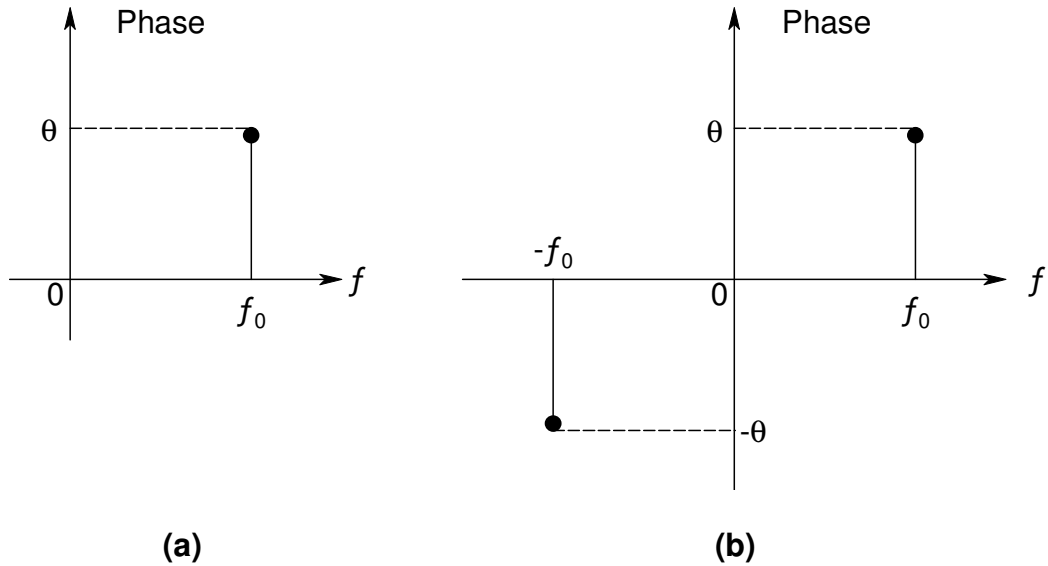


Figure 2.26: Phase spectra for the signal $V_0 \cos[\omega_0 t]$. (a) Single-sided. (b) Double-sided.

In Fig. 2.26 the phase spectra are visible for a cosine signal with no phase noise present.

In practice, however, the oscillator's output signal always contains some noise. This noise is a result of noise-like (*random*) signals that amplitude and phase modulates the signal, appearing as a large amount of separate, closely spaced sidebands around the carrier frequency f_0 . A typical oscillator output voltage can be written as,

$$v_o(t) = V_0[1 + A(t)]\cos[\omega_0 t + \theta(t)], \quad (2.55)$$

where

$A(t)$ = the amplitude fluctuations of the output, or *amplitude noise*

$\theta(t)$ = the phase variation of the output waveform, or *phase noise*.

As a result the new signal phase is now represented by, $\omega_0 t + \text{phase noise}$. Take note that the zero crossings are unaffected by the amplitude noise and that the amplitude of the signal peaks stays intact, despite the phase noise present.

When considering the addition of a noise voltage to a sinusoidal voltage, it is important to take the phase relationship into account. The following phasor diagram can be used to illustrate the effect of phase noise.

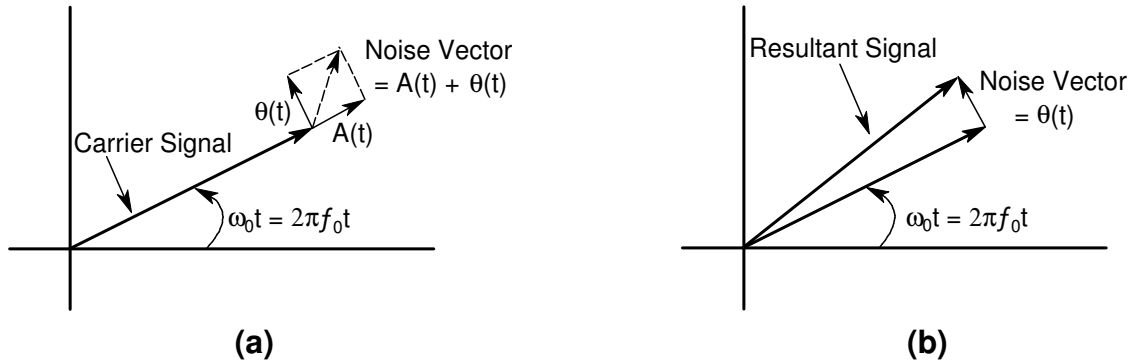


Figure 2.27: Noise Phasor Diagram. (a) Amplitude fluctuations taken into account. (b) Resultant signal phase, represented by $\omega_0 t + \text{phase noise } \theta(t)$.

Between amplitude- and phase noise, the former is usually well-controlled and is the less troublesome of the two when considering a well designed signal source. For example, $A(t)$ can easily be removed by passing the signal through a limiting amplifier or by making use of *Automatic Level Control* (ALC) systems. Removing phase noise is another matter. Phase noise can have a major impact on a system's performance and once it is present on a signal, it is very difficult to remove. For the rest of the discussion the assumption is made that $A(t) \ll 1$, thus the signal having only phase noise appears as,

$$v_0(t) = V_0 \cos[\omega_0 t + \theta(t)]. \quad (2.56)$$

The following figure illustrates the effect of phase noise $\theta(t)$, as viewed in the time domain on an oscilloscope. This effect is called **timing jitter** and is clearly visible at the zero crossings of the waveform (Fig. 2.28).

Significant changes to the spectrum of a signal can still occur, even if the levels of phase noise are far too small to detect on an oscilloscope. These changes can be very important when considering radio applications.

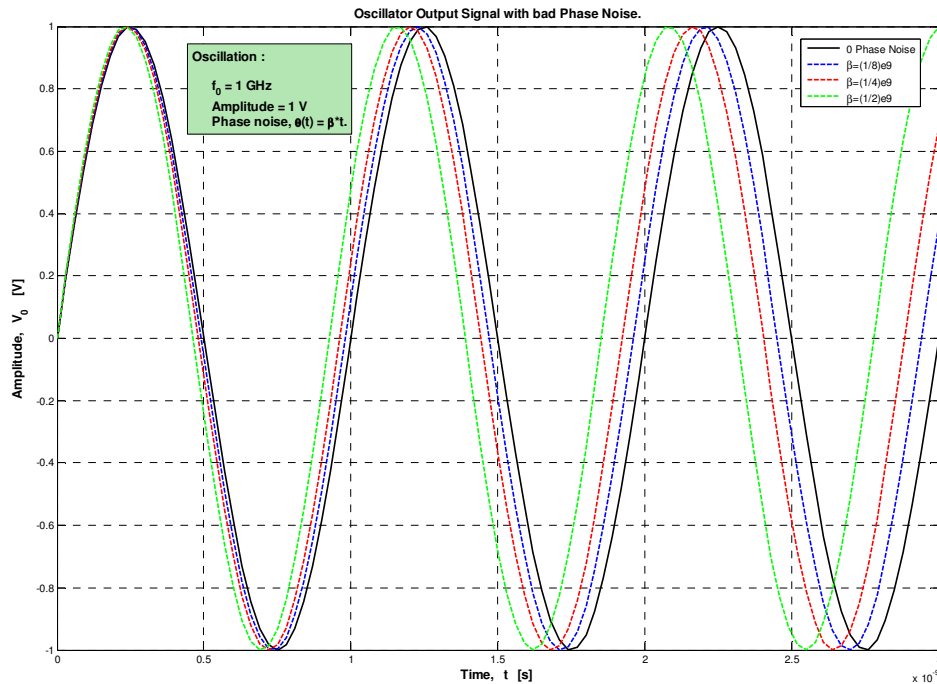


Figure 2.28: Timing Jitter. Phase noise illustration in the time domain.

The realistic oscillator's frequency spectrum will present something resembling the following,

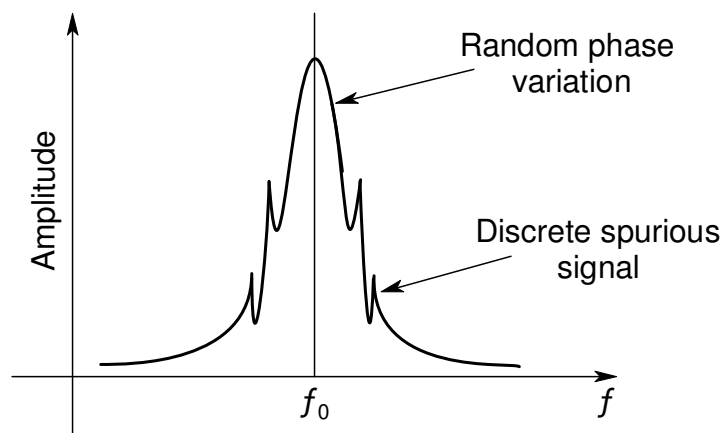


Figure 2.29: Output spectrum of a typical oscillator.

The phase term may be *discrete* or *random* and can be displayed on a spectrum analyser. As illustrated in Fig. 2.29, two types of fluctuating phase terms occur. The discrete spikes visible in the spectrum are called *spurious signals*. Those appear due to oscillator harmonics or mixer products. The random phase fluctuations that occur is called *phase noise* and are caused by 'thermal' and 'flicker' noise [14].

2.3.3 Review of Angle Modulation

Having an information-bearing signal that needs to be transmitted through a communication channel; it firstly has to undergo a modulation process to produce a signal that can easily be accommodated by the channel. When modulating the information-bearing signal (often referred to as the *message signal*, $m(t)$) it is being translated to a new spectral location, depending on the intended frequency of transmission. For example, if the signal is to be transmitted through the atmosphere of free space, *frequency translation* is necessary to raise the signal spectrum to a frequency that can be radiated efficiently with antennas of reasonable size. The latter is important, since the frequency of a signal is inversely proportional to the signal's wavelength, given as $\lambda = c/f$. Modulation is in particular useful when more than one signal makes use of a single communication channel, since the former allows translation of the different signals to different spectral locations. The receiver then has the obligation of selecting the desired signal. Also, modulation may be used to convert the message signal into a form less susceptible to noise and interference.

Since phase noise modulates a signal's phase, *angle modulation* will be reviewed in the following paragraphs. The two basic types of angle modulation entail *phase modulation* (PM) and *frequency modulation* (FM) respectively.

As mentioned earlier, the general oscillator output signal with phase noise can be represented by

$$v_0(t) = V_0 \cos[\omega_0 t + \theta(t)], \quad (2.57)$$

where $\theta(t)$ = the noise-like signal that phase modulates the carrier frequency ω_0 .

A direct relationship exists between FM noise and phase noise since frequency deviation is equal to the rate of change of phase deviation.

The *instantaneous angle* of $v_0(t)$ is defined as

$$\phi_i(t) = \omega_0 t + \theta(t), \quad (2.58)$$

while the *instantaneous frequency* of $v_0(t)$ is defined as,

$$\omega_i(t) = \frac{d\phi_i}{dt} = \omega_0 + \frac{d\theta}{dt}. \quad (2.59)$$

From (2.58) the *phase deviation* is described by the function $\theta(t)$, while the *frequency deviation* is expressed by the function $d\theta/dt$ in (2.59). *Phase or frequency modulation* are obtained by letting $\theta(t)$ or $d\theta/dt$ be linearly related to the modulating signal.

2.3.3.1 Phase Modulation (PM) Review

The following discussion will revisit the theory behind sinusoidal **phase modulation**. The latter involves, phase modulating the carrier frequency ω_0 , with a sinusoidal signal with known frequency ω_m .

Consequently, the PM carrier signal can be represented by

$$v_0(t) = V_0 \cos[\omega_0 t + \theta_{pk} \cdot \sin(\omega_m t)], \quad (2.60)$$

where

$$\theta(t) = \theta_{pk} \cdot \sin(\omega_m t), \text{ phase modulation by a sinusoidal signal}$$

$$\theta_{pk} = \text{the peak phase deviation, in [radians]}$$

$$\omega_m = \text{the modulation frequency, in [rad.s}^{-1}\text{].}$$

As an example the following signal was simulated in *MATLAB*. Illustrations in both the time domain and the frequency domain were considered.

$$v_0(t) = 3 \cdot \cos[2\pi(200)t + (2.5) \cdot \sin(2\pi(25)t)]. \quad (2.61)$$

From (2.61), the carrier signal and the message signal are individually characterised by the following values,

$$\text{Carrier Signal: } V_0 = 3 \text{ V;}$$

$$f_0 = 200 \text{ Hz.}$$

$$\text{Message Signal: } \theta_{pk} = 2.5 \text{ rad;}$$

$$f_m = 25 \text{ Hz.}$$

Considering (2.61) in the time domain, it gives quite a simple waveform, as portrayed in the following plots,

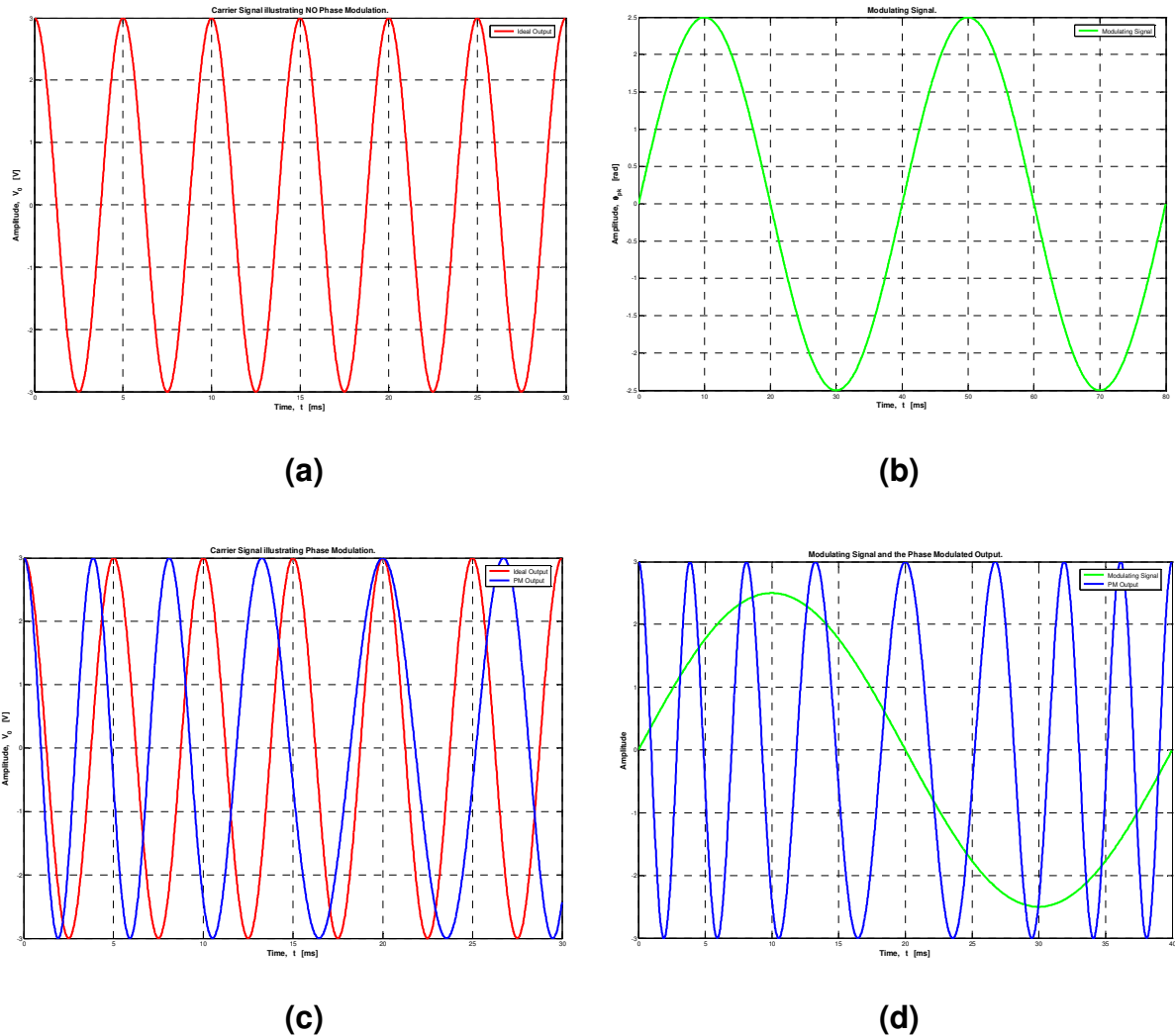


Figure 2.30: Time domain waveforms illustrating phase modulation.
(a) Unmodulated carrier $V_0 \cdot \cos(2\pi f_0 t)$. (b) Message signal $\theta_{pk} \cdot \sin(2\pi f_m t)$.
(c) Output of phase modulator with the unmodulated carrier. (d) Output of phase modulator with the message signal.

Take note from Fig. 2.30 (d) that the phase modulator output is proportional to the message signal, $m(t)$. Thus, the instantaneous frequency of the output of the phase modulator is at a maximum when the *slope* of $m(t)$ is a maximum, and is a minimum when the slope of $m(t)$ is a minimum.

Considering (2.61) in the frequency domain, gives anything but, a simple spectrum of the waveform. The signal from (2.60),

$$v_0(t) = V_0 \cos[\omega_0 t + \theta_{pk} \cdot \sin(\omega_m t)]$$

can be expressed as

$$v_0(t) = V_0 \cdot \text{Re}\left(e^{j\omega_0 t} \cdot e^{j\theta_{pk} \cdot \sin(\omega_m t)}\right). \quad (2.62)$$

Since the function $e^{j\theta_{pk} \cdot \sin(\omega_m t)}$ is periodic with frequency ω_m it can therefore be expanded in a Fourier series. With the help of Bessel functions, the Fourier series can be written as

$$e^{j\theta_{pk} \cdot \sin(\omega_m t)} = \sum_{n=-\infty}^{\infty} J_n(\beta) \cdot e^{jn\omega_m t} \quad (2.63)$$

where

n = sideband index ($n = 0$ for the carrier)

β = the modulation index (= θ_{pk} , the peak phase deviation).

Subsequently from (2.62) and (2.63), the modulated carrier can be written as

$$\begin{aligned} v_0(t) &= V_0 \cdot \text{Re}\left[e^{j\omega_0 t} \cdot \sum_{n=-\infty}^{\infty} J_n(\beta) \cdot e^{jn\omega_m t}\right] \\ &= V_0 \cdot \sum_{n=-\infty}^{\infty} J_n(\beta) \cdot \cos(\omega_0 + n\omega_m)t. \end{aligned} \quad (2.64)$$

Finally from (2.64), the spectrum of $v_0(t)$ can easily be determined by inspection.

Theoretically, the spectrum of the signal defined in (2.64), contains a component at the carrier frequency, and has an infinite number of sidebands separated from the carrier frequency by integer multiples of the modulation frequency f_m . The latter results in an infinite series of sidebands, where the amplitude of each spectral component can be determined from a table of values of the Bessel function [13]. The spectrum portrays the following,

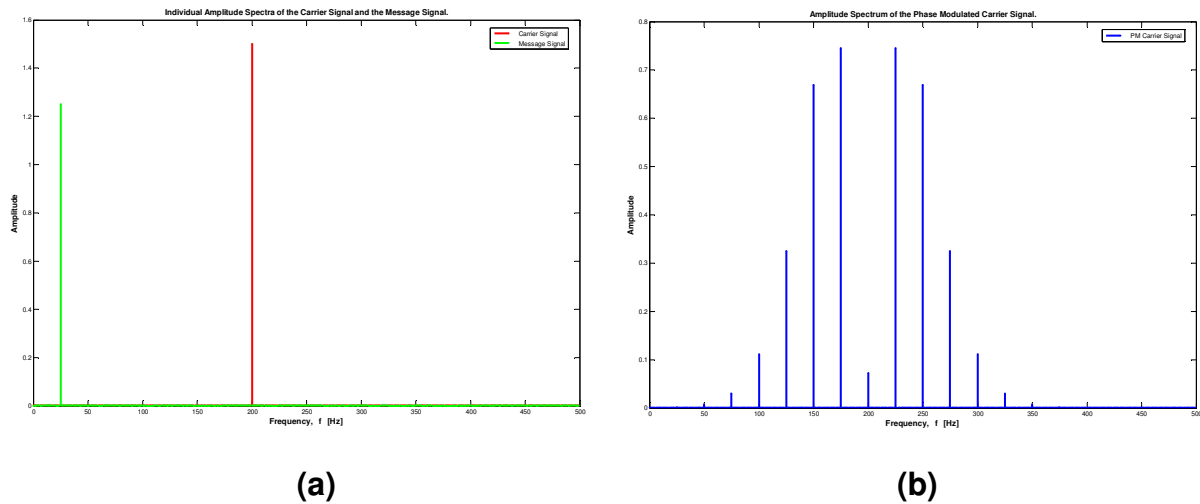


Figure 2.31: Amplitude spectra of the waveform, illustrating phase modulation. (a) Spectra of the unmodulated carrier signal (in red) and the message signal (in green). (b) Phase modulated carrier signal.

The amplitude spectra illustrated in Fig. 2.31 were computed using the fast Fourier transform (FFT) algorithm defined in *MATLAB*. The latter returns the discrete Fourier transform (DFT) of the time signal. Only the *positive frequency side* of the double-sided spectra is shown.

The sidebands illustrated in Fig. 2.31 (b) each represent an extra sinusoidal component present in the output signal of the phase modulator. By examining the time-domain waveform of the output, illustrated in Fig. 2.30 (c) and (d), there is a clear indication that extra frequency components are present in the spectrum.

Suppose a signal is phase modulated by a signal consisting of the sum of other signals. Upon investigating the modulation process, the assumption can not be made that the sum of the modulation responses due to each signal individually, will describe the process. This can be said, since phase modulation is a non-linear process.

When analysing noise modulation, one of the main techniques for treating noise is precisely to consider it as a sum of sine waves and consequently to consider the response to each sine wave separately. Therefore the non-linearity just mentioned, is potentially a problem when analysing noise in a signal.

One way of conquering the just mentioned problem is to allow phase noise to be treated using conventional linear techniques. But this is only possible if the level of phase modulation is kept low, since the latter gives surety that the modulation performs in a linear manner. Increasing the modulation index does not only linearly increase the levels of the spectral lines, but also adds new spectral lines to the existing spectrum. In one of the following paragraphs it is shown that for $\beta \ll 1$ some approximations can be made, which leads to the discussion of *Narrowband modulation*.

2.3.3.2 Frequency Modulation (FM) Review

The only difference between **frequency modulation** and phase modulation is the terminology. The modulated signal is identical. From the previously introduced equation for an ideal oscillator,

$$v_0(t) = V_0 \cos[\omega_0 t] \quad (2.65)$$

the phase of the signal at any time is given by $\omega_0 t$, and changes steadily over time with slope ω_0 , portraying a constant oscillation frequency.

In the previous section, the phase modulated signal was defined as

$$v_0(t) = V_0 \cos[\omega_0 t + \theta(t)] \quad (2.66)$$

with its phase at any time given by $\omega_0 t + \theta(t)$. Where, $\theta(t) = \theta_{pk} \cdot \sin(\omega_m t)$. From (2.59) the instantaneous frequency, defined as the rate of change of the phase of the signal $v_0(t)$ with time, can be written as,

$$\begin{aligned} \omega_i(t) &= \omega_0 + \frac{d\theta}{dt} \\ &= \omega_0 + \theta_{pk} \cdot \omega_m \cdot \cos(\omega_m t). \end{aligned} \quad (2.67)$$

From (2.67) it can be said that the carrier frequency ω_0 is sinusoidally modulated by

$$\omega_{pk} = \theta_{pk} \cdot \omega_m \quad (2.68)$$

where ω_{pk} = the peak frequency deviation.

Consequently, the **modulation index** β can be defined as the following,

$$\beta = \theta_{pk} = \frac{\omega_{pk}}{\omega_m} = \frac{f_{pk}}{f_m}. \quad (2.69)$$

In (2.69) it is stated that the modulation index is the ratio of the peak frequency deviation f_{pk} , to the modulating frequency f_m . β can be calculated using either frequencies as radian frequencies, or both in Hz. Take note that β also represents the peak phase deviation θ_{pk} , in radians.

The frequency modulated signal then becomes

$$v_0(t) = V_0 \cos[\omega_0 t + \beta \cdot \cos(\omega_m t)]. \quad (2.70)$$

The recently discussed theory is again illustrated by means of an example. The following signal was simulated in *MATLAB*. Illustrations in both the time domain and the frequency domain were considered.

$$v_0(t) = 3 \cdot \cos[2\pi(200)t + (\beta) \cdot \cos(2\pi(25)t)]. \quad (2.71)$$

From (2.71), the carrier signal and the message signal are individually characterised by the following values,

Carrier Signal: $V_0 = 3 \text{ V};$

$$f_0 = 200 \text{ Hz.}$$

Message Signal: $f_{pk} = [2.5, 25, 62.5] \text{ Hz};$

$$f_m = 25 \text{ Hz, and}$$

$$\beta = f_{pk} / f_m = [0.1, 1.0, 2.5].$$

In this example, the time domain waveform, and its spectra were studied for three diverse instances. Each was done for a different modulation index β , varied according to the peak frequency deviation, as just defined.

Considering (2.71) in the time domain, the equation gives quite a simple waveform, as portrayed in the following plots,

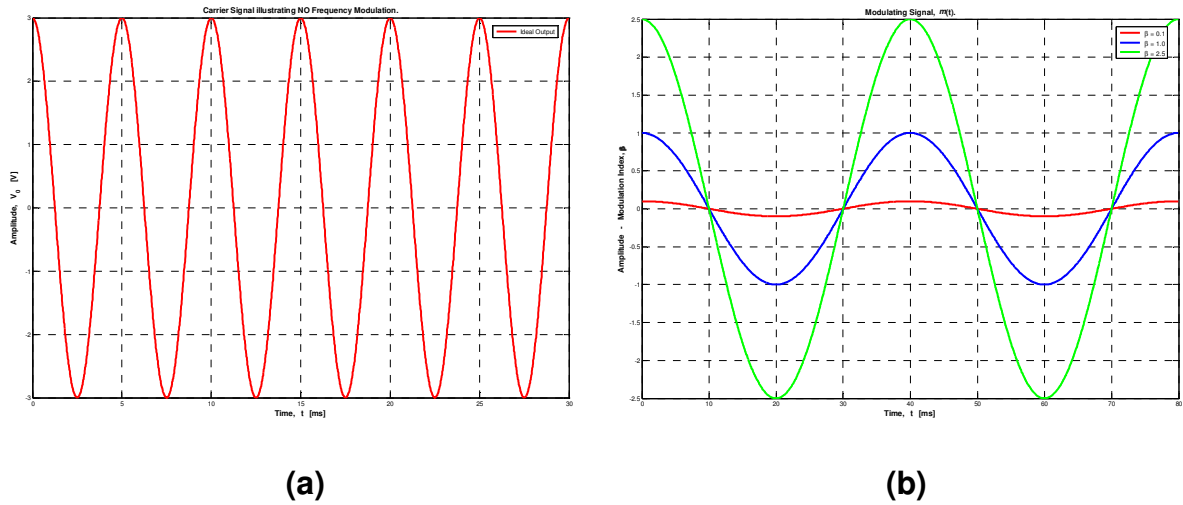
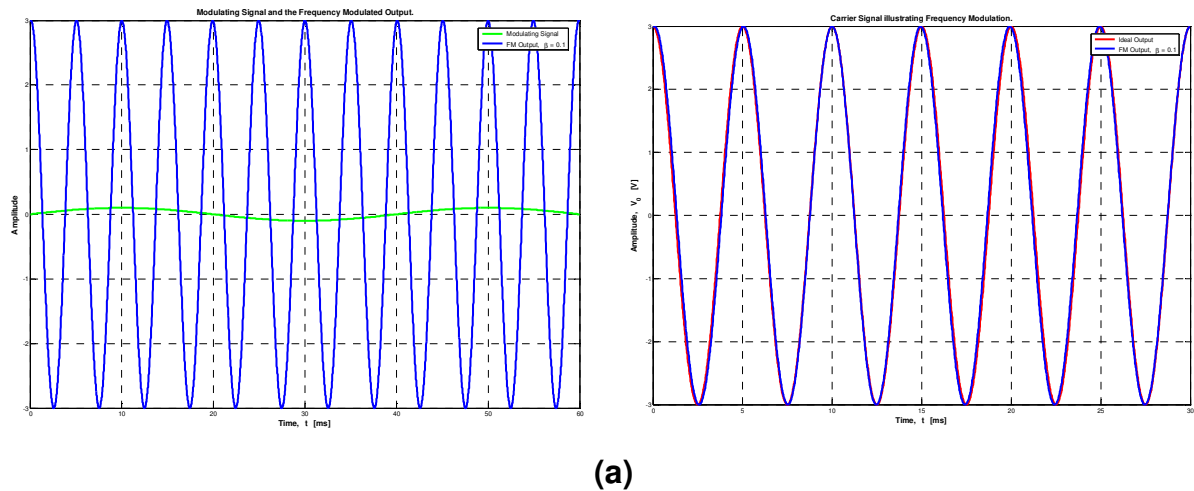


Figure 2.32: Time domain waveforms illustrating frequency modulation. (a) Unmodulated carrier $V_0 \cdot \cos(2\pi f_0 \cdot t)$. (b) Message signal $\beta \cdot \cos(2\pi f_m \cdot t)$, with the modulation index β , varied according to the peak frequency deviation.

In the following figure, the frequency modulation is illustrated by varying the modulation index; thus indicating the level of modulation applied to the carrier signal.



(a)

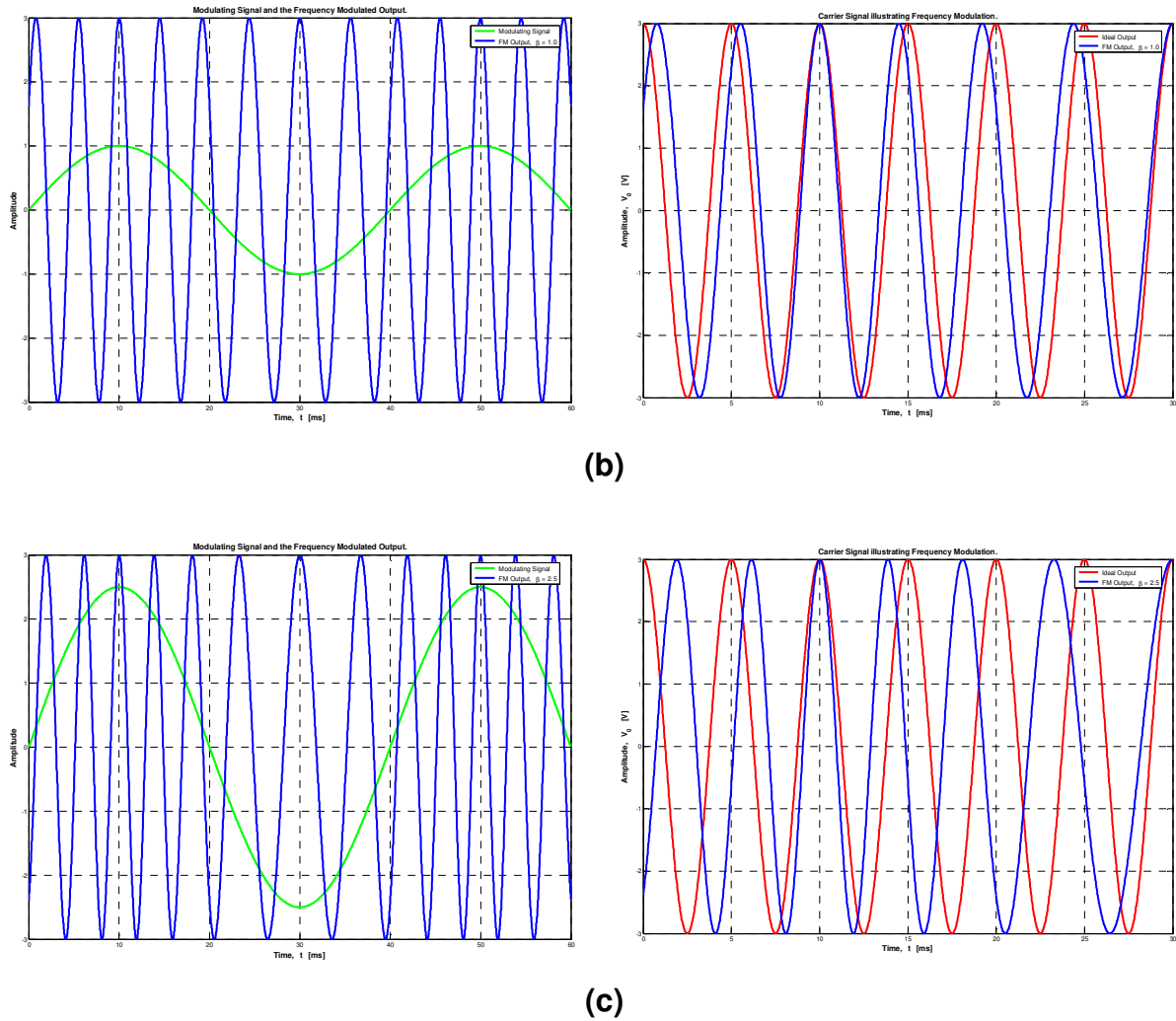


Figure 2.33: Time domain waveforms illustrating the varying modulation index, β . Left: FM output with the message signal. Right: FM output with the unmodulated carrier. For (a) $\beta = 0.1$, (b) $\beta = 1.0$, and (c) $\beta = 2.5$.

From Fig. 2.33 it is noticed that the frequency deviation of the FM modulator output is proportional to the message signal, $m(t)$. In other words, the modulated carrier signal (the instantaneous frequency of the FM modulator output) is a maximum when $m(t)$ is a maximum, and portrays a minimum whenever $m(t)$ is at its minimum [13].

When comparing the time-domain waveforms, illustrated in Fig. 2.30 (d) & 2.33 (c) the modulated signals appear identical. If $m(t)$ were not shown along with the modulator outputs, it would not be possible to distinguish between the PM and FM modulated carrier.

Frequency modulation is a non-linear modulation process, since the FM wave defined is a non-linear function of the modulating wave, $m(t)$. In the following figures, the spectral properties of the FM waveform are illustrated. Take note that the spectrum of the frequency modulated carrier signal is not related in a simple manner to that of its modulating wave [6]. In Fig. 2.35 and 2.36 the modulated output signal is illustrated for different values of the modulation index β .

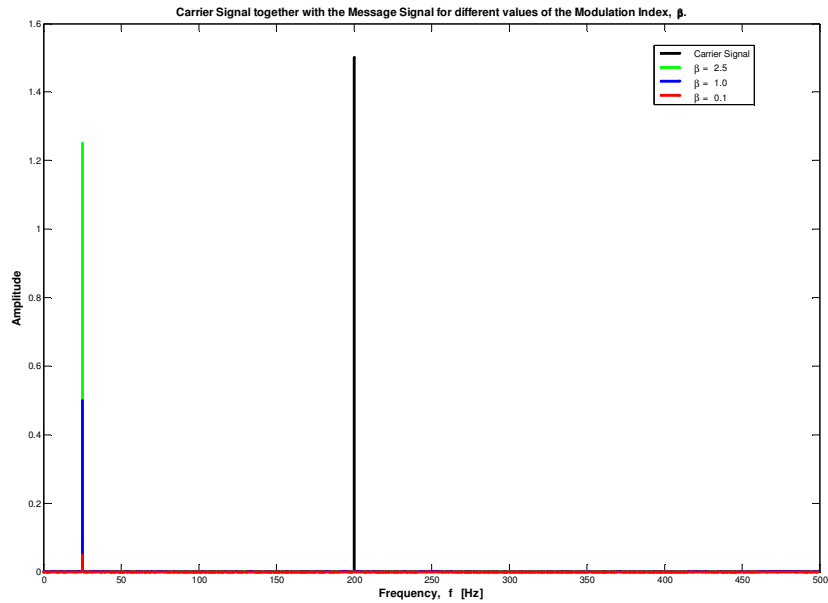


Figure 2.34: Amplitude spectra of the unmodulated carrier signal (in black) and the message signal $m(t)$. $m(t)$ is illustrated for three different values of the modulation index β . For $\beta = 0.1$ in red; $\beta = 1.0$ in blue, and $\beta = 2.5$ in green.

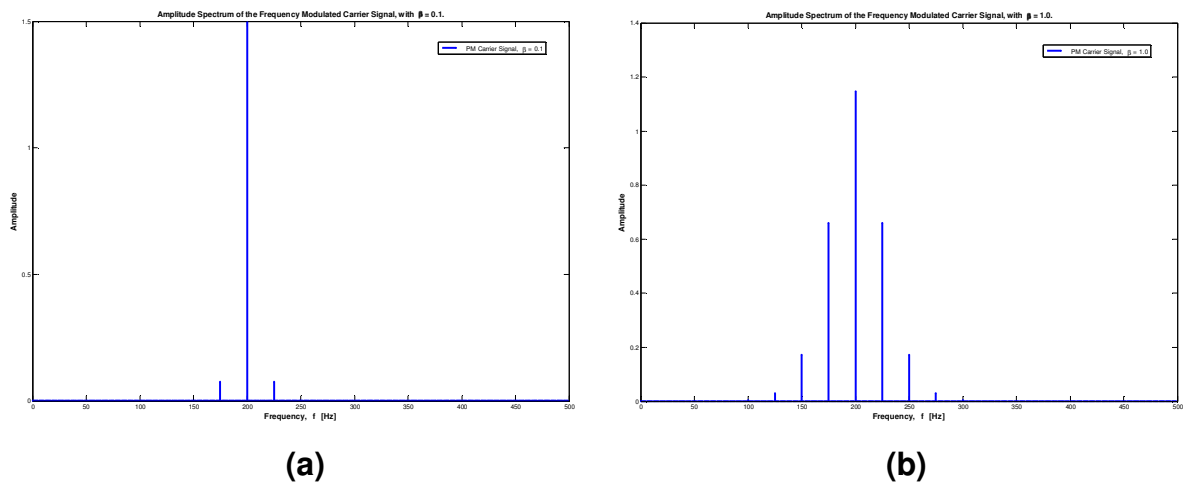


Figure 2.35: Amplitude spectra of the FM signal for different values of the modulation index β . (a) $\beta = 0.1$ and (b) $\beta = 1.0$.

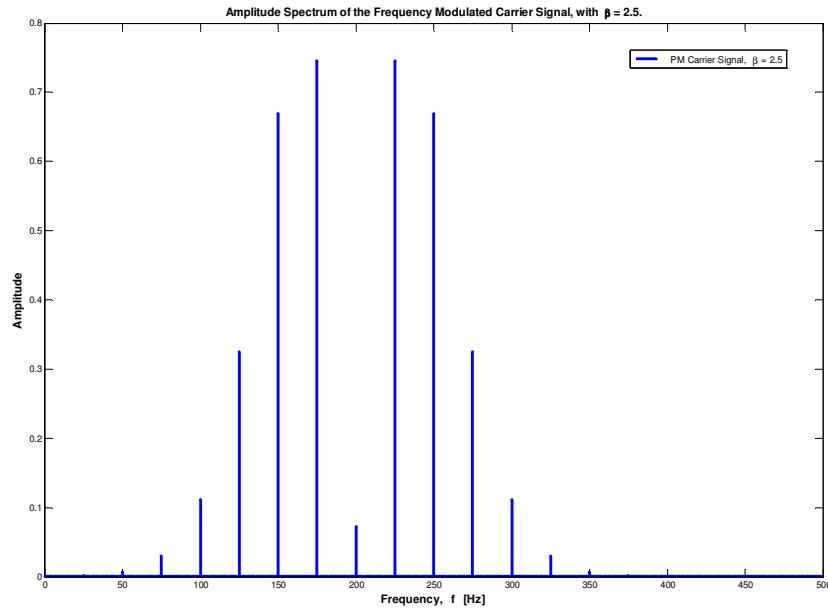


Figure 2.36: Amplitude spectrum of the FM signal for $\beta = 2.5$.

As mentioned earlier, the resulting modulated signal is the same for both the FM and PM processes. This is verified by the spectrum of the FM signal illustrated in Fig. 2.36, which is identical to that of the PM signal illustrated in Fig. 2.31 (b) [15].

2.3.3.3 Narrowband Phase & Frequency Modulation Approximations

Narrowband modulation originates when certain simplification approximations can be made to the expressions for the signal waveforms, due to certain modulation conditions met. The latter would be, for frequency modulation (FM) the modulation index $\beta \ll 1$; and for phase modulation (PM) the peak phase deviation $\theta_{pk} \ll 1$.

As an explanation to the necessary modulation conditions, *narrowband phase modulation* will be discussed. Previously in (2.60), the *phase modulation* signal was defined as,

$$v_0(t) = V_0 \cos[\omega_0 t + \theta_{pk} \cdot \sin(\omega_m t)].$$

By means of the following trigonometry identities,

$$\cos(\theta_1 \pm \theta_2) = \cos(\theta_1) \cdot \cos(\theta_2) \mp \sin(\theta_1) \cdot \sin(\theta_2) \quad (i)$$

$$A \cdot \sin(\theta_1) \cdot \sin(\theta_2) = -\frac{A}{2} \cdot \cos(\theta_1 + \theta_2) + \frac{A}{2} \cdot \cos(\theta_1 - \theta_2), \quad (ii)$$

and by assuming that $\theta_{pk} \ll 1$ which implies that,

$$\cos(\theta_{pk}) \approx 1, \quad (iii)$$

$$\sin(\theta_{pk}) \approx \theta_{pk}; \quad (iv)$$

equation (2.60) can be reintroduced as,

$$\begin{aligned} v_0(t) &= V_0 \cdot \cos[\omega_0 t + \theta_{pk} \cdot \sin(\omega_m t)] \\ &= V_0 \cdot \{\cos(\omega_0 t) \cdot \cos(\theta_{pk} \cdot \sin(\omega_m t)) - \sin(\omega_0 t) \cdot \sin(\theta_{pk} \cdot \sin(\omega_m t))\} \quad \text{from (i)} \\ &\approx V_0 \cdot \{\cos(\omega_0 t) \cdot 1 - \sin(\omega_0 t) \cdot \theta_{pk} \cdot \sin(\omega_m t)\} \quad \text{from (iii) and (iv)} \\ &= V_0 \cdot \{\cos(\omega_0 t) - \theta_{pk} \cdot \sin(\omega_0 t) \cdot \sin(\omega_m t)\} \\ &= V_0 \cdot \left\{ \cos(\omega_0 t) - \left[-\frac{\theta_{pk}}{2} \cdot \cos(\omega_0 t + \omega_m t) + \frac{\theta_{pk}}{2} \cdot \cos(\omega_0 t - \omega_m t) \right] \right\} \quad \text{from (ii)} \\ &= V_0 \cdot \left\{ \cos(\omega_0 t) + \frac{\theta_{pk}}{2} \cdot \cos[(\omega_0 + \omega_m)t] - \frac{\theta_{pk}}{2} \cdot \cos[(\omega_0 - \omega_m)t] \right\}. \quad (2.72) \end{aligned}$$

The *narrowband phase modulation* signal is represented by (2.72), while its amplitude spectrum is illustrated in the following figure.

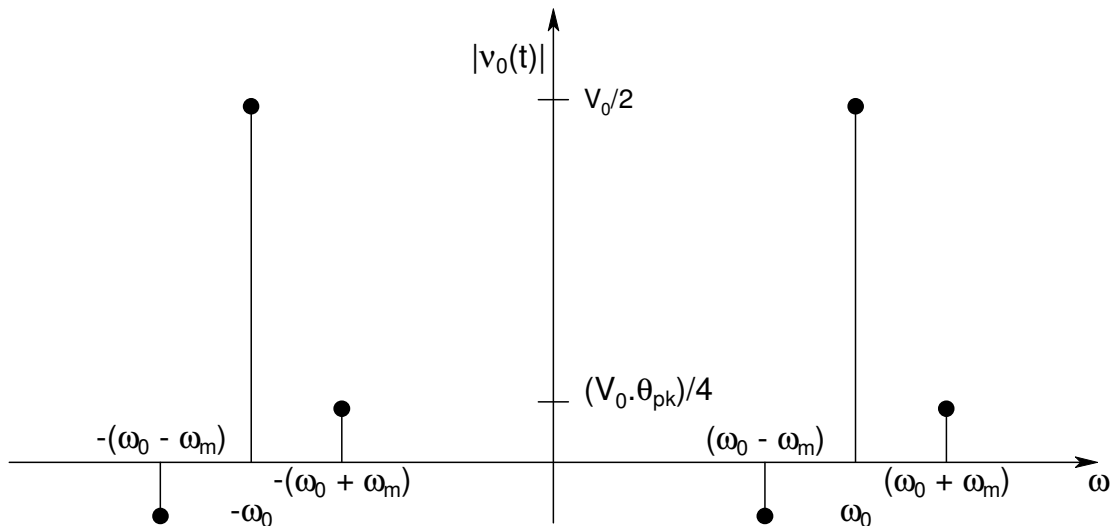


Figure 2.37: DSB Amplitude spectrum illustrating Narrowband Phase Modulation where $\theta_{pk} \ll 1$.

In Fig. 2.37 the carrier signal, as well as the modulation sidebands are clearly illustrated. Take note that due to the low level of phase modulation, the produced pair of sidebands has an amplitude of $\theta_{pk}/2$ relative to the carrier. If the modulation was repeated for a message signal consisting of two sinusoidal signals, the spectrum would have resulted in a pair of sidebands for each of the sinusoidal modulation signals.

Since a linear relationship (between the spectrum of the *modulating* signal and that of the *modulated* signal) is portrayed, the investigation into the spectrum of phase noise is made easier. It is important to notice that *only* as long as the total phase modulation results in a phase deviation much less than one radian (about 60 degrees), can the process be approached as linear. If the latter is true, the spectral components of the *modulating* signal can then be associated with that in the *modulation*.

The same argument could be followed for *narrowband frequency modulation*, since the modulation index β was shown to be equal to the peak phase deviation θ_{pk} . Thus for FM with $\beta \ll 1$, the spectrum consists of a pair of sidebands at an offset equal to the modulating frequency from the carrier, with an amplitude of $\beta/2$ relative to the carrier. Similar to that illustrated in Fig. 2.37 [15].

2.3.4 Representation of Phase Noise

Essentially all methods used to characterise the phase noise of an oscillator, either measures the frequency or the phase deviation of the source under test. The latter is either done in the time or the frequency domain. All the terms used to describe the phase noise are related, since frequency and phase are related to each other by means of,

$$\omega(t) = \frac{d}{dt}[\theta(t)] \quad (2.73)$$

where

$\theta(t)$ = the phase noise of the source under test, and

$\omega(t)$ = the frequency noise of the source under test.

The spectral density describes rms phase distributions as a continuous function; expressed in units of rms phase per unit bandwidth. In the frequency domain where the spectral density is characterised by measuring the noise “sidebands” on either side of the output signal centre frequency; is the best way to describe the phase noise of an oscillator. Since small FM deviations are difficult to measure, it is recommended to measure the single sideband phase noise for characterising the short term stability of a signal. Single sideband (SSB) phase noise is specified in dBc/Hz at a given offset frequency from the carrier and will be discussed in the next section.

2.3.4.1 Definition of Single Sideband Phase Noise

Signal sources such as signal generators, voltage controlled oscillators and many other are frequently accompanied by a phase noise specification such as the one shown below:

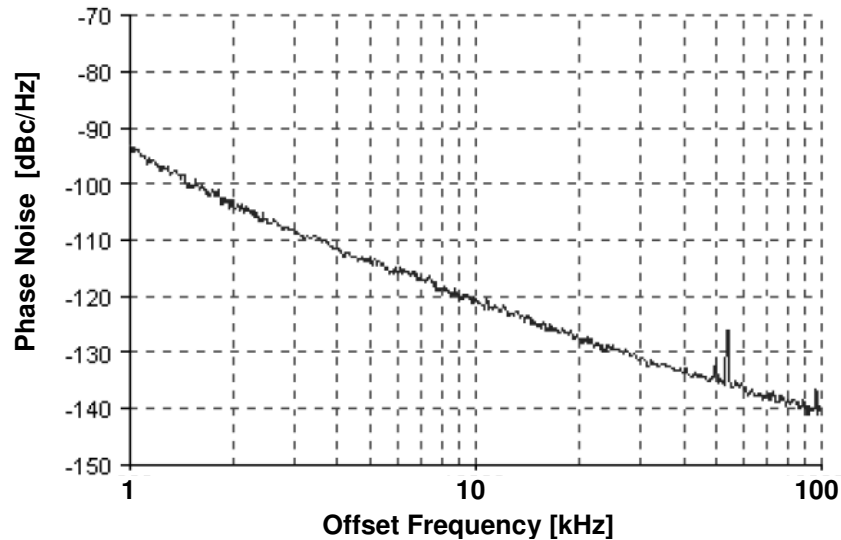


Figure 2.38: Phase Noise specification of a typical signal source.

Taken from the literature, the phase noise specification depicted in Fig. 2.38 serves only as an illustration of how a typical phase noise measurement appears. The spectrum analyser view of the same VCO is illustrated later on in Fig. 2.40.

How one would interpret the phase noise specification in Fig. 2.38, is to typically choose an offset frequency of interest; for example $f_m = 10$ kHz in this case. Then from Fig. 2.38 it is clear that the SSB phase noise of the VCO at 10 kHz offset is approximately -120 dBc/Hz. Stated otherwise, $L(f_m = 10 \text{ kHz}) = 10^{-120/10} = 10^{-12}$ [absolute value]; representing *the power ratio of the noise power to the carrier power in a 1 Hz bandwidth*. This means that if the VCO was producing 0 dBm at f_0 ; a 1 Hz wide filter situated at $f_0 + f_m$ would receive -120 dBm power, while a second filter at $f_0 - f_m$ would also receive -120 dBm power.

As previously defined in (2.56), a practical oscillator containing only phase noise is described by

$$v_0(t) = V_0 \cos[\omega_0 t + \theta(t)]. \quad (2.74)$$

Keep in mind the recently reviewed phase and frequency modulation techniques. Thus, any small change in the oscillator frequency are represented as a frequency modulation of the carrier by letting,

$$\theta(t) = \theta_{pk} \sin(\omega_m t) = \frac{\Delta f}{f_m} \sin(\omega_m t) = \beta \sin(\omega_m t) \quad (2.75)$$

where

$$f_m = \frac{\omega_m}{2\pi}, \text{ is the modulating frequency, in [Hz]}$$

$$\Delta f, \text{ is the peak frequency deviation; previously characterised as } f_{pk}$$

$$\theta_{pk} = \frac{\Delta f}{f_m}, \text{ is the peak phase deviation (PM) or the modulation index (FM).}$$

Assuming small phase (or frequency) deviations in the output of an oscillator, so that $\theta_{pk} \ll 1$ (or $\beta \ll 1$), simplifies (2.74) to the following,

$$v_o(t) = V_o \cdot \left\{ \cos(\omega_0 t) + \frac{\theta_{pk}}{2} (\cos[(\omega_0 + \omega_m)t] - \cos[(\omega_0 - \omega_m)t]) \right\} \quad (2.76)$$

which results in a pair of modulation sidebands at $\omega_0 \pm \omega_m$, located on either side of the carrier signal, with amplitude of $\frac{1}{2}\theta_{pk}$ relative to the carrier; as illustrated in Fig. 2.37. Recall Fig. 2.29 which illustrates the output spectrum of a typical RF oscillator where these deviations were caused by random changes in the temperature or device noise and resulted in a continuous distribution.

Single-sideband phase noise, $L(f_m)$, is defined as the *ratio of noise power* in one phase modulation sideband, *to the total signal power per unit bandwidth* at a given frequency offset f_m from the signal frequency. The SSB phase noise definition is depicted in the following figure, Fig. 2.39.

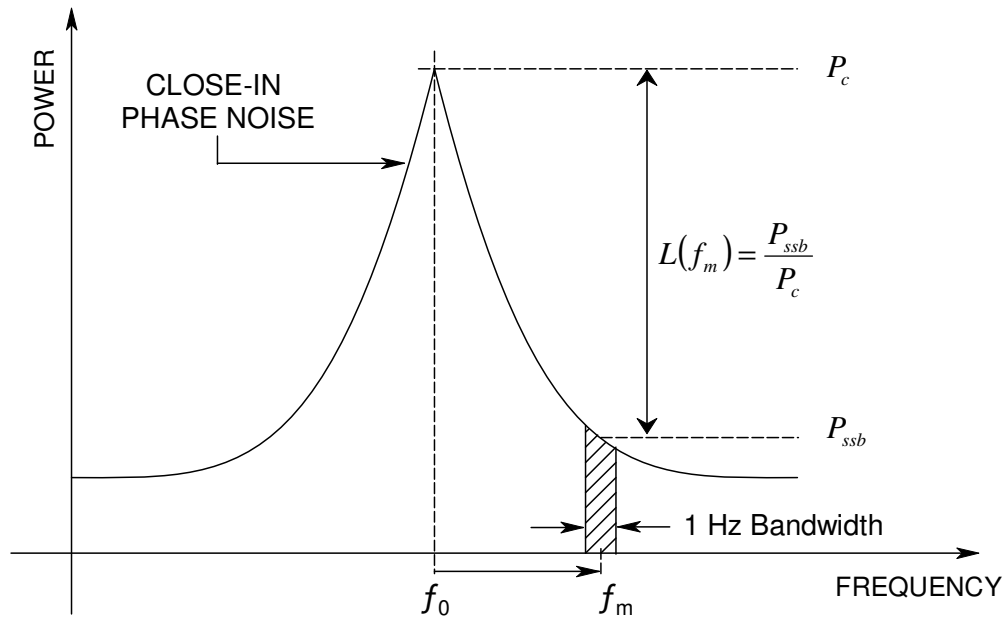


Figure 2.39: Single-sideband phase noise to carrier ratio representation.

The “skirt” of this output spectrum is due to noise frequency modulation of the oscillator. Note that the definition of phase noise implicitly *assumes* that the spectrum is symmetric, as it is for a signal that has only phase noise and no amplitude noise. When the signal has an asymmetric spectrum, i.e. when the spectrum at $f_0 + f_m$ differs from the spectrum at $f_0 - f_m$, then the signal has a combination of amplitude and phase noise. To be able to measure the SSB phase noise $L(f_m)$ on a spectrum analyser, it is important to remove the AM noise first. That can easily be done, as was discussed in section **2.3.2**.

The one-sided “*spectral density*” of phase fluctuations per unit bandwidth is one of the most common fundamental descriptions of phase noise. According to the definition of phase noise as the ratio of noise power per unit bandwidth to the carrier power, (2.76) has a corresponding phase noise of

$$L(f_m) = \frac{P_{ssb}}{P_c} = \frac{\frac{1}{2} \left(\frac{V_0 \theta_{pk}}{2} \right)^2}{\frac{1}{2} V_0^2} = \frac{\theta_{pk}^2}{4} = \frac{\theta_{rms}^2}{2} \quad (2.77)$$

where

P_{ssb} = the power density in one sideband per unit bandwidth at an offset frequency f_m away from the carrier

P_c = the total signal power, carrier power level

$\theta_{\text{rms}} = \frac{\theta_{pk}}{\sqrt{2}}$, is the root-mean-squared (rms) value of the peak phase deviation.

The SSB phase noise is usually expressed in decibels relative to the carrier power per Hz bandwidth. As it is a power ratio, the way to convert it to dBc/Hz is done by,

$$L(f_m)_{[\text{dBc/Hz}]} = 10 \log_{10}(L(f_m)). \quad (2.78)$$

Although the SSB phase noise is *traditionally defined in a 1 Hz bandwidth*, as follows

$$L(f_m) = \frac{P_{ssb}/1\text{Hz}}{P_c} = \frac{P_{ssb}}{1\text{Hz} \cdot P_c}, \quad (2.79)$$

in practice it often happens that the noise power in a bandwidth other than unity is desired. Suppose the bandwidth of interest is represented by B Hz; then from (2.79) the noise power in bandwidth B , centred a distance f_m from the carrier is approximately given by

$$\text{Noise Power, } P_{ssb} \text{ in } B \text{ Hz} = B \cdot L(f_m) \cdot P_c \quad (2.80)$$

It is important to notice that for (2.80) to be valid; the SSB phase noise needs to be approximately constant over the entire bandwidth (B) of interest.

In general it is easier to work with dB values; therefore the corresponding equation for (2.80) is given as,

$$(\text{Noise Power, } P_{ssb} \text{ in } B \text{ Hz})_{[\text{dBm}]} = 10 \log_{10}(B) + L(f_m)_{[\text{dBc/Hz}]} + (P_c)_{[\text{dBm}]}. \quad (2.81)$$

It is important to notice that the slope of the phase noise plot is not linear. It appears linear when studying it on a logarithmic scale, but in fact it is typically varying as $1/f_m^2$. Because of this, the accuracy of (2.80) and (2.81) degrades as the bandwidth (B) of interest increases.

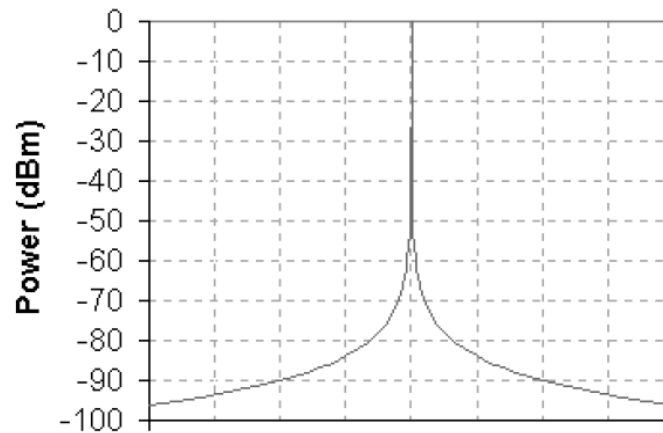


Figure 2.40: Spectrum analyser display of the VCO noise power, with a 10 kHz frequency per division.

Fig. 2.40 shows the noise power of the VCO as measured using a spectrum analyser. The spectrum analyser makes use of a bandpass filter with variable centre frequency. The filter only lets through the signal having the same frequency as the filter at that point. The power spectrum $S(\omega)$, associated with that signal is then measured as the rms noise power of the oscillator at that exact offset frequency from the carrier. Then, by associating the measured rms power with the corresponding offset frequency, a similar display as in Fig. 2.40 is obtained. Illustrated is the power received by a 3 kHz wide filter, as the filter centre frequency is varied over the display sweep range. The 3 kHz filter is represented by the *resolution bandwidth* (RBW), *intermediate frequency* (IF) filter inside the spectrum analyser.

On interpreting Fig. 2.40, recall from Fig. 2.38 that the SSB phase noise at an offset frequency $f_m = 10$ kHz was -120 dBc/Hz. Suppose the VCO produces 0 dBm at f_0 , then according to (2.81), the 3 kHz bandpass filter just mentioned, would receive a noise power of approximately -85 dBm at both frequencies, $f_0 + f_m$ and $f_0 - f_m$. The latter is clearly indicated in Fig. 2.40 for a VCO with phase noise as given in Fig. 2.38.

The best, most accurate way to determine the noise power in neighbouring channels is to integrate the phase noise curve. Any phase noise measurements can be integrated numerically.

The two-sided Power Spectral Density (PSD) associated with phase noise is given by

$$S_{\phi}(f_m) = 2.L(f_m) = \frac{\theta_{pk}^2}{2} = \theta_{rms}^2, \quad (2.82)$$

where $S_{\phi}(f_m)$ represents the power in both sidebands.

From the section about *Types of Noise* it was made clear that the output noise power of a noisy two-port network was given as kT_0BFG ; where $T_0 = 290$ K, B is the measurement bandwidth, F is the noise figure of the network, and G is the gain of the network. The noise, mainly generated by passive or active devices, was referred to as *white noise* (independent of frequency). By making use of the same definition as illustrated above, white noise can also be interpreted in terms of phase noise. Consequently, the ratio of output noise power density to output signal power for a 1 Hz bandwidth, gives the power spectral density as

$$S_{\phi}(f_m) = \frac{kT_0BFG}{G.P_c} = \frac{kT_0F}{P_c}, \quad (2.83)$$

where P_c is the input signal (carrier) power [14, 15, 16].

2.3.5 Leeson's Phase Noise Model

Another way for characterising the power spectral density of oscillator phase noise is by means of **Leeson's phase noise model**. Similar to the discussion in section 2.1, an oscillator can be modelled as an amplifier with a resonant device in the feedback path. The following figure provides an illustration.

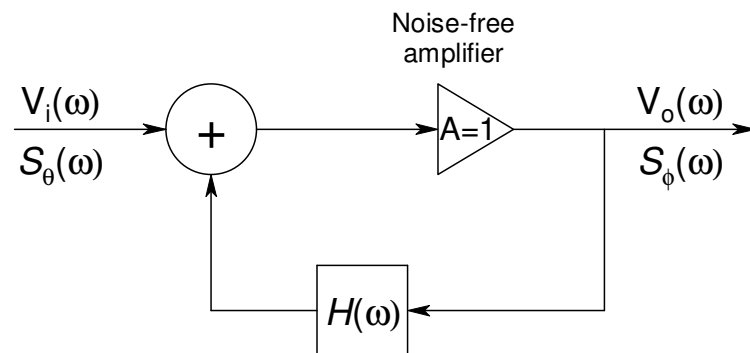


Figure 2.41: Feedback amplifier model for characterising oscillator phase noise.

In Fig. 2.41 the amplifier's voltage gain is illustrated as $A=1$, since it is included in the feedback transfer function $H(\omega)$. Consequently, the *voltage transfer function* for the oscillator circuit can be written as,

$$V_o(\omega) = \frac{V_i(\omega)}{1 - H(\omega)}. \quad (2.84)$$

For example, consider a high- Q resonant circuit in the feedback loop of a Colpitts oscillator circuit. Then, the *feedback transfer function* in (2.84) can be represented by that of a parallel RLC resonant circuit, which is of the form,

$$H(\omega) = \frac{1}{1 + jQ_L \left(\frac{\omega}{\omega_0} - \frac{\omega_0}{\omega} \right)} = \frac{1}{1 + 2jQ_L \frac{\omega_m}{\omega_0}}, \quad (2.85)$$

where ω_0 is the resonant frequency of the oscillator, and $\omega_m = \omega - \omega_0$ is the frequency offset relative to the resonant frequency.

By definition, the input and output power spectral densities are related by the *square of the magnitude* of the voltage transfer function, so that

$$S_{out}(\omega) = \left| \frac{V_{out}(\omega)}{V_{in}(\omega)} \right|^2 S_{in}(\omega). \quad (2.86)$$

From (2.84) it is clear that the voltage transfer function is represented by,

$$\frac{V_o(\omega)}{V_i(\omega)} = \frac{1}{1 - H(\omega)}, \quad (2.87)$$

so that, following from equations (2.85) and (2.86),

$$\left| \frac{1}{1 - H(\omega)} \right|^2 = \left| 1 + \frac{\omega_0}{2jQ_L \omega_m} \right|^2 = 1^2 + \left(\frac{\omega_0}{2Q_L \omega_m} \right)^2. \quad (2.88)$$

When substituting (2.88) back into (2.86), the output power spectral density of the oscillator phase noise can be written as,

$$S_{\phi}(\omega_m) = \left(1 + \frac{\omega_0^2}{\omega_m^2} \right) S_{\theta}(\omega_m), \quad (2.89)$$

where

$S_{\theta}(\omega_m)$ = PSD of phase noise at the input of the oscillator

$S_{\phi}(\omega_m)$ = PSD of phase noise at the output of the oscillator

ω_h = $\omega_0/2Q_L$, the half-power (3 dB) bandwidth of the resonator, in $[\text{rad}\cdot\text{s}^{-1}]$

ω_m = the frequency offset relative to the resonant frequency ω_0 , in $[\text{rad}\cdot\text{s}^{-1}]$.

The amplifier in the oscillator circuit characterise the input power spectral density $S_{\theta}(\omega)$. The following figure illustrates the noise spectrum of a typical transistor amplifier, with a sinusoidal input applied at f_0 .

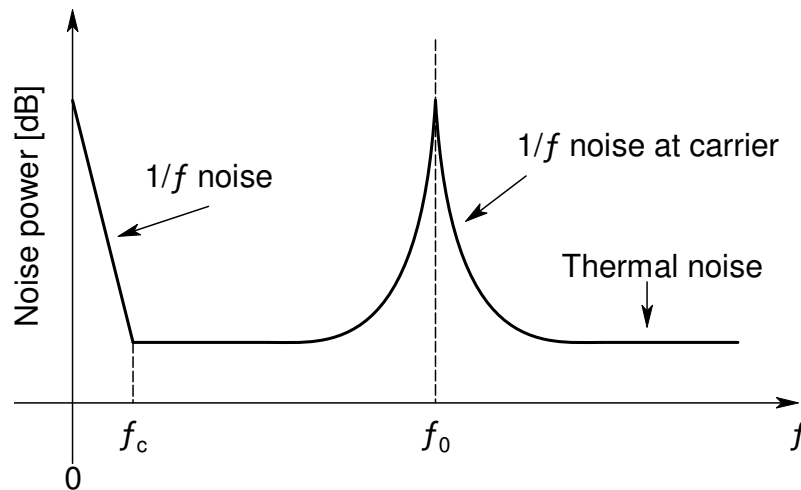


Figure 2.42: Amplifier noise power for an input signal at f_0 .

In Fig. 2.42 two major noise components are visible. Besides the electrical, inherent thermal noise (kTB); the additional transistor generated $1/f$ noise, which occurs at frequencies below f_c , is also present. $1/f$ noise is considered an important factor when describing the phase noise of an oscillator, since it dominates the phase noise power at frequencies *close* to the carrier. This is due to the non-linearity of the transistor, which enables the $1/f$ noise to modulate the applied signal and consequently give rise to the $1/f$ noise sidebands around the carrier.

As a result, from Fig. 2.42 the following illustration would be sufficient to describe the SSB, input power spectral density of an oscillator.

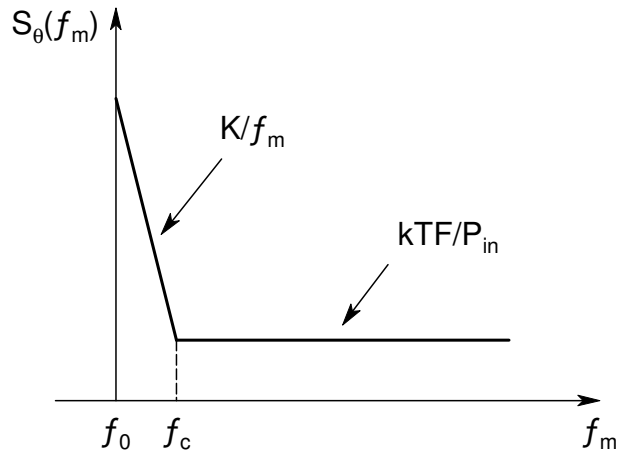


Figure 2.43: Input PSD of the oscillator.

In Fig. 2.43, K/f_m represents the $1/f$ noise component around the carrier, while the thermal noise is represented by kTF/P_{in} . The following expression can be written for the input power spectral density of the oscillator, when stating Fig. 2.43 mathematically,

$$S_{\theta}(\omega_m) = \frac{kTF}{P_{in}} \left(1 + \frac{K\omega_c}{\omega_m} \right). \quad (2.90)$$

The type of transistor present in the oscillator plays a key role in determining the frequency f_c , which is also called the “flicker”, cut-off frequency. Typical values are,

Silicon junction FETs : $50 \text{ Hz} \leq f_c \leq 100 \text{ Hz}$,

GaAs FETs : $2 \text{ MHz} \leq f_c \leq 10 \text{ MHz}$, and

Bipolar transistors : $5 \text{ kHz} \leq f_c \leq 50 \text{ kHz}$.

Finally, the *output power spectral density* of the oscillator is found by substituting (2.90) into (2.89), and so obtaining the following,

$$\begin{aligned} S_{\phi}(\omega_m) &= \left(1 + \frac{\omega_h^2}{\omega_m^2} \right) S_{\theta}(\omega_m) \\ &= \left(1 + \frac{\omega_h^2}{\omega_m^2} \right) \frac{kTF}{P_{in}} \left(1 + \frac{K\omega_c}{\omega_m} \right) \\ &= \frac{kTF}{P_{in}} \left(\frac{K\omega_c\omega_h^2}{\omega_m^3} + \frac{\omega_h^2}{\omega_m^2} + \frac{K\omega_c}{\omega_m} + 1 \right). \end{aligned} \quad (2.91)$$

Consequently from equation (2.91), the **output PSD** can be written as

$$S_{\phi}(f_m) = \frac{kTF}{P_{in}} \left(\frac{K \cdot f_c \cdot f_0^2}{4Q_L^2 \cdot f_m^3} + \frac{f_0^2}{4Q_L^2 \cdot f_m^2} + \frac{K \cdot f_c}{f_m} + 1 \right), \quad (2.92)$$

where

$k = 1.380 \times 10^{-23}$ [J/K], is Boltzmann's constant

$T = 290$ [K], the temperature

F = the noise factor (absolute terms) of the amplifier two-port network

P_{in} = the input signal power to the amplifier in the oscillator, in [W]

K = a constant accounting for the strength of the $1/f$ noise

f_c = the corner frequency of the $1/f$ noise, in [Hz]

f_0 = the fundamental frequency of oscillation, in [Hz]

$f_m = (f - f_0)$, is the offset frequency from the carrier, in [Hz]

$Q_L = f_0/(2B)$, is the loaded quality factor of the resonator in the oscillator

B = the half-power (3 dB) bandwidth of the resonator, in [Hz].

The following section will graphically discuss Leeson's model by dividing (2.92) up into four different terms. Since the Q-value determines the most significant of the middle two terms (terms ② and ③), two different instances occur in describing the phase noise of an oscillator; namely a low-Q or a high-Q instance respectively.

The following four terms represents the four major causes of oscillator noise.

First term: ['Flicker FM (f_m^{-3})' – Up-converted $1/f$ noise]

$$\frac{K \cdot f_c \cdot f_0^2}{4Q_L^2 \cdot f_m^3}$$

This term is valid for both low-Q and high-Q. The noise power at frequencies close to the carrier f_0 , will decrease as $1/f^3$, (-30 dB/decade).

Second term: ['White FM (f_m^{-2})' – Thermal FM noise]

$$\frac{f_0^2}{4Q_L^2 \cdot f_m^2}$$

This term represents the instance where the resonator has a *relatively low-Q*. In this case the half-power bandwidth f_h , is higher than the 'flicker' cut-off frequency f_c . The noise power at frequencies, $f_c < f < f_h$ will decrease as $1/f^2$, (–20 dB/decade).

Third term: ['Flicker PM (f_m^{-1})' – Flicker phase noise]

$$\frac{K \cdot f_c}{f_m}$$

The third term represents the instance where the resonator has a *relatively high-Q*. In this case the half-power bandwidth f_h , is lower than the 'flicker' cut-off frequency f_c . The noise power at frequencies, $f_h < f < f_c$ will decrease as $1/f$, (–10 dB/decade).

Fourth term: ['White phase (f_m^{-0})' - Thermal noise floor]

$$\frac{kTF}{P_m}$$

The PSD of the output phase noise of an oscillator at higher frequency offsets from the carrier, is predominantly represented by thermal noise power ($kTBF$) and accordingly constant with frequency. It is also perceived that the PSD is proportional to the noise figure of the amplifier. The bandwidth B , is taken as 1 Hz.

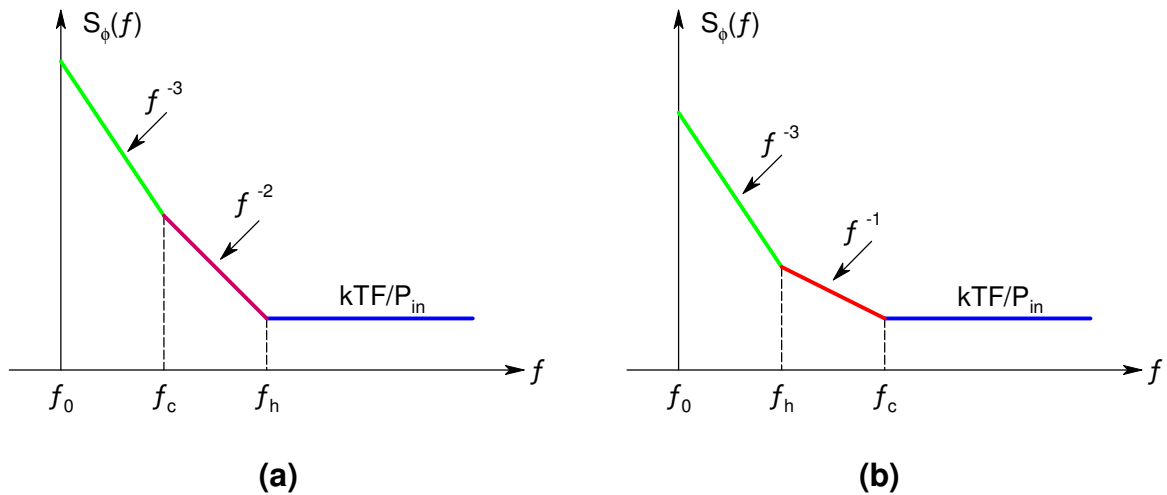


Figure 2.44: PSD of the output phase noise of an oscillator according to Leeson's Model. (a) Low-Q response ($f_c < f_h$). (b) High-Q response ($f_h < f_c$).

From Fig. 2.44 it is clear to see that the noise power experience a maximum at offset frequencies real close to the carrier. This problem can be minimised by making use of a high- Q resonator. The last statement is confirmed by the proportionality present in the first term considered, which stated that $1/f^3 \propto 1/Q^2$.

When considering the phase noise power at higher offset frequencies from the carrier, it is interesting to note that the former can be minimised in two ways. The first would be by using an amplifier with a very low noise figure; while the second is done by increasing the input signal power to the active element in the oscillator.

As will later be confirmed by the measurement results, it is important not to make the input power to the amplifier too big, since that would saturate the transistor; implying non-linear amplification of the input signal, which in turn would increase the phase noise power at the oscillator output.

A noiseless amplifier with $F = 1$ ($NF = 0$ dB), would help reduce the noise floor to a minimum with $kT = -174$ dBm/Hz. The noise floor illustrated in Fig. 2.44 will increase with F and decrease with the input signal power P_{in} , as follows,

$$\begin{aligned} \text{PSD - Phase noise power} &= \frac{kTF}{P_{in}} \\ &= (kT)_{dBm} + (F)_{dB} - (P_{in})_{dBm}. \end{aligned}$$

As mentioned previously, the output SSB phase noise is one-half of the output PSD represented in (2.92), written as

$$L(f_m) = \frac{1}{2} S_\phi(f_m),$$

so that,

$$L(f_m)_{[\text{dBc/Hz}]} = 10 \log_{10} \left\{ \frac{1}{2} \cdot \frac{kTF}{P_{in}} \left(\frac{K \cdot f_c \cdot f_0^2}{4Q_L^2 \cdot f_m^3} + \frac{f_0^2}{4Q_L^2 \cdot f_m^2} + \frac{K \cdot f_c}{f_m} + 1 \right) \right\}, \quad (2.93)$$

where

$$L(f_m)_{[\text{dBc/Hz}]} = \text{the ratio of sideband power in a 1 Hz bandwidth at } f_m, \text{ to the total power at the output of the oscillator, in [dBc/Hz]}$$

$$[\text{dBc/Hz}] = \text{dB relative to the carrier; measured in a 1 Hz bandwidth.}$$

By means of the above obtained results, a good model for oscillator phase noise was developed. It gives an insightful explanation how the noise power decreases as the offset frequency from the carrier increases [4, 14, 17].

2.3.6 Why is Low Phase Noise Important?

One of the most important considerations when evaluating the performance of wireless systems is the effect of noise. This is true because the threshold for the minimum signal level that can reliably be detected by a receiver is ultimately determined by the amount of noise present in the system. This is very important in radar applications, for example.

Since noise is inherent to all electrical systems, noise measurements have become an essential factor in the characterisation of a signal. As previously mentioned a system's noise is made up of internally generated noise, as well as noise entering the system through external sources.

Determining the phase noise present in a signal gives a clear indication of the limit it sets on the dynamic/operating range of a system. Just to mention a few systems that are negatively influenced by phase noise are for instance, the operating range of *radar*; the quality of television images; the precision of satellite positioning and the quality of data transmission.

Phase noise is illustrated as jitter in the time domain, and can be viewed on an oscilloscope, for example in Fig. 2.28. Phase noise can still cause changes to the spectrum of a signal, even if the level of phase noise is far too small to view on an oscilloscope. These changes are very important in radio applications, since it severely degrades the performance of a wireless system.

For instance, a transmitter can cause significant interference to other services even if minute amounts of phase noise is present on a transmitter signal.

In the case of a receiver, phase noise seriously degrades the receiver's selectivity by causing *reciprocal mixing*. The latter can be explained as follows. The receiver's local oscillator is used to down convert the desired signal to an intermediate frequency (IF) for further analysis. But due to phase noise present on the local oscillator, undesired signals nearby the desired signal frequency can be down converted to the same IF frequency. The phase noise located at an offset from the carrier equal to the IF frequency from the undesired signal, is the phase noise responsible for this conversion. The latter seriously degrades the receiver's selectivity and limits the space between adjacent channels.

Another example where phase noise plays an important role is especially in the case of PSK or QAM modulation, where it introduces an uncertainty during the detection of digitally modulated signals.

Sideband phase noise can convert into the information bandwidth and limit the overall system sensitivity [11, 14, 15, 18].

2.3.7 Requirements for Low Noise Oscillators

The key elements that determine the phase noise of an oscillator are:

- *The transistor:* Since the transistor's flicker-noise corner frequency mainly depends on the device current, it is important to try and keep the device current linear, which will minimise the phase noise.
- *The resonator:* The coupling between the resonator and the transistor has a great influence on the loaded Q of the resonator. The higher the Q value, the steeper the SSB phase noise curve will be, which indicates lower close-in phase noise.
- *The ultimate signal-to-noise ratio:* Maximize the RF output power, while the large-signal noise figure of the oscillator is kept to a minimum.

Only the first two key elements mentioned can be investigated using linear circuit analysis. Of the ultimate signal-to-noise ratio, only educated approximations can be made, since the active device's large-signal operation requires non-linear analysis techniques.

In using linear circuit analysis when investigating the first two key elements, the design goal is to keep the bias (DC) device current to a minimum, while the loaded Q of the resonator is pushed to a maximum.

When considering the former, minimum bias is important given that the flicker or $1/f$ noise of the device is highly dependent on the current. The flicker noise corner frequency f_c increases as the collector current for a typical bipolar transistor increases. Table 2.1 show some values. As mentioned earlier in the section discussing **Leeson's Phase Noise Model**, it was stated that the flicker noise dominates the phase noise power at frequencies *close* to the carrier. This is due to the non-linearity of the transistor, which enables the $1/f$ noise to modulate the applied signal and consequently give rise to the $1/f$ noise sidebands around the carrier. See Fig. 2.46 for an illustration.

Table 2.1: Collector Current for a Typical Bipolar Transistor vs. the Flicker Corner Frequency.

I_c [mA]	f_c [kHz]
0.25	1
0.5	2.74
1	4.3
2	6.27
5	9.3

In comparing transistor types, JFETs have much less flicker noise than bipolar transistors, while GaAs FETs have more.

Noise components are restricted to frequencies close to the frequency of oscillation, when the resonator consists of a high Q. The latter implies a steeper SSB phase noise curve for frequencies close to the carrier, while the phase noise is being minimised for an increasing offset frequency from the carrier.

Depending on the frequency of operation and the resonator type, several circuits have been developed to implement oscillators; each having their own advantages and disadvantages. Presently designed oscillators are likely to use capacitive feedback of the Colpitts or Clapp type, with transmission-line resonators if operating in the 400-2000 MHz range. When choosing between different transistors, the operating frequency is the main indication factor. When working in the last mentioned frequency range, BJT transistors are generally used instead of FETs, because only a few of the latter show sufficient gain-bandwidth product for use in UHF oscillator circuits. This is important to keep in mind, even though JFETs have less flicker noise than BJTs.

While flicker noise is largely dependent on the bias current, its *effect* can be reduced. Flicker noise contributes to the phase noise by modulating the oscillator's frequency via AM-to-PM conversion. This modulation conversion can be reduced by the use of negative feedback. In the following figure (Fig. 2.45) a simplified transistor noise model is shown.

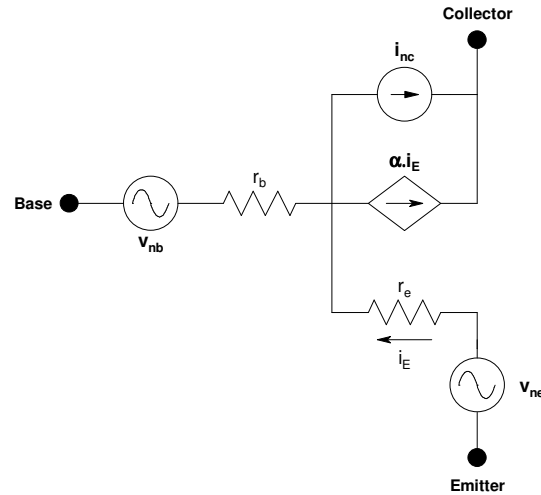


Figure 2.45: A simplified bipolar transistor noise model.

In section 2.3.1, various noise sources were discussed, amongst which were *thermal noise* and *shot noise*. When considering the noise sources as illustrated in Fig. 2.45; the noise source at the transistor base is represented by thermal noise, while the noise source at the transistor emitter is represented by shot noise.

Therefore, from the *Nyquist Theorem* the thermal noise present in electrical circuits is represented as the mean-squared noise voltage in a bandwidth B , and is given by (2.43) as,

$$v_n^2 = 4kTR_{eq}B \quad [V^2]$$

where

k = 1.380×10^{-23} [J/K], is Boltzmann's constant

T = the temperature, in degrees Kelvin [K], 290 K at room temperature

R_{eq} = is the Thevenin equivalent resistance of the one-port network, in [Ω]

B = the measuring bandwidth, in [Hz].

By representing the noise source at the transistor *base* as thermal noise, it can be written from the previous equation that the mean-squared noise voltage v_{nb} is defined as

$$\bar{v}_{nb}^2 \approx 4kTr_bB \quad (2.94)$$

where

r_b = the equivalent noise resistance at the transistor base.

From the *Schottky Theorem*, any shot noise present in an electrical circuit, indicates a randomly fluctuating noise power of mean-square value represented by (2.44) as

$$i_{sn}^2 = 2qIB, \quad [A^2]$$

where

$$q = 1.602 \times 10^{-19} [C], \text{ the charge of an electron}$$

$$I = \text{the DC current, in [A].}$$

Thus, from the previous equation the noise source at the transistor *emitter* can be represented as the mean-squared noise voltage v_{ne} , defined as

$$\bar{v}_{ne}^2 \approx 2qI_E r_e^2 B \cong i_{sn}^2 \cdot r_e^2 \quad (2.95)$$

where

$$I_E = \text{the emitter bias (DC) current, in [A]}$$

$$r_e = \text{the equivalent noise resistance at the transistor emitter.}$$

So that at high frequencies:

$$\bar{i}_{nc}^2 \approx 2q \left[\alpha_F I_E \left(\frac{1 - \alpha_F + f^2/f_0^2}{1 + f^2/f_0^2} \right) + I_{ce} \right] B \quad (2.96)$$

where

$$i_{nc} = \text{the noise current at the transistor collector}$$

$$\alpha_F = \frac{\beta_F}{1 + \beta_F}, \text{ the common-base current gain and is always slightly less than 1}$$

$$\beta_F = \frac{i_C}{i_B} = \frac{\alpha_F}{1 - \alpha_F}, \text{ is the common-emitter current gain, usually } 50 < \beta < 300.$$

The effect obtained when reducing the phase noise by applying negative feedback, is shown in the following figure [4].

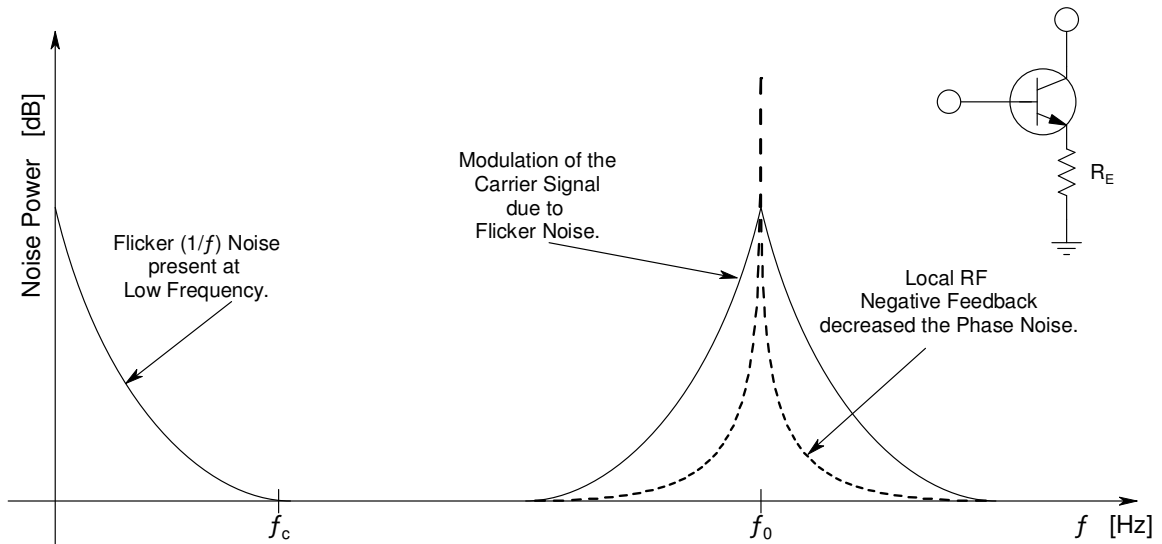


Figure 2.46: Adding negative feedback can reduce the amount of AM-to-PM modulation of the carrier by the transistor's flicker noise.

In the following section a discussion follows on ways to minimise phase noise, where it is mentioned how an *unbypassed emitter resistor*, as illustrated in the previous figure, can do exactly that.

Another interesting point to make is that phase noise performance is degraded by **frequency multiplication**. Suppose N is the multiplication factor, then the rate of degradation is represented by $20 \cdot \log(N)$. For instance, a doubler in an oscillator will degrade the phase noise by, $20 \cdot \log(2) = 6$ dB. While a ten times multiplication will degrade the phase noise by, $20 \cdot \log(10) = 20$ dB ≈ 6 dB/octave.

Environmental conditions, such as shock and vibration also play a major role in the degradation of phase noise. Unwanted side-bands can be induced by vibration in particular. It is recommended that the oscillator design is optimised to minimise the effects of shock and vibration by the inclusion of rugged mounts and bonding of components to the substrate [19].

2.3.7.1 Ways to Minimise Oscillator Phase Noise

In order to minimise the phase noise of an oscillator, it is important to guarantee the following:

(1) *Maximise the Q.*

- The easiest way of maximising the Q is by making use of a high-Q resonator such as a coaxial or dielectric resonator, instead of the usual lumped element resonator of which the loss is too high. In choosing a high-Q resonator, it is important to keep in mind what the frequency range is in which the oscillator operates, since this has a great influence on what kind of resonator to choose. A dielectric (or ‘pill’) resonator has an unloaded Q-value ranging from around 100 to several hundred and its operating frequency depends on the dimensions of the resonator and its dielectric constant ϵ_r . A coaxial (or transmission line) resonator has an unloaded Q-value ranging from several hundred up to about 10 000 and operates in the frequency range 100 to 1000 MHz. Another excellent choice for a high-Q resonator is the cavity resonator. The latter operates at frequencies above 1000 MHz and its Q-value easily ranges from 10 000 up to 40 000 or more [20].

(2) *Maximise the power.*

- A definite decrease in $L(f_m)$ will appear when maximising the power. This is confirmed by *Leeson’s Phase Noise Model* (see p. 62). The power can be maximised by applying a high RF voltage across the resonator, which will then be limited by the breakdown voltages of the active devices in the circuit.

(3) *Limit compression.*

- By maximising the power (point 2), the active device will be driven well into compression, which almost certainly will degrade the noise figure of the device. Again, by referring to *Leeson’s Phase Noise Model*, it is clear that a degraded noise figure will have a negative influence on the phase noise. One way to limit the RF power input is to employ some form of AGC circuitry on the active device front end clip.

- (4) *Use an active device with a low noise figure.*
- A good way to start is to make use of an active device with a sufficiently low noise figure for the specific application.
- (5) *High impedance active devices.*
- By making use of high impedance devices such as GaAs FETs and HEMTs, phase perturbation can be minimised. This is possible since the signal-to-noise ratio or the signal voltage relative to the equivalent noise voltage can be very high in these devices.
- (6) *Reduce flicker noise.*
- The thermally generated channel noise and the induced noise at the gate of a GaAs FET, serves as the inherent noise source in the device. Although no shot noise is present in a GaAs FET; a significant flicker noise ($1/f$ -noise) is apparent at frequencies below 10 to 50 MHz.
 - As mentioned in the previous section, RF feedback is an excellent way of reducing flicker noise. For example, a reduction in flicker noise by as much as 40 dB can easily be obtained by adding an un-bypassed emitter resistor, R_E of 10 to 30 ohms. When working with low-noise oscillators, it is preferable to use bipolar devices. The reason being that bipolar devices have a much lower flicker noise than GaAs FETs. For example a 2N5829 Si Bipolar transistor has a flicker corner frequency of approximately 5 kHz, while a GaAs FET typically owns a value of, $f_c = 6$ MHz.
- (7) *Couple at the resonator output.*
- By logical reasoning it is clear that a narrow bandwidth will consist of less noise than a wider bandwidth. Since the resonator acts as a band pass filter, it can undoubtedly be said that less noise will exist at the output of the resonator than at its input. Thus the resonator limits the amount of noise let through. Therefore it is wise to rather couple the energy from the resonator output than from any other point of the active device [21].

Take note that to be able to reach a suitable middle ground sufficient for a specific oscillator application; the just mentioned steps would have to be played against one another to reach that optimum point of minimum phase noise.

2.3.8 Voltage Controlled Oscillator (VCO) Noise

By referring to a 'VCO', it is understood that the designed oscillator's output frequency can easily be changed by means of a voltage applied to the oscillator's control/tuning port. This is often done by means of varactor diodes, which adds a variable amount of capacitance to the resonator circuit, thus changing the resonant frequency of the oscillator.

When investigating the factors that determine the phase noise generated by a VCO, the following are important. For example:

- (1) *Frequency.*
 - Good phase noise gets more difficult to achieve as the carrier frequency increases.
- (2) *Frequency Range.*
 - When the frequency range is kept narrow, it is easier to achieve good phase noise.
- (3) *Tuning Sensitivity.*
 - The phase noise is degraded, as the tuning sensitivity is being increased. Tuning sensitivity is referred to as the slope of the frequency versus tuning voltage performance for a given VCO (also called the tuning characteristic) and is expressed as frequency change per unit voltage change (in MHz/V).
- (4) *Supply Current.*
 - When working with designs where a high supply current (thus, a larger signal) is present, it is generally easier to achieve good phase noise at higher offset frequencies (> 1 kHz). This is true since phase noise normally is characterised by the ratio of phase noise power compared to the signal power.
- (5) *Tuning Voltage.*
 - Working with designs having a wide tuning voltage range, it is typically easy to achieve good phase noise for a given frequency range.

- (6) *Temperature.*
- There is typically a 3 dB variation in phase noise, in the range between - 55 °C and + 85 °C.
- (7) *Frequency Pushing.*
- Frequency pushing is referred to as the corresponding change in output frequency, when the tuning voltage is kept fixed and a given change in supply voltage is applied (expressed in MHz per volt). Because an increase in sensitivity to the power supply noise occurs when high pushing is applied, phase noise degradation is possible [12].

Additional factors that determine the phase noise generated by a VCO are:

- (1) The Q-factor of the resonator
- (2) The Q-factor of the varactor diode used
- (3) The active device used for the oscillating transistor
- (4) The power supply noise
- (5) The external tuning voltage supply noise

By choosing the power supplies carefully, the noise added by (4) and (5) can be minimised. Therefore it can be said that, *the phase noise of a VCO is primarily determined by the overall Q of the circuit*, which includes (1) and (2). To ensure a high-Q circuit, the tuning bandwidth must be minimised. Therefore, a VCO with a smaller tuning range is more appropriate for low phase noise performance designs.

In trying to minimise the phase noise of a VCO, there are some additional steps to be taken in comparison with those taken for an oscillator. By following these additional steps, the best overall performance can be expected from the VCO.

1. It is important to keep the *ground plane* of the VCO and the PCB *the same*. In order to do that, all the VCO ground pins should be soldered directly to the PCB ground plane. It is also recommended that the returns of the supply voltages, V_{cc} (power supply) & V_{tune} (tuning voltage), be connected to the PCB ground plane.
2. *Supply all chips* with the necessary *RF grounding*, by adding decoupling capacitors between the V_{cc} supply and ground.

3. When considering appropriate power supplies, it is important to look for a *high-quality, low-noise power supply*. The best overall performance will be achieved with the use of DC batteries. The latter should be used for both the supply (V_{cc}) and tuning (V_{tune}) voltages.
4. To ensure safe coupling to an external load, it is recommended that a *resistive pad* is added between the VCO output and the external load. Make sure that the output of the VCO is correctly terminated with a sufficient load impedance.
5. When connecting to the *tuning port* of the VCO, it is recommended that all *connections* are kept as *short* as possible, well screened, shielded and decoupled. In doing all of the above, the VCO will be kept from being modulated by external noise sources [16].

Depending on the application, a high tuning range or a narrow tuning range may be required for the VCO design. Amongst other things, this will directly determine the kind of tuning diodes used to achieve the specific requirement. Hyperabrupt diodes are tuning diodes with a high capacitance range and are mostly used in high tuning range applications. Tuning diodes are characterised by their transfer function or change of capacitance as a function of voltage. Since hyperabrupt diodes have such a high capacitance range, their transfer characteristic is not very linear. In other words, the range in which the diode's capacitance ratio is still useful is limited. The reason for this limitation is that the diode must not be driven into breakdown by the RF voltage superimposed on the tuning voltage, V_{tune} . Since this limitation exists, the situation may occur that more of the same tuning diode is needed to realise the tuning range which is being designed for. In general, the diodes are then placed in parallel to achieve a greater variation in capacitance.

Another decisive factor on the type of tuning diode used is the desired Q-factor of the overall system. When a high-Q design is kept in mind, it is important to make use of high-Q tuning diodes; since the diodes have a considerable effect on the overall Q of the system. The difficulty with high-Q tuning diodes is that their useful capacitance range is not that high at all. This means that several diodes might have to be utilized in parallel, to achieve the desired tuning range.

As just mentioned, capacitance is contributed to the resonant circuit by means of tuning diodes. This is a direct result of an alternating voltage at the resonant circuit. But, this capacitance contribution may produce some undesirable effects, especially in the case of a high alternating voltage. Three of these effects are:

- As mentioned earlier, a nonlinearity of capacitance exists. The effect that the latter has on the oscillator circuit mainly depends on the amplitude of the RF voltage across the tuning diodes. Therefore it is important to *keep the RF voltage as small as possible*; otherwise the nonlinearity may produce more harmonics than what the oscillator circuit would have by itself.
- Due to the previously mentioned nonlinear capacitance factor involved, it can be said that even if a sinusoidal voltage is applied to the tuning diodes, their capacitance variation will not necessarily follow the sine law. Under certain conditions, another undesirable effect that might occur is bistable behaviour. The latter refers to an effect called *squegging*. Under squegging is understood that the active element, the transistor in particular, switches on and off; which results in 'oscillation' and 'no oscillation' conditions of the oscillator respectively.
- Another kind of disturbance which exists due to nonlinearities in the diode characteristics is called *intermodulation*. The latter is practically independent of the oscillator amplitude. As mentioned previously, it is known that the oscillator transistor generates noise internally. Due to intermodulation, the transfer of an undesired signal (the transistor noise) to the oscillator output signal is possible. This action is often referred to as AM-to-PM conversion and occurs in BJT PN and NP junctions, as well as in their FET equivalents [4].

CHAPTER 3

SYSTEM: OSCILLATOR

3.1 RESONATOR

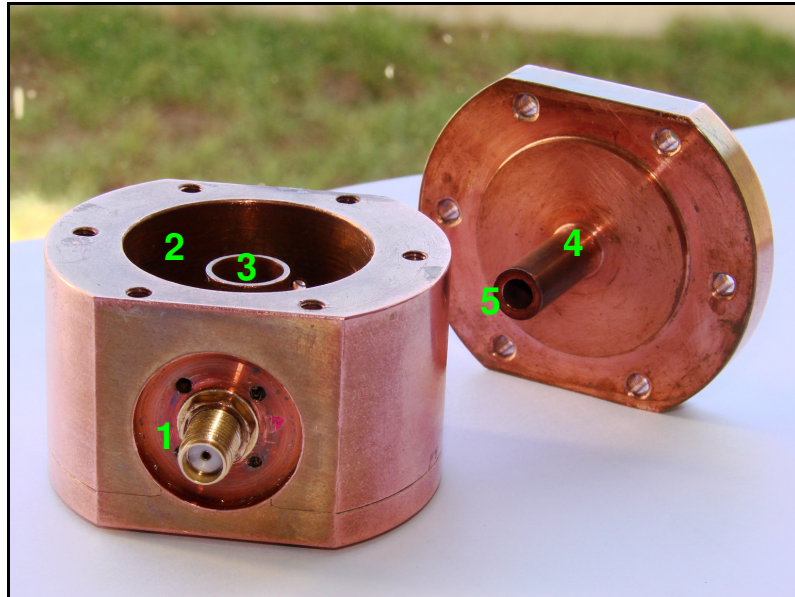


Figure 3.1: The designed Transmission-line, Cavity Resonator.

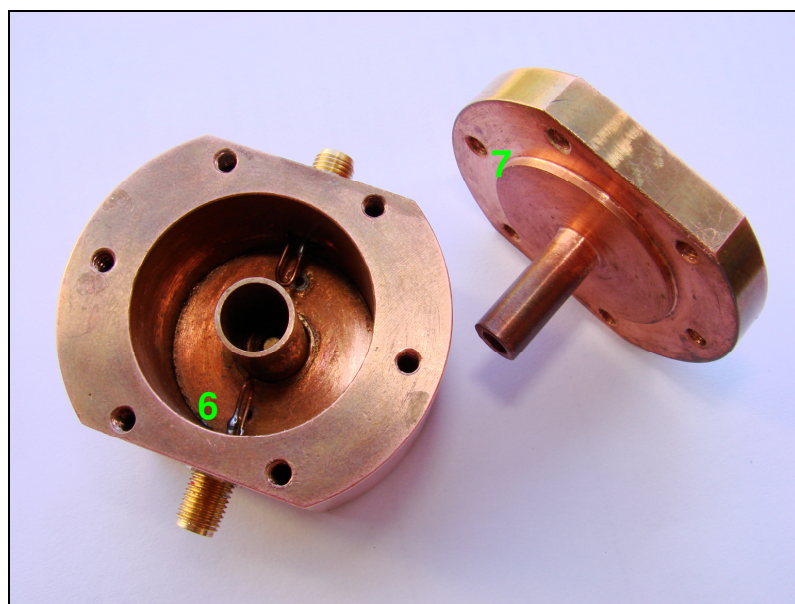


Figure 3.2: Top view of the Resonator, showing the coupling loops.

From figures 3.1 and 3.2 the following characteristics are noticeable:

- 1 : SMA connector onto which the coupling loop inside the cavity is soldered.
- 2 : The shorted transmission line (line 2), with characteristic impedance Z_{02} . The air cavity serves as its dielectric.
- 3 : The inner conductor of line 2, but also the outer conductor of the open transmission line (line 1). Line 1 has a characteristic impedance Z_{01} .
- 4 : The inner conductor of line 1, also with air as its dielectric.
- 5 : A gap was made in the inner conductor of line 1, to minimise the additional charge that exists due to the fringing electric field at the open-circuit end of the line. This additional charge is modelled by a capacitance, C_0 .
- 6 : Coupling to the magnetic field present in the cavity is made possible by means of the coupling loops visible.
- 7 : The lid to the cavity. The extra step introduced in the material was made to seal off the fields more effectively. Six screws secured the lid to the base.

3.1.1 Derivation Of The Optimum Point For Minimum Phase Noise

As mentioned in Chapter 1, an optimum point of minimum phase noise was derived, from which the design and the amount of coupling to the resonator was established. The derivation was done by examining a typical oscillator block-diagram, as illustrated in the following figure:

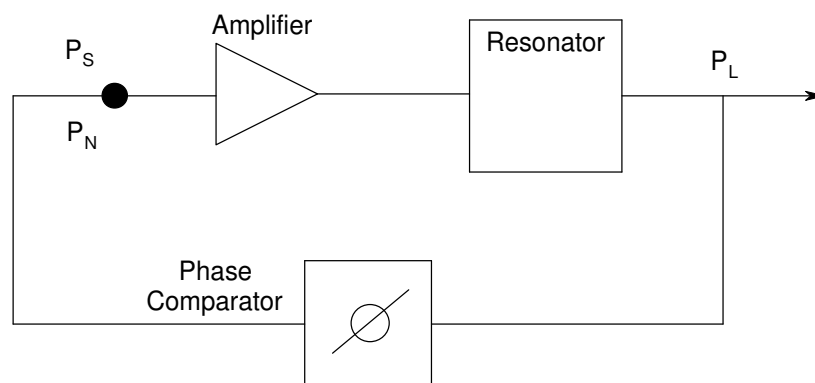


Figure 3.3: Block diagram representation of an oscillator.

where

P_S = the input signal power to the amplifier in the oscillator

P_N = the input noise power to the amplifier in the oscillator

P_L = the output signal power, dissipated in the load.

Firstly – revisit the definition of the spectrum $S_\theta(\omega_m)$, of the uncertainty $\theta(t)$ of the oscillator input phase, due to noise.

From (2.89) in Section 2.3.5, *Leeson's Phase Noise Model* or Leeson's letter called 'A Simple Model of Feedback Oscillator Noise Spectrum' [22]; the output power spectral density of the oscillator phase noise is defined as:

$$S_\phi(\omega_m) = \left[1 + \left(\frac{\omega_0}{2Q_L \omega_m} \right)^2 \right] S_\theta(\omega_m). \quad (3.1)$$

For the event in which the offset frequency is smaller than the half-power bandwidth of the resonator, thus $\omega_m < (\omega_0/2Q_L)$, the previous equation can be rewritten as,

$$S_\phi(\omega_m) = \left(\frac{\omega_0}{2Q_L} \right)^2 S_\theta(\omega_m), \quad (3.2)$$

where

$S_\theta(\omega_m)$ = PSD of phase noise at the input of the oscillator (also described as the spectrum of the uncertainty $\theta(t)$, of the oscillator input phase due to noise)

$S_\phi(\omega_m)$ = PSD of phase noise at the output of the oscillator

ω_0 = the oscillator resonant frequency, in [rad.s⁻¹]

$\omega_0/2Q_L$ = the half-power (3 dB) bandwidth of the resonator, in [rad.s⁻¹]

ω_m = the frequency offset relative to the resonant frequency ω_0 , in [rad.s⁻¹]

$\theta(t)$ = the uncertainty of the oscillator input phase due to noise present.

The additive noise component of $S_\theta(\omega_m)$, is flat with frequency if the additive noise is white noise. The two-sided power spectral density of a feedback oscillator with an effective noise figure F , is

$$S_\theta(\omega_m) = \frac{1}{2} \cdot \frac{FkT}{P_s}, \quad (3.3)$$

where P_s = the signal level at the oscillator's active element input.

By substituting (3.3) back into (3.2), the following equation is reached:

$$\begin{aligned}
 S_{\phi}(\omega_m) &= \left(\frac{\omega_0}{2Q_L} \right)^2 \cdot \frac{1}{2} \frac{FkT}{P_S} \\
 &= \frac{1}{P_S Q_L^2} \cdot \frac{\omega_0^2 FkT}{8}.
 \end{aligned}
 \tag{3.4}$$

So from (3.4), the following proportionality exists,

$$S_{\phi}(\omega_m) \propto \frac{1}{P_S Q_L^2}.
 \tag{3.5}$$

From (3.4) it is clear that the output phase noise spectrum will illustrate a minimum when $P_S Q_L^2$ portrays a maximum.

Secondly – the previous oscillator illustration in Fig. 3.3 may for example be represented by circuit elements as follows:

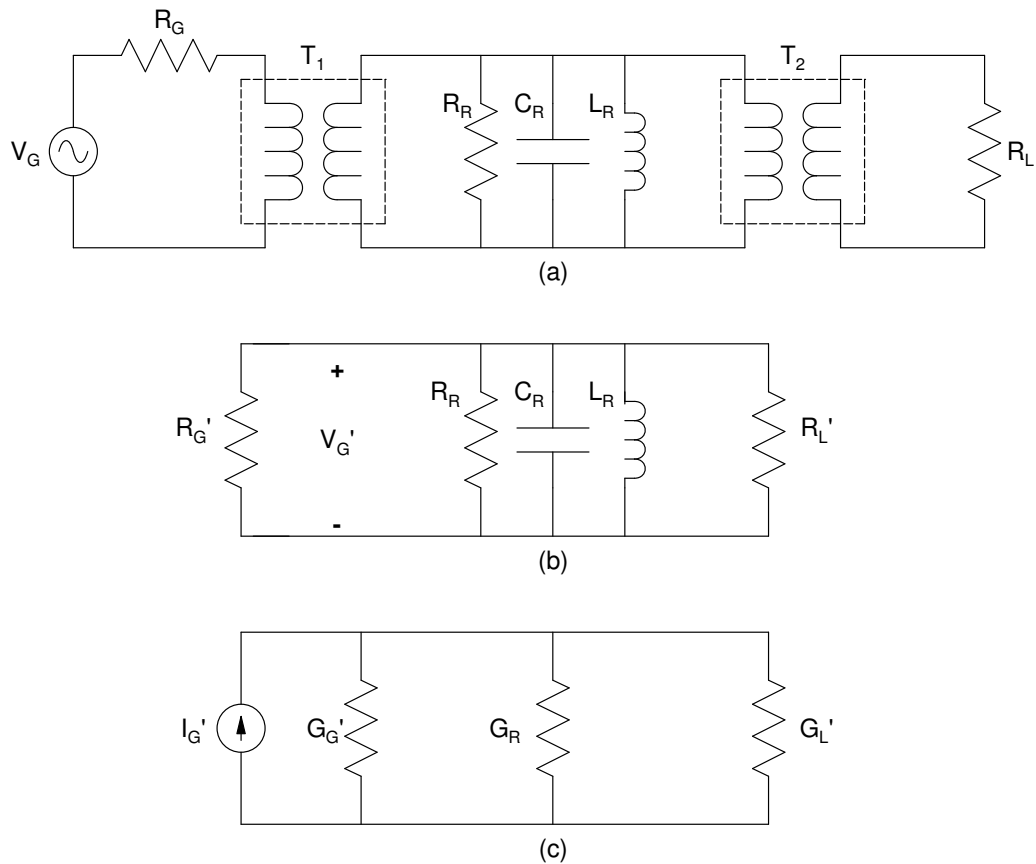


Figure 3.4: Circuit element representation of the resonator in Fig. 3.3. (a) Coupling represented by transformers. (b) Transformed resistance values. (c) 'Dissipation' circuit, with the corresponding conductance values.

The coupling between the source and the resonator, and the load and the resonator; can respectively be represented by transformers since the latter electrically isolate the one from the other, as depicted in Fig. 3.4 (a). Fig. 3.4 (b) illustrates the transformed resistance values and Fig. 3.4 (c) illustrates the 'dissipation' circuit with the corresponding conductance values.

Where

T_1 = the transformer connection between the generator and the resonator

T_2 = the transformer connection between the resonator and the load

V_G = the applied AC generator, source voltage

V_G' = the transformed, applied source voltage

I_G' = the transformed, applied source current

R_G = the generator, source resistance, in [Ω]

R_R = the equivalent, resonator resistance, in [Ω]

C_R = the equivalent, resonator capacitance, in [F]

L_R = the equivalent, resonator inductance, in [H]

R_L = the load resistance, in [Ω]

G_G' = the transformed, source conductance, in [S]

G_R = the equivalent, resonator conductance, in [S]

G_L' = the transformed, load conductance, in [S].

From basic circuit theory, the following equations can easily be written down. For the parallel circuit illustrated in Fig. 3.4 (c) the equivalent resistance is,

$$\frac{1}{R_{eq}} = \frac{1}{R_G'} + \frac{1}{R_R} + \frac{1}{R_L'}. \quad (3.6)$$

But, since it is easier to write the previous equation in terms of the equivalent conductance ($G = 1/R$), it can be written that

$$G_{eq} = G_G' + G_R + G_L'. \quad (3.7)$$

Consequently, the power delivered by the generator as available power, can easily be written as:

$$P_{available} = \frac{|I_G'|^2}{4G_G'} \quad (3.8)$$

The Q-value of the resonator and the oscillator can respectively be written as follows, keeping in mind that Q_U represents the unloaded Q-value, thus only taking the resonator into account; while Q_L represents the loaded Q-value, thus the Q-value of the entire oscillator:

$$Q_U = \omega_0 L_R G_R', \quad (3.9)$$

$$Q_L = \omega_0 L_R [G_G' + G_R' + G_L']. \quad (3.10)$$

In the following paragraph the derivation will be illustrated. Consider the denominator of (3.5) and substitute equations (3.8) and (3.10) into the former. Let the available power $P_{available}$, represent P_S the signal level at the oscillator's active element input. Hence, the following can be written:

$$\begin{aligned} P_S Q_L^2 &= \left(\frac{|I_G'|^2}{4G_G'} \right) \cdot (\omega_0 L_R [G_G' + G_R' + G_L'])^2 \\ &= \frac{|I_G'|^2 \cdot \omega_0^2 L_R^2}{4} \cdot \frac{(G_G' + G_R' + G_L')^2}{G_G'}. \end{aligned} \quad (3.11)$$

By substituting (3.11) back into (3.5), the following proportionality is obtained:

$$S_\phi(\omega_m) \propto \frac{G_G'}{(G_G' + G_R' + G_L')^2}. \quad (3.12)$$

Let $G_G' = G_L'$, thus the proportionality in (3.12) can be rewritten as,

$$S_\phi \propto \frac{G_G'}{(G_R' + 2G_G')^2}. \quad (3.13)$$

As mentioned earlier, the output phase noise spectrum will only illustrate a minimum, when $P_S Q_L^2$ portrays a maximum. Therefore, by taking the derivative of (3.13) with respect to G'_G , a minimum will be obtained when,

$$\frac{\partial S_\phi}{\partial G'_G} = 0. \quad (3.14)$$

Determine the **optimum point for minimum phase noise**:

$$\begin{aligned} \frac{\partial S_\phi}{\partial G'_G} &= \frac{\partial}{\partial G'_G} \left(\frac{G'_G}{(G_R + 2G'_G)^2} \right) \\ &= \frac{(G_R + 2G'_G)^2 \cdot \frac{\partial}{\partial G'_G} (G'_G) - G'_G \cdot \frac{\partial}{\partial G'_G} [(G_R + 2G'_G)^2]}{[(G_R + 2G'_G)^2]^2} \\ &= \frac{[G_R^2 + 4G_R G'_G + 4(G'_G)^2] \cdot 1 - G'_G [2(G_R + 2G'_G)(0 + 2)]}{(G_R + 2G'_G)^4} \\ &= \frac{G_R^2 + 4G_R G'_G + 4(G'_G)^2 - 4G_R G'_G - 8(G'_G)^2}{(G_R + 2G'_G)^4} \\ &= \frac{G_R^2 - 4(G'_G)^2}{(G_R + 2G'_G)^4}. \end{aligned} \quad (3.15)$$

Set (3.15) equal to zero:

$$\begin{aligned} \frac{\partial S_\phi}{\partial G'_G} &= \frac{G_R^2 - 4(G'_G)^2}{(G_R + 2G'_G)^4} = 0. \\ \Rightarrow \quad G_R^2 - 4(G'_G)^2 &= 0 \\ [4(G'_G)^2]^{1/2} &= [G_R^2]^{1/2} \\ \sqrt{4}G'_G &= G_R \\ 2G'_G &= G_R. \end{aligned} \quad (3.16)$$

Finally, from (3.16) it is clear that,

$$\boxed{G'_G = \frac{G_R}{2} = G'_L} \quad \text{and,} \quad \boxed{R'_G = 2R_R = R'_L} \quad (3.17)$$

Therefore, to be able to reach the **optimum point for minimum phase noise**, it is important that the transformed values of the source and load resistances, be *equal* and *double* the value of the resonator's equivalent resistance R_R . Thus, a *quarter* of the available power will be dissipated in the source and a *quarter* in the load; while *half* of the available power must be dissipated inside the resonator [23].



To give a brief explanation of what to expect through the rest of chapter 3: Firstly the technical specifications of the resonator design is discussed, where one of the transmission lines' characteristic impedance value is chosen, while the other is obtained through calculations. Once the latter is completed, a few basic transmission line equations are being discussed; from where the **Incremental Inductance Rule** is being implemented to determine some starting values for the resonator dimensions. The latter will also provide an indication of the corresponding Q-value of the resonator. These values are computed in **MATLAB** and then used in **CST** to simulate for instance, the electromagnetic fields and Q-value of the designed resonator. Subsequently, the resonator is measured. The resonator results are compared to the simulated ones and discussed. Thereafter the effect of every oscillator element is measured, either on the *Rohde & Schwarz ZVB8 Vector Network Analyser* or the *Rohde & Schwarz FSEK30 Spectrum Analyser* and consequently discussed. Lastly the phase noise of the oscillator is predicted by **Leeson's Phase Noise Model**, after which it is measured; firstly on the *Spectrum Analyser* and finally on the *Aeroflex PN9000B Phase Noise Test System*.

3.1.2 Resonator Design

As mentioned in Chapter 2, there are quite a few resonator designs to choose from. The right one for the application mainly depends on the operational frequency, as well as the Q-value preferred.

For the common lumped element LC resonator, a typical unloaded Q-value of approximately 300 can be expected, while a transmission line resonator can easily have an unloaded Q-value of 3000 [20, 23]. However, the lower the operational frequency, the longer the transmission-line becomes. For instance, a quarter-wavelength transmission line with a characteristic impedance of $Z_0 = 50 \Omega$, will be 75 mm long at 1 GHz. The length (physical size) might become a problem. One possible way to shorten the transmission line is to make use of two transmission lines with different widths but the same length. Take note that the characteristic impedance of the two lines will also differ due to the different widths. The wider the line, the lower its characteristic impedance.

For this project, it was decided to design a transmission line – cavity resonator. The end product would be a VCO, tuneable from 900 MHz and lower. It was decided to design the resonator at approximately a 10 % increase in resonant frequency, since the later addition of varactor diodes would decrease the frequency. The rest of the frequency difference, after addition of the varactor diodes, would then be tuned out to 900 MHz by means of a microwave tuning element.

3.1.2.1 Technical Specifications

The resonator's technical specifications were as follows. Design a transmission line – cavity resonator. The cavity had to be cylindrical with a height of 20 mm and a diameter of 30 mm. It was also added that the resonator would be made out of copper instead of yellow-copper, since the latter's loss is double that of the former and would result in a Q-value half of what copper could provide. Take note that the loss of silver-plated, yellow-copper is again less than that of copper. But that is a high risk and time consuming process to follow [23].

The proposed resonator design:

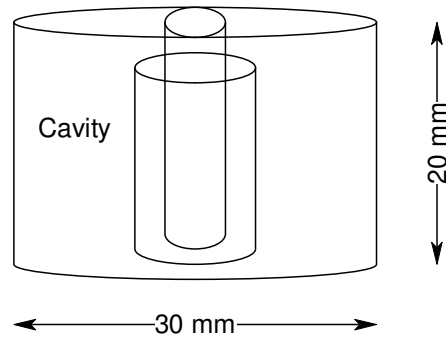


Figure 3.5: Schematic representation of the proposed Cavity Resonator.

Fig. 3.5 portrays a schematic representation of how the cavity resonator will appear. The inner cylinders represent two transmission lines – having different characteristic impedances – as illustrated in the following figure.

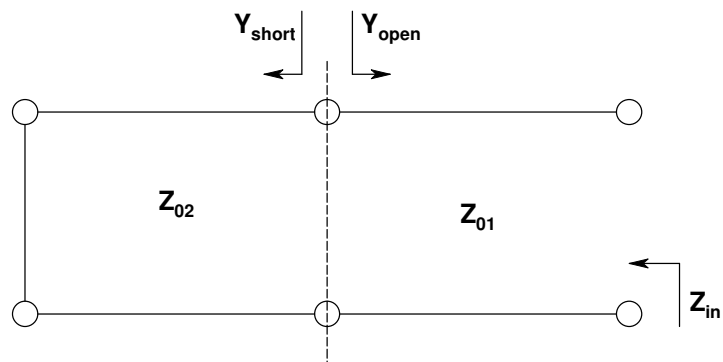


Figure 3.6: Transmission line representation of Fig. 3.3.

By the definition of resonance – it can be said that the resonator, as illustrated in Fig. 3.6; will resonate when the impedance [23],

$$Z_{\text{short}} + Z_{\text{open}} \rightarrow \infty . \quad (3.18)$$

Or stated otherwise, when

$$Y_{\text{short}} + Y_{\text{open}} \rightarrow 0 , \quad (3.19)$$

where

Y_{short} = the admittance seen looking into the short-circuit transmission line, in [S]

Y_{open} = the admittance seen looking into the open-circuit transmission line, in [S].

From the theory it is known that the impedance of an ideal, open-circuit transmission line is given as [24]:

$$Z_{\text{open}} = -jZ_0 \cdot \cot(\beta\ell);$$

so that the admittance can be written as,

$$Y_{\text{open}} = \frac{1}{-jZ_0} \cdot \tan(\beta\ell). \quad (3.20)$$

On the other hand, the impedance of an ideal, short-circuit transmission line is:

$$Z_{\text{short}} = jZ_0 \cdot \tan(\beta\ell);$$

so that the admittance can be written as,

$$Y_{\text{short}} = \frac{1}{jZ_0} \cdot \cot(\beta\ell), \quad (3.21)$$

where

Z_0 = the characteristic impedance, in [Ω]

β = $2\pi/\lambda$, the phase constant, in [rad/m]

ℓ = the physical length of the transmission line, in [m].

Suppose you have two transmission lines, as illustrated in Fig. 3.6; each having their own thickness but both having the same length ℓ . Choose one of the lines to have a characteristic impedance of 70Ω and determine the other impedance. By substituting equations (3.20) & (3.21) back into (3.19) and applying the equations to Fig. 3.6; the following relation can be written for:

$$Y_{\text{short}} + Y_{\text{open}} = 0$$

$$\left[\frac{1}{jZ_{02}} \cdot \cot(\beta\ell_2) \right] + \left[\frac{1}{-jZ_{01}} \cdot \tan(\beta\ell_1) \right] = 0. \quad (3.22)$$

As mentioned previously, it was chosen that the transmission line lengths have the same value. Thus, $\ell_1 = \ell_2 = \ell$. Choose $\ell = 20 \text{ mm}$ and $Z_{02} = 70 \Omega$. Use equation (3.22) and the recently mentioned values to determine Z_{01} :

$$\frac{1}{jZ_{02}} \cdot \cot(\beta\ell) + \frac{j}{Z_{01}} \cdot \tan(\beta\ell) = 0. \quad (2.23)$$

Do the necessary algebra:

$$\times jZ_{01}Z_{02} : Z_{01} \cdot \cot(\beta\ell) - Z_{02} \cdot \tan(\beta\ell) = 0$$

$$Z_{01} = Z_{02} \cdot \frac{\tan(\beta\ell)}{\cot(\beta\ell)}.$$

Since $\tan \theta = 1/\cot \theta$, the previous equation can be rewritten as:

$$Z_{01} = Z_{02} \cdot \tan^2(\beta\ell). \quad (3.24)$$

For $\ell = 20 \text{ mm}$, what is the value of the electrical length ($\beta\ell$)? The following transmission line equation is used to determine $\beta\ell$:

$$\beta\ell = \left(\frac{2\pi}{\lambda} \right) \cdot \ell = 2\pi \cdot \frac{1}{\lambda} \cdot \ell = 2\pi \cdot \frac{f}{c} \cdot \ell, \quad [\text{radians}] \quad (3.25)$$

where

$$f = 900 \times 10^6, \text{ the resonant frequency, in [Hz]}$$

$$c = 2.998 \times 10^8, \text{ the speed of light, in [m.s}^{-1}\text{]}$$

$$\lambda = c/f, \text{ the wavelength, in [m].}$$

Thus, from (3.24) and (3.25) the open-circuit transmission line has a characteristic impedance of:

$$\begin{aligned} Z_{01} &= Z_{02} \cdot \tan^2(\beta\ell) \\ &= (70) \cdot \tan^2(0.37725) \\ &= 10.99 \Omega. \end{aligned} \quad (3.26)$$

It is important to notice that two transmission lines with the same length but different widths, will have different characteristic impedances.

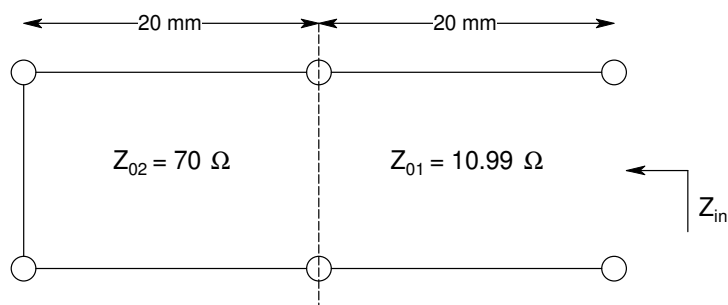


Figure 3.7: Transmission line resonator with the relevant values.

3.1.2.2 The Incremental-Inductance Rule

Before one can discuss the *Incremental Inductance Rule* as defined by H.A. Wheeler; it is important to cover a few basic transmission line equations. A two-wire line is often the schematic representation of a transmission line, as illustrated below. This is the case, since transmission lines always have at least two conductors for transverse electromagnetic (TEM) wave propagation.

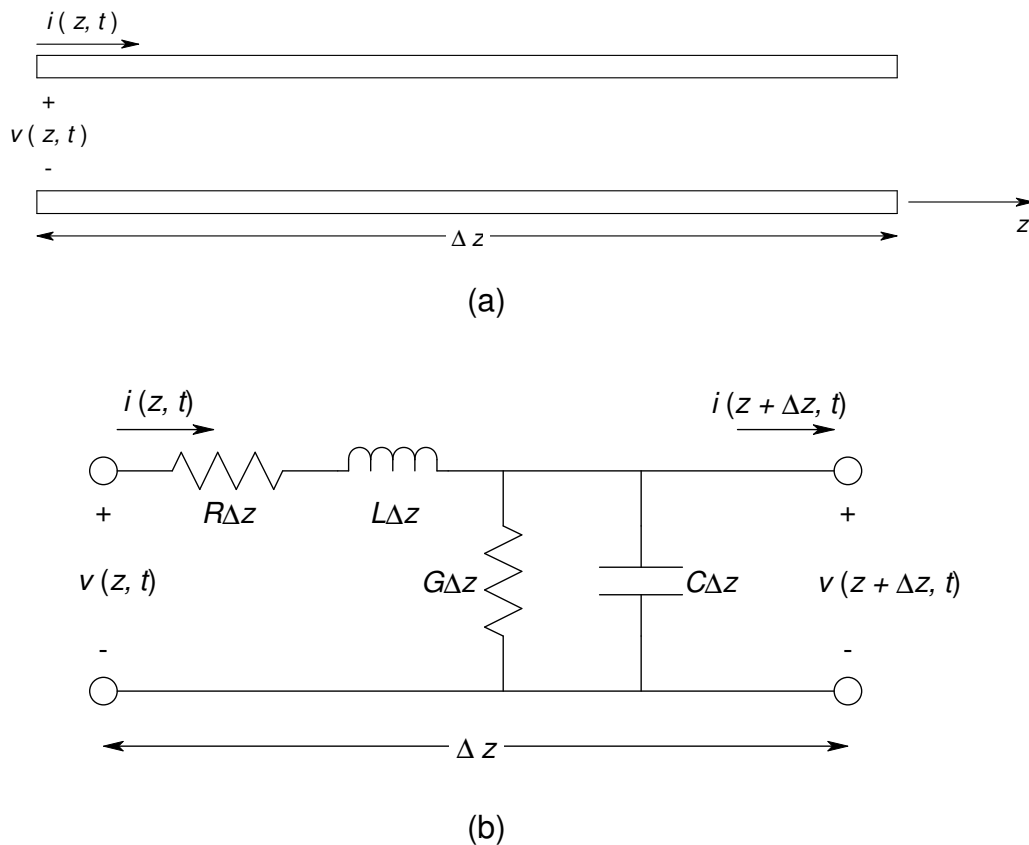


Figure 3.8: Representation of an incremental length of transmission line. (a) Illustration of the current and voltage on the line. (b) The Lumped-element equivalent circuit [14].

The form of transmission line as shown in Fig. 3.8 (b) is of infinitesimal length Δz . A cascade of the latter will form a finite length of transmission line. The different lumped elements represent different characteristics of the line. For instance, R and G represent the loss in the line; where the finite conductivity of the conductors is represented by R ; while G represents the dielectric loss in the material between the conductors. L on the other hand, represents the total self-inductance and C represents the close proximity of the two conductors respectively.

In general, the characteristic impedance Z_0 , of a transmission line can be defined as

$$Z_0 = \frac{R' + j\omega L'}{\gamma} = \sqrt{\frac{R' + j\omega L'}{G' + j\omega C'}}; \quad (3.27)$$

with

$$\gamma = \alpha + j\beta = \sqrt{(R' + j\omega L')(G' + j\omega C')}, \quad (3.28)$$

where

γ = the complex propagation constant, which is a function of frequency

α = the attenuation constant, in [dB/m]

$\beta = 2\pi/\lambda$, the phase constant, in [rad/m]

R' = the series resistance per unit length for both conductors, in [Ω /m]

L' = the series inductance per unit length for both conductors, in [H/m]

G' = the shunt conductance per unit length, in [S/m]

C' = the shunt capacitance per unit length, in [F/m].

In the case of a lossless transmission line where $\alpha=0$ and thus $\gamma = j\omega\sqrt{L'C'}$, it can be written from (3.27) that the unit length, characteristic impedance of the lossless transmission line is given as,

$$Z_0 = \sqrt{\frac{L'}{C'}}. \quad (3.29)$$

The phase velocity is,

$$v_p = \frac{\omega}{\beta} = \frac{1}{\sqrt{L'C'}}. \quad (3.30)$$

So that,

$$v_p^2 = \frac{1}{L'C'},$$

$$\text{and } C' = \frac{1}{L'v_p^2}. \quad (3.31)$$

All of the above are general transmission line equations [14].

When substituting (3.31) back into (3.29) it can be written that,

$$Z_0 = \sqrt{L' \cdot (L' \cdot v_p^2)} = L' \cdot v_p. \quad (3.32)$$

Since the phase velocity is also defined as,

$$v_p = \frac{1}{\sqrt{\mu \cdot \epsilon}}, \quad (3.33)$$

and copper is a non-magnetic material; with the permittivity of air given by $\epsilon = 1$ [F/m]; (3.33) can be defined as constant. Thus, from (3.32) and (3.33) the assumption can be made that,

$$\boxed{Z_0 \propto L'}. \quad (3.34)$$

Take note that the characteristic impedance of a coaxial transmission line is defined as,

$$\begin{aligned} Z_0 &= \frac{138}{\sqrt{\epsilon}} \cdot \log_{10} \left(\frac{D}{d} \right) \\ &= \frac{60}{\sqrt{\epsilon}} \cdot \log_e \left(\frac{D}{d} \right), \end{aligned} \quad (3.35)$$

so that for $\epsilon = \epsilon_0 \cdot \epsilon_r$, with $\epsilon_r = 1$ for air, it can be written that;

$$\boxed{Z_0 = 60 \cdot \ln \left(\frac{D}{d} \right)}. \quad (3.36)$$

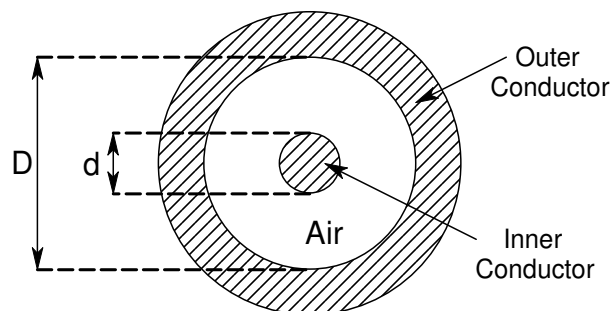


Figure 3.9: Transmission line parameters for a Coaxial Line.

Equation (3.36) defines the characteristic impedance of a coaxial transmission line, with only air as its dielectric material; as illustrated in Fig. 3.9 [25].

The '**Incremental-Inductance Rule**' as defined by H.A. Wheeler [26], provides an easy way to determine the unloaded Q-value of the resonator. This is done by looking at the magnetic loss power factor (p) of the resonator, which is directly proportional to the inverse of the Q-value. In other words, one can design the cavity resonator's dimensions for a particular loss factor, hence a particular Q-value.

High-frequency alternating currents and magnetic flux portrays the tendency to penetrate into the surface of a conductor. This behaviour is known as the '**skin effect**'. Depending on the frequency and the properties of the conductive material; a '*depth of penetration*' can be determined. In the case that the 'depth of penetration' is a lot smaller than the thickness of the conductor; this behaviour can be seen as a surface, rather than a volume occurrence.

A formula providing the effective resistance caused by the skin effect is precisely what the '*incremental-inductance rule*' is. It is important to notice that the latter is obtained only through inductance computations. Therefore, the incremental-inductance rule states *that the effective resistance in a circuit, is equal to the change of reactance caused by the penetration of magnetic flux into metal objects*. This rule is valid for any metal surface where the thickness and the radius are at least twice as great as the depth of penetration.

Thus, practically implementing the incremental-inductance rule involves relating the skin loss to the inductance. The PF of conductor loss is usually determined by the skin effect.

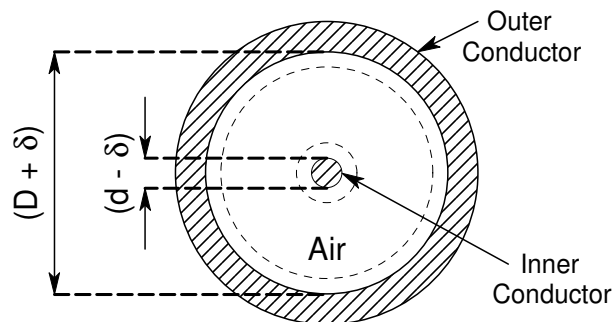


Figure 3.10: Coaxial Transmission line – illustrating the skin effect.

For the coaxial transmission line illustrated in Fig. 3.10 made out of perfect, non-magnetic conductors, the wave resistance (characteristic impedance) is uniquely related to the inductance, provided no dielectric is present (as explained up to (3.34)). The change in inductance that occur due to the skin effect can be defined as,

$$\Delta L = L_{\delta} - L. \quad (3.37)$$

The relative increment in inductance ($\Delta L/L$) is caused by removing a thickness ($\delta/2$) from the face of every conductor bounding the field, as illustrated in Fig. 3.10. Thus, representing the incremental-inductance rule and expressing the **loss PF of the magnetic field** (as bounded by the conductors) as,

$$p = \frac{\Delta L}{L}. \quad (3.38)$$

Increasing the wave resistance (Z_0) for a perfect conductor in the same ratio would be possible if the boundaries were modified in the same manner. From (3.34) and (3.36) it can be written that,

$$Z_{0\delta} = 60 \cdot \ln\left(\frac{D+\delta}{d-\delta}\right) \propto L_{\delta}. \quad (3.39)$$

Take note that if the conductors are made out of copper, the skin depth, δ can be calculated as [26],

$$\delta_c = 3.81\sqrt{\lambda} \text{ } \mu\text{m}. \quad (3.40)$$

Subsequently this change, from Z_0 to $Z_{0\delta}$, is used to compute the loss PF. Following from (3.37) and (3.38); expressed as follows,

$$\boxed{p = \frac{\Delta L}{L} = \left(\frac{Z_{0\delta} - Z_0}{Z_{0\delta}}\right) = \left(1 - \frac{Z_0}{Z_{0\delta}}\right) \ll 1.} \quad (3.41)$$

In the following paragraph, some of the formulas will be illustrated to determine the unloaded Q-value of this specific resonator. In the process, typical starting values are determined for the resonator's dimensions [26, 27].

The following figure illustrates a cut right through the middle of the resonator, displaying the different transmission lines, with the previously determined impedance values, for

- the open-circuit line, $Z_{01} = 10.99 \Omega$, and
- the short-circuit line, $Z_{02} = 70 \Omega$.

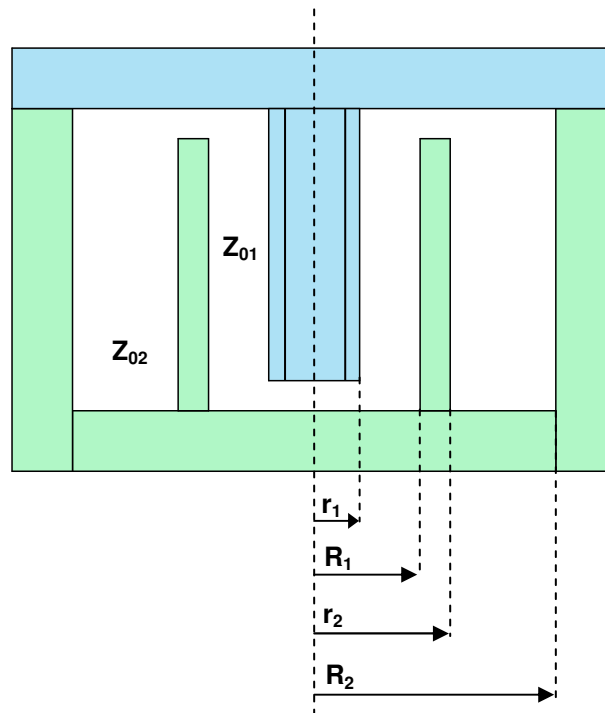


Figure 3.11: Resonator Dimensions as determined by Wheeler.

Subsequently, some initial values are determined for the resonator's dimensions, by means of the 'incremental-inductance rule'. The following equations were used to determine the dimensions illustrated in Fig. 3.11:

$$(3.36): \quad Z_0 = 60 \cdot \ln\left(\frac{D}{d}\right).$$

$$(3.39): \quad Z_{0\delta} = 60 \cdot \ln\left(\frac{D + \delta_c}{d - \delta_c}\right).$$

$$(3.40): \quad \delta_c = 3.81\sqrt{\lambda} \text{ } \mu\text{m} = 2.2 \text{ } \mu\text{m}.$$

$$(3.41): \quad p = \frac{Z_{0\delta} - Z_0}{Z_{0\delta}}.$$

$$\text{And:} \quad Q_U = \frac{1}{p}.$$

MATLAB was used to implement the above mentioned equations. In the first instance; the short-circuit transmission line was evaluated. While $D_2 = 30$ mm was specified, a vector was defined for d_2 . Firstly the characteristic impedance Z_{02} was calculated with the vector defined for d_2 . Plotting Z_{02} against d_2 , illustrates how the characteristic impedance of the coaxial line varies as its inner diameter varies. From the latter the value for d_2 was taken at exactly the point where $Z_{02} = 70 \Omega$ (as chosen). Consequently, the predicted unloaded Q-value for the specific line could be calculated from the loss PF, using the ‘incremental-inductance rule’.

In the second instance, the open-circuit transmission line was evaluated. The recently obtained value for d_2 was used to determine the value for D_1 by subtracting a conductor thickness of 0.5 mm; thereby subtracting 1 mm from the diameter value. Subsequently the value for d_1 was determined in exactly the same way as was done for d_2 . The predicted Q-value for line 1 was also calculated, thus providing all the necessary starting values for the resonator’s dimensions.

The curves plotted for both instances are illustrated in Fig. 3.17 and Fig. 3.18 respectively, on page 114. Table 3.1 summarises the starting values obtained for the dimensions of the resonator. The **MATLAB** code used to conduct the above mentioned calculations is attached in Appendix A.

Table 3.1: Starting values for the resonator’s dimensions.

	Line 1: <i>Open-circuit line</i>	Line 2: <i>Short-circuit line</i>
Z_0	10.99 Ω	70 Ω
$Z_{0\delta}$	11.0605 Ω	70.0320 Ω
$D_2 = 2 * R_2$	-	30 mm
$d_2 = 2 * r_2$	-	9.34 mm
$D_1 = 2 * R_1$	8.34 mm	-
$d_1 = 2 * r_1$	6.94 mm	-
Predicted Q_U	317.54	3780.3

3.1.2.3 Q calculation by means of the Susceptance Slope Parameter

By calculating the *susceptance slope parameter*, another, quite interesting way to determine the resonance properties of resonators is provided, for instance the Q-value of the resonator regardless of their form.

In the following two paragraphs a brief discussion will be given, with an example of what exactly to look for.

Recall Fig. 3.7 on page 91. Firstly, the short-circuit transmission line (line 2) is evaluated by computing its input impedance through transmission line theory. The latter will then be used as the load impedance of line 1, in order to compute its input impedance. In this case, the transmission lines are considered as having loss; thus $\alpha \neq 0$.

From theory, it is known that

$$Z_{in} = R_{in} \pm jX_{in} \quad (3.42)$$

so that, for $Y_{in} = 1/Z_{in}$, it can be written that

$$Y_{in} = G_{in} \pm jB_{in}, \quad (3.43)$$

where

Z_{in} = the input *impedance* of the transmission line (resonator), in [Ω]

R_{in} = the input *resistance*, in [Ω]

X_{in} = the input *reactance*, in [Ω]

Y_{in} = the input *admittance*, in [S]

G_{in} = the input *conductance*, in [S]

B_{in} = the input *susceptance*, in [S].

In determining the input admittance at different locations along a transmission line (illustrated in the following figure, Fig. 3.12) different values can be expected for Y_{in} and consequently, different values for the input conductance and input susceptance as well. But, even though the previously mentioned difference

exists, the overall Q-value for the transmission line resonator will stay the same; no matter at what location the admittance was determined.

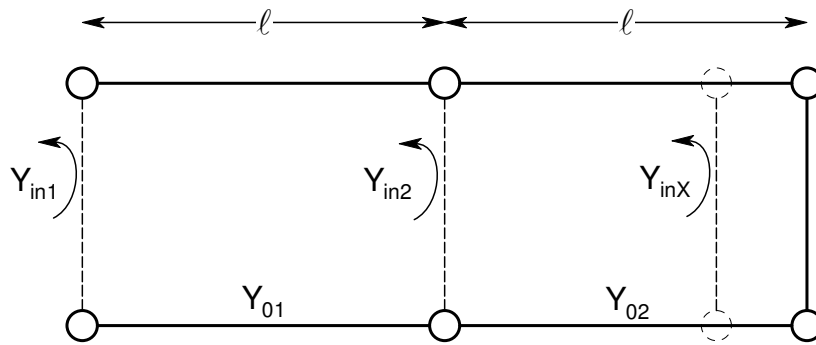


Figure 3.12: Illustrating the input admittance at different locations along the transmission line.

Fig. 3.13 illustrates how the input conductance and the input susceptance vary, as the location at which Y_{in} is being determined changes.

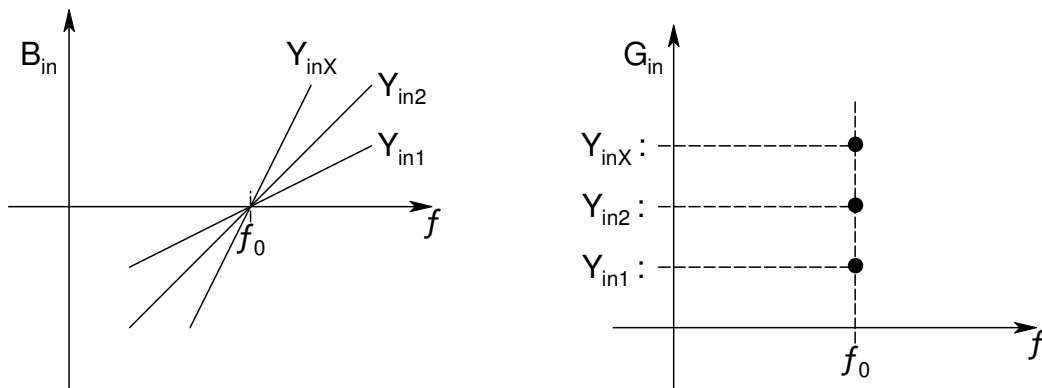


Figure 3.13: Illustration of how B_{in} and G_{in} vary, at different locations along the transmission line.

Therefore, once the input admittance Y_{in} of the resonator has been determined, it is easy to determine the overall unloaded Q-value of the resonator. This is done by determining the susceptance slope parameter, as mentioned earlier. The Q-value of a resonator having a shunt-type resonance with a susceptance slope parameter b_n , and a shunt conductance G_{in} ; has a Q-value of,

$$Q_u = \frac{b_n}{G_{in}}. \tag{3.44}$$

Where the **susceptance slope parameter** is defined as,

$$b_n = \frac{\omega_0}{2} \cdot \frac{dB_{in}}{d\omega} \Big|_{\omega_0} = \frac{\omega_0}{2} \cdot \frac{1}{2\pi} \cdot \frac{dB_{in}}{df} \Big|_{f_0} = \frac{f_0}{2} \cdot \frac{dB_{in}}{df} \Big|_{f_0}, \quad (3.45)$$

for any resonator displaying a shunt-type resonance (case of zero susceptance at ω_0); where B_{in} represents the input susceptance of the resonator, in [S]. The derivative of B_{in} represents the *slope* of the curve around the *point of resonance*; as illustrated in Fig. 3.13 [28].

In the following paragraph, the transmission line theory and all the necessary equations are explained, in order to obtain the results as just mentioned above. It explains exactly how the mathematics for the two transmission lines were implemented in **MATLAB** and ends with the relevant plotted figures to illustrate the Q-value calculations.

3.1.2.4 Transmission Line Theory

The following coaxial transmission line equations were used to calculate the input admittance Y_{in} , of the resonator [29, 30].

Firstly, the short-circuit transmission line (Line 2) was evaluated. The starting values as determined by means of Wheeler's 'incremental-inductance rule' (Table 3.1 – p.98) were used; with the following equations summarised in Tables 3.2 and 3.3. In the latter only the *General Line* equations were made use of. Take note that only the relevant equations have been numbered.

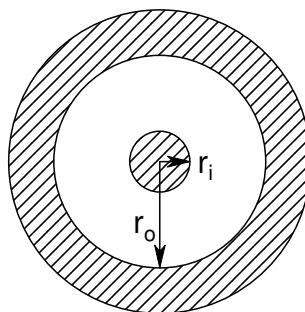


Figure 3.14: Coaxial Transmission Line Configuration.

Table 3.2: Formulas for the Coaxial Transmission Line Configuration.

Line Element	[unit]	Equation	
Capacitance, C	[farads/meter]	$\frac{2\pi\epsilon}{\ln\left(\frac{r_o}{r_i}\right)}$	(3.46)
External inductance, L	[henrys/meter]	$\frac{\mu}{2\pi} \cdot \ln\left(\frac{r_o}{r_i}\right)$	(3.47)
Conductance, G	[siemens/meter]	$\frac{2\pi\sigma}{\ln\left(\frac{r_o}{r_i}\right)} = \frac{2\pi\omega\epsilon''}{\ln\left(\frac{r_o}{r_i}\right)}$	(3.48)
Resistance, R	[ohms/meter]	$\frac{R_s}{2\pi} \cdot \left(\frac{1}{r_o} + \frac{1}{r_i}\right)$	(3.49)
Internal Inductance, L_i (for high frequencies)	[henrys/meter]	$\frac{R}{\omega}$	(3.50)
Characteristic impedance, Z_0 (at high frequency)	[ohms]	$\frac{\eta}{2\pi} \cdot \ln\left(\frac{r_o}{r_i}\right)$	
Z_0 for air dielectric	[ohms]	$60 \cdot \ln\left(\frac{r_o}{r_i}\right)$	(3.51)
Attenuation constant, α (for low-loss lines)		$\frac{1}{2} \cdot \sqrt{LC} \cdot \left(\frac{R}{L} + \frac{G}{C}\right)$	(3.52)
Phase constant, β (for low-loss lines)		$\omega \cdot \sqrt{LC} ; \omega \sqrt{\mu\epsilon'} = \frac{2\pi}{\lambda}$	(3.53)
Propagation constant, γ		$\gamma = \alpha + j\beta$	(3.54)

with,

$$\left. \begin{aligned} \epsilon &= \epsilon' - j\epsilon'' = \text{permittivity, [F/m]} \\ \mu &= \text{permeability, [H/m]} \\ \eta &= \sqrt{\mu/\epsilon} \text{ [\Omega]} \end{aligned} \right\} \text{for the dielectric}$$

$$\epsilon'' = \sigma/\omega = \text{loss factor of dielectric}$$

$$\lambda = \text{wavelength in dielectric}$$

$$R_s = 2.61 \times 10^{-7} \cdot \sqrt{f_0} = \text{skin effect surface resistivity of conductor (copper, in this case), [\Omega].}$$

Table 3.3: General Transmission Line Formulas.

Quantity	General Line	Ideal Line	Low-Loss Lines (Approximation)	Equation
Propagation constant, γ $\gamma = \alpha + j\beta$	$\sqrt{(R + j\omega L)(G + j\omega C)}$	$j\omega\sqrt{LC}$	(See α and β below)	(3.55)
Phase constant, β	$\text{Im}(\gamma)$	$\omega\sqrt{LC} = \frac{\omega}{v} = \frac{2\pi}{\lambda}$	$\omega\sqrt{LC} \cdot \left[1 - \frac{RG}{4\omega^2 LC} + \frac{G^2}{8\omega^2 C^2} + \frac{R^2}{8\omega^2 L^2} \right]$	
Attenuation constant, α	$\text{Re}(\gamma)$	0	$\frac{R}{2Z_0} + \frac{GZ_0}{2}$	
Characteristic impedance, Z_0	$\sqrt{\frac{(R + j\omega L)}{(G + j\omega C)}}$	$\sqrt{\frac{L}{C}}$	$\sqrt{\frac{L}{C}} \cdot \left[1 + j \left(\frac{G}{2\omega C} - \frac{R}{2\omega L} \right) \right]$	(3.56)
Input impedance, Z_i	$Z_0 \left[\frac{Z_L \cdot \cosh(\gamma\ell) + Z_0 \cdot \sinh(\gamma\ell)}{Z_0 \cdot \cosh(\gamma\ell) + Z_L \cdot \sinh(\gamma\ell)} \right]$	$Z_0 \left[\frac{Z_L \cdot \cos(\beta\ell) + jZ_0 \cdot \sin(\beta\ell)}{Z_0 \cdot \cos(\beta\ell) + jZ_L \cdot \sin(\beta\ell)} \right]$		(3.57)
Impedance of shorted line	$Z_0 \cdot \tanh(\gamma\ell)$	$jZ_0 \cdot \tan(\beta\ell)$	$Z_0 \left[\frac{\alpha\ell \cdot \cos(\beta\ell) + j \cdot \sin(\beta\ell)}{\cos(\beta\ell) + j\alpha\ell \cdot \sin(\beta\ell)} \right]$	(3.58)
Impedance of open line	$Z_0 \cdot \coth(\gamma\ell)$	$-jZ_0 \cdot \cot(\beta\ell)$	$Z_0 \left[\frac{\cos(\beta\ell) + j\alpha\ell \cdot \sin(\beta\ell)}{\alpha\ell \cdot \cos(\beta\ell) + j \cdot \sin(\beta\ell)} \right]$	
Impedance of quarter-wave line	$Z_0 \left[\frac{Z_L \cdot \sinh(\alpha\ell) + Z_0 \cdot \cosh(\alpha\ell)}{Z_0 \cdot \sinh(\alpha\ell) + Z_L \cdot \cosh(\alpha\ell)} \right]$	$\frac{Z_0^2}{Z_L}$	$Z_0 \left[\frac{Z_0 + Z_L \cdot \alpha\ell}{Z_L + Z_0 \cdot \alpha\ell} \right]$	

Table 3.3: General Transmission Line Formulas...

Quantity	General Line	Ideal Line	Low-Loss Lines (Approximation)	Equation
Impedance of half-wave line	$Z_0 \left[\frac{Z_L \cdot \cosh(\alpha \ell) + Z_0 \cdot \sinh(\alpha \ell)}{Z_0 \cdot \cosh(\alpha \ell) + Z_L \cdot \sinh(\alpha \ell)} \right]$	Z_L	$Z_0 \left[\frac{Z_L + Z_0 \cdot \alpha \ell}{Z_0 + Z_L \cdot \alpha \ell} \right]$	
Voltage along line $V(z)$	$V_i \cdot \cosh(\gamma z) - I_i \cdot Z_0 \cdot \sinh(\gamma z)$	$V_i \cdot \cos(\beta z) - j I_i \cdot Z_0 \cdot \sin(\beta z)$		
Current along line $I(z)$	$I_i \cdot \cosh(\gamma z) - \frac{V_i}{Z_0} \cdot \sinh(\gamma z)$	$I_i \cdot \cos(\beta z) - j \frac{V_i}{Z_0} \cdot \sin(\beta z)$		
Reflection coefficient, ρ	$\frac{(Z_L - Z_0)}{(Z_L + Z_0)}$	$\frac{(Z_L - Z_0)}{(Z_L + Z_0)}$		
Standing-wave ratio	$\frac{1 + \rho }{1 - \rho }$	$\frac{1 + \rho }{1 - \rho }$		

with,

R, L, G, C = the resistance, inductance, conductance and capacitance, distributed per unit length.

ℓ = the length of the line.

Subscript i = symbolises quantities at the input-end of the transmission line.

Subscript L = symbolises quantities at the load-end of the transmission line.

z = measured distance from the input-end, along the transmission line.

λ = measured wavelength, along the transmission line.

v = the phase velocity of the signal along the transmission line; when considering an ideal line, then the phase velocity is equal to the velocity of light in the dielectric of the line.

Line 2: Short-circuit Transmission Line:

Firstly, the equations portrayed in Table 3.2 were used to determine the transmission line's characteristics. All the values are summarised in the following table, Table 3.4:

Table 3.4: Characteristics of the Shorted Transmission Line (Line 2).

Equation	Element		Value	Unit
Copper Constants				
	Conductivity	σ_{Cu}	5.80×10^7	[S/m]
	Permeability	μ_{Cu}	$(4\pi) \cdot 1 \times 10^{-7} = 1.257 \times 10^{-6}$	[H/m]
	Skin depth, at $f = f_0^*$	δ_{Cu}	$0.066/\sqrt{f} = 2.2 \times 10^{-6}$	[m]
	Surface Resistance	R_s	$(2.61 \times 10^{-7}) \cdot \sqrt{f} = 7.83 \times 10^{-3}$	[Ω]
	Permittivity of free-space	ϵ_0	8.854×10^{-12}	[F/m]
	Permittivity of dielectric (air)	ϵ	$\epsilon_r \cdot \epsilon_0 = (1 \cdot \epsilon_0) = 8.854 \times 10^{-12}$	[F/m]
Starting Values				
	Outer diameter	D_2	30.0×10^{-3}	[m]
	Inner diameter	d_2	9.34×10^{-3}	[m]
Line Characteristics				
(3.46)	Capacitance	C_2	47.6748×10^{-12}	[F/m]
(3.47)	Inductance	L_2	233.3782×10^{-9}	[H/m]
(3.48)	Conductance	G_2	0	[S/m]
(3.49)	Resistance	R_2	350.122×10^{-3}	[Ω /m]
(3.50)	Internal Inductance [high - f]	L_{i2}	61.8464×10^{-12}	[H/m]
(3.51)	Characteristic Impedance	Z_{02}	70.013	[Ω]

* Take note that in the calculations above, the resonant frequency is taken as, $f_0 = 900$ MHz . This was the initial design frequency; and is later optimised in **CST** to a 1 GHz resonator.

Thus, by making use of all the characteristic values as determined in Table 3.4; it is easy to calculate the propagation constant and the input impedance/admittance of the shorted line. The values of the latter are all summarised in the following table, Table 3.5:

Table 3.5: γ_2 , Z_{in2} and Y_{in2} of the Shorted Transmission Line (Line 2).

Equation	Element		Value	Unit
Line Characteristics				
(3.52)	Attenuation constant	α_2	0.0025021	-
(3.53)	Phase constant	β_2	18.8834	-
(3.54)	Propagation constant	γ_2	$(0.0025021) + j(18.8834)$	-
	Line length	ℓ_2	20×10^{-3}	[m]
Impedance Values				
	Load Impedance	Z_{L2}	0	[Ω]
(3.56)	Complex Characteristic Imp.	Z_{02k}	$(69.9658) - j(9.27064 \times 10^{-3})$	[Ω]
(3.57)*	Input Impedance	Z_{in2}	$(7.72999 \times 10^{-3}) + j(27.7562)$	[Ω]
Matching Admittance				
	Input Admittance	Y_{in2}	$(10.0337 \times 10^{-6}) - j(36.0281 \times 10^{-3})$	[S]

* Take note that it is also possible to make use of equation (3.58) for this particular calculation of the input impedance, since this line is shorted at its load.

As one would recall, this resonator is designed by making use of two different transmission lines. Take note that Tables 3.4 and 3.5 are highlighted in green; while the following, Tables 3.6 and 3.7 are highlighted in blue. This is done to give a visual idea of which transmission line's characteristics are currently being calculated. This can be viewed by reflecting on Fig. 3.11 on page 97.

Line 1: Open-circuit Transmission Line:

Secondly, the open-circuit transmission line (Line 1) was evaluated in exactly the same way as line 2. To begin with, the equations portrayed in Table 3.2 were used to determine the transmission line's characteristics. The *Copper Constants* shown in Table 3.4 were also used for the calculations below. All the values are summarised in the following table, Table 3.6:

Table 3.6: Characteristics of the Open Transmission Line (Line 1).

Equation	Element		Value	Unit
	Starting Values			
	Outer diameter	D_1	8.34×10^{-3}	[m]
	Inner diameter	d_1	6.94×10^{-3}	[m]
	Line Characteristics			
(3.46)	Capacitance	C_1	302.7367×10^{-12}	[F/m]
(3.47)	Inductance	L_1	36.7523×10^{-9}	[H/m]
(3.48)	Conductance	G_1	0	[S/m]
(3.49)	Resistance	R_1	658.341×10^{-3}	[Ω /m]
(3.50)	Internal Inductance [high - f]	L_{i1}	116.291×10^{-12}	[H/m]
(3.51)	Characteristic Impedance	Z_{01}	11.0257	[Ω]

Thus, by making use of all the characteristic values as determined in Table 3.6; it is easy to finally calculate the propagation constant and the input impedance/admittance of the open-circuit line. The values of the latter are all summarised in the following table, Table 3.7.

Take note that the input impedance of line 2 as calculated in Table 3.5, serves as the load impedance to line 1, with which the final input admittance Y_{in} , to the resonator is calculated.

Table 3.7: γ_1 , Z_{in1} and Y_{in1} of the Open Transmission Line (Line 1).

Equation	Element		Value	Unit
Line Characteristics				
(3.52)	Attenuation constant	α_1	0.029875	-
(3.53)	Phase constant	β_1	18.8834	-
(3.54)	Propagation constant	γ_1	$(0.029875) + j(18.8834)$	-
	Line length	ℓ_1	20×10^{-3}	[m]
Impedance Values				
	Load Impedance	Z_{L1}	$(7.7299 \times 10^{-3}) + j(27.7562)$	[Ω]
(3.56)	Complex Characteristic Imp.	Z_{01k}	$(11.0182) + j(17.4318 \times 10^{-3})$	[Ω]
(3.57)	Input Impedance	Z_{in1}	$(23.4949) + j(34.1242)$	[k Ω]
Matching Admittance				
	Input Admittance	Y_{in1}	$(13.6879) - j(19.8804)$	[μ S]

Table 3.8: b_n and Q_u calculated for the Resonator.

Equation	Element		Value	Unit
Final Resonator Calculations				
	Input Impedance	Z_{in}	$(23.4949) + j(34.1242)$	[k Ω]
	Input Admittance	Y_{in}	$(13.6879) - j(19.8804)$	[μ S]
(3.43)	Input Conductance	G_{in}	13.6879	[μ S]
(3.43)	Input Susceptance	B_{in}	-19.8804	[μ S]
	Difference in B_{in} , around f_0	ΔB_{in}	1.5235×10^{-3}	[S]
	Difference in f , around f_0	Δf	20.00	[MHz]
	Gradient	m	76.1764×10^{-12}	
(3.45)	Susceptance Slope Parameter	b_n	34.279×10^{-3}	[S]
(3.44)	Unloaded Q-value	Q_u	2504.3515	

All of the necessary calculations for the resonator have been shown in the previous tables. The latter values are confirmed by means of the relevant plotted curves, illustrated in an upcoming section reporting on the *Simulation Results*.

3.1.2.5 Coupling Techniques Considered

As mentioned in Chapter 1, different coupling techniques to the resonator were considered during its design. Since a specific amount of coupling was sought after, the coupling mechanism had to be practically feasible, in other words, easily tuneable.

One of the many functions one could perform in **CST**, would be to simulate the electromagnetic fields present in the resonator's cavity. When performing the latter, it is desired to locate the area where either of the fields' strength is at its maximum and then try and couple at exactly that position. Coupling to either the magnetic-field or the electric-field involves different techniques [30].

Coupling to the magnetic field requires a loop, e.g. extending from a coaxial line through which the magnetic flux lines can thread, in order to induce a current in the loop. But if coupling to the electric field provides a better solution, one only needs the inner conductor of a coaxial line (for example) to extend straight into the field, to make coupling possible.

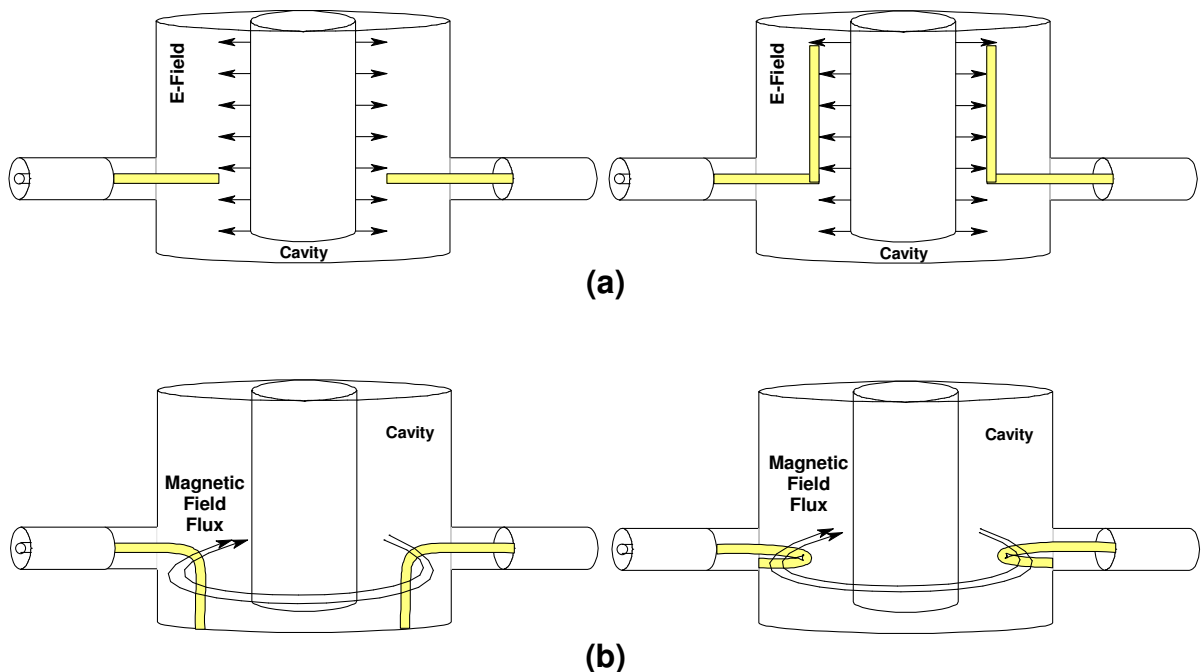


Figure 3.15: Different Coupling Techniques. (a) Coupling to the Electric Field. (b) Coupling to the Magnetic Field.

In this resonator design, the problem experienced with the coupling illustrated in Fig. 3.15 (a) was, that the conductor had to extend to nearly touching the inner cylinder of the resonator, before the desired amount of coupling was reached. This happened since the electric field was practically too small to couple to at that point. Secondly, to make it tuneable, pieces had to be cut from the conductor, until the desired amount of coupling was reached. The latter would mean that once the conductor was cut too short, a new one would have to be inserted and the process would repeat itself.

In the second illustration of Fig. 3.15 (a), the conductor was extended to close to the top of the resonator, since the electric field strength appeared to be stronger there. With the latter, the tuneability turned out as not practical.

Suppose coupling to the magnetic field was considered, as illustrated in Fig. 3.15 (b). The problem with the first picture was that once the conductor was soldered to the floor (ground) of the resonator, the coupling was no longer tuneable. The task of then trying to tune the coupling would involve designing a new loop, soldering it in position and then measure again. This process seems entirely unpractical.

Finally, the coupling loop was made in a manner where the loop closed back onto the ground of the connector itself. Therefore, the coupling loop was not soldered directly to the resonator at all. This made tuning the amount of coupling practical, since the connector could be turned in any direction, making the amount of coupling more or less; just as desired. See Fig. 3.16 for an illustration.

In the paragraph reporting on the Simulation Results for **CST**, a detailed, technical illustration will be given of exactly how the connector and the coupling loop appears.



Figure 3.16: Image of the utilised coupling loop.

3.1.2.6 Microwave Tuning Element

As mentioned earlier, the initial design of the resonator was at a frequency of 900 MHz. It was also mentioned that, since varactor diodes were going to be added to the design, which would lower the operating frequency of the resonator, it was decided to optimise the first design to a 1 GHz resonant frequency. Thus, after adding the varactor diodes (which lowered the frequency) the circuit had to be tuned to precisely 900 MHz. This was done with a **microwave tuning element**, which adds reactance to the resonator and as a result lower the operating frequency. Once the latter was realised, tuning of the varactor diodes started in order to form a VCO operating from 900 MHz.

The information provided below gives the details on the tuning element used in this project. Some general applications, features and technical data are provided [31].

MICROWAVE TUNING ELEMENTS

General matters

GENERAL MATTERS

Description

Microwave tuning elements are an economical means of introducing variable reactance to waveguides, cavities and other microwave structures. They are excellent for applications requiring precision, low loss high resolution tuning. The self-locking, constant torque drive mechanism eliminates the need for locking nuts and assures stable, noise free adjustment in application from DC to W band.

A microwave tuning element consists of a mounting bushing with an integral tuning rotor.

Features

- High tuning resolution
- Excellent tuning stability and very low dynamic noise
- Frequency range from 0 to 100 GHz and more
- Easy to use, one hand tuning
- Gold and chromate finish (other plating upon request)
- Metallic, dielectric and resistive types available
- All tuning rotors available separately
- High reliability versions available upon request

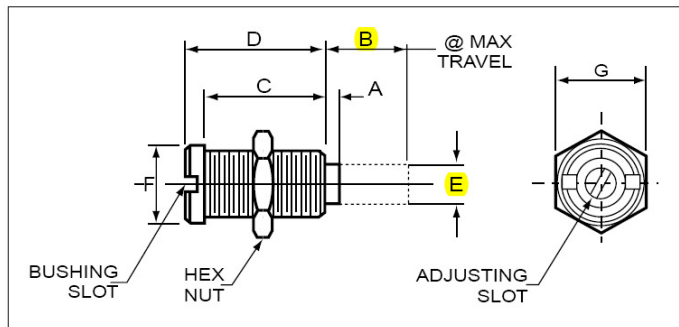


Applications

- Combine filters - Interdigital filters
- Impedance transformers - Attenuators
- Impatt and Gunn oscillators
- Microstrip and strip-line circuits
- Coaxial structures - Waveguide circuitry

A - BUSHING WITH METALLIC ROTOR

Tuning elements with metallic posts are simple and straight-forward in design. Each tuning unit consists of two parts, a threaded mounting bushing and a self-locking rotor screw that won't vibrate loose. Noise free, low resistance contacting is maintained between both parts by the "spring loaded" webbing which forces the threads together. High Q tuning is possible from the smooth, short, non threaded slug with less exposed surface area than with standard screws.



Technical data

Dimensions (mm)

Temex Part N°	Nominal frequency band	Bushing thread	Tap reference	Typ. tap drill	Mounting torque g. cm	A	B	C	D	E	F	G
AT6924-0 SL	X and K	.120 - 80	7060	2.75	700	0	3.8	5.1	6.0	1.8	3.4	4.0
AT6924-1 SL	X and K	.120 - 80	7060	2.75	700	1.2	1.9	2.2	3.1	1.8	3.4	4.0
AT6924-2 SL	X and K	.120 - 80	7060	2.75	700	0	1.9	5.1	6.0	1.8	3.4	4.0
AT6924-3 SL	X and K	.120 - 80	7060	2.75	700	0	0.8	2.2	3.1	1.8	3.4	4.0
AT6925-0 SL	C and X	10 - 64	7061	4.45	2100	0	3.8	5.4	6.4	3.2	5.3	5.6
AT6925-1 SL	C and X	10 - 64	7061	4.45	2100	0	0.6	2.2	3.2	3.2	5.3	5.6
AT6925-2 SL	C and X	10 - 64	7061	4.45	2100	0	3.2	5.4	6.4	1.6	5.3	5.6
AT6925-3 SL	C and X	10 - 64	7061	4.45	2100	3.3	7.1	5.4	6.4	3.2	5.3	5.6
AT6925-7 SL	C and X	10 - 64	7061	4.45	2100	1.1	4.9	5.4	6.4	3.2	5.3	5.6
AT6925-8 SL	C and X	10 - 64	7061	4.45	2100	0.2	2.0	3.2	4.2	3.2	5.3	5.6
AT6925-9 SL	C and X	10 - 64	7061	4.45	2100	0	2.3	6.6	7.6	3.2	5.3	5.6
AT6926-0 SL	C and X	15/64 - 64	7062	5.5	3500	0	2.7	4.6	5.4	4.1	6.8	7.0
AT6926-1 SL	C and X	15/64 - 64	7062	5.5	3500	0	0.7	2.4	3.2	4.1	6.8	7.0
AT6926-4 SL	C and X	15/64 - 64	7062	5.5	3500	2.3	8.8	5.5	9.1	4.1	6.8	7.0
AT6926-5 SL	C and X	15/64 - 64	7062	5.5	3500	0.6	2.7	4.0	4.8	4.1	6.8	7.0
AT6926-6 SL	C and X	15/64 - 64	7062	5.5	3500	2.6	11.5	5.4	11.5	4.1	6.8	7.0
AT6926-7 SL	C and X	15/64 - 64	7062	5.5	3500	1.9	4.6	4.6	5.4	4.1	6.8	7.0
AT6926-9 SL	C and X	15/64 - 64	7062	5.5	3500	0	2.7	5.5	9.1	4.1	6.8	7.0
AT6926-10 SL	C and X	15/64 - 64	7062	5.5	3500	0	4.6	5.5	9.1	4.1	6.8	7.0
AT6927-0 SL	C and X	15/64 - 64	7062	5.55	3500	0	6.5	5.5	9.7	4.1	6.8	7.0
AT6928-0 SL	C	15/64 - 64	7062	5.55	3500	0	8.8	5.4	11.5	4.1	6.8	7.0
AT6928-2 SL	C	15/64 - 64	7062	5.55	3500	6.1	8.8	4.6	5.4	4.1	6.8	7.0
AT6929-0 SL	C	10 - 64	7061	4.45	2100	0	11.4	13.0	14.0	3.2	5.3	5.6
AT6948-0 SL	C and X	.312 - 64	7065	7.55	8400	0	5.9	8.2	9.2	5.3	9.5	10
AT6965-0 SL	L and S	.469 - 32		11.10	16800	0	12.7	17.3	18.3	8.8	13.5	14.2

The tuning element used in this project is highlighted in the table above. Its mechanism was simulated in **CST**, where about a 50 MHz tuneability in frequency was recognised.

3.1.3 Simulation Results

3.1.3.1 MATLAB

The results shown in this section summarise the discussions of the previous paragraphs (3.1.2.2) to (3.1.2.4).

Firstly, figures 3.17 and 3.18 on the next page illustrate the values summarised in Table 3.1 on page 98. The latter provides the starting values for the resonator's dimensions; as determined by *Wheeler's Incremental-Inductance Rule*. Subsequently, the values summarised in Table 3.1 were used in the simulation program **CST** (Computer Simulation Technology) to simulate the fields in the resonator as well as its unloaded Q-value.

Secondly, the resonator was analysed in **MATLAB** from the first principles for transmission line theory. The plotted figures appear on pages 115 and 116.

In Fig. 3.19 the resonant frequency is confirmed by plotting the input impedance of the resonator. Fig. 3.20 illustrates the input conductance, G_{in} of the resonator. G_{in} is directly dependant on the attenuation constants described for each line. When making use of the *Susceptance Slope Parameter* to calculate the unloaded Q-value of the resonator, G_{in} serves as the denominator in the equation. Thus, the higher the attenuation in the transmission lines, the higher G_{in} will be and consequently it will result in a lower overall Q_u value.

In Fig. 3.21, the gradient of the input susceptance curve versus the frequency is illustrated, from which the susceptance slope parameter, b_n was calculated.

Finally, the unloaded Q-value of the resonator is portrayed in Fig. 3.22. The latter is calculated using the parameter, b_n and the input conductance, G_{in} .

Results obtained for the Incremental-Inductance Rule:

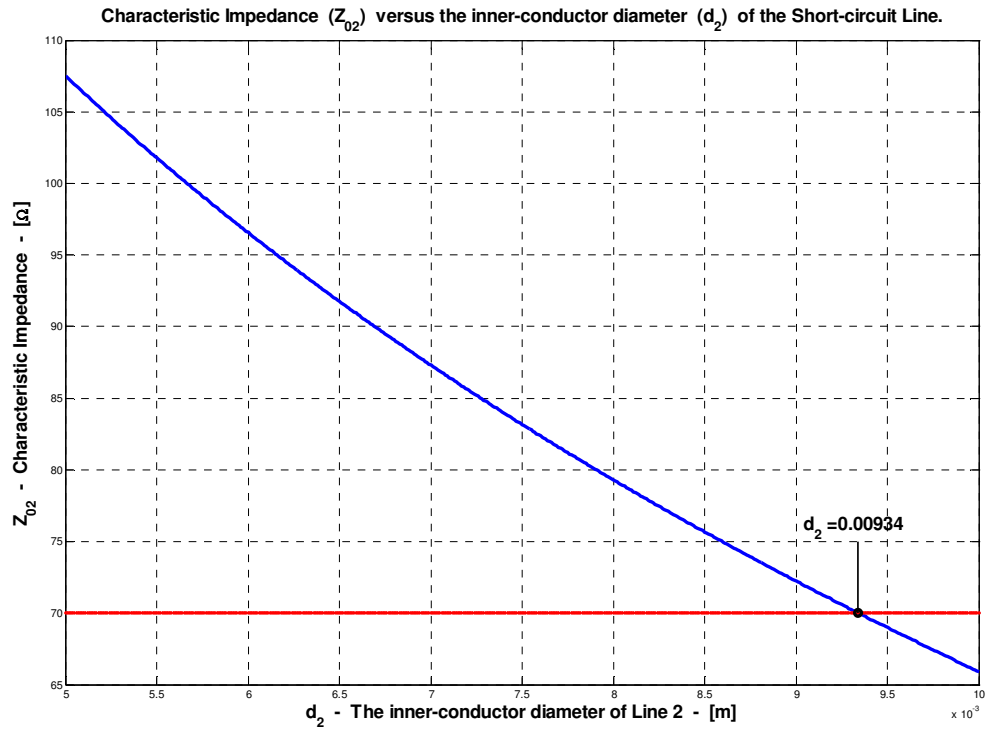


Figure 3.17: Illustration of Z_{02} versus d_2 .

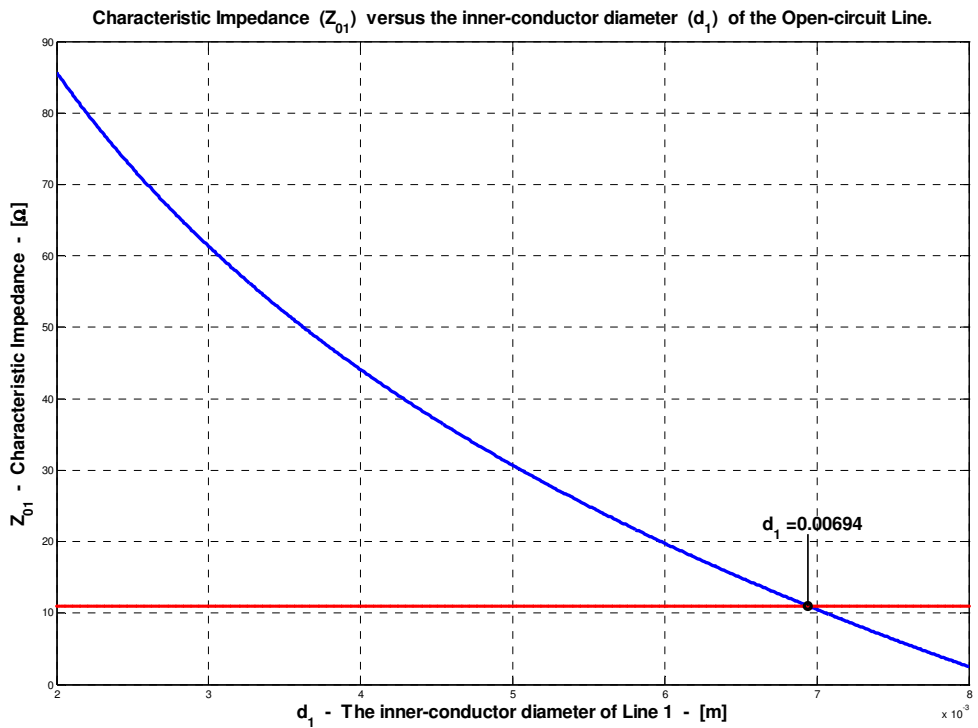


Figure 3.18: Illustration of Z_{01} versus d_1 .

Results for the Transmission Line Theory & the Susceptance Slope Parameter:

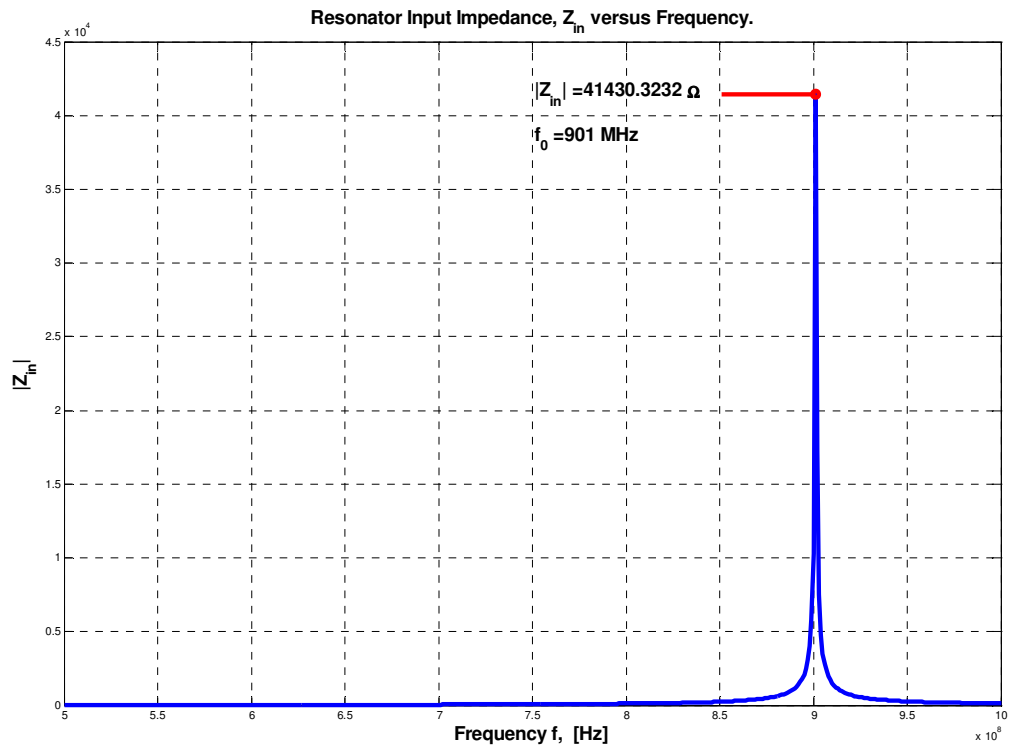


Figure 3.19: Magnitude of the Resonator's Input Impedance.

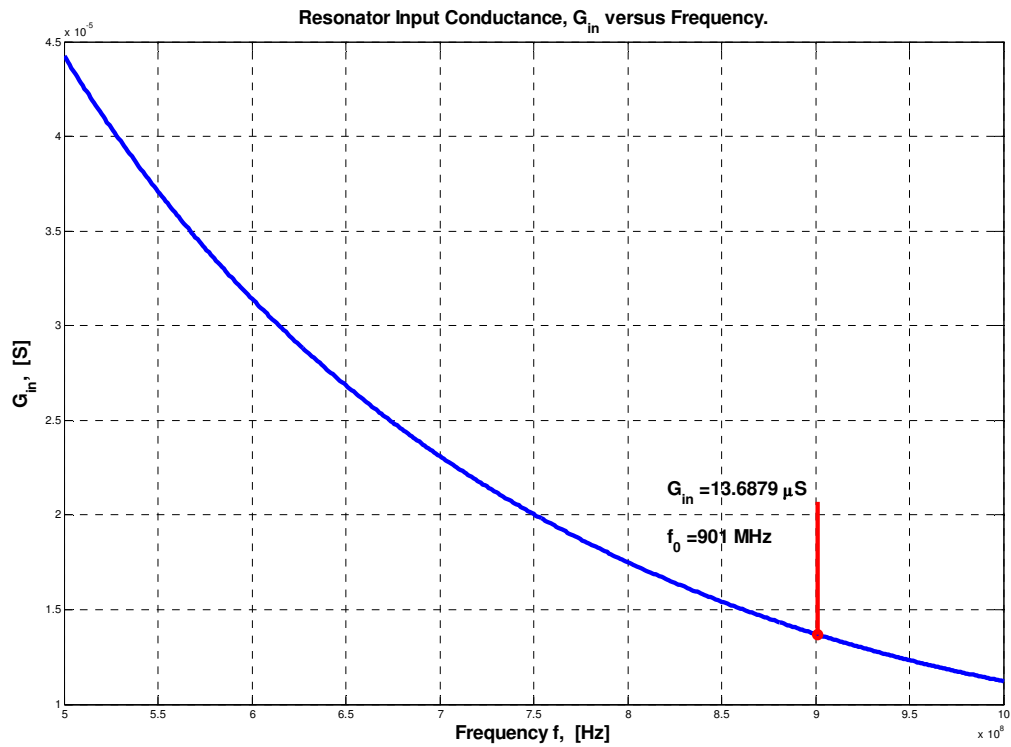


Figure 3.20: Resonator's Input Conductance, G_{in} .

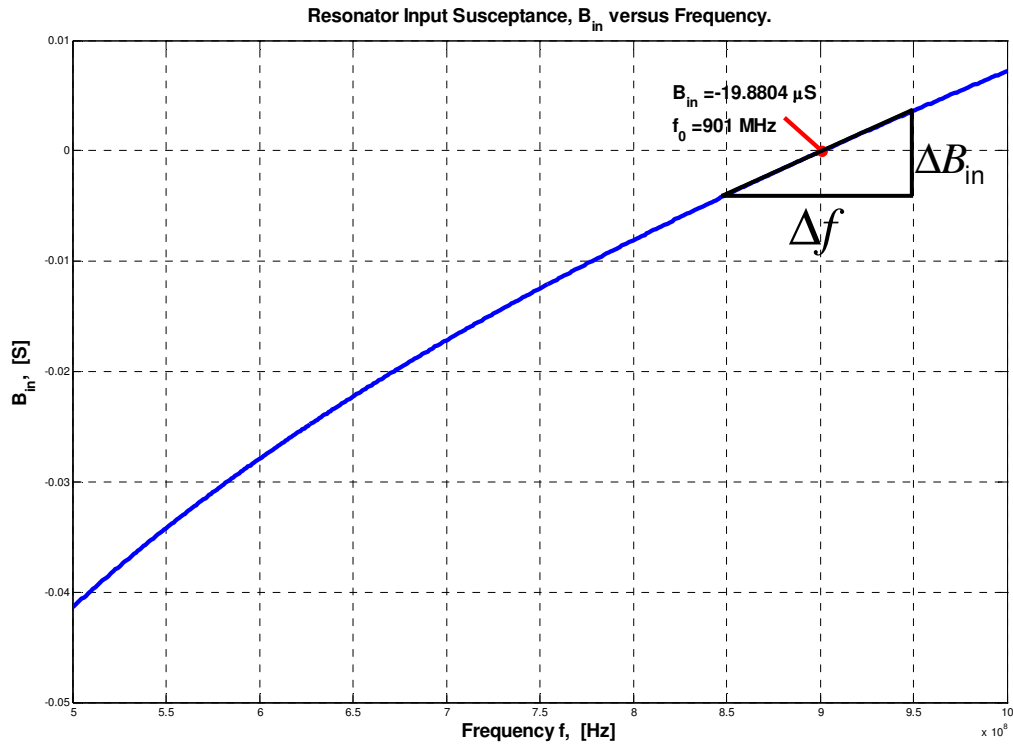


Figure 3.21: Calculating the Slope of the Input Susceptance Curve, B_{in} .

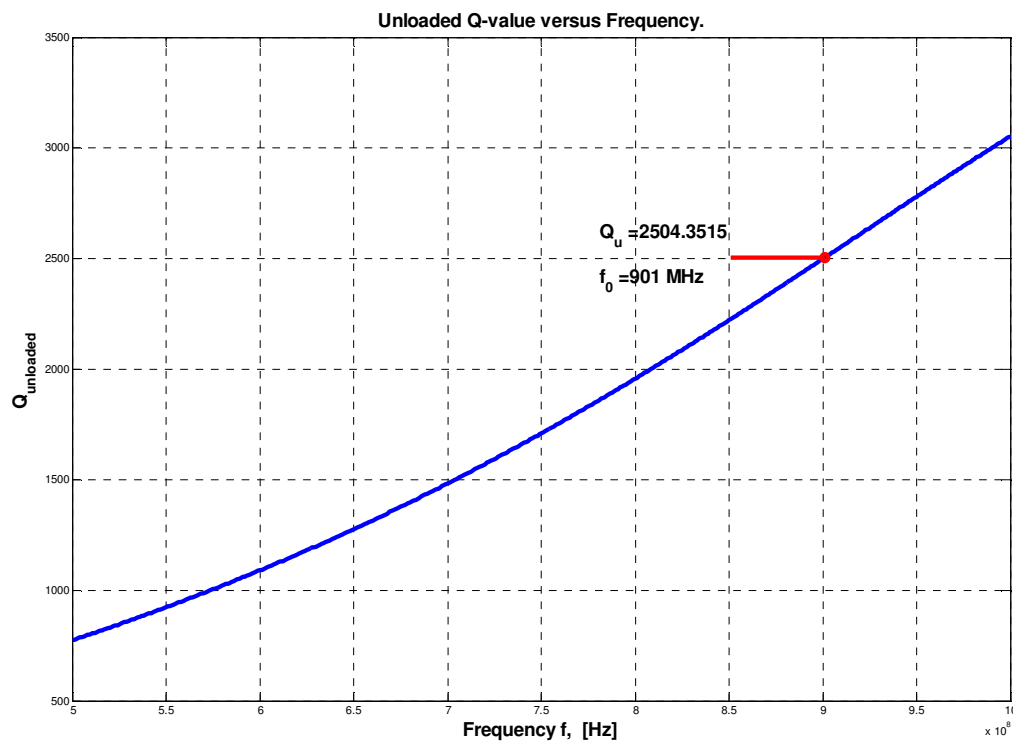


Figure 3.22: Unloaded Q-value, Q_u of the designed Resonator.

The **MATLAB** code used to conduct all of the above mentioned figures and calculations is attached in Appendix B.

3.1.3.2 MICROWAVE OFFICE

These simulations were done as an alternative to **MATLAB**; in order to confirm the calculated Q-value of the resonator. In Fig. 3.23, the simulated resonator circuits are shown. The values determined in **MATLAB** were used in this simulation, with a view to obtaining the same results.

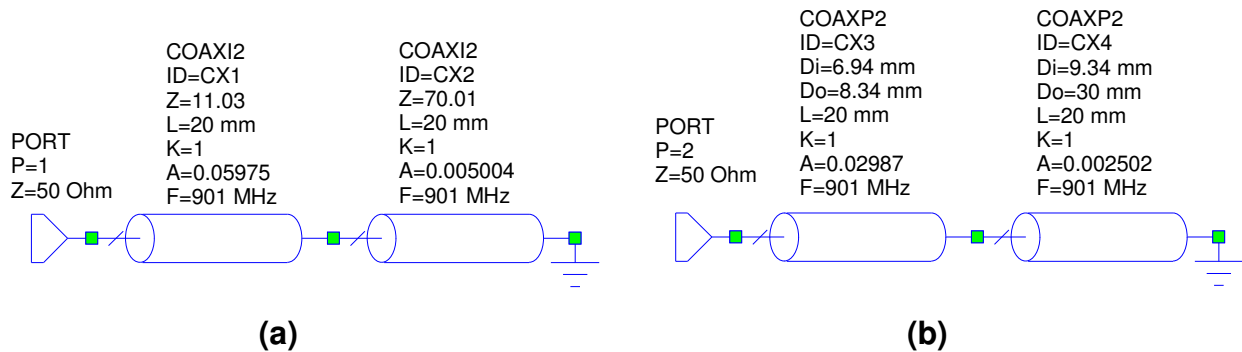


Figure 3.23: Resonator Circuits as simulated in MWO, illustrating different parameters specified. (a) Line Impedance. (b) Coaxial Diameters.

The elements making up the circuits as shown above were the two transmission lines; represented by coaxial cables, with the different parameters specified. Parameter '**K**' refers to the dielectric constant, which was taken as unity for air; while parameter '**A**' represents the attenuation of the line. The rest are self explanatory. Take note that a simulation was done for each of the circuits shown in Fig. 3.23, specifying different parameters.

Pay attention to the attenuation constants (α_1 and α_2) in Fig. 3.23 (b). The latter have exactly the same values as those calculated in **MATLAB**. While in Fig. 3.23 (a), the attenuation constants are exactly *double* the value of those calculated in **MATLAB**. Consequently, the resulting difference in the unloaded Q-values for the two circuits above was exactly a factor of 2.

Therefore, the only way the same result for Q_u could be obtained in **MWO**, as to that calculated in **MATLAB**, was to *double* the attenuation constants for both lines. The latter is illustrated by Fig. 3.23 (a). Once the attenuation constants in Fig. 3.23 (b) were doubled the same value for Q_u was obtained as in Fig. 3.23 (a).

The susceptance slope parameter stayed the same for every simulation. It was only the input conductance that varied. It was thought that maybe, instead of entering the diameter values as illustrated in Fig. 3.23 (b), it was meant to rather enter the radius values for the respective lines. However this step did not seem to make any difference to the unloaded Q-value. It was still measured as $Q_u = 5066.62$. Thus, the only difference was obtained when the attenuation constants were doubled, which in fact doubled the value of G_{in} as well. Other than this, no apparent reason could be found for this result generated by *MWO*.

Below are the results obtained for the simulation of Fig. 3.23 (a). In Fig. 3.24, the curves for G_{in} and B_{in} are illustrated and in Fig. 3.25 the calculated value for the unloaded Q value is shown as, $Q_u = 2533.75$.

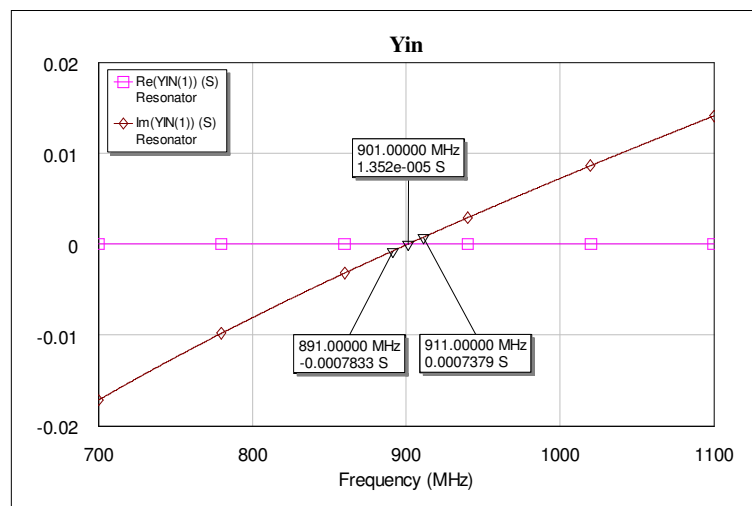


Figure 3.24: Input Admittance, illustrating G_{in} and the calculation of b_n .

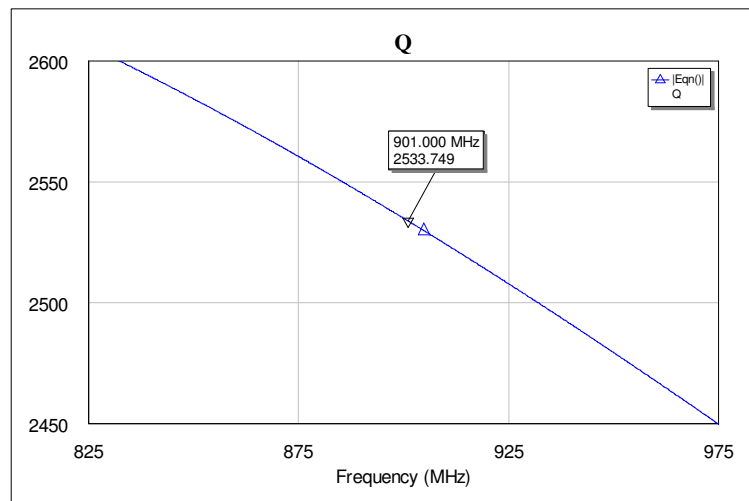


Figure 3.25: Unloaded Q-value as calculated in MWO.

3.1.3.3 CST

The resonator was designed with the help of the software program **CST** (*Computer Simulation Technology*). As mentioned earlier, the resonator was first designed at a resonant frequency of 900 MHz, which was later optimised to a frequency of 1 GHz. This was done to take the effect that the addition of the varactor diodes to the cavity will have on the frequency, into account.

The electromagnetic fields inside the cavity of the resonator are illustrated below.

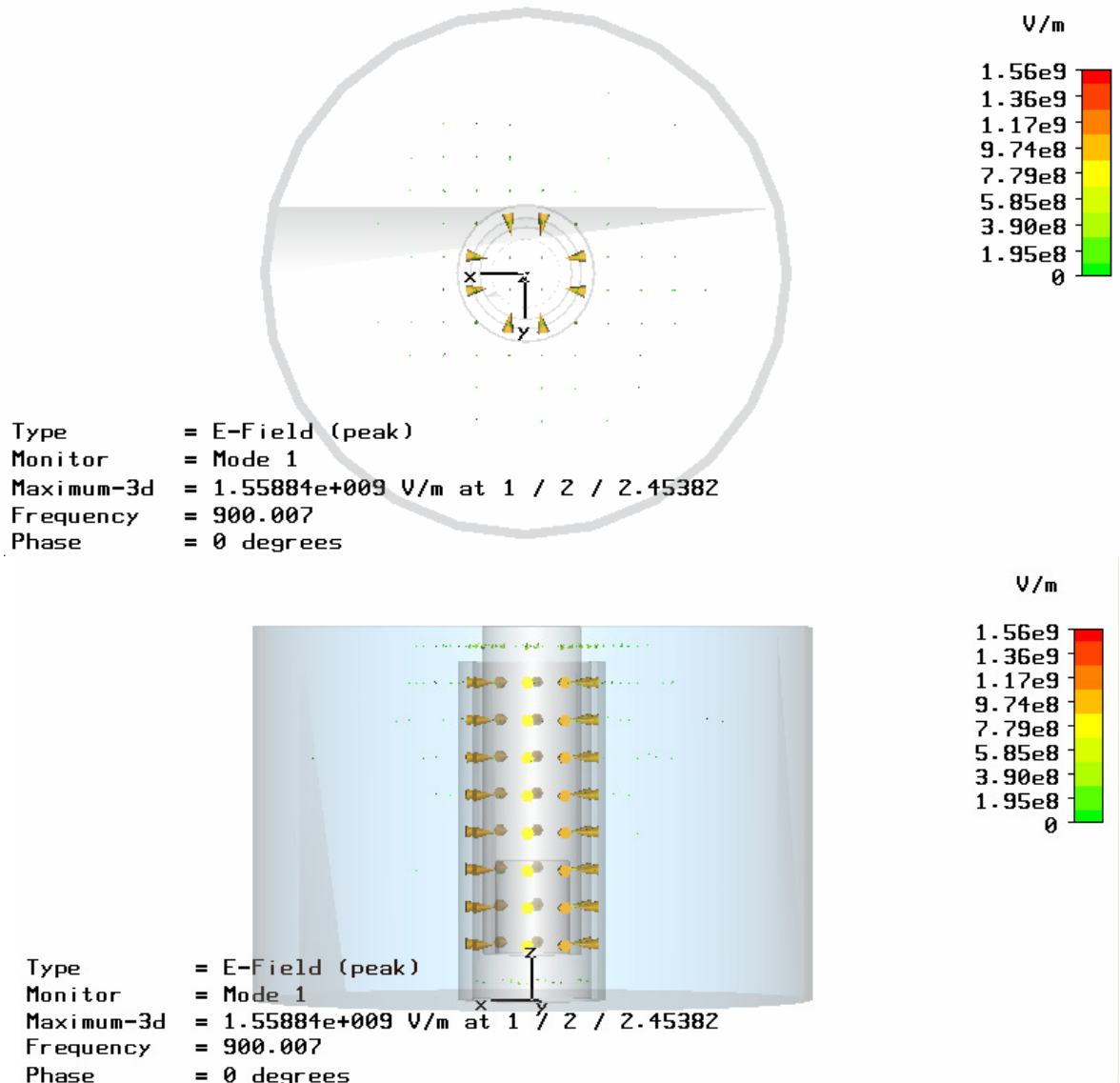


Figure 3.26: Top- and Side View of the Electric Field inside the cavity of the Resonator.

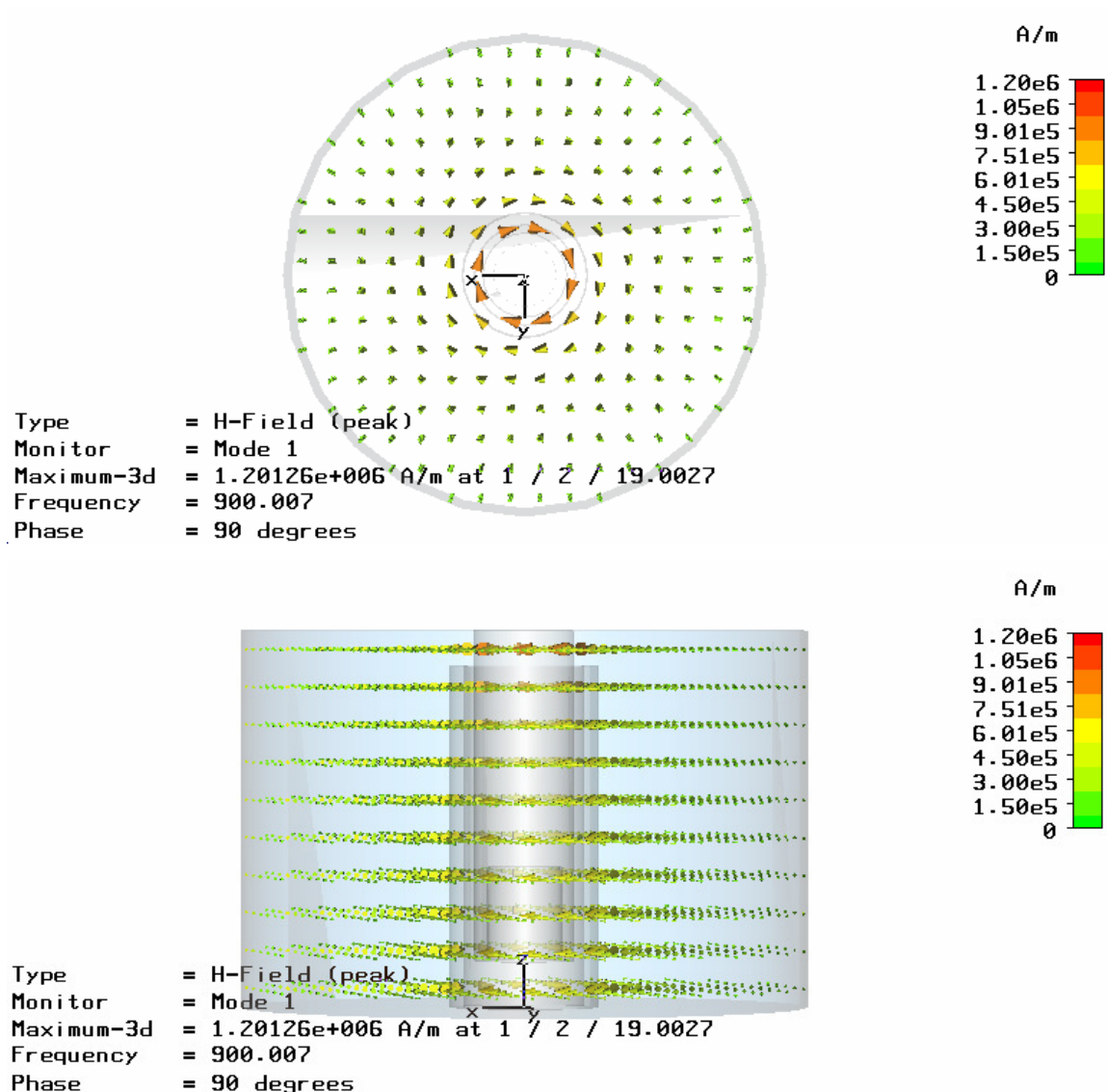


Figure 3.27: Top- and Side View of the Magnetic Field inside the cavity of the Resonator.

As it is clearly visible from figures 3.26 and 3.27, the magnetic field provides more opportunity to couple to than the electric field, mostly because it is easily accessible.

Because of the additional charge present at the open-circuit end of line 1 due to the fringing electric field at that point, a gap was introduced in the inner conductor to minimise this extra charge. The latter is modelled by a capacitance, C_0 . The gap (hole) is visible in the figures above, as well as in Fig. 3.1 on p. 80. The main reason for minimising C_0 is to increase the unloaded Q-value.

The following two pages show the designs for the 900 MHz, as well as the 1 GHz resonator, with the initial coupling loops presented.

Resonator at $f_0 \approx 910$ MHz:

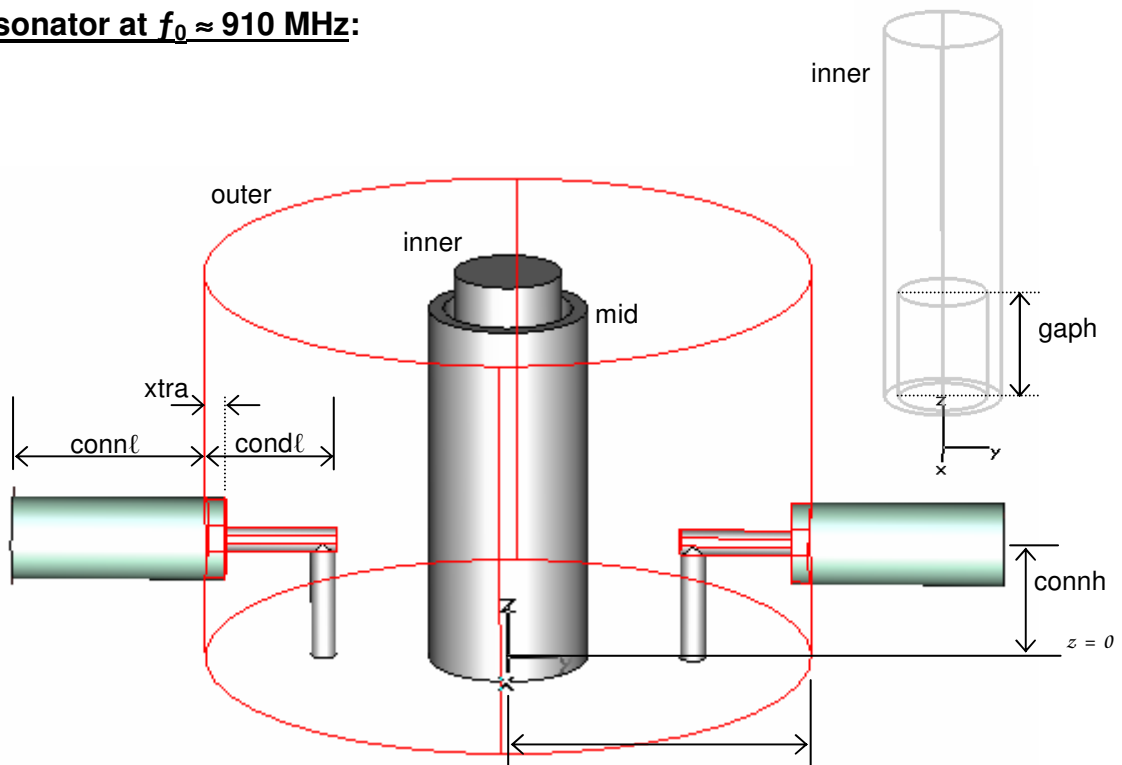


Figure 3.28: CST representation of the cavity resonator at 900 MHz.

Table 3.9: Resonator Dimensions at $f_0 = 900$ MHz.

Variable Name	Value	Description	Unit
Connectors			
concl	6.5	Length of conductor inside cavity	[mm]
condra	0.95/2	Inner radius of the inner SMA conductor	[mm]
condrb	1.28/2	Outer radius of the inner SMA conductor	[mm]
connh	6	SMA centre conductor height	[mm]
connl	9.5	Length of connector	[mm]
teflonr	4.1/2	Outer radius of the Teflon	[mm]
xtra	1	Increase only the Teflon length	[mm]
Gap (hole)			
gaph	7.45382225883	Gap height	[mm]
gapr	2	Gap radius	[mm]
Resonator			
innerh	17.546177741168	Inner conductor height	[mm]
innerr	2.6449215189991	Inner conductor radius	[mm]
midh	18.11	Middle conductor height	[mm]
midra	3.1939526201104	Inner radius of middle conductor	[mm]
midrb	3.9433652331284	Outer radius of middle conductor	[mm]
outerr	15	Outer conductor radius	[mm]
resh	20	Resonator height	[mm]
width	3	Outer conductor width	[mm]

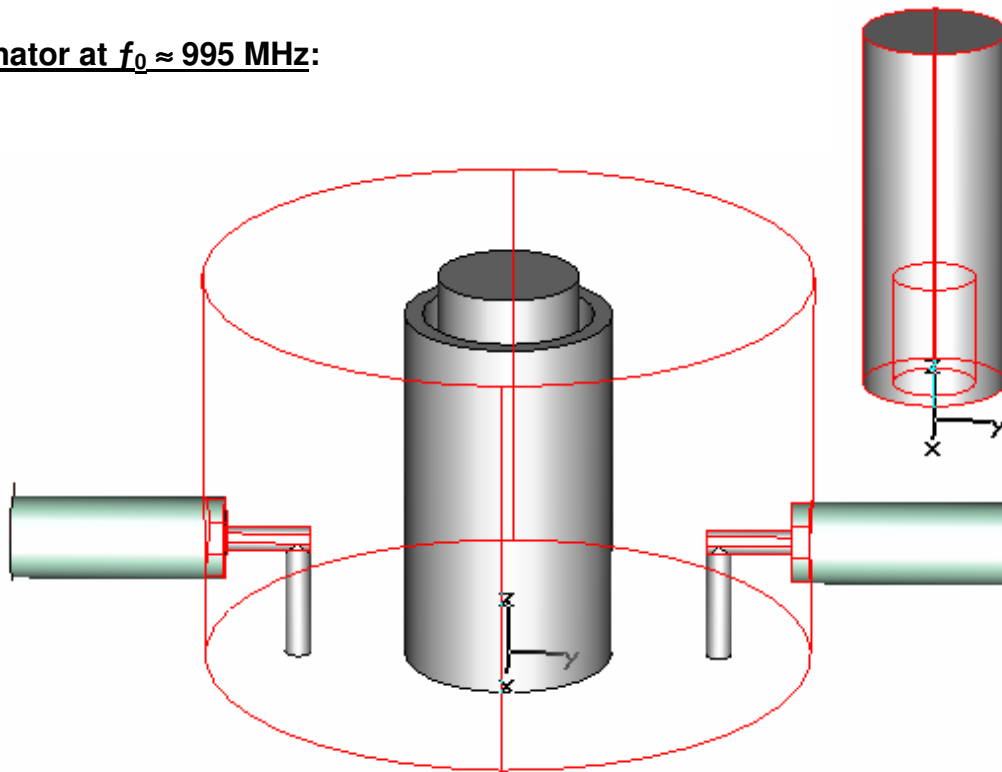
Resonator at $f_0 \approx 995$ MHz:

Figure 3.29: CST representation of the cavity resonator at 1 GHz.

Table 3.10: Resonator Dimensions at $f_0 = 1$ GHz.

Variable Name	Value	Description	Unit
Connectors			
condℓ	5.218	Length of conductor inside cavity	[mm]
condra	0.95/2	Inner radius of the inner SMA conductor	[mm]
condrb	1.28/2	Outer radius of the inner SMA conductor	[mm]
connh	6	SMA centre conductor height	[mm]
connℓ	9.5	Length of connector	[mm]
teflonr	4.1/2	Outer radius of the Teflon	[mm]
xtra	1	Increase only the Teflon length	[mm]
Gap (hole)			
gaph	7.45382225883	Gap height	[mm]
gapr	2	Gap radius	[mm]
Resonator			
innerh	18	Inner conductor height	[mm]
innerr	3.4788837850118	Inner conductor radius	[mm]
midh	18	Middle conductor height	[mm]
midra	4.2282809419031	Inner radius of middle conductor	[mm]
midrb	5.1275	Outer radius of middle conductor	[mm]
outerr	15	Outer conductor radius	[mm]
resh	20	Resonator height	[mm]
width	3	Outer conductor width	[mm]
Tuning Element – Rotor Screw			
screwℓ	7.1	Screw length	[mm]
screwr	3.2/2	Screw radius	[mm]
shift	0	Amount of distance screwed in	[mm]

In the following table, the simulation done with the resonator 'starting values' as determined by Wheeler, is compared to the optimised values for the 900 MHz and 1 GHz simulations respectively. The corresponding simulated Q-values are also listed.

Table 3.11: Comparing the different CST Simulations.

Name	Value			Description	Unit
	Wheeler's Incremental Inductance Rule	Optimised to...			
		900 MHz	1 GHz		
Connectors					
condl	6.5	6.5	5.218	Length of SMA conductor inside the cavity	[mm]
condra	0.95/2	0.95/2	0.95/2	Inner radius of the inner SMA conductor	[mm]
condrb	1.28/2	1.28/2	1.28/2	Outer radius of the inner SMA conductor	[mm]
connh	6	6	6	SMA centre conductor height	[mm]
connl	9.5	9.5	9.5	Length of the connector	[mm]
teflonr	4.1/2	4.1/2	4.1/2	Outer radius of the Teflon	[mm]
xtra	1	1	1	Increase only the Teflon length	[mm]
Resonator					
gaph	7.45	7.4538	7.4538	Gap height	[mm]
gapr	2	2	2	Gap radius	[mm]
innerh	18	17.5462	18	Inner conductor height	[mm]
innerr	3.47	2.6449	3.4789	Inner conductor radius	[mm]
midh	18	18.11	18	Middle conductor height	[mm]
midra	4.17	3.1940	4.2283	Inner radius of middle conductor	[mm]
midrb	4.67	3.9434	5.1275	Outer radius of middle conductor	[mm]
outerr	15	15	15	Outer conductor radius	[mm]
resh	20	20	20	Resonator height	[mm]
width	3	3	3	Outer conductor width	[mm]
f	948.46	909.70	995.12	Resonant frequency	[MHz]
Q_u	2604	2097	2460.9	Unloaded Q-value	

In Table 3.11 the different simulation results are compared. It is important to notice that in the optimisation of the resonator to the respective frequencies, the most significant changes took place in the dimensions of the transmission line conductors. Take note that these were the initial values obtained for the resonator and that in the following paragraph the coupling loops were changed to those described in section 3.1.2.5 on page 109 (see Fig. 3.30 below). The Q-values shown in Table 3.11 are the internal Q-value of the resonator, calculated in **CST** by means of the '*Q-Factor Calculation*'-function.

In the following discussion the internal Q-value will be calculated by the '*Q-Factor Calculation*'-function as well, while the external Q-value will be calculated by means of the S_{21} measurement. Both will be demonstrated. The final resonator design is presented in the following figure.

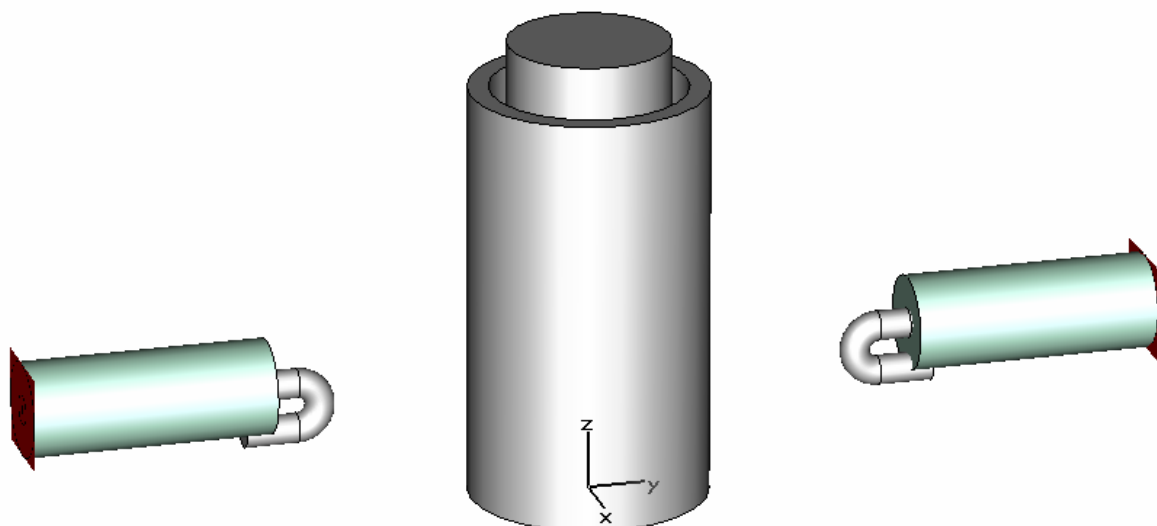


Figure 3.30: The Final Resonator Design and its Coupling Loops.

As mentioned, the internal Q-value is determined by **CST** itself. CST offers different ways in which the Q-factor can be calculated, depending on which solver is currently being used. For the **Eigenmode Solver**, the '*Results – Loss & Q Calculation*' option is used. But for the **General Purpose Frequency Domain Solver**, electric (E) and magnetic (H) field monitors are necessary. Then the same function, '*Results – Loss & Q Calculation*' is used, but instead of choosing 'Mode 1' as the H-field data to calculate, choose '2D/3D Results\H-Field\h-field (f=979.4) [1]', the H-field monitor's data.

Internal Q-factor Calculation:

Direct results from CST:

Q Factor ASCII Export

H-Field "2D/3D Results\H-Field\h-field (f=979.65) [1]"

Frequency/Hz 9.79650000e+008

Energy/J 1.33174363e-007

Layer	Solid	Conductivity	Mue	Loss/W(peak)	Q

Cond. Enclosure		5.8000e+007	1.0000e+000	2.8692e-001	5.7141e+003
PEC		5.8000e+007	1.0000e+000	4.8143e-001	3.4054e+003
	Resonator:mid			3.4684e-001	4.7268e+003
	Resonator:inner			1.2569e-001	1.3044e+004
	SMA_in:conductor			5.0148e-003	3.2693e+005
	SMA_out:conductor			3.8858e-003	4.2191e+005

Sum				7.6835e-001	2.1337e+003

External Q-factor Calculation:

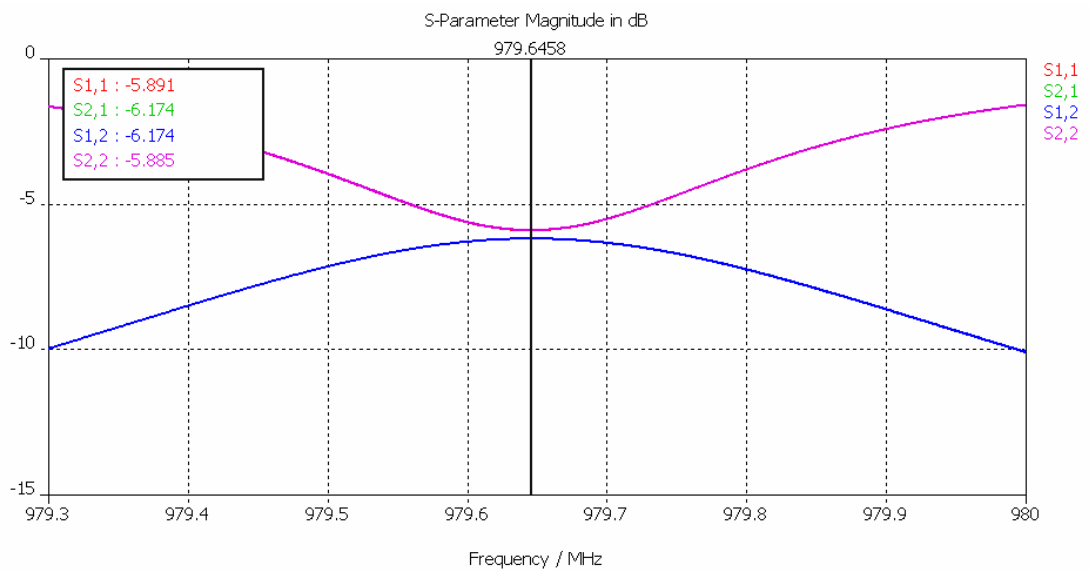


Figure 3.31: The CST simulated S-parameters of the Resonator.

From Fig. 3.31 only the plot for S_{21} was extracted. With the use of the S_{21} , the 3 dB bandwidth could be determined, as follows.

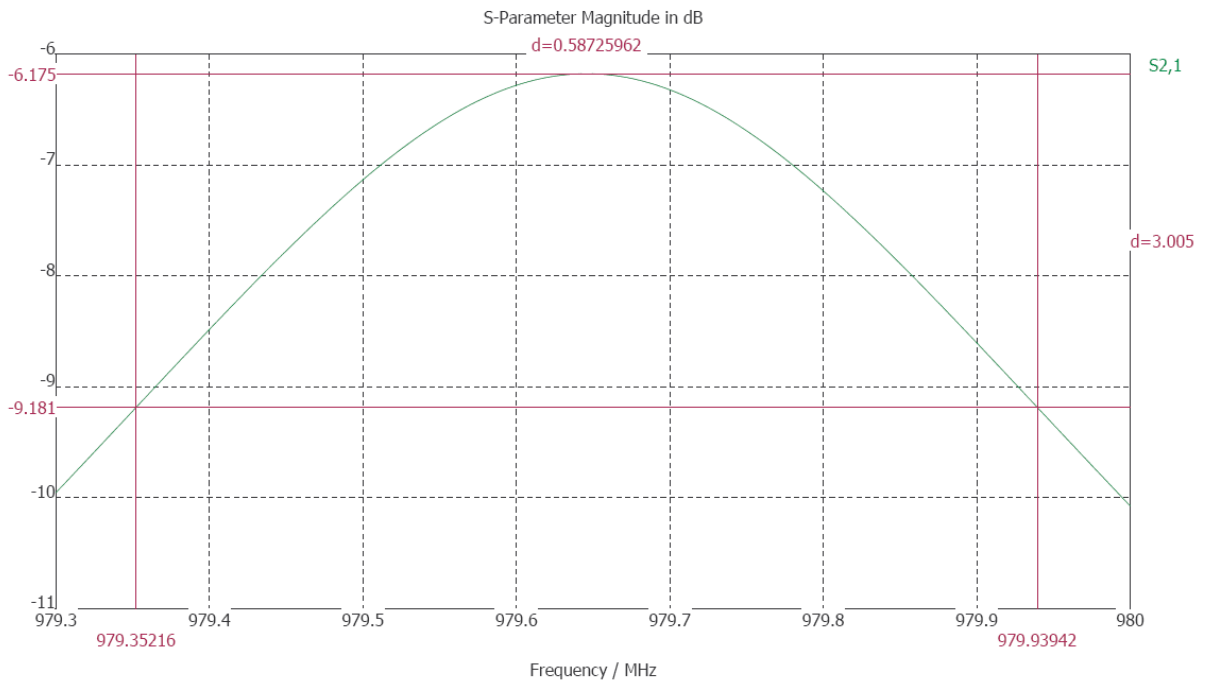


Figure 3.32: Illustration of the Resonator 3 dB Bandwidth.

From the 3 dB bandwidth illustrated in Fig. 3.32 the loaded Q-value can be determined as mentioned in earlier theory:

$$Q_L = \frac{f_0}{3\text{dB BW}} = \frac{979.646 \times 10^6}{587.259 \times 10^3} = 1668.17.$$

To summarise, the resonator design which finalised the oscillator had the following Q-values:

$$\text{Internal Q: } Q_U = 2133.7, \text{ and} \quad (3.59)$$

$$\text{External Q: } Q_L = 1668.2. \quad (3.60)$$

Subsequently, the resonator illustrated in Fig. 3.30 was then built and measured. The details will be discussed in the following section reporting on the 'Measurements and Results'.

3.1.4 Measurements and Results

3.1.4.1 S-Parameters at Resonance – Network Analyser Measurement

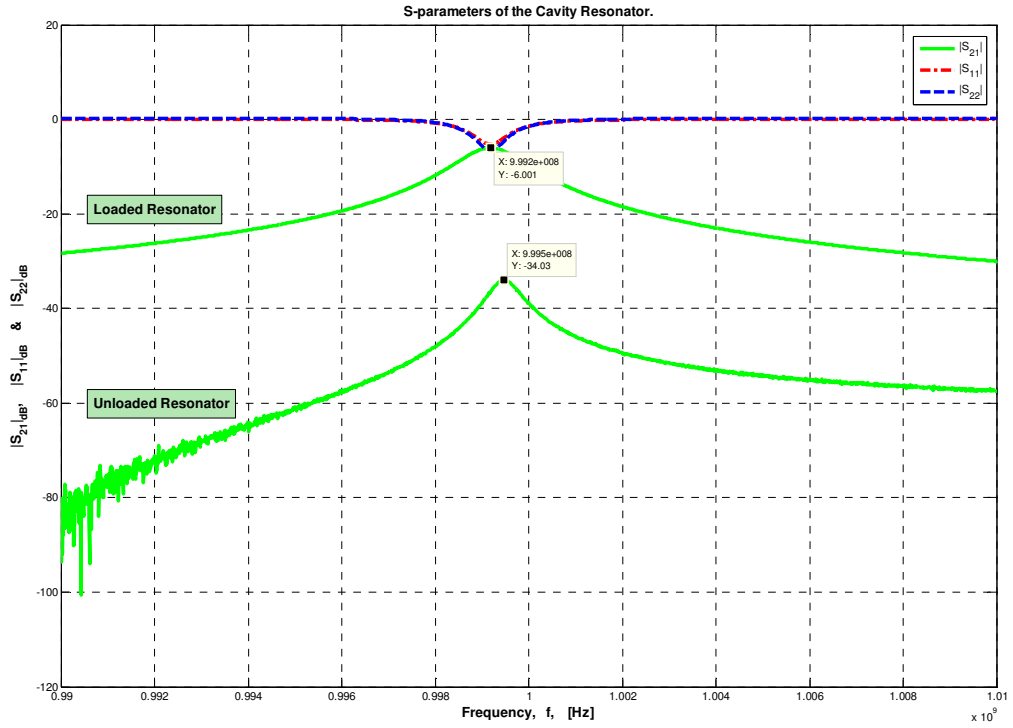


Figure 3.33: S-parameters of the Cavity Resonator.

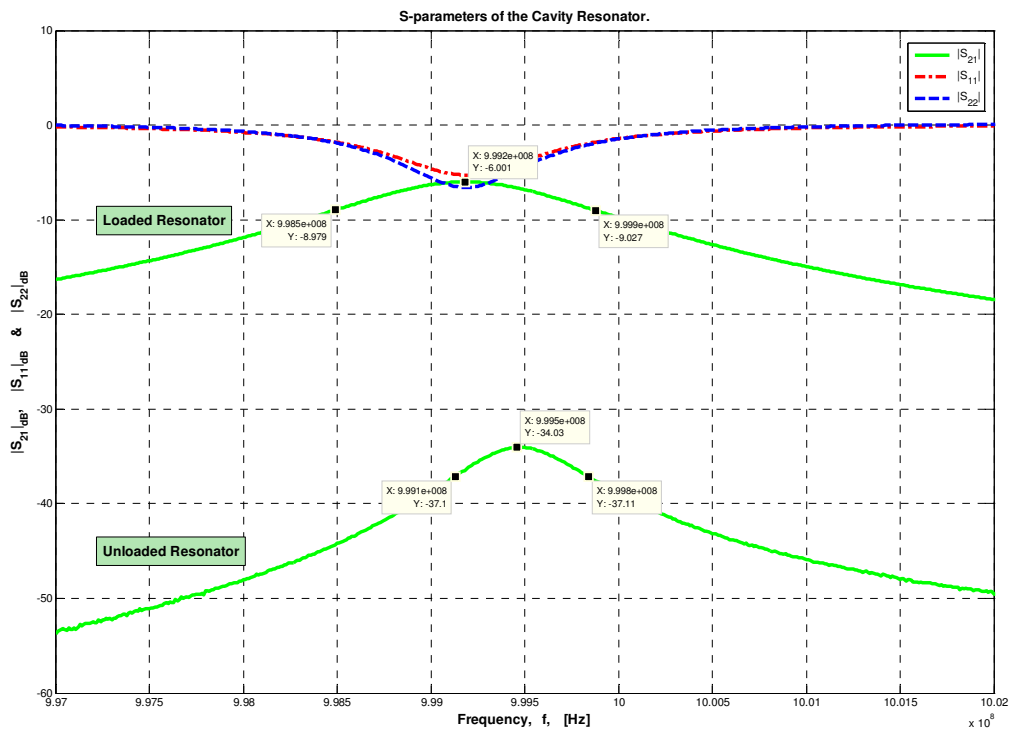


Figure 3.34: S-parameters of the Resonator, illustrating the 3 dB Bandwidth.

See Appendix **C** for the **MATLAB** code used to conduct the illustrations above.

The measurements shown on the previous page were made on the *Rohde & Schwarz ZVB 8 – Vector Network Analyser* (illustrated in the following, Fig. 3.35). The measurement was done over a frequency span of 1.455 GHz (i.e. 45 MHz \rightarrow 1.5 GHz).

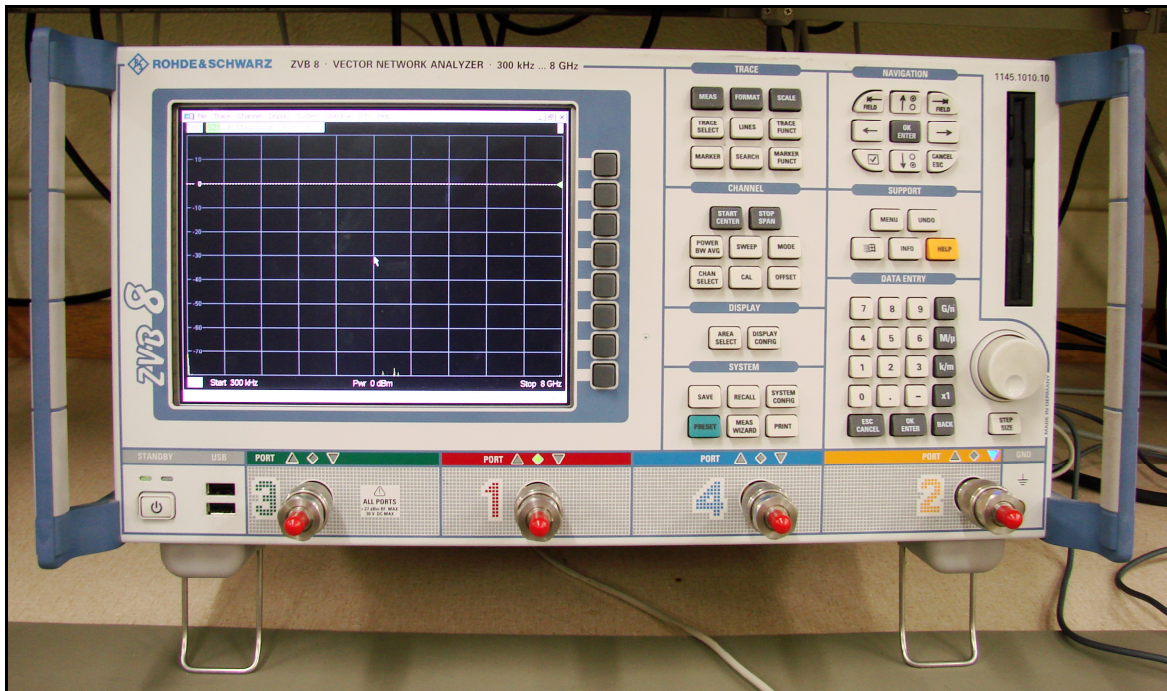


Figure 3.35: Photograph of the Rohde & Schwarz ZVB 8 – Vector Network Analyser.

In Fig. 3.33 the measured S-parameters are displayed over a frequency span of 20 MHz, while in Fig. 3.34 the 3 dB bandwidth is illustrated over 5 MHz.

From Fig. 3.34 the S-parameters at resonance are measured as:

$$S_{11} = -5.261 \text{ dB} ,$$

$$S_{22} = -6.587 \text{ dB} ,$$

$$S_{21} = -6.001 \text{ dB} .$$

Take note that the measured resonant frequency $f_0 = 999.2 \text{ MHz}$ (according to the loaded resonator plot, in the latter two figures), is not consistent with that simulated in **CST** (illustrated in Fig. 3.31 and Fig. 3.32). This inconsistency is not important, since it can easily be tuned equal by means of the added tuning element mentioned in paragraph 3.1.2.6. The tuning element being present in the measured resonator is most likely the reason that the frequencies do not match.

Subsequently the unloaded Q-value, as well as the loaded Q-value of the resonator, is being calculated by means of the values obtained from Fig. 3.34.

3.1.4.2 Unloaded Q-value

In the case of calculating the unloaded Q-value of the resonator, the measurement was done with the coupling loops turned flat and as far out of the cavity as possible. The technique ensures as little coupling as possible. A good indication that the device being measured is unloaded is when the measured S_{21} value is at least below -30 dB at resonance. See Fig. 3.34. Thus doing the necessary calculation provides the following result,

$$Q_U = \frac{f_0}{3\text{dB BW}} = \frac{999.5 \times 10^6}{(999.8 \times 10^6 - 999.1 \times 10^6)} = 1427.857 \quad (3.61)$$

3.1.4.3 Loaded Q-value

When determining the loaded Q-value of the resonator, the 3dB bandwidth was measured at resonance with $S_{21} = -6$ dB, ensuring minimum phase noise. Thus, tuning the coupling loops to the latter value gave,

$$Q_L = \frac{f_0}{3\text{dB BW}} = \frac{999.2 \times 10^6}{(999.9 \times 10^6 - 998.5 \times 10^6)} = 713.714 \quad (3.62)$$

3.1.5 Resonator Results Compared

In the following table, the simulated results are compared to that obtained through the measurements of the resonator system.

Table 3.12: The Simulated- versus the Measured Q-values of the Resonator.

	Unloaded Q-value Q_U	Loaded Q-value Q_L	Equations
Simulated	2133.7	1668.2	(3.59) & (3.60)
Measured	1427.9	713.71	(3.61) & (3.62)

From Table 3.12 it is clear that the simulated results do not concur with the measured results. Several procedures were followed to try and establish why this distinction exists.

First of all, it was thought that possibly some of the captivated energy inside the resonator's cavity was leaking out at its lid. Consequently, a conductive paste was applied between the lid and the bottom-half of the resonator in hope that it would provide a better seal. Unfortunately, no improvement was noticed for the Q-value.

Secondly, it was thought that since the Q-value of the resonator is related (inversely proportional) to the loss inside the resonator, that maybe the problem was that the cavity of the resonator was 'unclean'. As a result the resonator was put in an 'acid-bath' at Reutech Radar Systems (RRS), Stellenbosch. It was left in the 'acid-bath' for more than 24 hours, hoping to get rid of all possible debris that might be left inside from its manufacturing. This debris could be responsible for unwanted loss inside the resonator. But again, no improvement in the Q-value was obtained.

Thirdly, a strong 'acid-paste' was directly applied to the inside-boundaries of the cavity. It was left for more than 24 hours. With this course of action it was attempted to clean the resonator's cavity as much as possible, in the hope that any unnecessary loss in energy inside the resonator would be eliminated.

Lastly, the supplier of the copper bar, which the resonator was made out of, was contacted. This was done to confirm the alloy-mix of the material, to exempt any possible loss that might exist due to the material itself. In the **CST** simulation done for the resonator, the conductivity was entered as: $\sigma_c = 5.8 \times 10^7$ S/m for solid copper [25]. On the 'Test Certificate' received from the supplier, no conductivity is specified, but only that the copper bar is 99.97 % copper. See the next page for the Cu specification.



NON-FERROUS METAL WORKS



EXTRUSION DIVISION

1 The Avenue East, Prospecton, Kwa-Zulu Natal, South Africa
 Telephone: (031) 902 7470 Fax: (031) 902 8865

(SA) (PTY) LTD
 Reg. No. 1951/000553/07

TEST CERTIFICATE

CUSTOMER UNIVERSITY OF STELLENBOSCH				TEST CERTIFICATE No. BATCH No. (LOT No.) WORKS ORDER No. SALES CONTRACT No. ALLOY QUANTITY ORDERED WEIGHT DESPATCHED		21955 6189 2652687 2652687 120 120				
PURCHASE ORDER No.				SPECIFICATION 120						
DESCRIPTION EXTRUDED AND DRAWN COPPER ROUND BAR				SIZE 50MM DIA						
MECHANICAL/PHYSICAL PROPERTIES										
Dia mm	Area mm ²	Yield Kg/mm ²	Strength PSI	0,2% P.S. PSI	TENSILE STRENGTH		Elong %	Hardness		
					PSI	Kg/mm ²		Vickers Actual	Brinell Calculated	
CHEMICAL COMPOSITION										
Cu	Zn	Fe	Mn	Al	Ni	Sn	Pb	Si	As	P
99.97		0.001			0.002	0.002	0.002			0.01
REMARKS				We certify that material is free from mercury contamination.						
				Signed for and on behalf of Non-Ferrous Metal Works (SA) (Pty) Ltd T. MUTHUBAMY V. MOODLEY Quality Manager Chief Chemist						
				11/09/2007 Date						

Even after following all of the above mentioned steps, no apparent reason could be found for the difference between the results obtained from the **CST** simulation and that measured on the Network Analyser. For any further designs, the measured results were used. For interesting copper-alloy websites visited, see [32- 34].

3.2 ACTIVE COMPONENT: AMPLIFIER (ZX60-2522M+)

3.2.1 Technical Data

One of *Mini-Circuits'* Coaxial Amplifiers, the **ZX60-2522M+**, was used as the active device in the oscillator circuit.

Inside the ZX60 casing, *Mini-Circuits'* Monolithic Amplifier, **MNA-6+** is visible, with its recommended biasing.

See Appendix **D** for both datasheets.

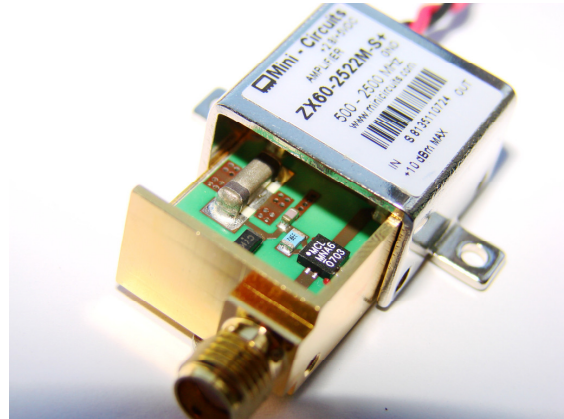


Figure 3.36: Photograph of the ZX60 Amplifier.

The ZX60-2522M+ amplifier has a wide bandwidth from 0.5-2.5 GHz, with a typical gain of 22 dB at 1 GHz and a maximum input power of +10 dBm. In the following section, the Noise Figure (NF) and S-parameter measurements made on the amplifier, are illustrated.

3.2.2 Measurements and Results

3.2.2.1 Noise Figure, NF_{dB}

The Noise Figure and Gain of the amplifier were measured on the *Hewlett Packard 8970B Noise Figure Meter*. Firstly, the instrument was set-up and calibrated for the specific bandwidth, after which the following measurements were taken.

Table 3.13: Amplifier, Noise Figure (NF) measurements.

f [Hz]	NF [dB]	Gain [dB]
900×10^6	2.90	22.60
1000×10^6	2.85	23.14

3.2.2.2 S-parameters – Network Analyser

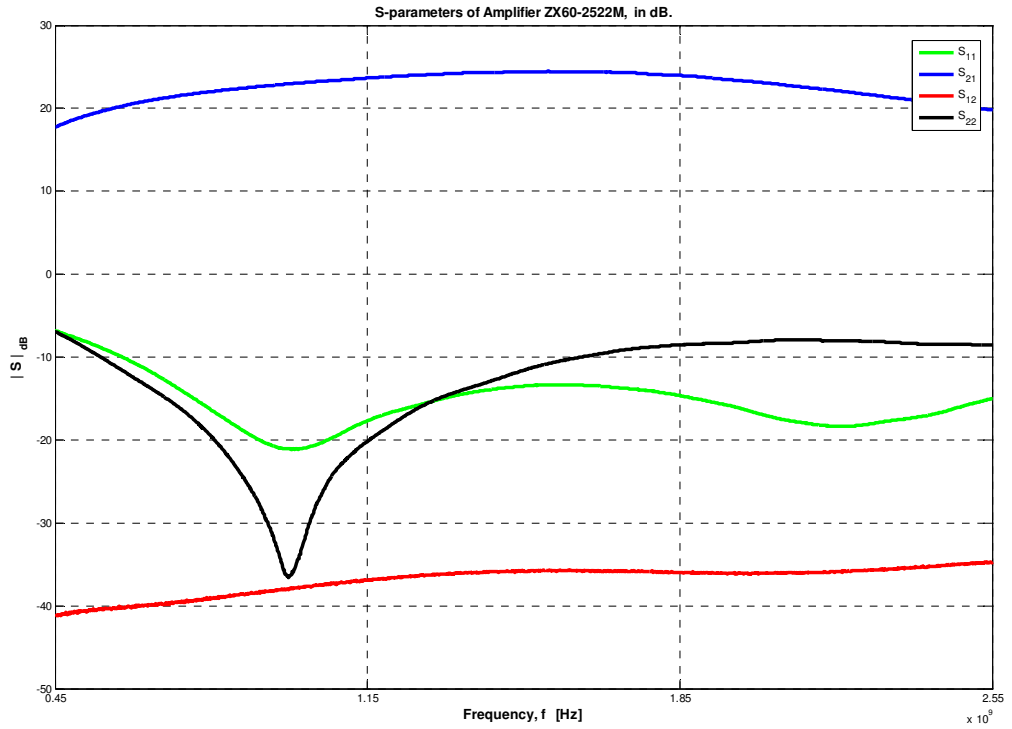


Figure 3.37: S-parameters of the Mini-Circuits ZX60-2522M+ Amplifier.

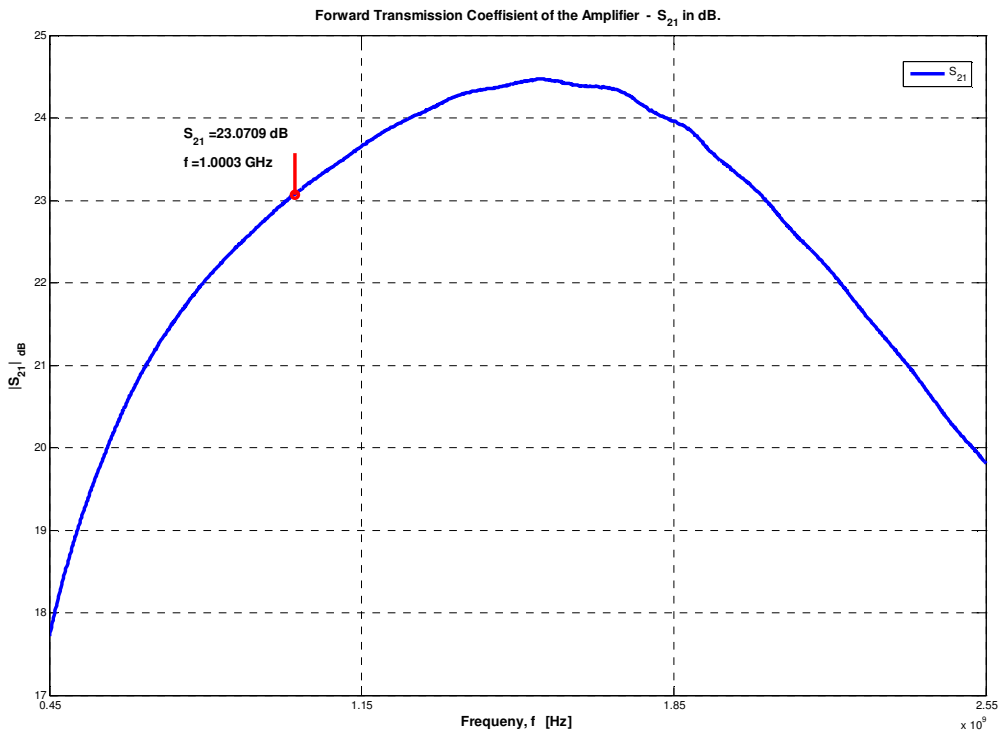


Figure 3.38: S_{21} of the ZX60-2522M+ Amplifier.

Figures 3.37 and 3.38 illustrate the measured S-parameters of the amplifier.

3.3 OPEN-LOOP OSCILLATOR ELEMENTS

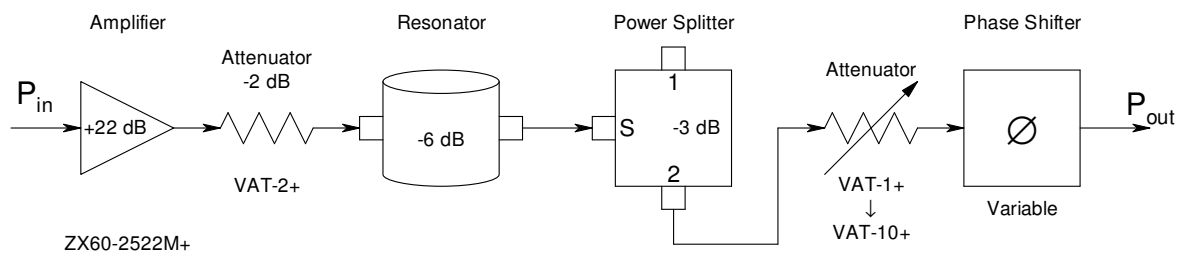


Figure 3.39: Open-loop Oscillator Block Diagram.

From Fig. 3.39 the different oscillator circuit elements are visible. It is arranged in an open-loop and coupled to the *Rohde & Schwarz VNA*. The latter is done to determine the effect of every component and the phase over the whole length of the loop. According to oscillator theory (Chapter 2); the total phase shift around the loop should either be 0 degrees or a multiple of 360 degrees.

The VNA was firstly set up and calibrated for the desired bandwidth. The input power, $P_{in} = -15$ dBm was set and obtained from port 1 of the VNA, while the output power, P_{out} was then measured at port 2 of the VNA. All measurements made and results obtained are illustrated in the upcoming section 3.3.4.

All of the elements portrayed in Fig. 3.39 are discussed in the following sections, with their datasheets visible in the appendices.

3.3.1 Power Splitter: 3 dB Coupler (ZFSC-2-5-S+)

This power splitter is manufactured by Mini-Circuits, and operates over a frequency band of 10-1500 MHz. It has a maximum power input of 1W.

See Appendix E for the couplers

Datasheet with all the relevant information.

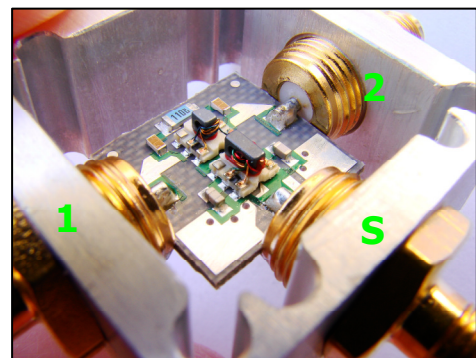


Figure 3.40: Photograph of the 3 dB Coupler.

3.3.2 Attenuators (VAT-X+)

There are two attenuators implemented in the oscillator circuit, with both serving different purposes.

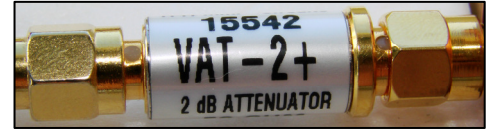


Figure 3.41: The 2 dB Attenuator.

When driving an amplifier, there are three different ways in which the gain can be limited. The first is done by the amplifier itself, thus driving the amplifier into saturation and consequently having non-linear operation. The second is by designing a 'diode-bridge', which will limit the current flow. The third option is by making use of attenuators in the feedback loop.

The first attenuator is similar to a '3 dB attenuation pad'. Since the amplifier is matched to 50Ω and the resonator is not; the load that the amplifier sees is not 50Ω . This will result in not having a maximum power transfer between the amplifier and the resonator. Therefore, the **2 dB** attenuator is used to reduce any reflections that might occur due to the mismatch in the impedance values, thus making the resonator look more like a 50Ω load to the amplifier. This attenuator is fixed and does not get interchanged with other values. See Appendix **F** for its datasheet.

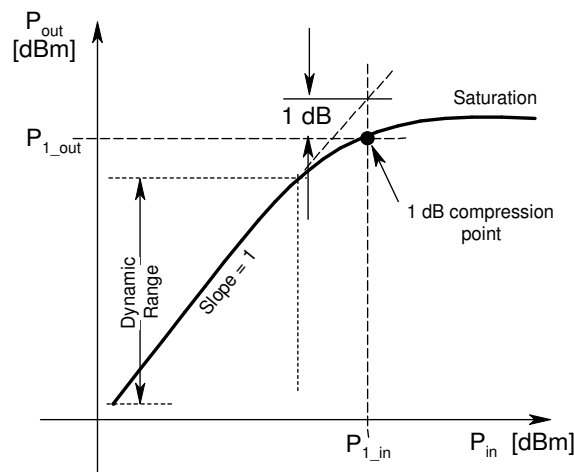


Figure 3.42: Illustration of the 1 dB Compression Point for an Amplifier.

The purpose for the second attenuator comes from amplifier theory. From the definition of the *1 dB compression point*, that represents the power level for which the

output power has decreased by 1 dB from the ideal characteristic, the linear operating range of the amplifier is quantified, as illustrated in Fig. 3.42. Every designed amplifier portrays a similar characteristic.

As long as the input power to the amplifier is kept small (within the amplifier's dynamic range), the amplifier will not be driven into saturation and therefore the amplifier will still be operating linearly.

However as soon as the input power becomes too big, so that the output power is bigger than P_{1_out} (stated in terms of P_{out}), then the amplifier is operating in the saturation region, outside its dynamic range and therefore operating non-linearly.

The input power (P_{in}) to the amplifier is varied by interchanging the attenuator in the feedback loop. The bigger the attenuation, the smaller P_{in} will be and vice versa. For P_{in} too small, the oscillation will stop, meaning that there is not enough energy present in the feedback loop to at least match the losses present in the circuit (Chapter 2 – Oscillator Theory).

For the attenuator in the feedback loop, it would be more practical to build an electronic attenuator. It will show exactly when the oscillation turns off (thus not having enough energy in the feedback loop), when the oscillator is just oscillating (linear operation) and when it is going into saturation (non-linear operation).

In this project it is important to attempt to keep the oscillation as linear as possible, given that non-linear operation has non-linear currents involved, which cause the phase noise level present in the oscillator to rise. The increased phase noise level is contradictory to the aim of this project.

3.3.3 Phase Shifter

As mentioned earlier, according to oscillator theory (Chapter 2) the total phase shift around the loop should either be 0 degrees or a multiple of 360 degrees.

By measuring the phase (on the VNA) and length of two different length identical cables, the effective wavelength inside the cables could be established by means of the following equations. Consequently the relative permittivity of the cables could be determined as well.

$$\lambda_{\text{eff}} = \frac{\lambda}{\sqrt{\epsilon_r}} \quad (3.63)$$

$$\Delta\phi = \beta\Delta\ell \quad (3.64)$$

$$\beta = \frac{\Delta\phi}{\Delta\ell} = \frac{2\pi}{\lambda_{\text{eff}}} \quad (3.65)$$

$$\lambda_{\text{eff}} = \frac{2\pi}{\Delta\phi} \cdot \Delta\ell \quad (3.66)$$

where

λ = the wavelength in free space, in [m]

λ_{eff} = the effective wavelength inside the cables, in [m]

ϵ_r = the dielectric constant, in [F/m]

β = the phase constant, in [rad/m]

$\Delta\phi$ = the difference in phase between the two cables, in [m]

$\Delta\ell$ = the difference in length between the two cables, in [m].

Following from the results obtained in the previous equations, a more accurate estimation can be made on the precise length of transmission line needed; to ensure a total phase shift of 0 degrees around the loop. The required length of transmission line would then be made from the same cable just measured [14].

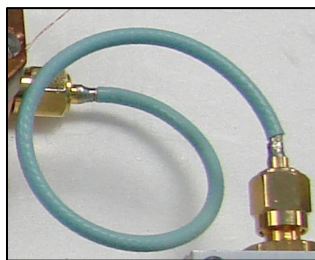


Figure 3.43: Typical piece of Transmission Line used.

Adding a *phase shifter* to the feedback loop provides a dynamic way of adding or removing length to the path. It acts as an all pass filter, keeping the amplitude the same while the phase shift around the loop is being tuned.

Illustrated in Fig. 3.44 is a photograph of the phase shifter used in this project. The phase shifter acts as an extractable piece of transmission line.

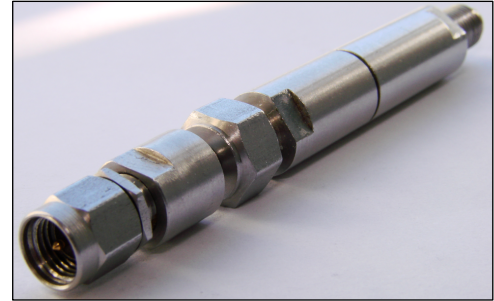


Figure 3.44: Phase Shifter.

3.3.4 Measurements and Results

All of the measurements illustrated in this section were of the open-loop oscillator, measured on the VNA. In the first measurements, the effect of every element in the loop is demonstrated. That is the effect on both the amplitude and phase of the system. In the last measurements, the operation of the phase shifter is shown.

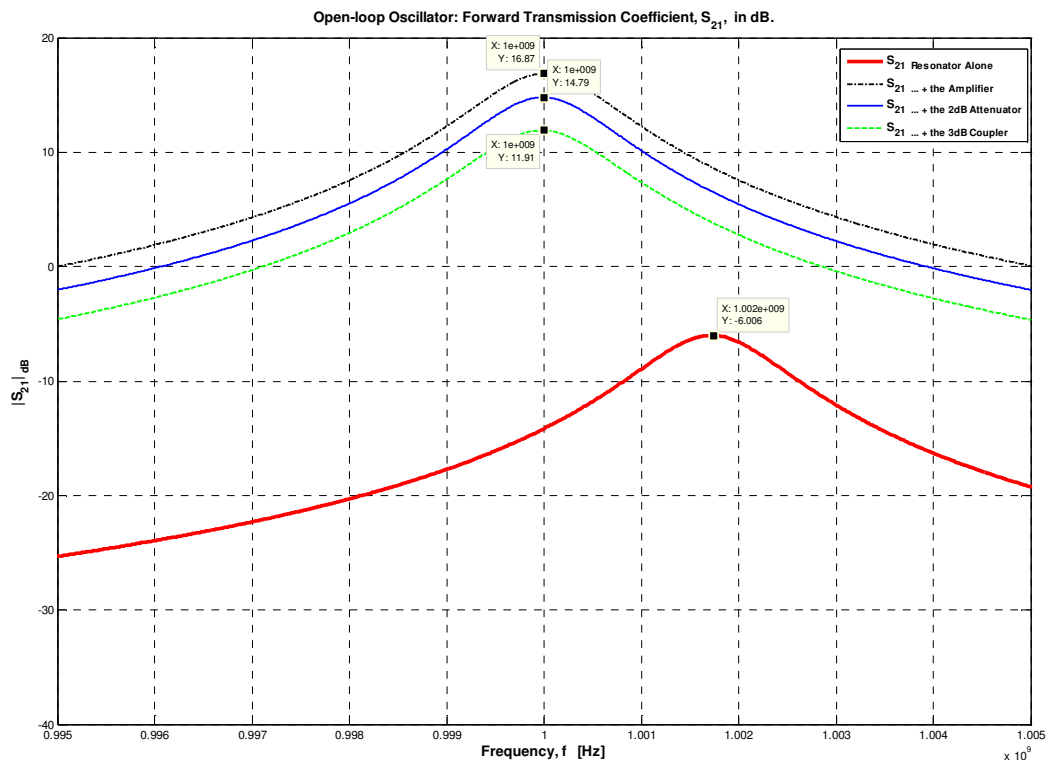


Figure 3.45: Effect of the circuit elements on S_{21} of the open-loop Oscillator.

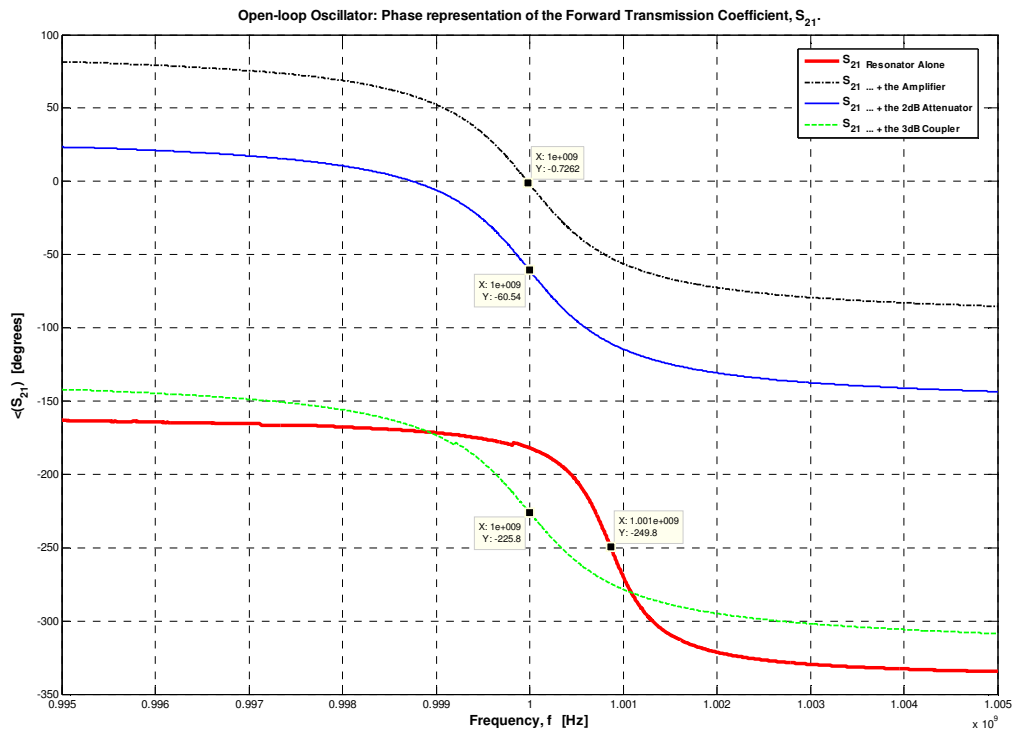


Figure 3.46: Effect of the circuit elements on the phase of the open-loop Oscillator.

The measurements in Fig. 3.45 and Fig. 3.46 show what effect each element in the loop has on the system's S_{21} . Take note that the resonant frequency of the resonator plot does not match those of the other measurements. This took place since the resonator on its own was measured last, and its frequency was tuned to 1 GHz by means of the **microwave tuning element** (as discussed in section 3.1.2.6).

In the following figures, Fig. 3.47 and Fig. 3.48 the operation of the added Phase Shifter is shown. Take note in Fig. 3.47 that the latter has almost no effect on the amplitude of the open-loop's S_{21} . While it easily tunes the total phase shift of the system back to 0 degrees; as illustrated in Fig. 3.48.

The blue plot in Fig. 3.48 illustrates the open-loop system, with the added phase shifter, but with the latter at its minimum setting. The red plot illustrates that the phase shifter has been tuned to obtain a total phase shift of 0 degrees.

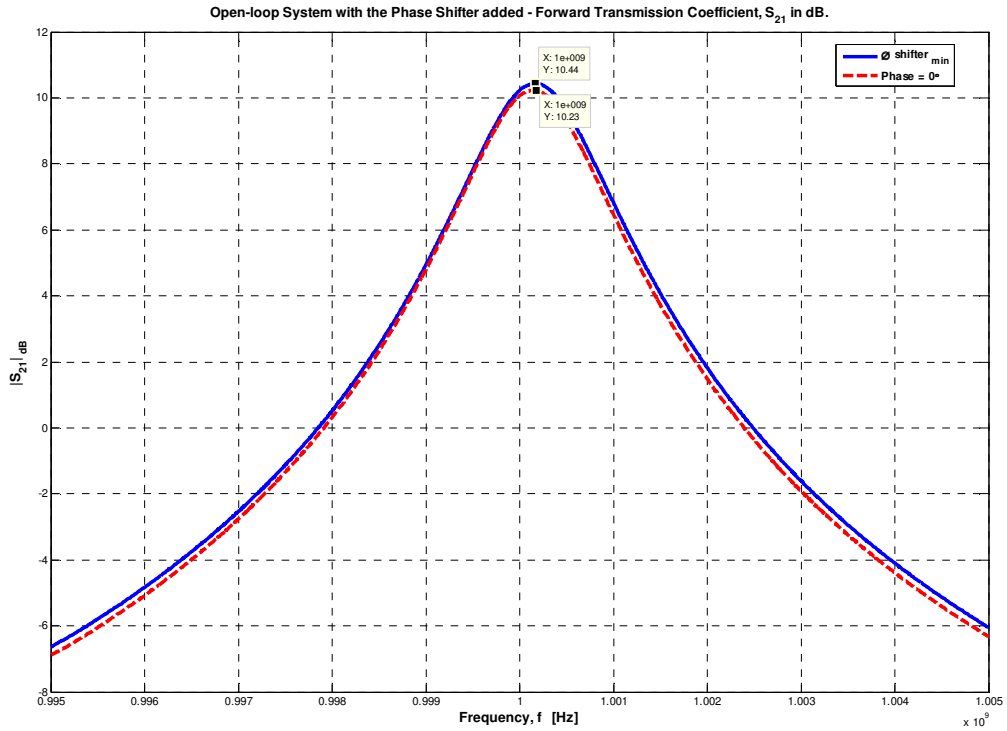


Figure 3.47: S_{21} of the open-loop Oscillator with the Phase Shifter.

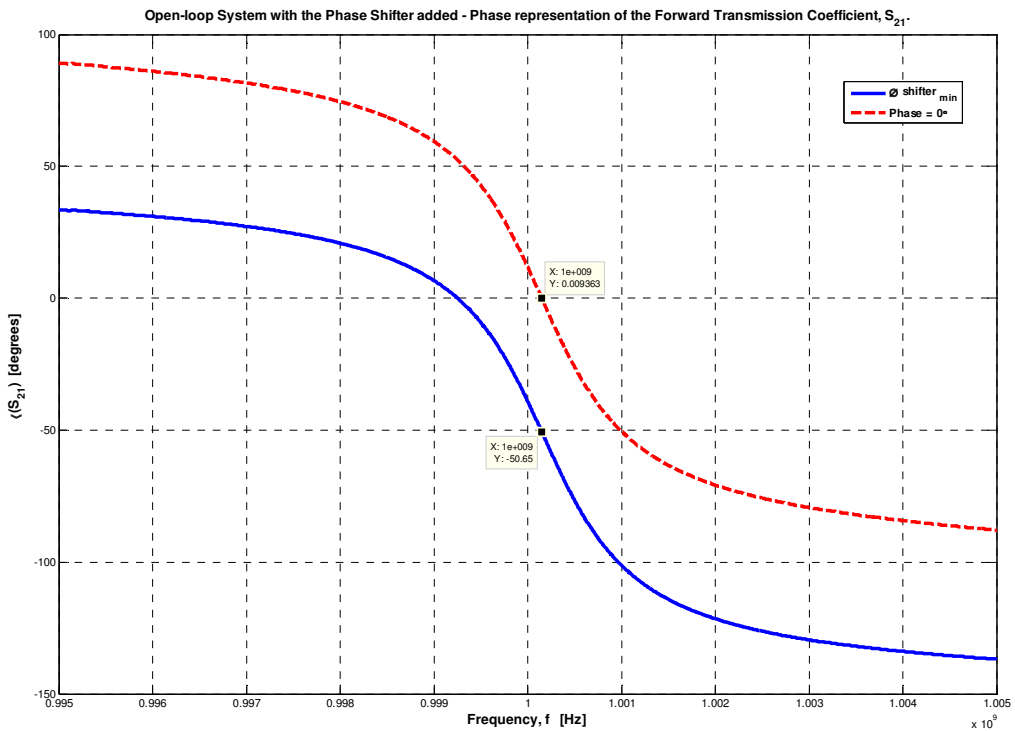


Figure 3.48: Effect of the Phase Shifter on the phase of the open-loop Oscillator.

3.4 CLOSED LOOP – OSCILLATOR

3.4.1 Element Block Diagram

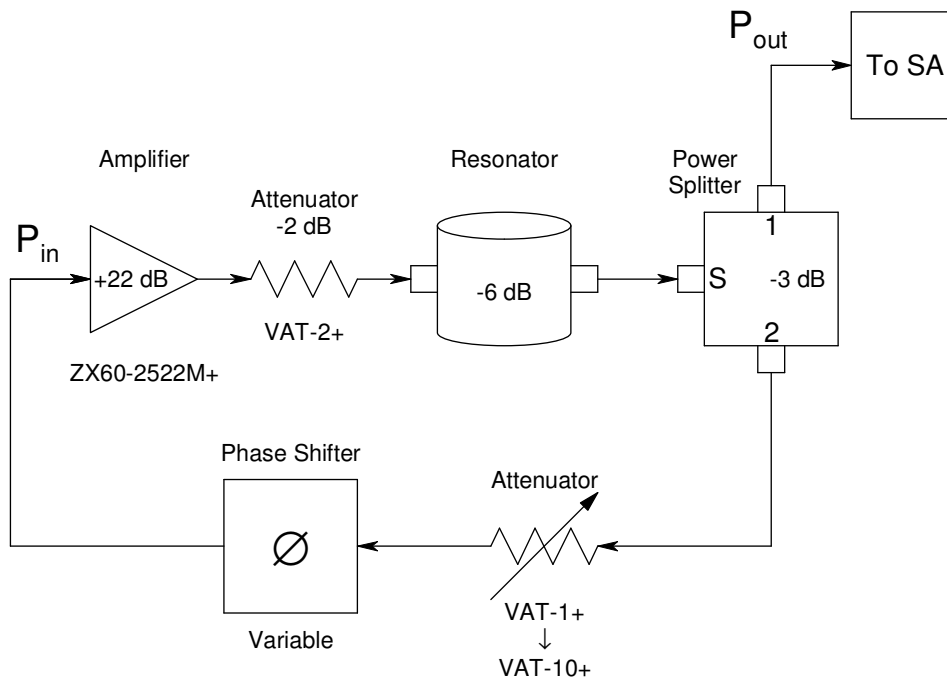


Figure 3.49: Block Diagram of the closed-loop Oscillator.

3.4.2 Measurements and Results

3.4.2.1 Expected Power Levels

It is important to be familiar with the different power levels present in the circuit. Especially when connecting the circuit to expensive measuring equipment.

The power level at different locations in the circuit were determined by moving the 3 dB coupler around, connecting it at specific points of interest and then measuring the power level on the *Rohde & Schwarz FSEK30* Spectrum Analyser.

According to the datasheet (Appendix **D**) of the ZX60-2522M+ amplifier, it has a gain of about 22 dB, and $P_{1_out} = 19.5$ dBm, at 1 GHz.

Table 3.14: Measured Power Levels along the oscillator circuit in Fig. 3.49.

	Measured [dBm]
Amplifier Output	18.5
Resonator Input	16.5
Power Splitter Input	10.4
1 dB Attenuator Input = P_{out}	7.4
Amplifier Input, P_{in}	6.1

From the measured power levels, it is clear that the amplifier was operating in its saturation region. This happened since the input power to the amplifier was too big. The latter was minimised by varying the feedback (1 dB) attenuator value. By increasing the latter, the input power to the amplifier decreased and consequently the amplifier operated more linearly. The ideal place to have an oscillator operating is just before the saturation region, thus having linear operation but also stable oscillation.

3.4.2.2 Oscillation

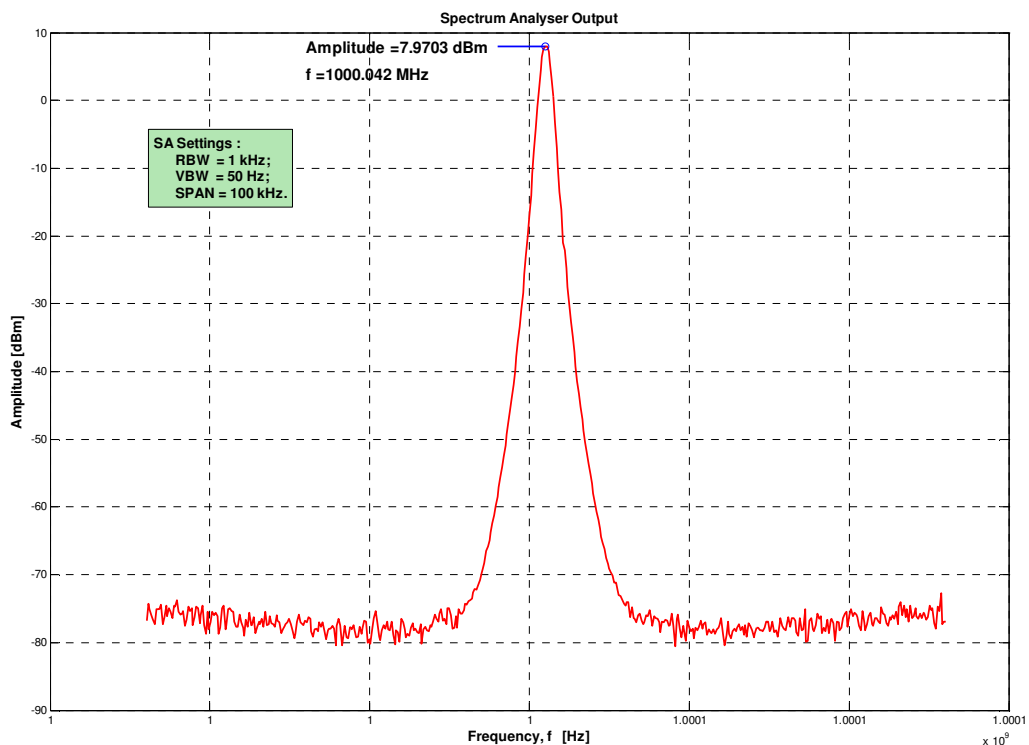
**Figure 3.50: Spectrum Analyser Output of the closed-Loop Oscillator.**

Fig. 3.50 illustrates the oscillation as measured on the SA. Take note that the measured amplitude value agrees well with the expected power level, P_{out} shown in Table 3.14.

3.4.2.3 Phase Shifter

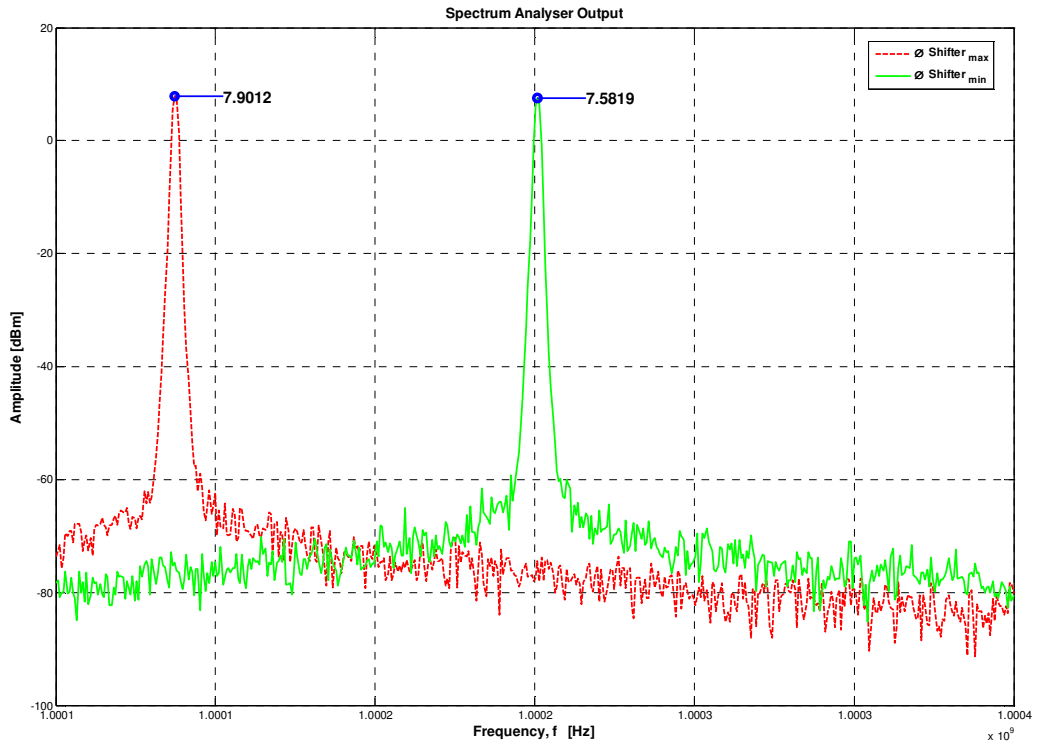


Figure 3.51: Phase Shifter at its Minimum and Maximum settings.

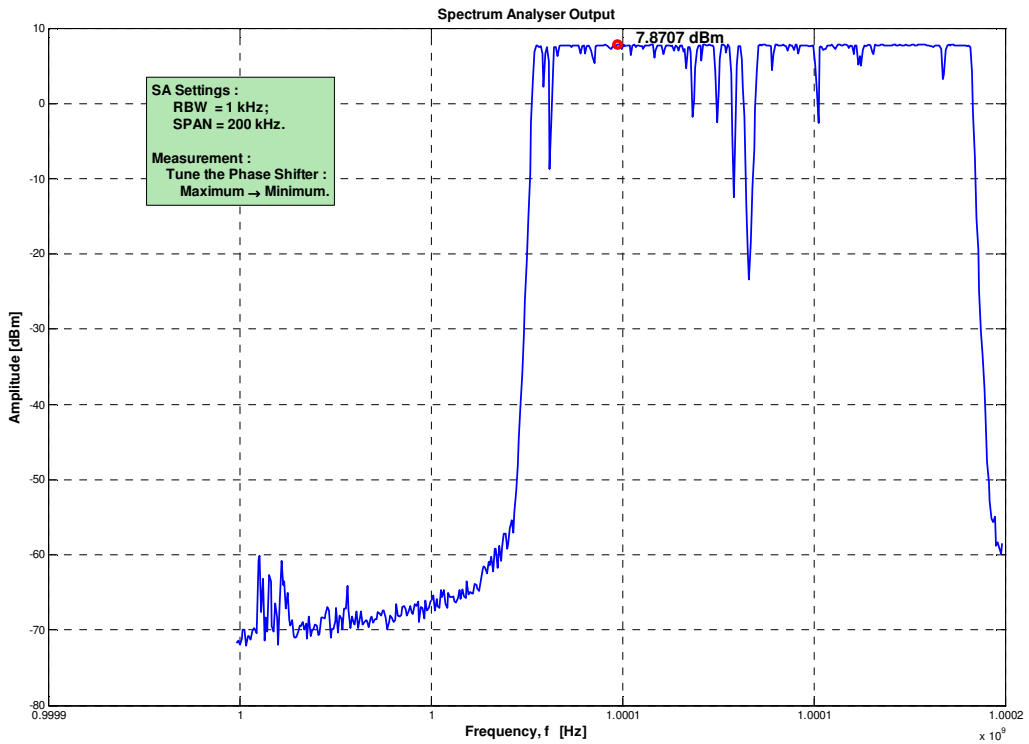


Figure 3.52: Frequency Response of the Phase Shifter – tuning it from its maximum to its minimum setting.

Fig. 3.51 and Fig. 3.52 illustrate measurements made on the SA of the closed-loop oscillator system, with the phase shifter added to the feedback loop. The latter was done to demonstrate the effect of the phase shifter while tuning it from its maximum to its minimum setting, to obtain the setting of the phase shifter that would produce the maximum oscillator output signal, thus where the phase shift is equal to 0 degrees. In Fig. 3.51 the red plot represents the phase shifter at its maximum setting, while the green plot represents the minimum setting. In Fig. 3.52, the phase shifter was tuned from its maximum to its minimum setting, while the 'max hold' setting on the SA was activated for the duration of the tuning. The visible 'inverted spikes' appeared when the phase shifter was tuned to fast.

3.5 OSCILLATOR PHASE NOISE

3.5.1 Theoretical Prediction by Leeson's Phase Noise Model

Revisit Section 2.3.5 *Leeson's Phase Noise Model* on page 60, in Chapter 2. In (2.93) on p.67, the single-sideband (SSB) phase noise relative to the carrier, $L(f_m)_{[\text{dBc/Hz}]}$ was defined as follows. See Appendix G.

$$L(f_m)_{[\text{dBc/Hz}]} = 10 \log_{10} \left[\frac{1}{2} \cdot \frac{kTF}{P_{in}} \cdot \frac{K \cdot f_c \cdot f_0^2}{4Q_L^2 \cdot f_m^3} + \frac{f_0^2}{4Q_L^2 \cdot f_m^2} + \frac{K \cdot f_c}{f_m} + 1 \right]$$

where

$k = 1.380 \times 10^{-23}$ [J/K], is Boltzmann's constant.

$T = 290$ [K], the temperature.

$F = 1.928$ (abs), the noise factor of the amplifier (NF = 2.85 dB).

$P_{in} = 4.07$ W, the input signal power to the amplifier (= 6.1 dBm).

$K =$ a constant accounting for the strength of the $1/f$ noise.

$f_c = 5$ MHz, the corner frequency of the $1/f$ noise (Chapter 2, p. 63).

$f_0 = 1$ GHz, the fundamental frequency of oscillation.

$f_m = [1:100:10e6]$ Hz, is the offset frequency from the carrier.

$Q_U = 1427.9$, the measured unloaded Q-value of the resonator.

$Q_L = Q_U/2 = 713.71$, also measured.

$f_h = f_0/2Q_L = 700.57$ kHz, the half-power 3 dB BW of the resonator.

3.5.1.1 Implementation in *MATLAB*

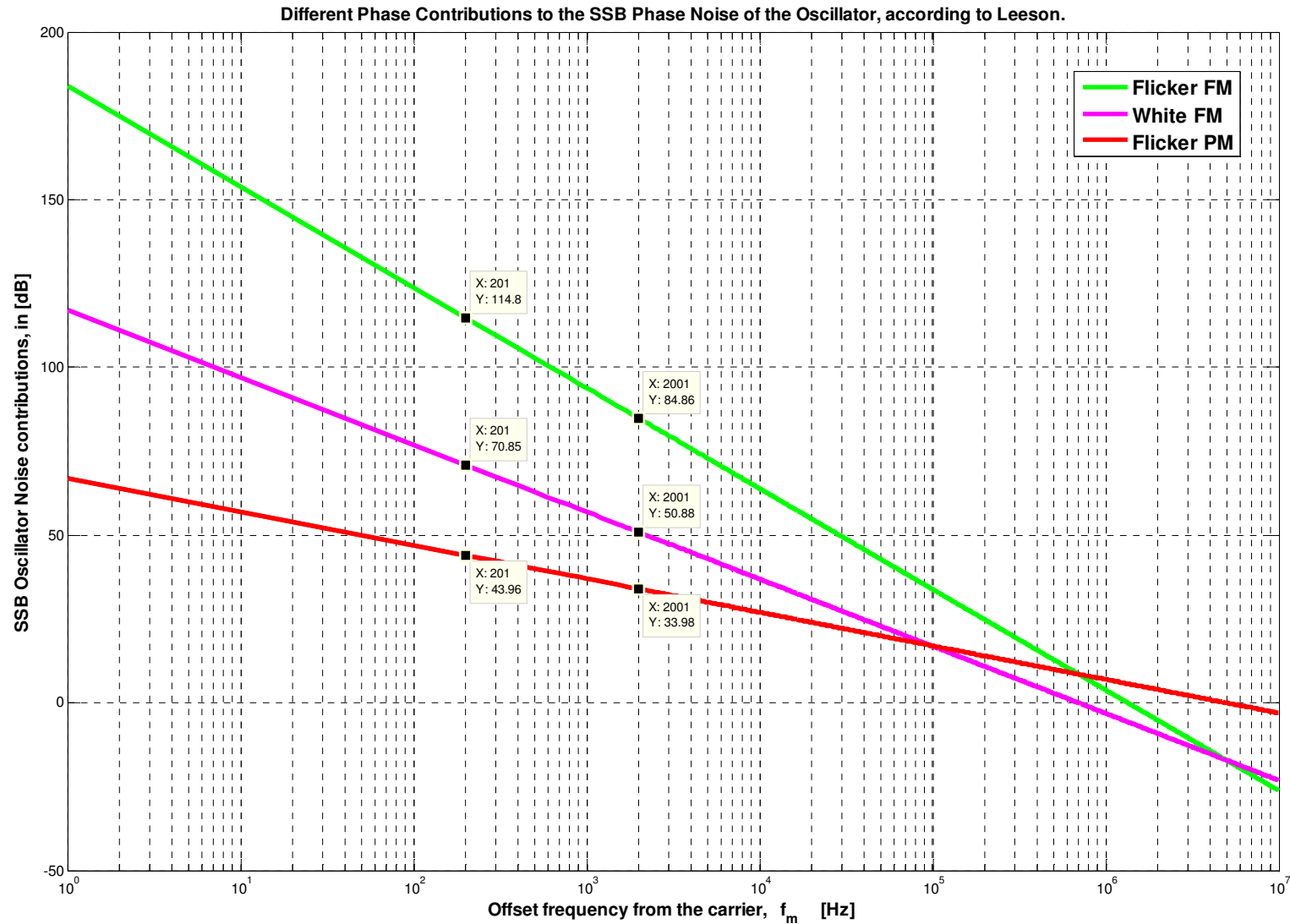


Figure 3.53: Noise Contributions to the Oscillator SSB Phase Noise relative to the Carrier.

The different terms present in Leeson's Phase Noise Model, are illustrated in Fig. 3.53. All except the predicted noise floor, this lies at about -178 dBm. Every term represents a different noise contribution to the oscillator phase noise.

For example the '*Flicker FM*' plot is dominant at offset frequencies close to the carrier. It has a slope of -30dB/decade.

The '*White FM*' noise portrays a slope of -20dB/decade.

The '*Flicker PM*' plot has a slope of -10dB/decade.

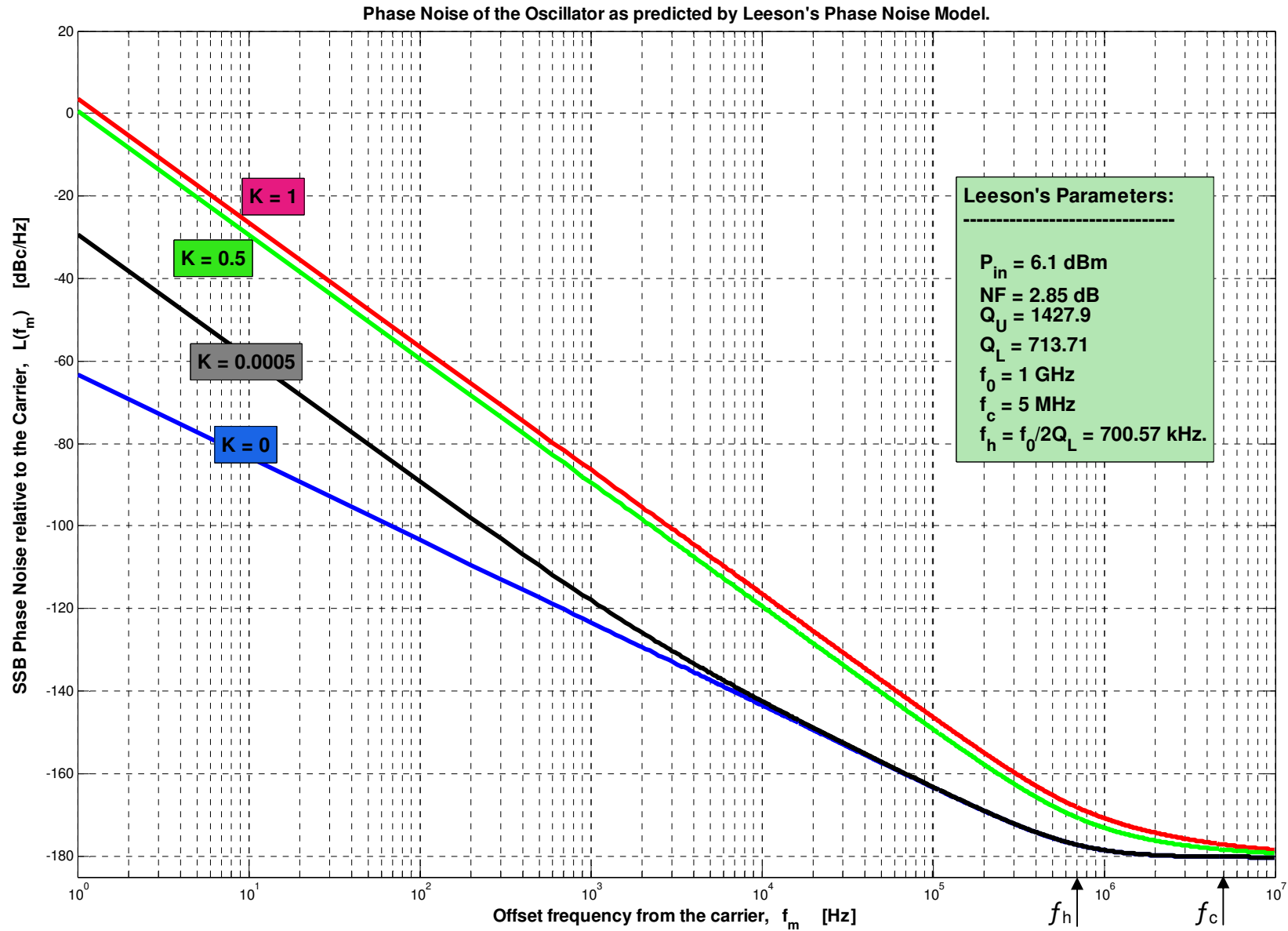


Figure 3.54: Phase Noise of the Oscillator as predicted by Leeson's Phase Noise Model.

Fig. 3.54 portrays the SSB phase noise of the oscillator system, relative to the carrier.

K represents the strength of the $1/f$ noise. Illustrated is a few simulations done in **MATLAB** for four different values of K.

Take note of the marked 'half-power 3dB BW' of the resonator at 700.57 kHz.

The corner frequency of the $1/f$ noise, f_c is also shown. It was chosen as 5 MHz.

3.5.2 Measurements and Results

The first phase noise measurement was made on the *Spectrum Analyser*. Only thereafter it was measured on the automatic *Aeroflex PN9000B Phase-Noise Test System*.

3.5.2.1 Spectrum Analyser

Confirmation of the Oscillation

In the following Fig. 3.55 the oscillation of the oscillator system is shown. It was measured on the SA, with its settings summarised in the figure as well. The 1 kHz and 10 kHz offset frequencies are also displayed, i.e. for easy comparison with Fig. 3.56. See Appendix H for the **MATLAB** implementation.

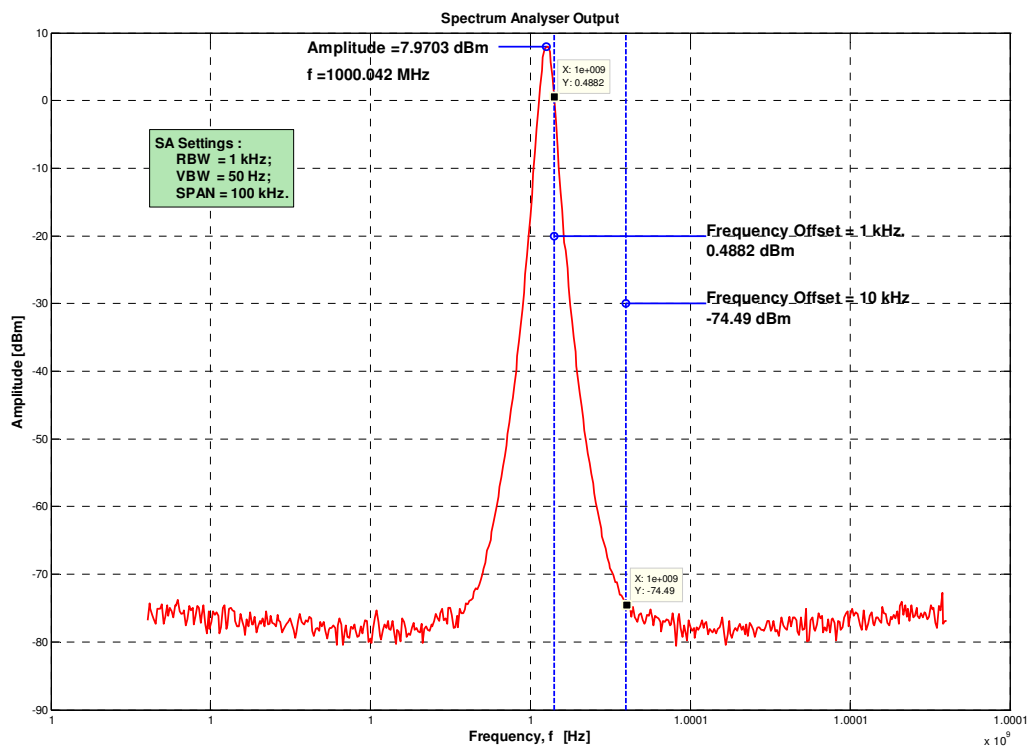


Figure 3.55: Spectrum Analyser Output, illustrating the offset frequencies.

See the following section for the single-sideband phase noise representation of Fig. 3.55.

Single-sideband Phase Noise Representation

The data for the following plot was calculated from the SA measurement in Fig. 3.55. It was implemented in **MATLAB** in order to obtain the data for the SSB phase noise relative to the carrier. The latter is illustrated in Fig. 3.56.

In Fig. 3.56, for the offset frequencies below 1 kHz the curve tends to flatten. This occurs, because the measurement was done with the SA set to a Resolution Bandwidth (RBW) of exactly 1 kHz. Thus, for measurements made at offset frequencies less than the RBW, a loss in accuracy is evident. The solution to this problem would be to minimise the RBW to for instance 1 Hz (ideal). But this will increase the measurement time tremendously. A 1 Hz BW is chosen since the SSB phase noise relative to the carrier is specified in dBc, measured in a 1 Hz BW.

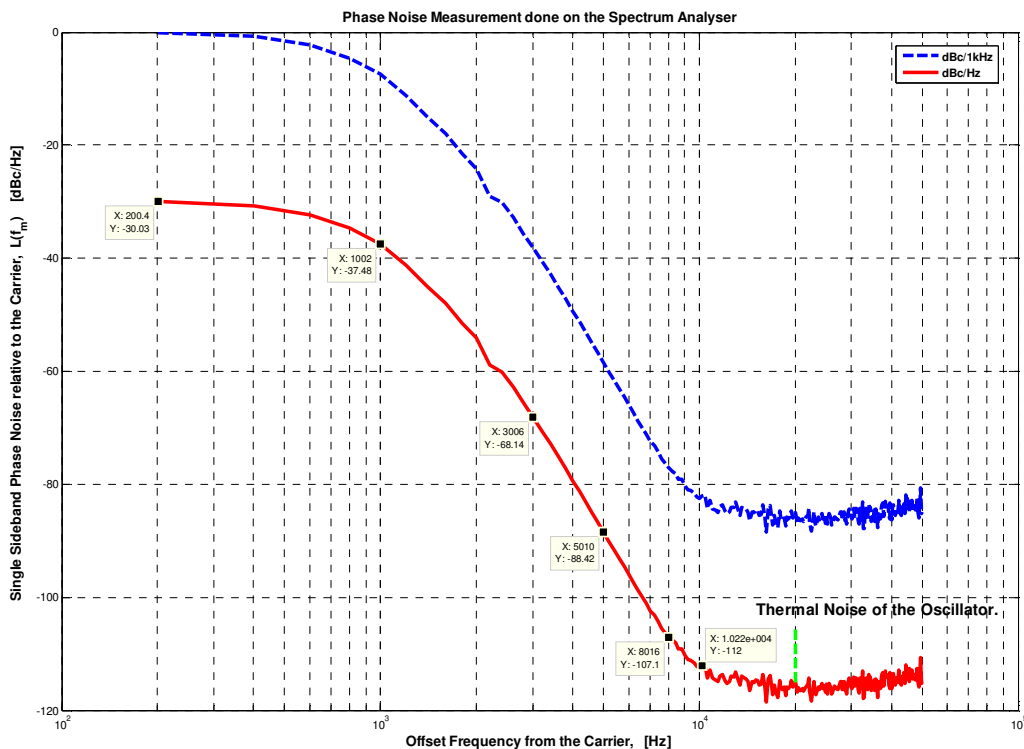


Figure 3.56: Illustration of the SSB phase noise of the measurement in Fig. 3.55.

The SA has a built-in function to measure the SSB phase noise. The latter was utilised to confirm the previous measurement and calculations. In the following table the calculated SSB phase noise (illustrated in Fig. 3.56) is compared to that measured by the SA SSB phase noise function. In Fig. 3.56 the relevant offset frequencies are marked for easy reference between the table and the figure.

Table 3.15: Compared SSB Phase Noise values.

Offset Frequency f_m , [kHz]	SSB Phase Noise relative to the Carrier [dBc/Hz]	
	Calculated	Measured
1	-37.48	-42.10
3	-68.14	-68.65
5	-88.42	-86.20
8	-107.1	-105.15
10	-112.5	-113.60
15	-114.6	-115.80
30	-114.2	-114.30

From Table 3.15 it is clear that the calculated- and measured values for the single-sideband phase noise, coincides.

▪ Oscillator Noise Floor Measurement

Since the SSB phase noise values at the offset frequencies are plotted *relative* to the carrier, it was thought a good idea to filter out the carrier and thereby establish a setup to measure *only* the noise floor of the oscillator. The setup is illustrated in Fig. 3.57.

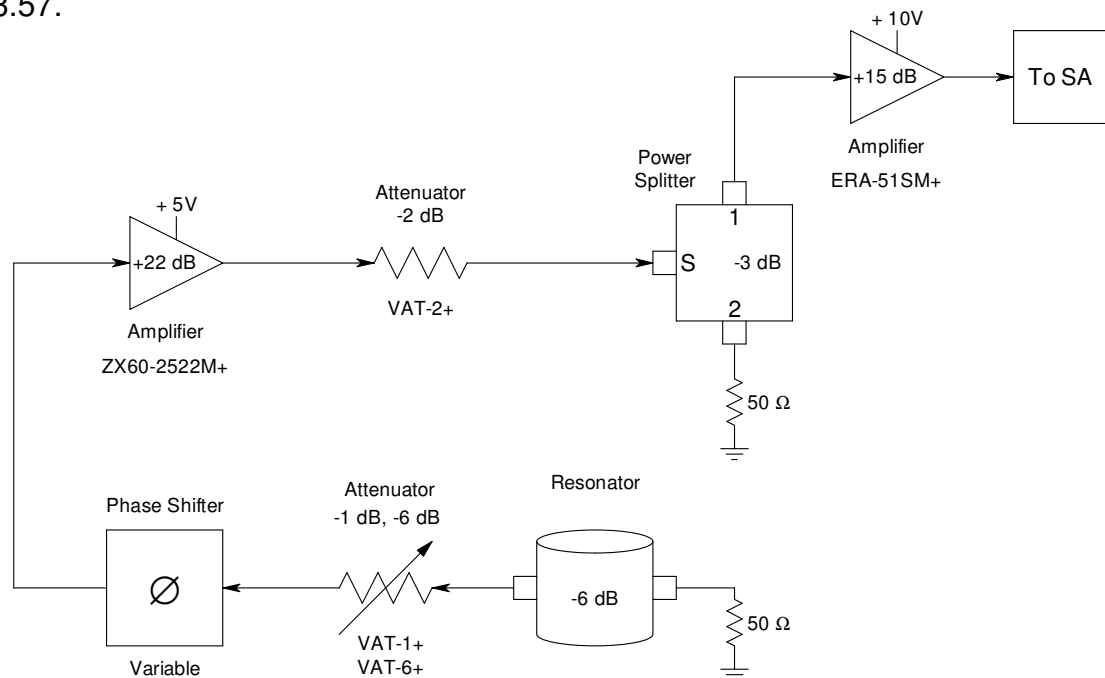


Figure 3.57: Block diagram of the setup to measure the oscillator noise floor.

The second amplifier used in the open-loop, was the **ERA-51SM+**. The latter is a *Mini-Circuits* manufactured, monolithic amplifier. That is an integrated circuit (IC) device operating in the microwave frequencies. See Appendix **H** for its datasheet. The following figure illustrates its measured S-parameters.

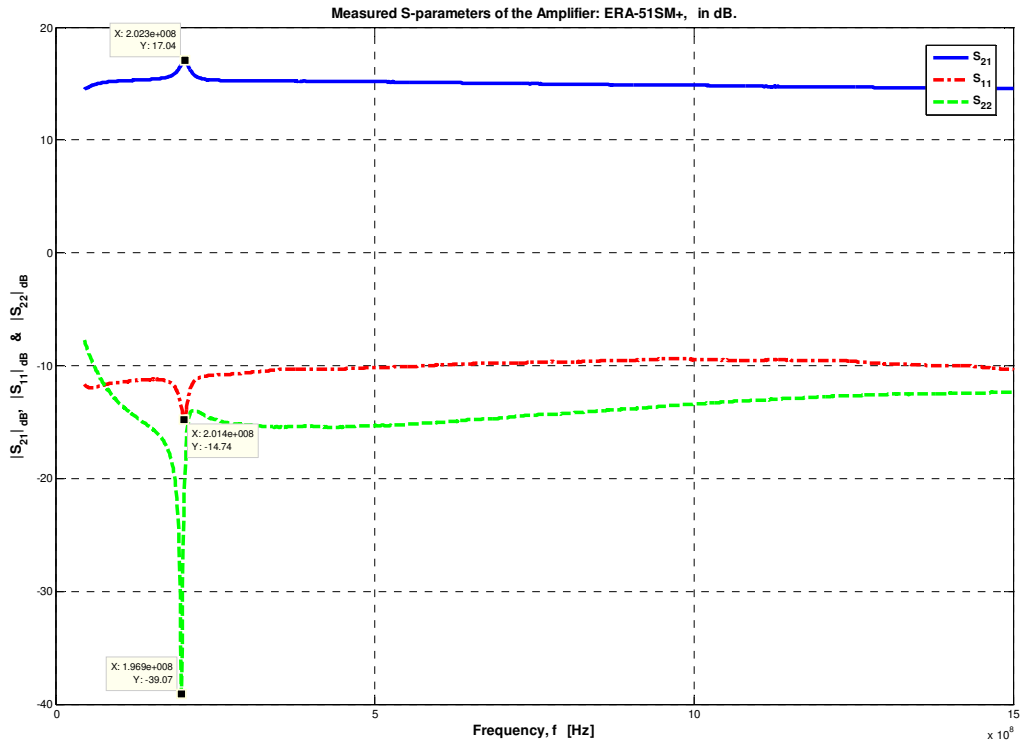


Figure 3.58: Measured S-parameters of the ERA-51SM+.

Subsequently, the elements were connected as demonstrated in Fig. 3.57 (block diagram) and the following measurements were taken on the SA.

In Fig. 3.59 only the red plot was measured on the SA, the rest were calculated from the former. The SA was set to a RBW of 1 kHz. As mentioned in previous theory (Chapter 2), the SSB phase noise is specified in a 1 Hz BW. As a result $10\log(1 \times 10^3) = 30$ dB has to be subtracted from the measured plot, resulting in the pink plot which represents the measurement made in a 1 Hz BW. Furthermore, the gain and noise figure of the output amplifier (ERA-51SM+) are subtracted as well, providing the measured oscillator noise floor in [dBm/Hz]. Lastly the carrier amplitude is subtracted, ending in the measured oscillator noise floor specified in [dBc/Hz] that is relative to the carrier.

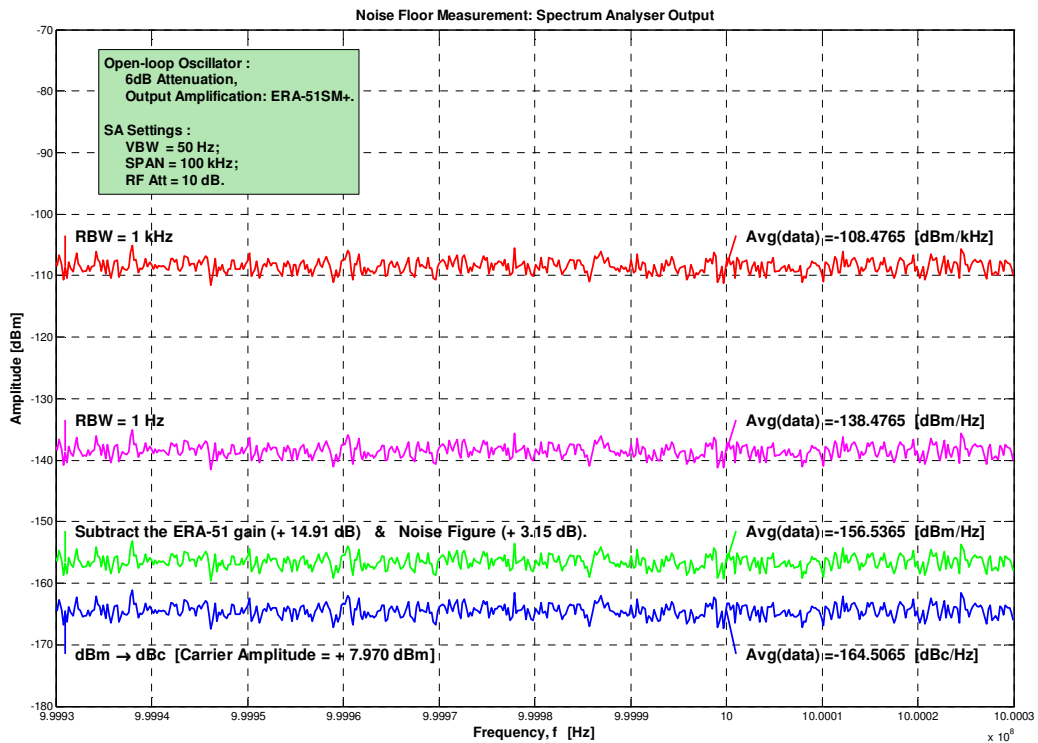


Figure 3.59: SA Oscillator Noise Floor Measurement.

This results in an oscillator noise floor of -164.51 dBc/Hz. This value is high in relation to the theoretical predicted value of Section 3.5.1. The suggested reason for this is that the noise floor of the SA is too high to accurately perform this measurement. In the *Rohde & Schwarz FSEx Spectrum Analysers* brochure it specifies that the FSEK30 SA used in this project, displays an average noise floor of -138 , -140 dBm typical in the 10 MHz to 3.5/6 GHz frequency range. The specifications extracted from the brochure are added in Appendix I.

As a conclusion to the results obtained above, the decision to make use of the ***Aeroflex PN9000B Phase Noise Measurement System*** was confirmed. In doing this, a more accurate measurement of the SSB phase noise of the oscillator system would be attained.

3.5.2.2 PN9000B – Automatic Phase Noise Test System

The Aeroflex PN9000 is an Automatic Phase Noise Test System. It is simple, fast and covers a wide frequency range, from 2 MHz to 140 GHz. Measurements of any kind of frequency source are possible, e.g. Crystal Oscillators, Synthesizers, VCO's, DRO's etc. This is possible due to the systems versatile modular architecture. Some of the built-in modules are the 'Reference Phase Locking Method', 'Delay Line Method', 'Ultra Low Noise Reference Synthesizer' and 'MW, mmW down-converters'.

▪ Theory of Operation (*Reference Phase Locking Method*)

By making use of a quadrature-locked low-noise reference signal, the *phase fluctuations of the source under test* are being *demodulated* by the PN9000B system. See the following block diagram of the PN9000 system.

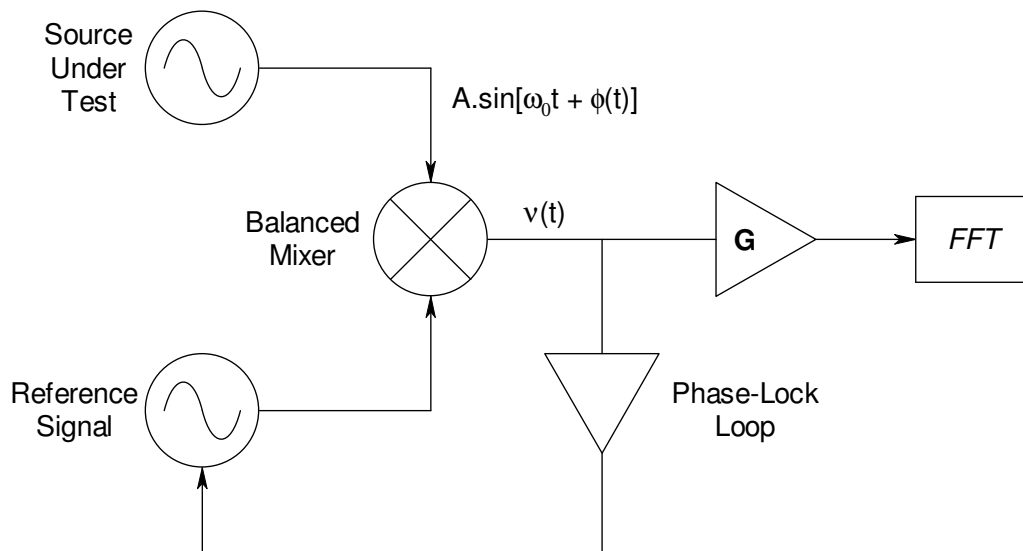


Figure 3.60: Simplified block diagram of the PN9000B system.

As part of the system a balanced mixer is present. The mixer operates by comparing the phase of the *source under test* to that of the *low-noise reference signal*. The output of the mixer is a signal which consists of the time representation of the phase fluctuations of the source:

$$v(t) = K[\phi(t) - \phi_{ref}(t)] \quad (3.67)$$

where

K = defines the 0 dBc reference of the phase noise spectrum. It is the demodulation factor of the mixer in volts/radian.

$\phi(t)$ = the phase noise of the source to be measured.

$\phi_{ref}(t)$ = the phase noise of the reference signal.

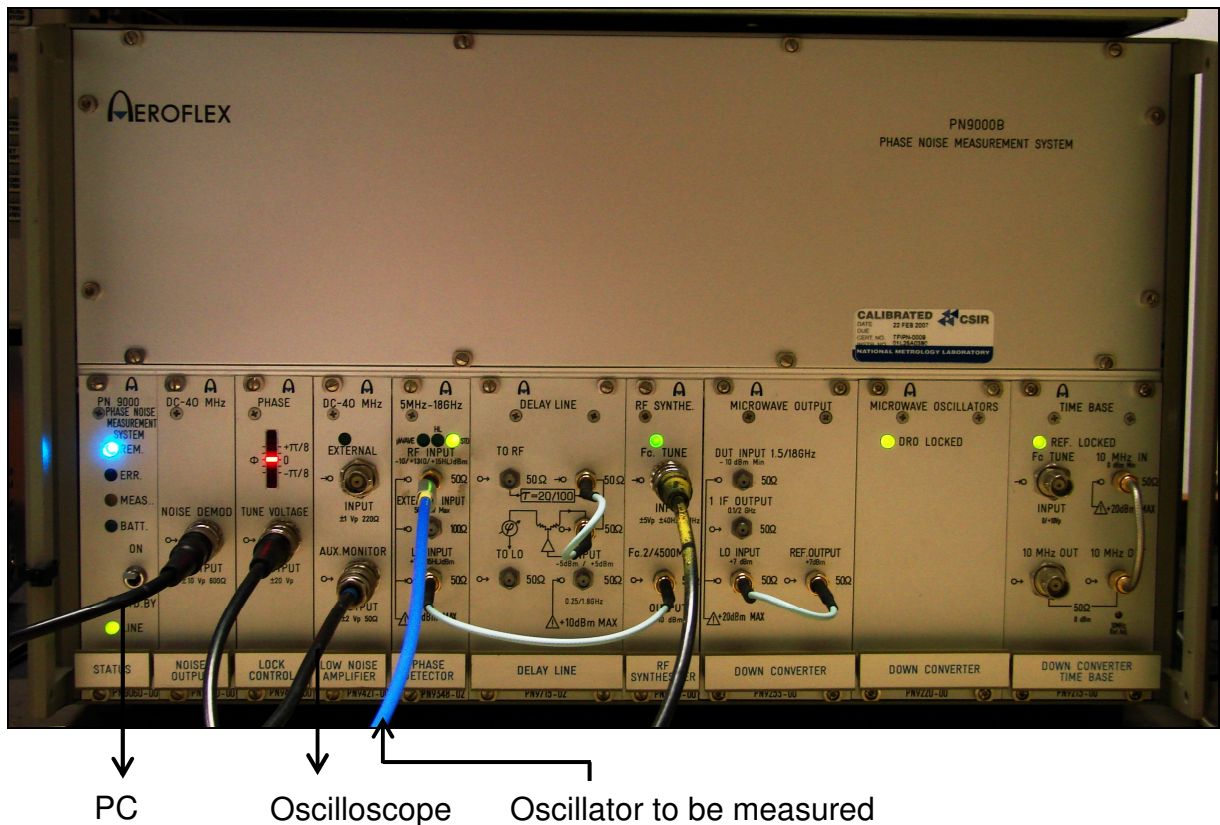


Figure 3.61: Photograph of the Aeroflex Phase Noise Measurement System.

The photograph of the PN9000B system, shown in Fig. 3.61, was taken during one of the phase noise measurements of the oscillator system (SUT). Upon zooming in on the photograph, the different modules are clearly visible. For instance, the third module from the left is the 'PHASE Lock Control' module and shows the phase difference between the SUT and the reference signal. In this case the light indicates that $\phi = 0$, signifying that the reference source is locked on the SUT. The reference signal in Fig. 3.60 is represented by the 'RF Synthesizer' module, fourth from the right. It is directly connected to the previously mentioned 'PHASE Lock Control' module, as suggested by the block diagram in Fig. 3.60, which completes the Phase-Lock Loop (PLL). The demodulated noise output is then connected to the PC for baseband analysis.

Another important feature of this system is that it allows measurement on a frequency drifting source. The latter is possible due to proportional and integral gain included in the phase locked loop. All necessary parameters are programmable by means of the PC interface. All of these parameters are automatically verified by the system to ensure self consistency.

- **Setup for the Oscillator Phase Noise Measurement**

The PN9000 reference manual provides an extensive description of exactly how to connect the device to be measured and the necessary cabling for the system itself. Included in Appendix J, are the relevant pages taken from the manual [35].

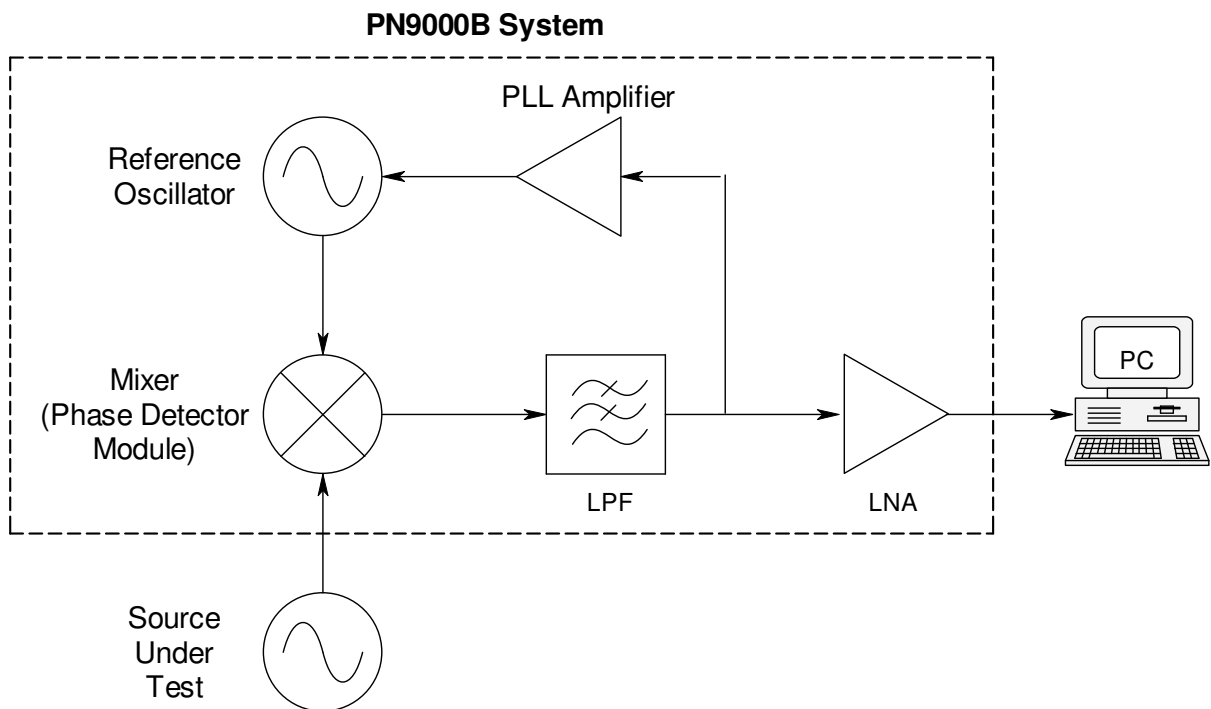


Figure 3.62: Block diagram of the Oscillator measurement setup in Fig.3.61.

In Fig. 3.62 the block diagram of the photograph shown in Fig. 3.61 is illustrated. Both of these figures demonstrate the oscillator measurement setup, as made when the oscillator was measured. In the following section, a brief discussion is given on the exact parameters that need to be set before the measurement can take place.

When using the Aeroflex Phase Noise Measurement System in *Manual* mode, there are some parameters that need to be set before the measurement can take place. After the cabling is done and the source under test is connected, the following, very briefly discussed, list of steps need to be taken.

1. **Settings:** Specline – indication of the residual phase noise of the system. See Appendix J for the table of SSB Noise (dBc/Hz) – FM Range 1.
2. **Method:** PLL SYNTH or VCO (but in this case, it is PLL SYNTH).
3. **Config:** Internal VXCO (use an external VXCO if the phase noise of the SUT is lower than that of the system). When measuring a VCO, choose 'Delay Line' as an option.
Set the frequency range, f_{range} to cover that of the SUT.
4. **Measurement:** Auto or Manual. With the latter the operator has the opportunity of controlling the measurement setup. In Auto, the system takes care of everything.
5. **Manual:** (Complete the following settings.)
 - a. Turn the Synthesizer on with RF ON.
 - b. Set the Synthesizer frequency.
 - c. Check it – check the SUT frequency, and set the reference close to the latter.
 - d. Choose FM1
 - e. Measure IF frequency
 - f. Approach frequency
 - g. Type: High-Level if possible, since it provides a better resolution.
 - h. Detection Mode: Normal.
 - i. RF Gain: 0 dB
 - j. LO Gain: 0 dB
 - i. j. } Increasing these might increase the internal amplifier- and oscillator noise as well.
 - k. Measure K_{phi} , Measure.
 - l. Lock Bandwidth: Default.
 - m. Close Loop...

Only click on Measure when the red LEDs stop flickering and LOCK ON is established. Minor changes might have to be made to the settings to obtain lock on.

In the following section the phase noise measurements are illustrated.

- Measured Results

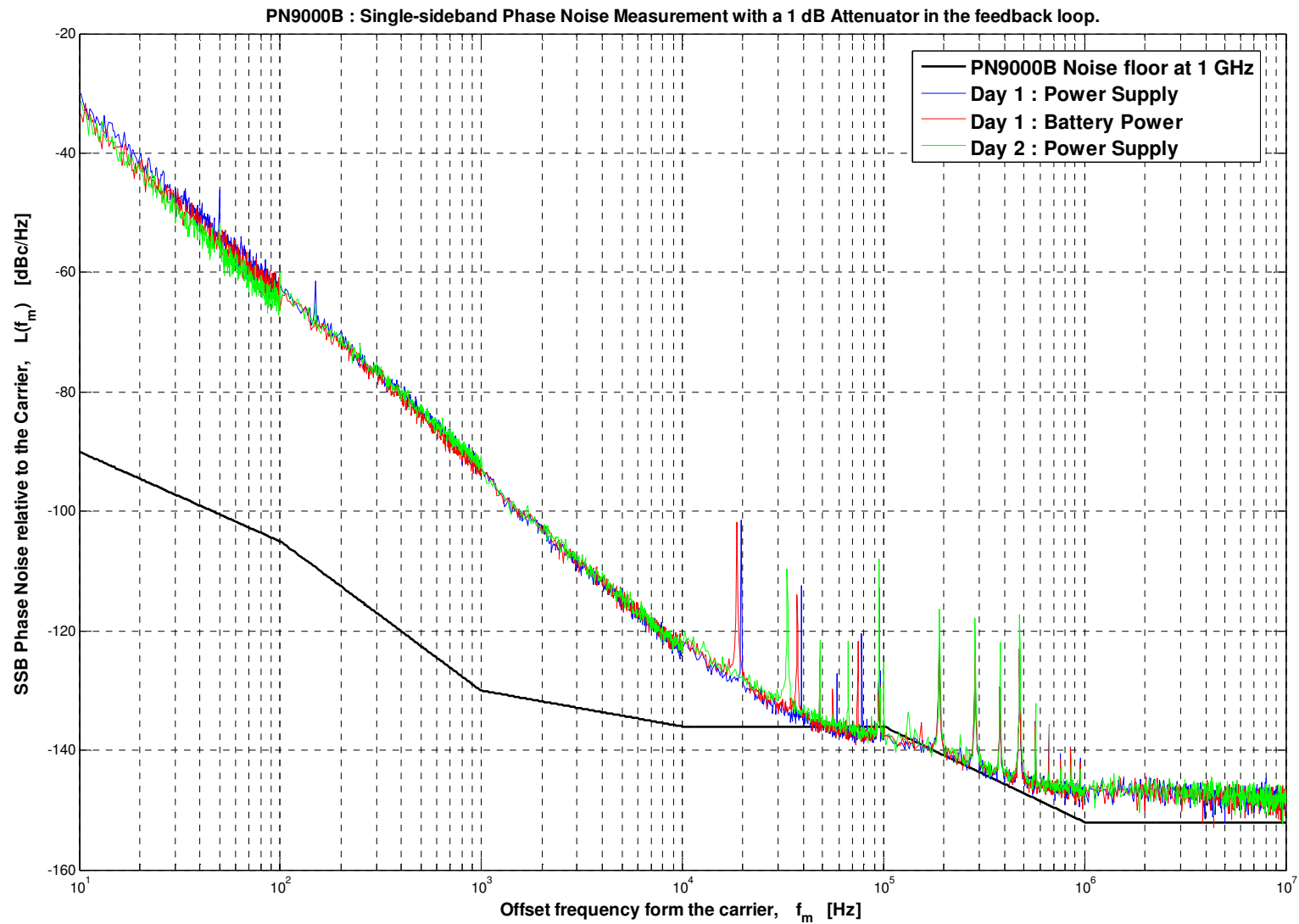


Figure 3.63: Measured SSB Phase Noise of the Oscillator, comparing the effect of a 5V power supply to that of a 5V battery.

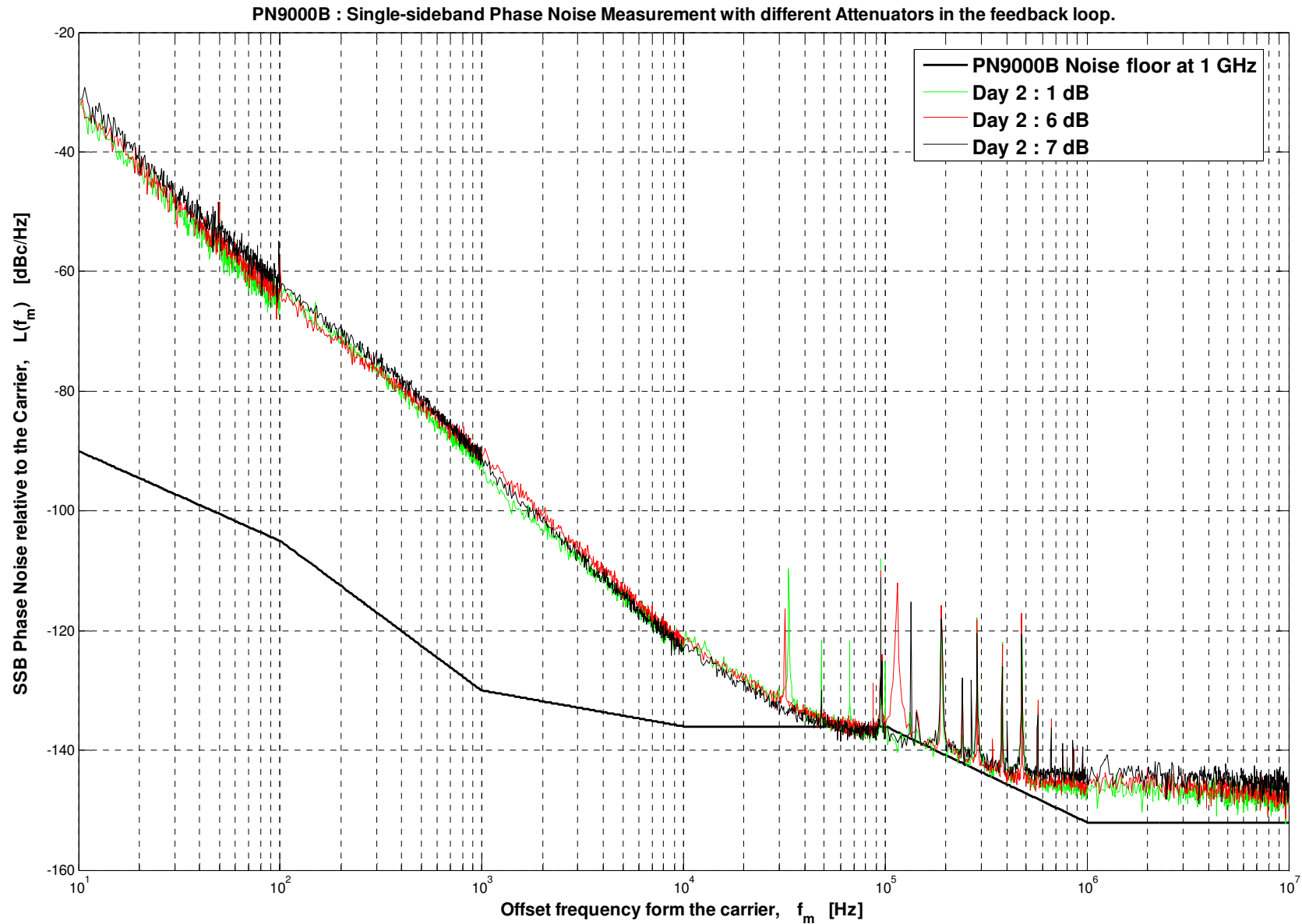


Figure 3.64: Measured SSB Phase Noise of the Oscillator, comparing the effect of different attenuators in the feedback loop.

In Fig. 3.63 the SSB phase noise of the oscillator was measured with a 1 dB attenuator in the feedback loop. The effect of a 5V power supply to that of a 5V battery was compared. From the plot it is clear that no substantial difference between the battery operated and the power supply measurements exist. The only visible difference is that for frequencies close to the carrier. While the battery operated measurement shows no spurs, the power supply measurements for both days depict spurs at the same frequency instances (i.e. at 50 Hz and at 150 Hz, offset). This only means that the battery operated system tend to bring about a smoother phase noise measurement.

In Fig. 3.64 the SSB phase noise of the oscillator was measured with different attenuators in the feedback loop respectively. As mentioned in an earlier section 3.3.2, discussing Attenuators, the input power P_{in} to the amplifier will decrease as the attenuation in the feedback loop increases. This results in a linearly operating amplifier if the feedback attenuation is big enough. Consequently, the amplifiers noise contribution is minimised. However, according to Leeson's phase noise model, the bigger P_{in} is the lower the phase noise. Therefore one could make the statement that, the smaller the feedback attenuation is the lower one would expect the measured phase noise to be. This is indeed the case. Recall from Fig. 3.64, that for all offset frequencies less than 10 kHz from the carrier, the phase noise is the lowest for the 1 dB attenuation in the feedback loop. At about 40 kHz offset frequency, the effect of the residual noise floor of the phase noise meter becomes evident, causing unreliable measurement results for all offset frequencies above 40 kHz. The same applies to the results in Fig. 3.63.

In the following Fig. 3.65 the theoretical predicted oscillator phase noise is plot against the measured result. The figure is discussed on the page following Fig. 3.65.

See Appendix **K** for the implementation of the PN9000B measured data in **MATLAB**.

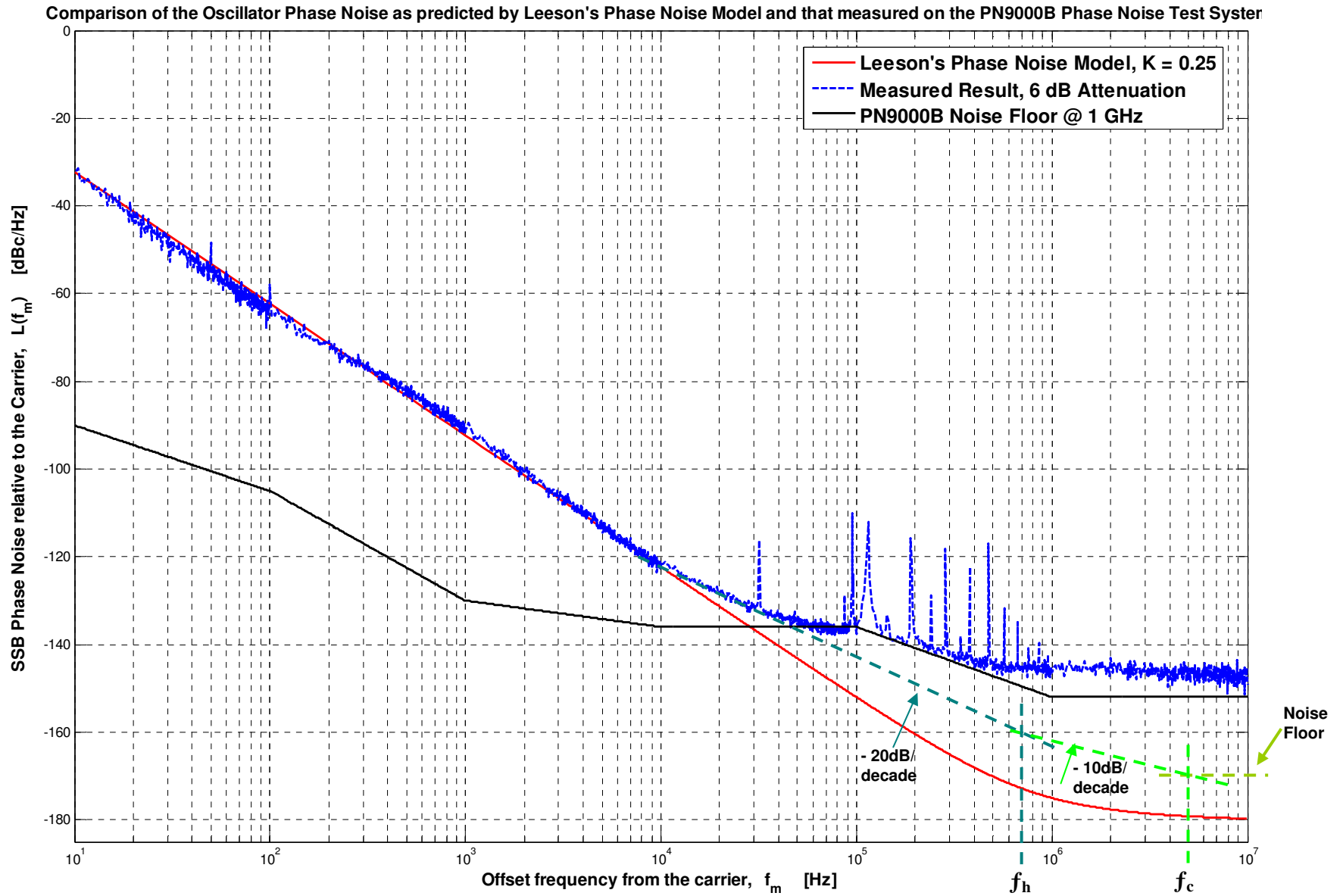


Figure 3.65: Comparison of the Oscillator Phase Noise as predicted by Leeson's Phase Noise Model to that measured on the PN9000B Phase Noise Test System.

In Fig. 3.65, the measured result shown is for the case in which a 6 dB attenuator was present in the feedback loop. The same could have been done for any of the other attenuator values. From the equation for Leeson's phase noise model (p. 144), the constant K represents the strength of the $1/f$ noise present in the system. In this case, K is set to a value of 0.25 to match the measured result.

In comparing the measured results to that of Leeson's theoretical prediction (p. 146), a truly good resemblance is evident. For example, consider the measured result illustrated in Fig. 3.65 (the same applies to that in Fig. 3.63 and Fig. 3.64). For all offset frequencies less than 10 kHz the measurement portray a decrease in noise power of -30 dB/decade.

The same holds true for the theoretical predicted plot, with the only difference that in this case, the decrease in noise power is apparent for all offset frequencies less than 200 kHz. Between 200 kHz and 2 MHz Leeson's model suggest that the noise power decrease by -20 dB/decade, before it reach the thermal noise floor of -177.22 dBm at the 10 MHz offset frequency.

On the other hand, the measured plot starts to illustrate a -20 dB/decade decrease from the 10 kHz offset frequency and on. But then the residual noise floor of the PN9000B measurement system becomes dominant, causing all of the measurements done at offset frequencies greater than 40 kHz to be unreliable.

The residual phase noise of the Phase Detector present in the PN9000B system is an indication of how low the phase noise can be that the measurement system is able to measure. That is for that specific frequency range. The synthesizer, which serves as the local oscillator (reference signal) to the measurement, is the decisive factor in the ultimate noise of the meter. For example, in this project it became known that the phase noise of the designed oscillator is lower than what either the SA or the PN9000B can measure, especially at frequencies far from the carrier. Therefore another external reference oscillator is needed, one with a phase noise lower than that of the internal reference oscillator of the PN9000B. A good example of such an oscillator would be an identical replica to the one designed in this project.

This completes the design and measurements of the oscillator system. In the following chapter, the VCO system is described in detail.

CHAPTER 4

SYSTEM: VOLTAGE CONTROLLED OSCILLATOR

Provided is a brief explanation of what to expect from chapter 4: In chapter 4 the *VCO system* is described. Firstly, the use of variable tuning diodes is discussed. For example, what diodes to use and how many diodes would be sufficient. The diode section also includes all the necessary design theory involved in obtaining the optimum point to connect the varactor diodes inside the resonator. All necessary measurement results for the VCO system are shown. Phase noise measurements of the VCO, made on the Aeroflex PN9000B Phase Noise Test System are also included. The chapter ends by discussing several *CST* simulations done on the resonator.



Figure 4.1: Photograph of the Voltage Controlled Oscillator System as a whole.

4.1 VARIABLE TUNING DIODES

As mentioned in chapter 2, the phase noise of a VCO is primarily determined by the overall Q of the circuit, which includes (1) the Q-factor of the resonator, and (2) the Q-factor of the varactor diode used. Since the goal of this project is to bring about

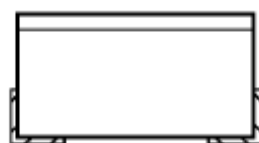
the design of a low phase noise oscillator and as a result a low phase noise voltage controlled oscillator, it is important to keep the overall Q-value of the system as high as possible. As shown in chapter 3, one of the techniques applied to achieve the latter was to design a high Q-value resonator. Adding variable tuning diodes to the resonator will undoubtedly cause a decrease in the current Q-value. Therefore, by keeping this in mind, the search began for varactor diodes signifying 'high-Q tuning performance'.

4.1.1 What Diodes were used?

The varactor diodes that were decided on for use in this project were from the MA46H Series, manufactured by M/A-COM. The MA46H Series represents surface mount GaAs tuning varactors, which are low cost and have very high quality factors. To be more specific, the diode chosen to use was the **MA46H201**. The latter is of the MA46H200 through MA46H206 family, which has hyperabrupt junctions with constant gamma of 1.25 from 2 to 20 volts and a higher quality factor than some of the other families. It also has the largest capacitance ratio (C_{max}/C_{min}) of all the families, and is well suited for VCOs where the optimum combination of a wide tuning range and a high quality factor is required. See Appendix L for the datasheets.

Take note that the Q-value given in the datasheet is specified at 50 MHz. This design was done at a frequency of 1 GHz, which means that the Q-value of the diode will approximately be $(50/1000) = 1/20^{\text{th}}$ smaller than that specified in the datasheet.

The case style that was chosen is shown below in Fig. 4.2. To its right is a photograph of the **MA46H201** varactor diode, with its bypass capacitor.



1056

(a)



(b)

Figure 4.2: (a) Case Style and (b) photograph of the MA46H201 Varactor Diode.

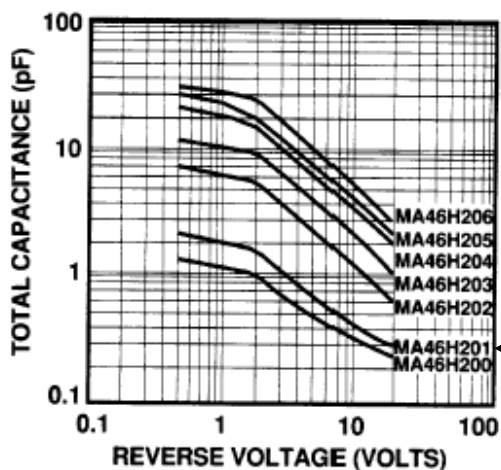


Figure 4.3: C_{Tot} vs. $V_{Reverse}$.

In Fig. 4.3, the total capacitance of the diode, vs. the reverse voltage is shown. The diode of concern is the MA46H201, second from the bottom.

It has a capacitance ratio of 3.3, with the capacitance range from 1.0 pF to 0.3 pF. The reverse voltage is tuned from 3 V (1 pF setting) to 22 V (0.3 pF setting).

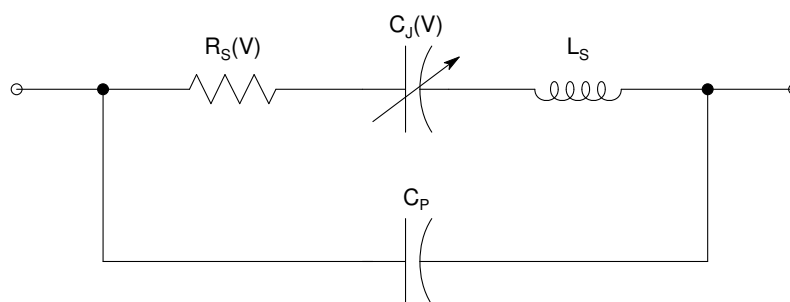


Figure 4.4: Equivalent Circuit for the packaged Tuning Varactor.

The series resistance illustrated in Fig. 4.4 is calculated as follows:

$$\begin{aligned}
 r_s &= \frac{1}{Q_{50\text{ MHz}} \cdot 2\pi \cdot f_{50\text{ MHz}} \cdot C_D} \\
 &= \frac{1}{(3000) \cdot (2\pi) \cdot (50 \times 10^6) \cdot (1 \times 10^{-12})} \\
 &= 1.061 \Omega.
 \end{aligned}$$

The case parasitics (C_p and L_s) for case style 1056, are given (in the datasheet) as:

$$C_p = 0.15 \text{ pF (typical)} \pm 0.02 \text{ pF (tolerance)}$$

$$L_s = 0.45 \text{ nH (typical)}.$$

For any other details, please see Appendix L for the datasheet.

4.1.2 How many Diodes would be sufficient?

The aim of this paragraph is to confirm the amount of diodes sufficient to obtain the maximum tuning bandwidth, while at the same time preventing the designed Q-value to decrease below the chosen limit of 1000.

The effect of the varactor diodes on the Q-value of the resonator, as well as the tuning bandwidth (Δf) obtained for that specific setting, was investigated. The investigation included the coupling of the diodes at different positions (L) along line 2 of the resonator, as illustrated in Fig. 4.5.

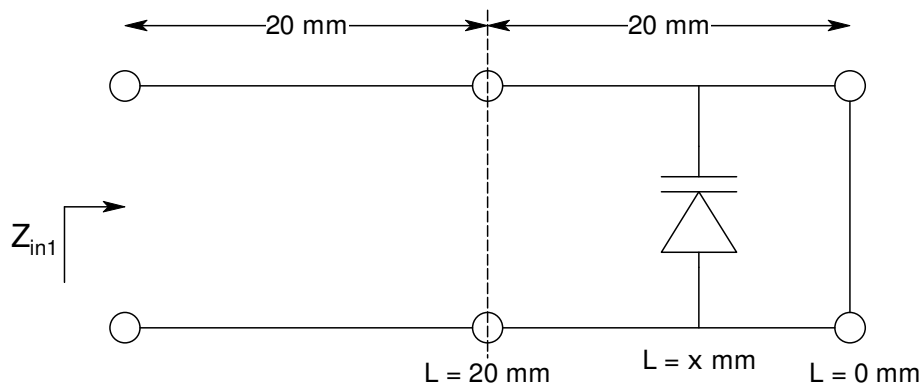
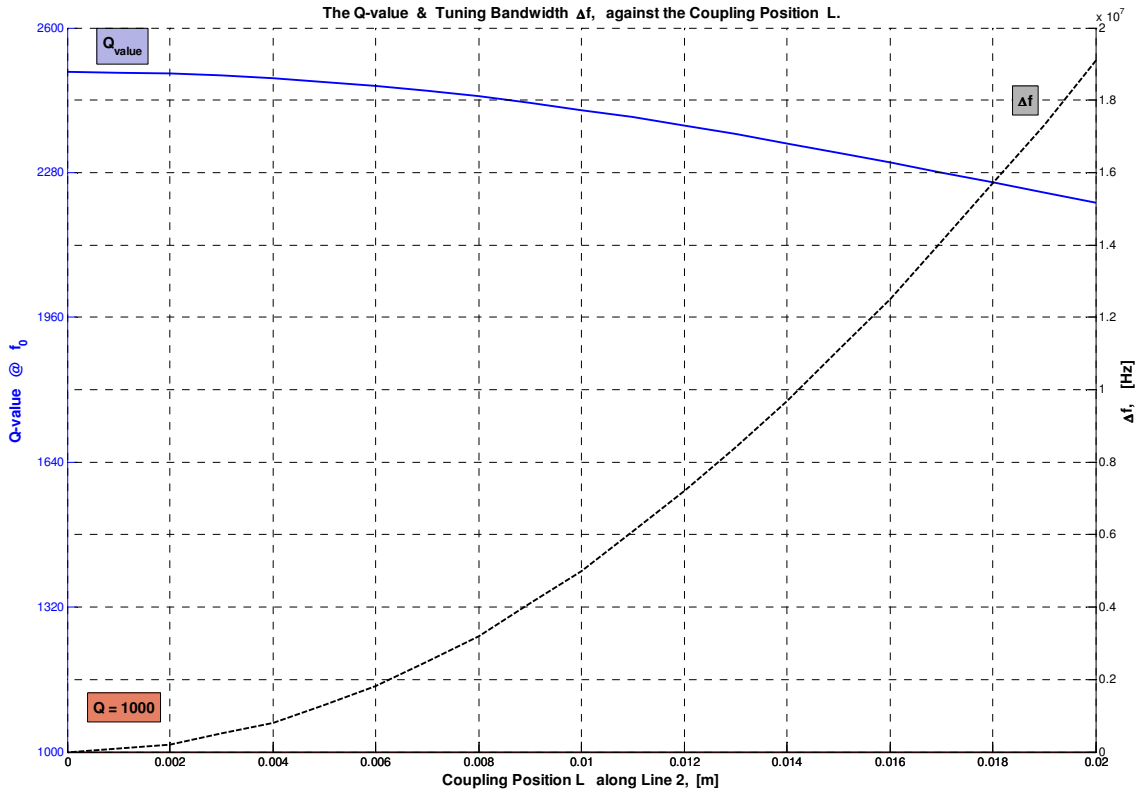


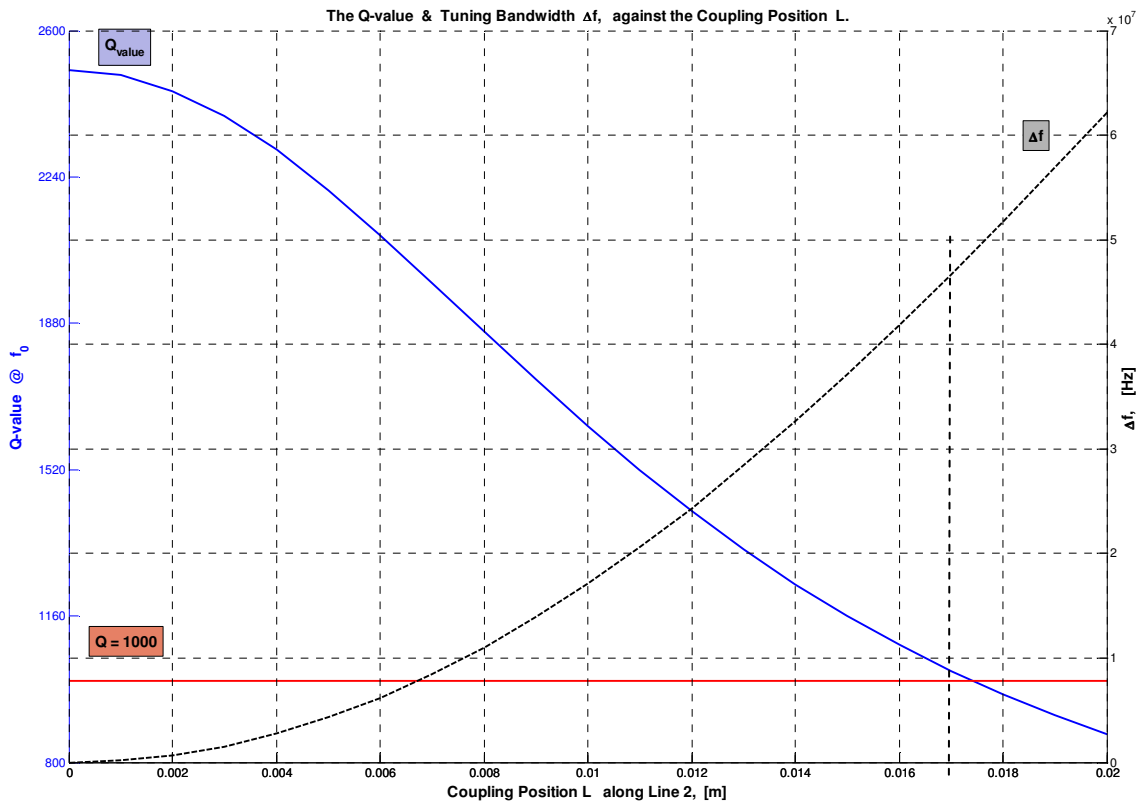
Figure 4.5: Transmission line representation of the resonator, showing the coupling of the varactor diodes along line 2.

In the following figures the effect of several diodes in parallel is illustrated. Figure (a) shows the diode at its minimum setting (0.3 pF), and for figure (b) it was set to its maximum (1.0 pF).

In Fig 4.6 only one diode is coupled to the resonator showing the effect of its minimum and maximum settings. In Fig. 4.7 two diodes are connected, and in Fig. 4.8 a total of four diodes. When studying the latter figures, two y-axes are visible. The y-axis to the left represents the change in the Q-value as the diodes are coupled at different positions along line 2, and the y-axis to the right represents the tuning bandwidth (Δf) obtained when coupling the diodes at different positions of L . The x-axis represents the different coupling positions (L) in steps of 1 mm.

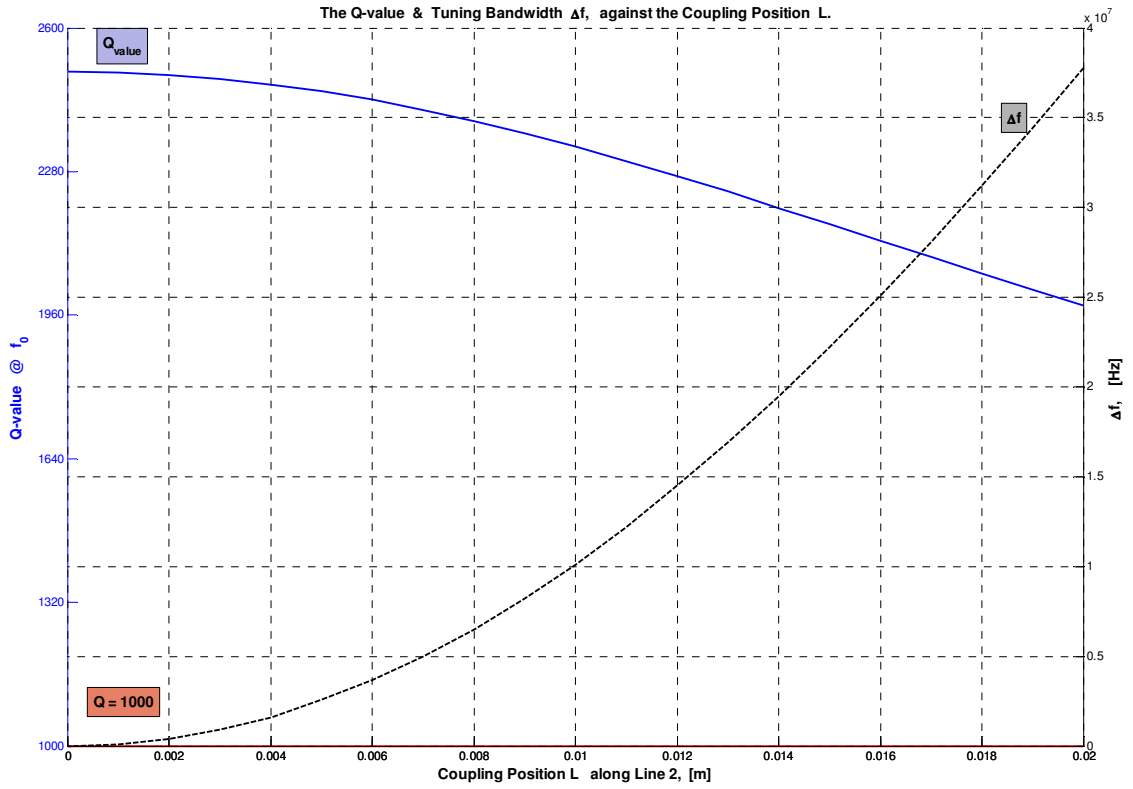


(a). Connect: (1 x 0.3pF) Varactor Diode

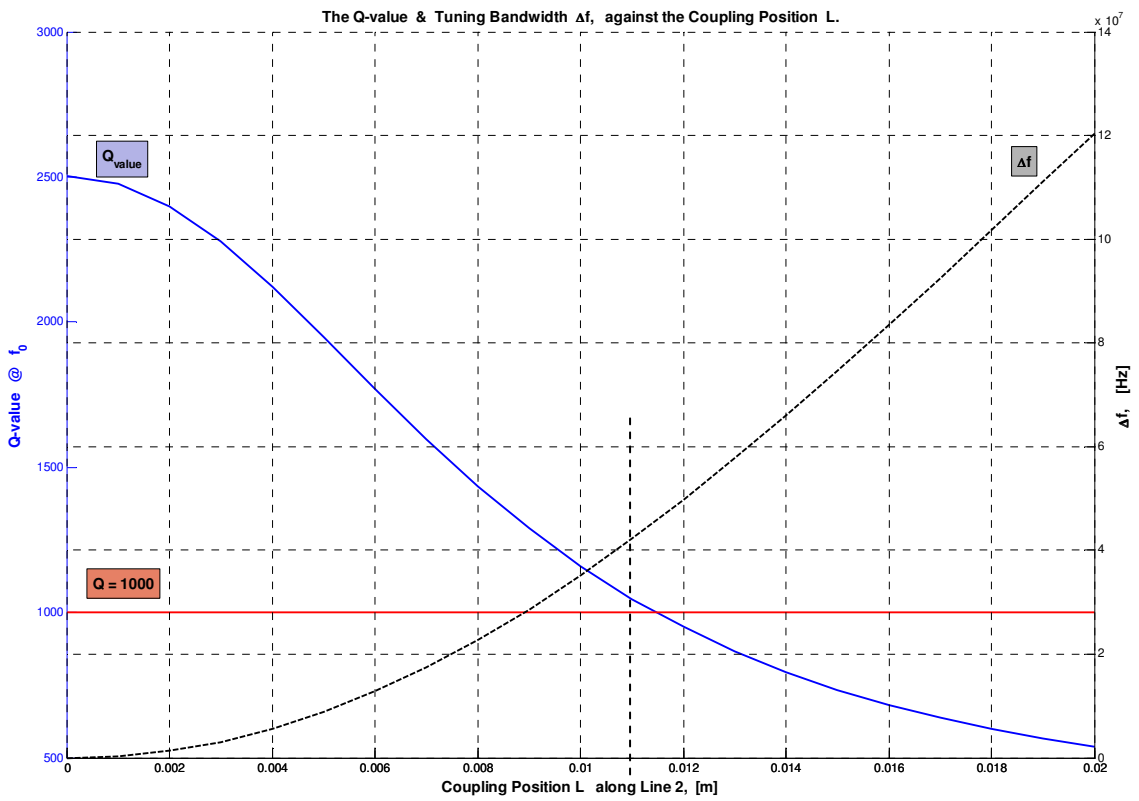


(b). Connect: (1 x 1pF) Varactor Diode

Figure 4.6: Q-value and Δf against the coupling position L, for 1 diode connected.

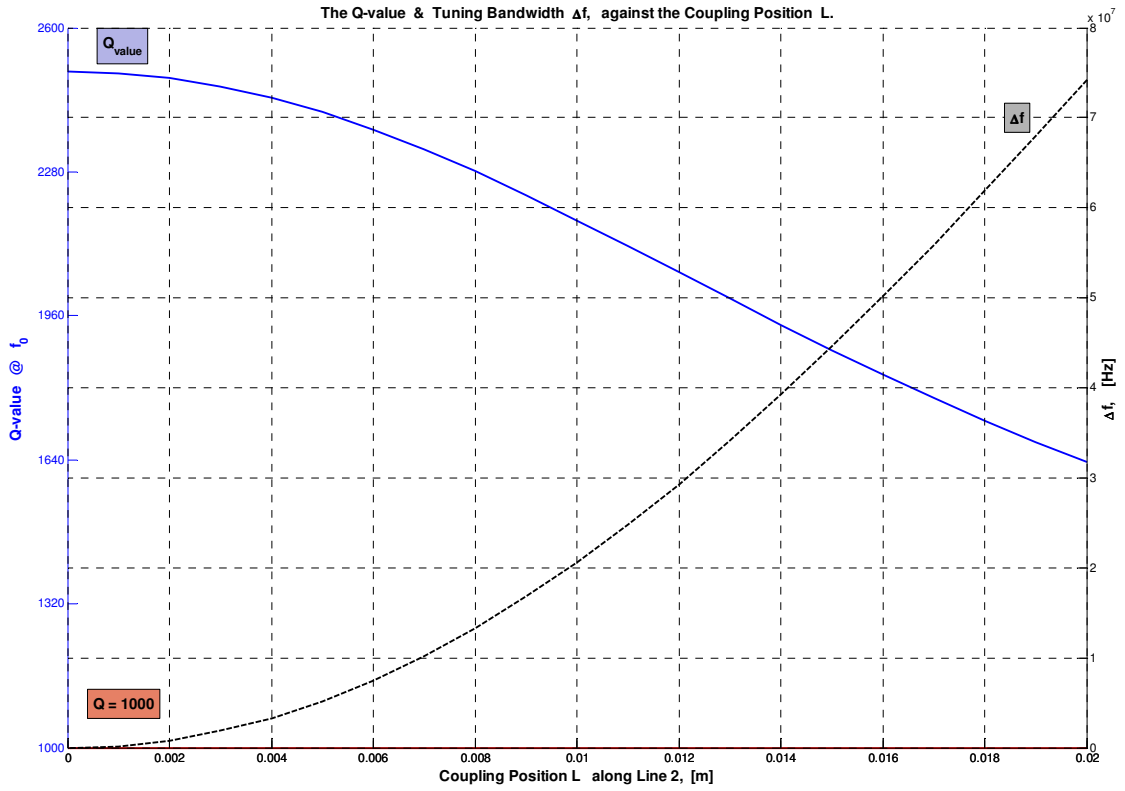


(a). Connect: (2 x 0.3pF) Varactor Diodes

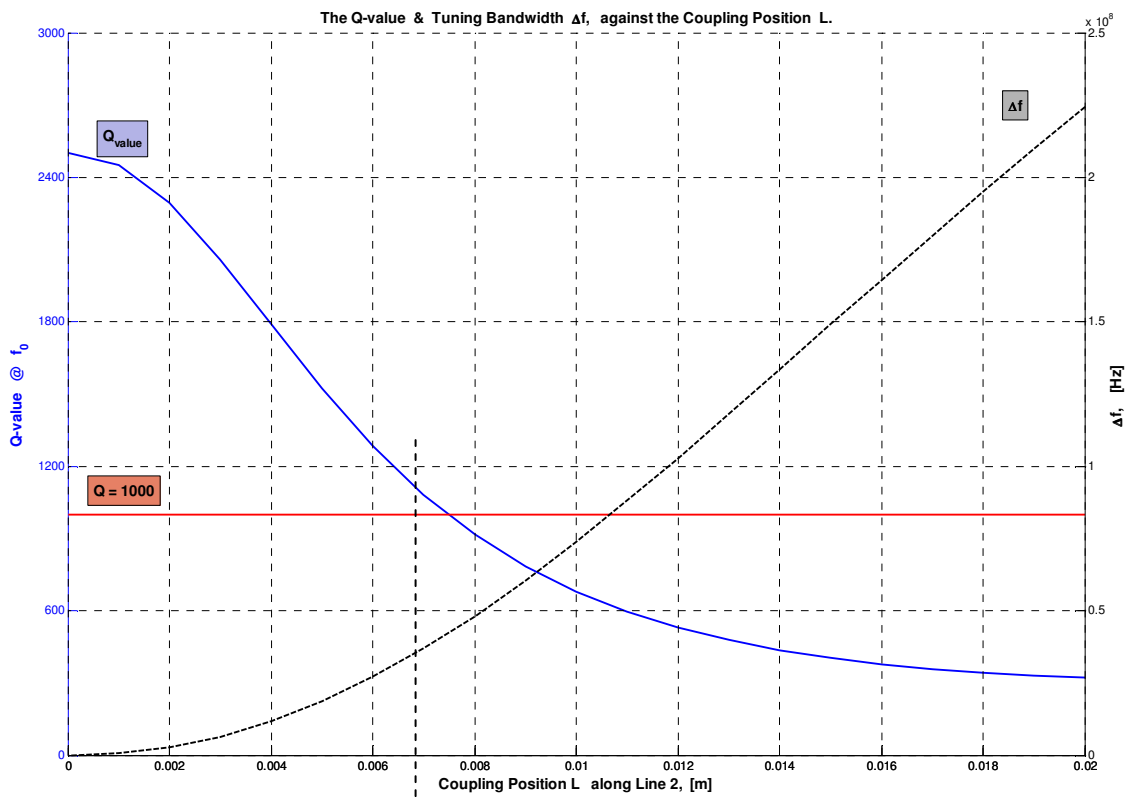


(b). Connect: (2 x 1pF) Varactor Diodes

Figure 4.7: Q-value and Δf against the coupling position L, for 2 diodes connected.



(a). Connect: (4 x 0.3pF) Varactor Diodes



(b). Connect: (4 x 1pF) Varactor Diodes

Figure 4.8: Q-value and Δf against the coupling position L, for 4 diodes connected.

After studying Fig. 4.6 to Fig. 4.8, it was decided to make use of four varactor diodes due to the following reasons:

Table 4.1: Proposed Q-value and Δf for different number of diodes coupled.

# Diodes Coupled 1pF Setting	Coupling position, L [mm]	Proposed Q-value (> 1000)	Tuning Bandwidth, Δf [MHz]
0	0	2502	0
1	17	1025	46.7
2	11	1047	42.2
4	7	1082	36.9

It is important to keep in mind, that the voltage along line 2 decreases from $L = 20$ mm to the short-circuit end, $L = 0$ mm. Therefore, should one couple the diodes at a voltage half the value of the previous one, one would have to couple double the amount of diodes, to get the same effect. But, then you have the advantage of getting more power into the resonator, which means that more power is being dissipated inside the resonator. As a result, the phase noise floor will be less, while at the same time the signal-to-noise ratio (SNR) will increase [23].

Thus, by coupling four diodes at $L = 7$ mm, firstly one is coupling at a lower line voltage, secondly P_{in} is higher and lastly the Q-value is still greater than 1000.

4.1.3 Where these Diodes should be connected?

In this section the most suitable position to connect the diodes is concluded. This specific location is determined through considerably detailed transmission line theory, where the loaded Q-value, the tuning bandwidth and the amount of power dissipated inside the resonator, are measured against each other.

The overall Q-value of the resonator and the varactor diodes was calculated by means of the susceptance slope parameter (discussed in Chapter 3 and Appendix B), as follows:

$$Q = \frac{b_n}{G_{in}} \quad (4.1)$$

with

$$b_n = \frac{\omega_0}{2} \cdot \left. \frac{dB_{in}}{d\omega} \right|_{\omega_0} = \text{the susceptance slope parameter}$$

B_{in} = the input susceptance of the resonator, in [S]

G_{in} = the input conductance of the resonator, in [S].

The power dissipated inside the resonator is calculated by the following equation:

$$P_{in} = V_{in}^2 \cdot G_{in} \quad (4.2)$$

with

P_{in} = the dissipated power inside the resonator, in [W]

V_{in} = the applied voltage to the input of the resonator, in [V].

The tuning bandwidth (Δf), which is different for every number of diodes coupled, was calculated as follows:

$$\Delta f = \left| f_{(\text{resonant, for current diode coupling})} - f_{(\text{resonant, with no diodes coupled})} \right| \quad (4.3)$$

with

$f_{(\text{resonant, for current diode coupling})}$ = that frequency where Z_{in1} is at its maximum

$f_{(\text{resonant, with no diodes coupled})}$ = that frequency when no diodes are coupled ($=f_0$).

Something to keep in mind before the relevant figures are shown, is that since the practical measurements for the Q-value did not agree with that which was predicted by theory and simulation, the theoretical values had to be adjusted to match the practical values. This was necessary, to accurately determine the coupling position of the varactor diodes along line 2 of the resonator. Recall Table 3.12 (p.130):

	Unloaded Q-value Q_U	Loaded Q-value Q_L
Simulated	2133.7	1668.2
Measured	1427.9	713.71

Consequently a new limit was set for the minimum Q-value, which was $Q_L / 2 \approx 350$.

In the previous section it was decided to make use of four varactor diodes, therefore the calculations illustrated in Fig. 4.9 and Fig. 4.10 are all done for four diodes coupled along line 2 of the resonator, calculated at frequency f_0 .

In Fig. 4.9 on the next page, there are again two y-axes present. The y-axis to the left represents the Q-value of the system at the resonant frequency, f_0 . The y-axis to the right represents the tuning bandwidth (Δf) obtained with four varactor diodes. The x-axis represents the coupling positions (L), incremented in 1 mm sections.

Considering the different curves present in Fig. 4.9 – the subscripts are as follows, indicating different factors taken into account:

- R : **R**esonator
- D : Varactor **D**iodes
- C : SMA **C**onnectors.

Therefore, the first plot labelled **Theoretical $Q_{R\&D}$** represents the Q-value predicted by theory ((4.1) on p.169) and simulation (**CST**). The latter takes into account the Q-value of the resonator and how it changes as the varactor diodes are coupled at different positions along line 2.

The second plot labelled **Tailored $Q_{R\&D}$** represents the ‘new’ Q-value predicted by theory and simulation. This result is obtained from the latter theoretical plot, which was modified to agree with the measured results.

The third plot labelled **Loaded $Q_{R\&D\&C}$** represents the loaded quality factor of the system, which is equal to a half of the **Tailored $Q_{R\&D}$** plot.

The fourth plot demonstrates the **limit** set to the loaded Q-value; it is labelled **Min.Limit, $Q_{R\&D\&C} \geq 350$** . It is selected as about half of the Loaded $Q_{R\&D\&C}$ of the system.

Lastly the plot for the tuning bandwidth is labelled **Δf** . It represents the variation in frequency obtained when 4 diodes are connected at various coupling positions along line 2 of the resonator. It was calculated by (4.3) on p.169.

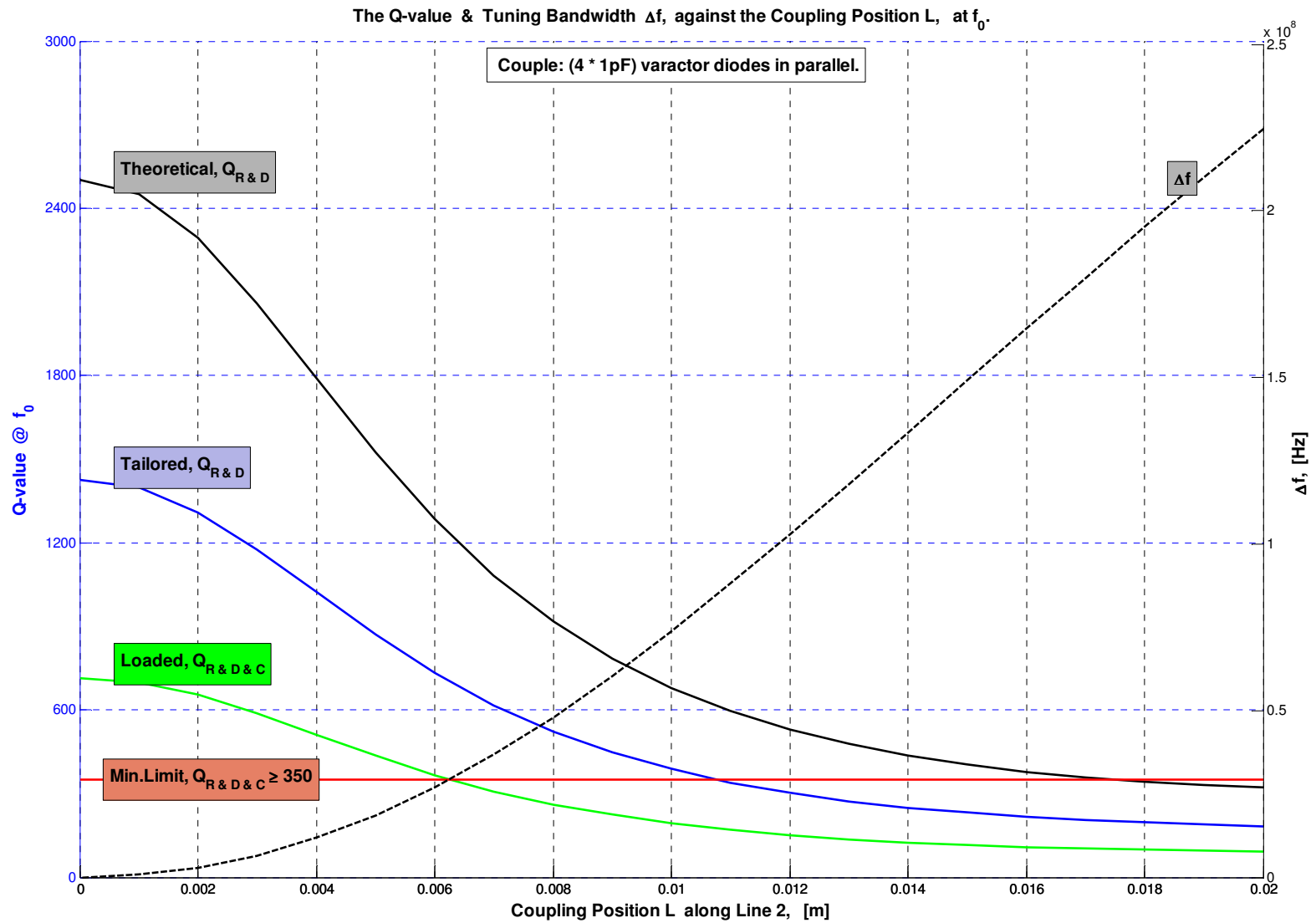


Figure 4.9: The Q-value and Tuning Bandwidth Δf , against the coupling position L, at f_0 .

Table 4.2: Q-values when no diodes are coupled. Taken from Fig. 4.9, p.171.

Parameter @ L = 0 mm	Value	Description
Theoretical - $Q_{R\&D}$	= 2502.6	= Q_U , of the unloaded resonator
Tailored - $Q_{R\&D}$	= 1427.4	= Q_U , VNA measurement, p. 169
Loaded - $Q_{R\&D\&C}$	= 713.7	= Q_L , VNA measurement, p. 169
Min.Limit - $Q_{R\&D\&C}$	≥ 350	Chosen

Take note from Fig. 4.9 that, because the measured Q-value is so much lower than what was expected (Table 3.12, p.130), the total tuning bandwidth that could have been reached is greatly decreased. According to Fig. 4.9, the highest possible coupling position L, that could be reached before the loaded Q-value drops below the chosen limit, is just higher than L = 6 mm.

In Fig. 4.10 following on the next page, the power dissipated in the resonator, taking the effect of the coupled diodes into consideration, is illustrated. The plot is labelled **$P_{\text{dissipated}}$, [dBm]**. These values were calculated with (4.2) on p. 169. The latter represents the power dissipated inside the resonator when the line voltage, $V_{\text{line}2} = 4$ V, across the diodes. It is important to keep in mind, that as one vary the input voltage (V_{in}) to the resonator, the voltage along line 2 ($V_{\text{line}2}$) will vary as well. Therefore, for every coupling position (L) a different V_{in} is required to maintain a voltage of 4V across the diodes, at that specific L. The latter are illustrated in Fig. 4.11 to Fig. 4.14 appearing on p. 175, 176.

Consequently from figures 4.9 and 4.10, it is clear that the closer the diodes are coupled to the short circuit (SC) end of line 2, the less influence it has on the overall Q-value. That is because most of the power is dissipated in the resonator itself, and very little in the diodes. The tuning bandwidth (Δf) is then also smaller. Since the line voltage declines towards the SC end (for a constant V_{in}), the voltage across the diodes (V_{diodes}) will also decrease, unless a greater V_{in} is applied to maintain $V_{\text{diodes}} = 4$ V. Should the diodes be coupled closer to the L = 20 mm end of line 2, the diodes will start to dominate as most of the power gets dissipated in them. Consequently the resonator is heavily loaded causing the Q-value to drop tremendously. But, then Δf is at its maximum.

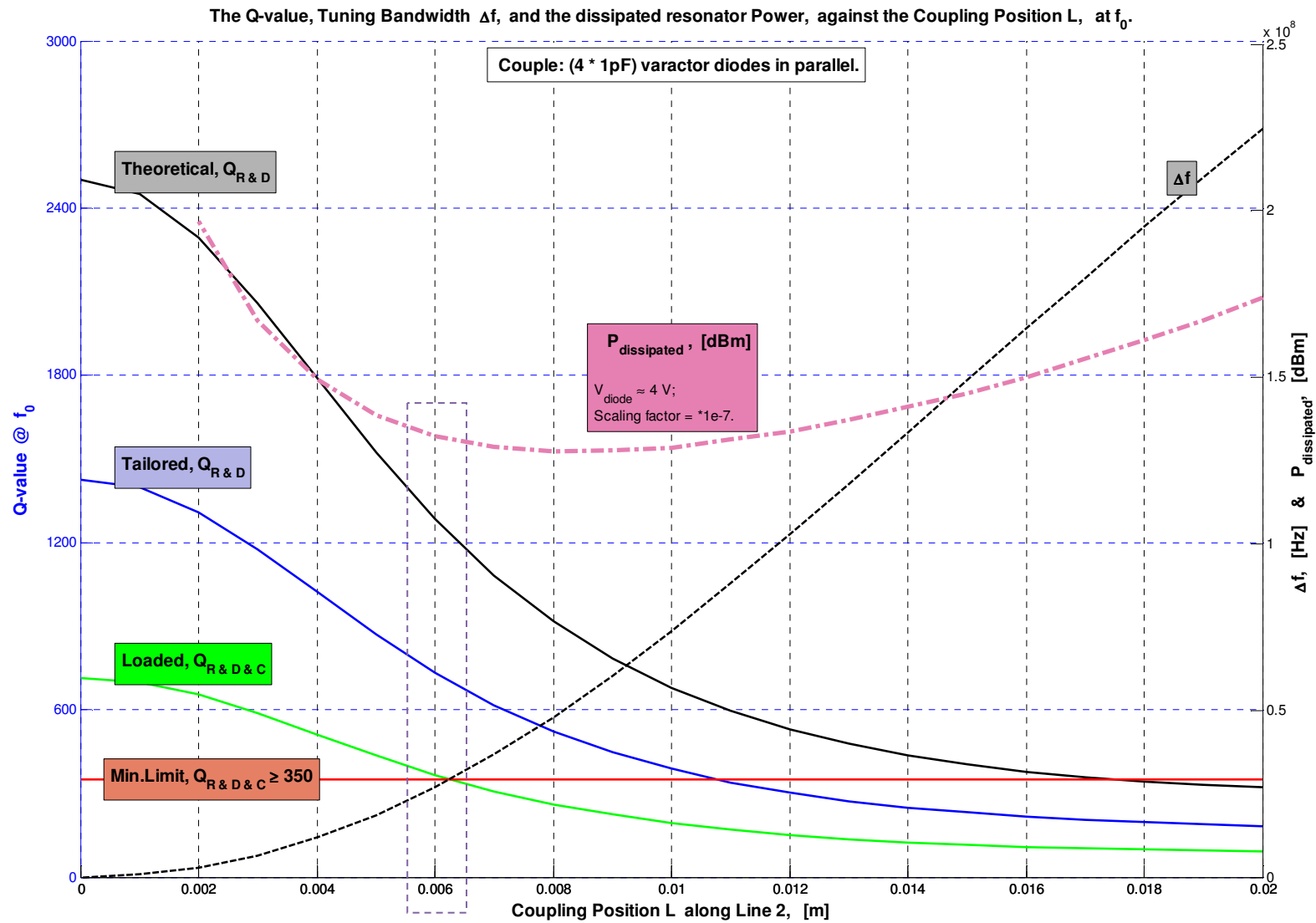


Figure 4.10: The Q-value and Tuning Bandwidth Δf , against the coupling position L, at f_0 .

In Fig. 4.10 the curve labelled $P_{\text{dissipated}}$, [dBm] reaches two maximum and one minimum point. For the diodes coupled at $L = 20$ mm they are dominant as most of the power gets dissipated inside the varactors. Consequently the Q-value is at its minimum, while Δf portrays a maximum. In the case that the diodes are coupled at $L = 2$ mm, they have little influence and most of the power gets dissipated in the resonator itself, leaving the Q-value at a maximum and consequently Δf at its minimum. At about $L = 8$ mm the dissipated power reaches its minimum, concluding that a balance is reached between the power dissipated inside the varactor diodes and the resonator itself. From Fig. 4.10 it was decided to connect the diodes at $L = 6$ mm.

Table 4.3: Summary of the expected (calculated) values for the VCO system.

Parameter @ $L = 6$ mm	Expected Value
Tailored, $Q_{R\&D}$ ($= Q_U$)	≈ 750
Loaded, $Q_{R\&D\&C}$ ($= Q_L$)	≈ 370
Tuning BW, Δf	≈ 27 MHz
$P_{\text{dissipated}}$	$\approx (1.323e8 \cdot 1e-7) = 13.22$ dBm

The latter results are compared to those measured, and reported on in the section called *Measurements and Results* (page 186).

In the following figures (Fig. 4.11 – Fig. 4.14), the dissipated power ($P_{\text{dissipated}}$) and the calculated voltage along line 2 (V_{line2}) of the resonator are illustrated against the input voltage (V_{in}) to the resonator, and the coupling position (L), respectively.

In Fig. 4.11, $P_{\text{dissipated}}$ are plotted against V_{in} . For example, follow the curve for coupling position $L = 10$ mm. Take note that as the input voltage increases that the power dissipated inside the resonator increases quadratic.

In Fig. 4.12, V_{line2} are plotted against V_{in} . For example, follow the curve for coupling position $L = 4$ mm. Take note that as the input voltage increases that the line voltage also increases (linearly) for that specific coupling position.

$P_{\text{dissipated}}$ against L are illustrated in Fig. 4.13. Take note from this figure, that for the diodes coupled at $L = 0$ mm, and $V_{\text{in}} = 17$ V, the dissipated power is 3.964 mW ≈ 4 mW = 6 dBm. The latter is equal to what the resonator is designed for when no diodes are coupled.

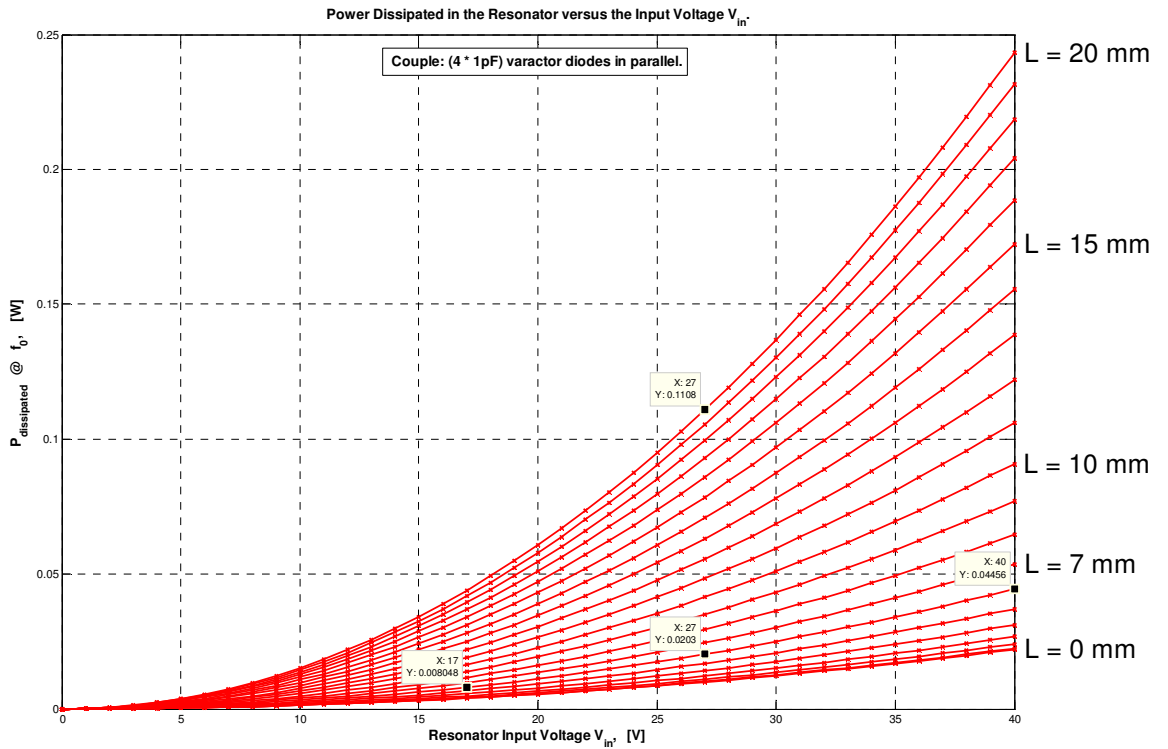


Figure 4.11: Power dissipated in the Resonator versus the input Voltage, V_{in} .

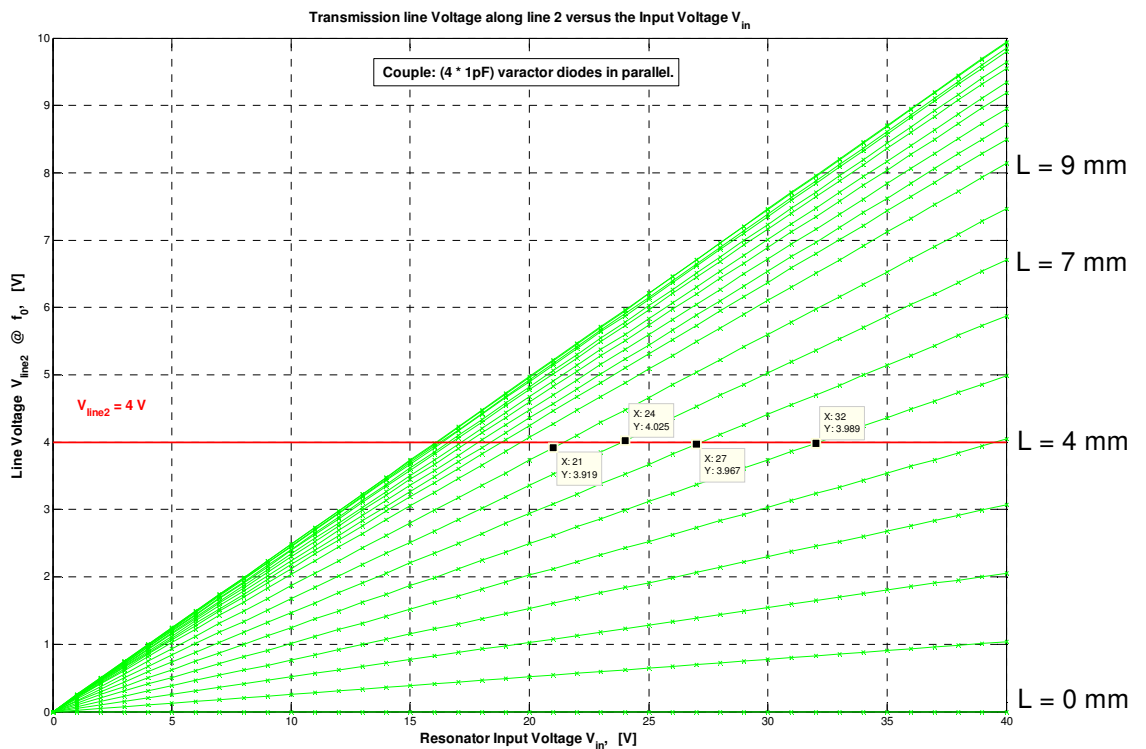


Figure 4.12: Line Voltage, V_{line2} versus the resonator input Voltage, V_{in} .

Finally in Fig. 4.14 the calculated voltage along line 2 (V_{line2}) are plotted against the coupling position L . From this plot it is clear to see how the line voltage differs at the different coupling positions. Follow for example the plot for $V_{in} = 20$ V

(constant). Take note how the line voltage increases from $L = 0$ mm, reaches a maximum (peak of the wave) and then decrease again. The latter is representative of the standing wave present on the line [10].

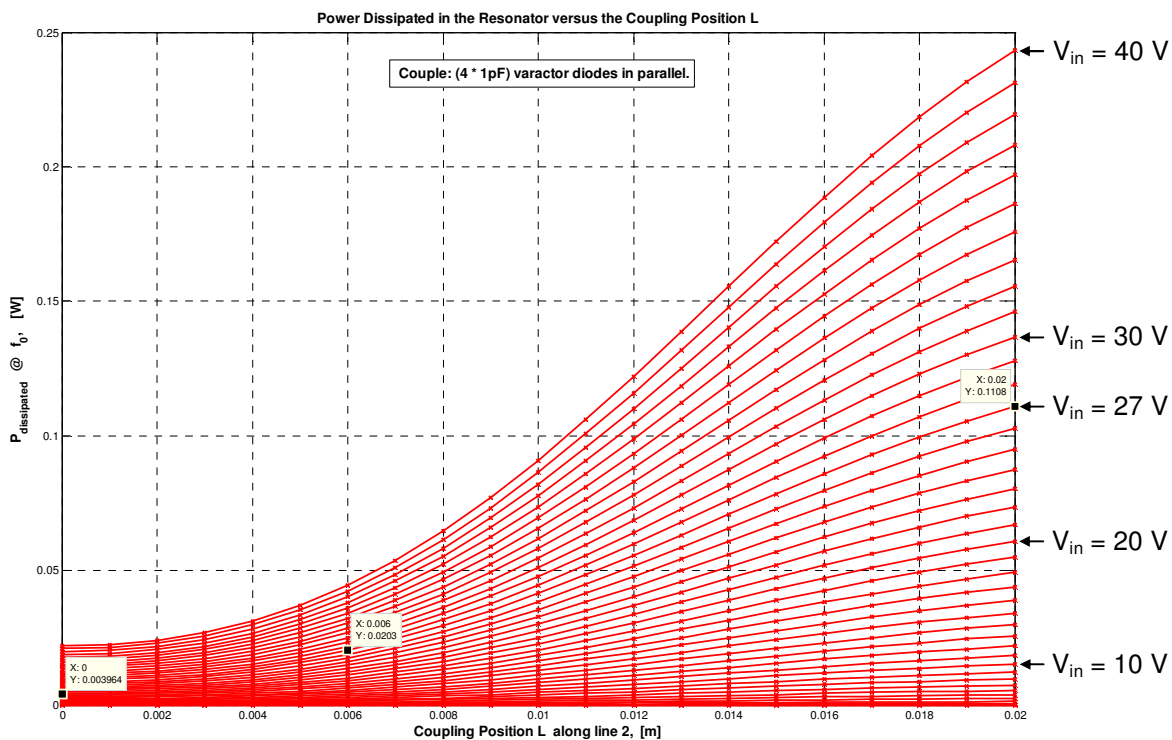


Figure 4.13: Power dissipated in the Resonator versus the Coupling position, L.

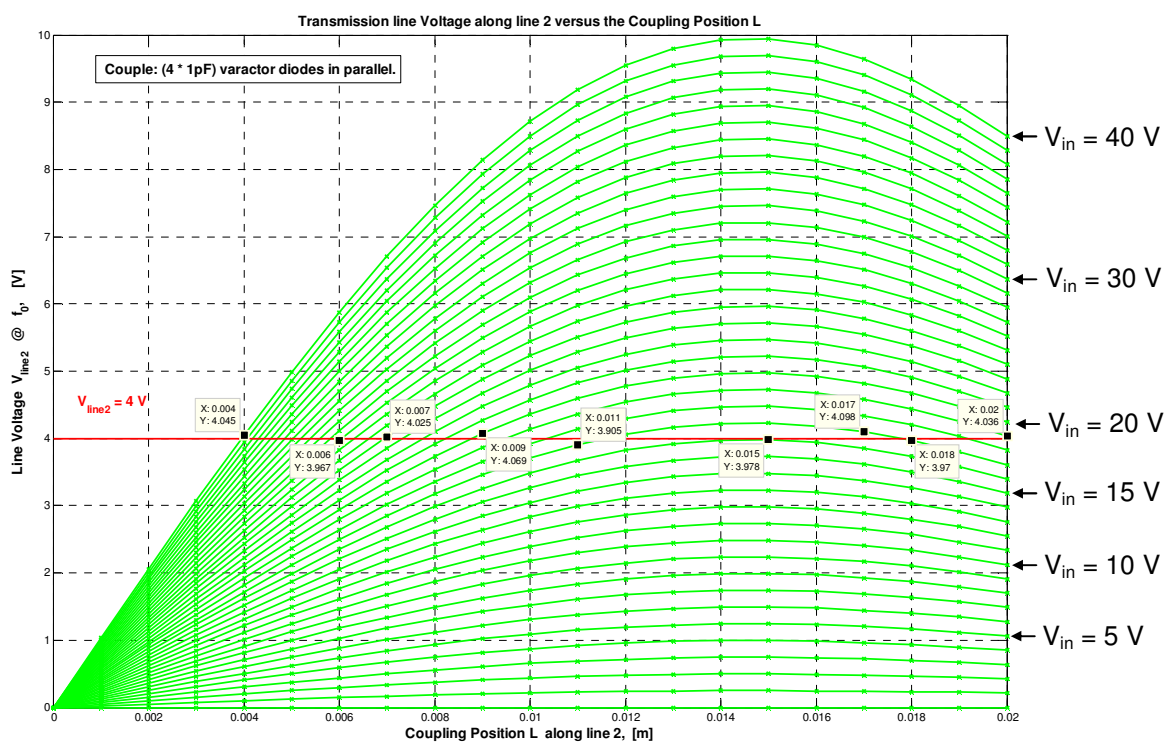


Figure 4.14: Line Voltage, V_{line2} versus the Coupling position, L.

4.1.4 Bypass Capacitors for the Varactor Diodes

The definition of a bypass capacitor is provided as [36]:

‘Bypass capacitor: A capacitor employed to conduct an alternating current around a component or group of components. Often the AC is removed from an AC/DC mixture, the DC being free to pass through the bypassed component’.

Bypass capacitors are often referred to as ‘filter caps’. The reason for the latter name is because bypass capacitors help filter any electrical noise out of a circuit. They operate by removing the alternating currents (AC) that is caused by ripple voltage that might be present. It is custom to add one bypass capacitor for every integrated circuit (IC) on the printed circuit board (PCB). It is also recommended to add bypass capacitors whenever a long power line (connector) is present. Adding a capacitor to both ends of the line will help filter out any electrical noise picked up from a nearby magnetic field, should the power line act as an antenna. While higher frequencies require lower valued capacitors, a good default value would be $0.1 \mu\text{F}$ (or even, $0.01 \mu\text{F}$). Here is a good example of a typical ‘bypass capacitor bank’ that is frequently used to respond to most frequencies:

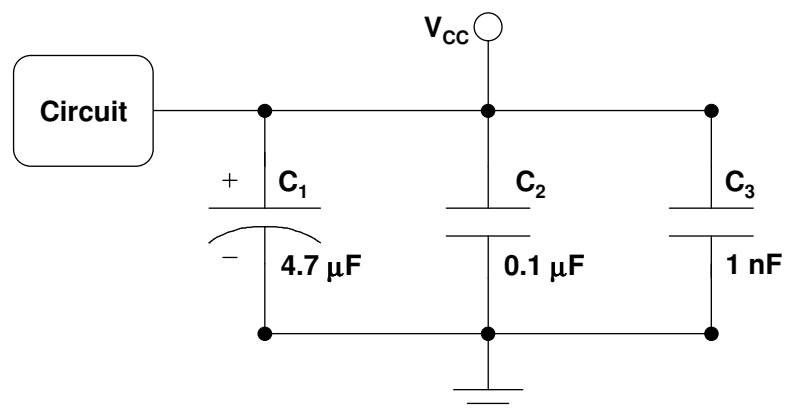


Figure 4.15: Typical Bypass Capacitor parallel bank.

The $4.7 \mu\text{F}$ capacitor illustrated in Fig. 4.15 is utilized to filter larger voltage dips which are associated with reasonably low frequencies. The $0.1 \mu\text{F}$ capacitor would take care of the midrange frequencies, while the $0.001 \mu\text{F}$ (1 nF) capacitor takes care of the higher frequency range.

Fig. 4.15 illustrates the simplest way of utilizing bypass capacitors. Connecting them directly to the power source and to ground, allows the AC components of V_{CC} to directly pass through to ground. Should there be any 'dips' present in the V_{CC} voltage, the capacitors will be able to fill them since they act as a reserve of current. The charged capacitor releases its charge whenever the voltage drops. The larger the size of the capacitor, the bigger 'dip' it can fill [36].

In determining the bypass capacitors that would be sufficient for this project, it is important to keep in mind that the equivalent impedance (Z_{eq}) of the capacitor should be very small (a SC), typically less than 1Ω at f_0 . This means that $1/\omega C < 1$.

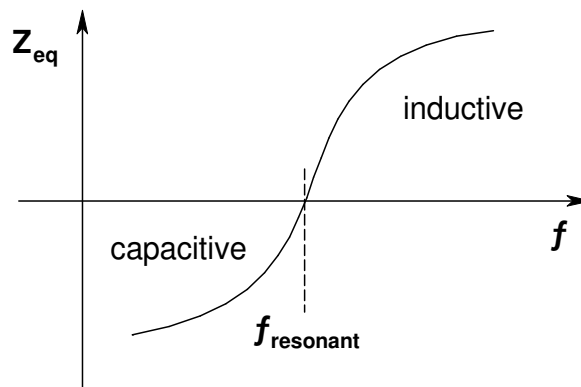


Figure 4.16: Frequency response of a capacitor.

Since all capacitors portray the frequency response illustrated in Fig. 4.16, it is important to find a capacitor with its resonant frequency (that frequency where all imaginary components are equal to zero), at least two to three times larger than the BW of your system. From Fig. 4.16 it is easy to see, that as long as the capacitor is used at frequencies below $f_{resonant}$, the capacitor still behaves like a capacitor, meaning that it filters out all AC to ground, while there exists no DC path to ground. The latter will exist, should the capacitor be used at frequencies above its $f_{resonant}$.

The size of the capacitor itself also shows a tremendous contribution to its $f_{resonant}$. The following represents a surface mount capacitor's equivalent circuit:

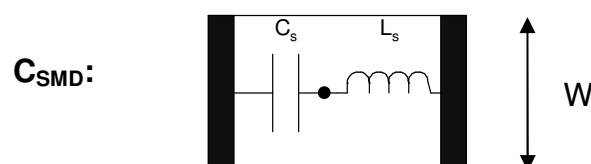


Figure 4.17: Equivalent model of a surface mount capacitor.

The inductive component is defined as $L \propto \text{length}/\text{width}$. Any added inductance will result in the capacitor resonating at a lower frequency. From the latter, the value for a 0603 capacitor typically is $L \approx 800 \text{ pH}$ [37]. Consequently, from the resonance equation,

$$\omega = \frac{1}{\sqrt{L.C}} \quad (4.4)$$

the bypass capacitor value is calculated as,

$$\begin{aligned} C &= \frac{1}{\omega^2 \cdot L_{\text{series}}} \\ &= \frac{1}{(2\pi \cdot (1.1 \times 10^9))^2 \cdot (800 \times 10^{-12})} \\ &= 26.17 \text{ pF}. \end{aligned}$$

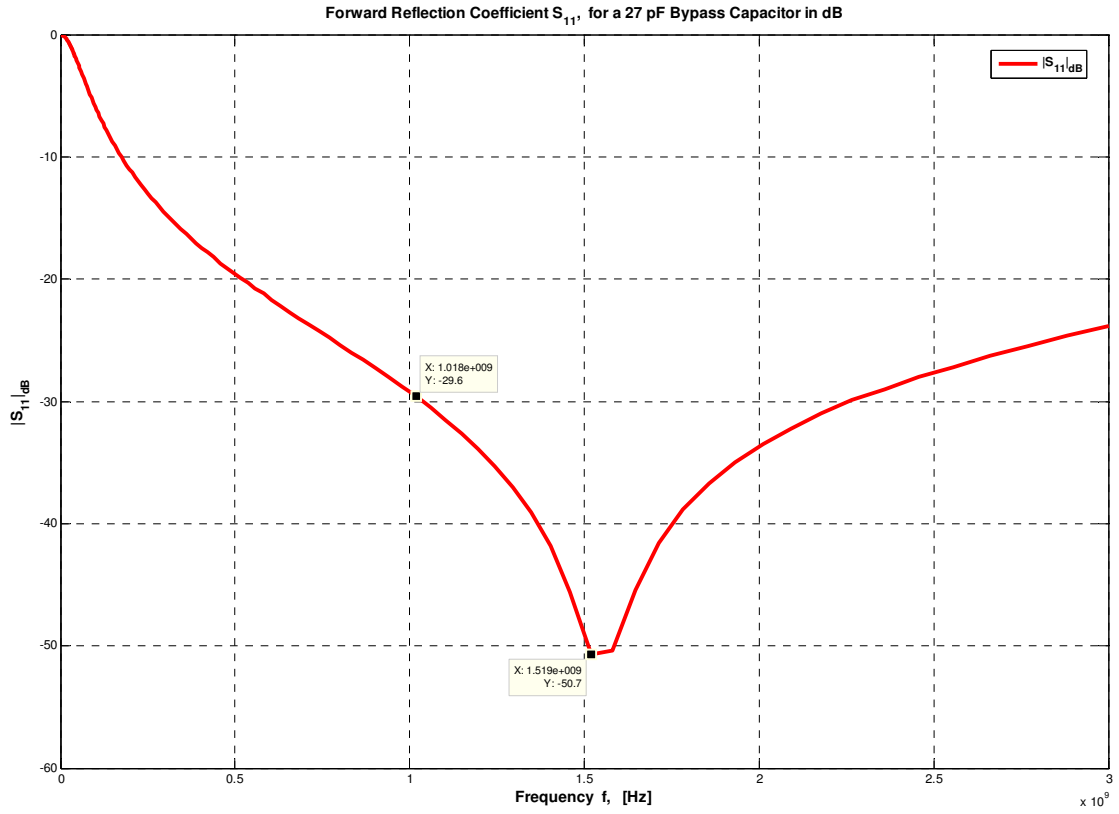
In the preceding equation, the resonant frequency was chosen a little bit higher than previously mentioned. This was done because the addition of the varactor diodes to the resonator will undoubtedly decrease f_0 . Any frequency difference that still exists after the addition may be tuned out by means of the 'Microwave Tuning Element' discussed in Chapter 3. As a result for this project, four, 27 pF bypass capacitors were used. One for each of the varactor diodes utilized.

Fig. 4.18 illustrates the forward reflection coefficient, S_{11} . From Fig. 4.18 (a) it is easy to see that the capacitor has quite a wide BW, its -30 dB BW $\approx 1.25 \text{ GHz}$. It is well matched to 50Ω , which is confirmed in Fig. 4.20.

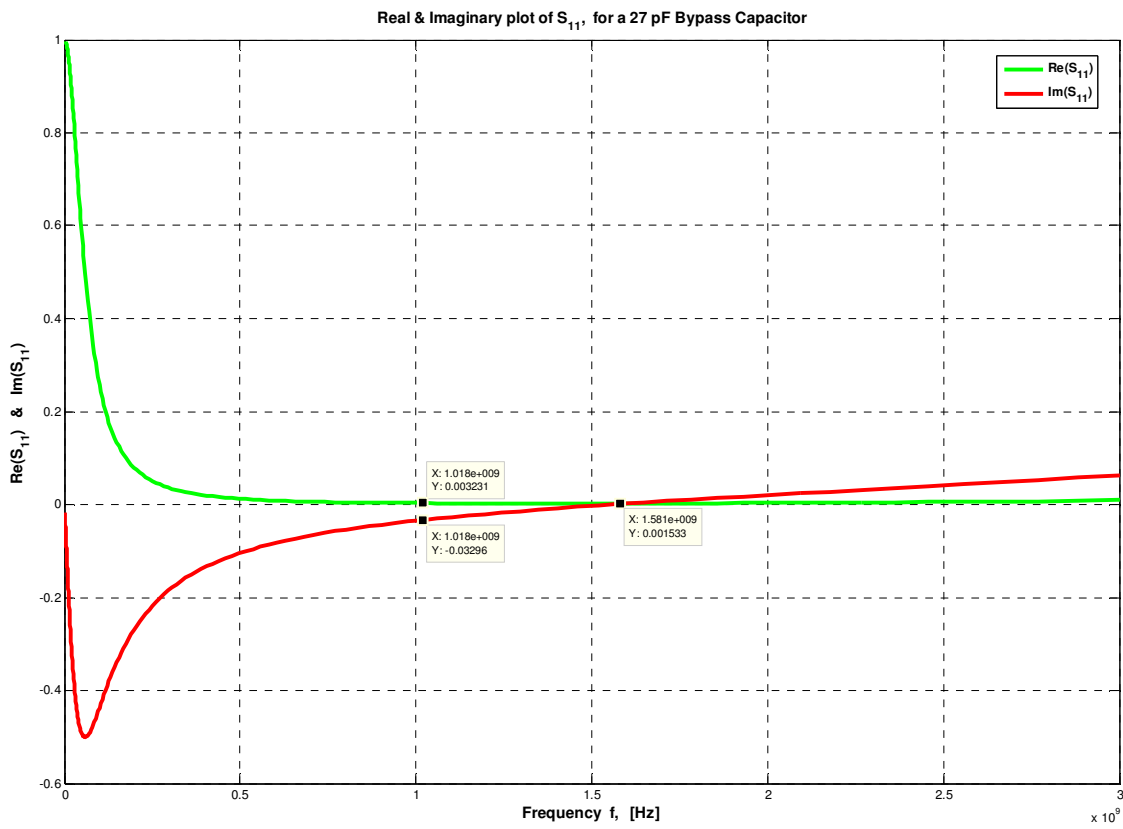
Fig. 4.19 (a) represents the Smith Chart illustration of S_{11} , while Fig. 4.19 (b) does the same, but for Z_{eq} . Take note how both plots start at the OC and stay capacitive until f_{resonant} is reached, where it crosses the real axis and become inductive.

In Fig. 4.21 the statement made in Fig. 4.16 is confirmed. Take note that for the 27 pF capacitor, $f_{\text{resonant}} \approx 1.103 \text{ GHz}$.

In Fig. 4.22 a typical capacitance versus frequency plot is shown. Take note at about 1 GHz, the capacitor still acts as one, having a value of about 29 pF.



(a)



(b)

Figure 4.18: (a) $|S_{11}|$ in dB, and (b) $\text{Re}\{S_{11}\}$ and $\text{Im}\{S_{11}\}$, all versus frequency.

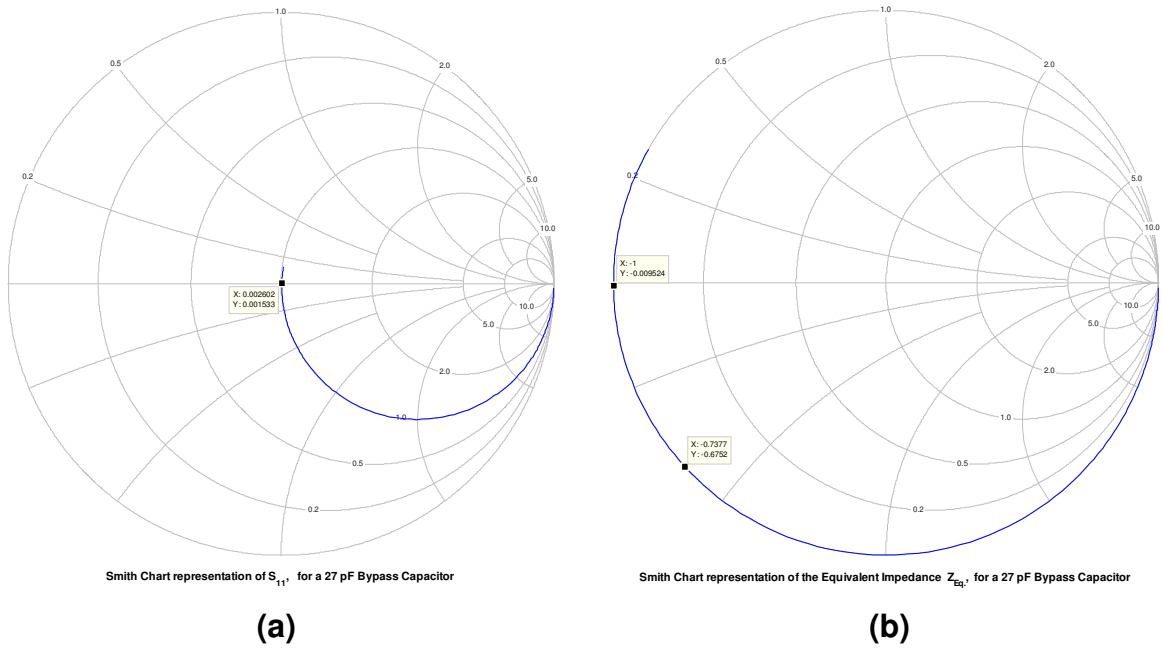


Figure 4.19: Smith Chart representations of (a) S_{11} , and (b) Z_{eq} of the 27 pF capacitor.

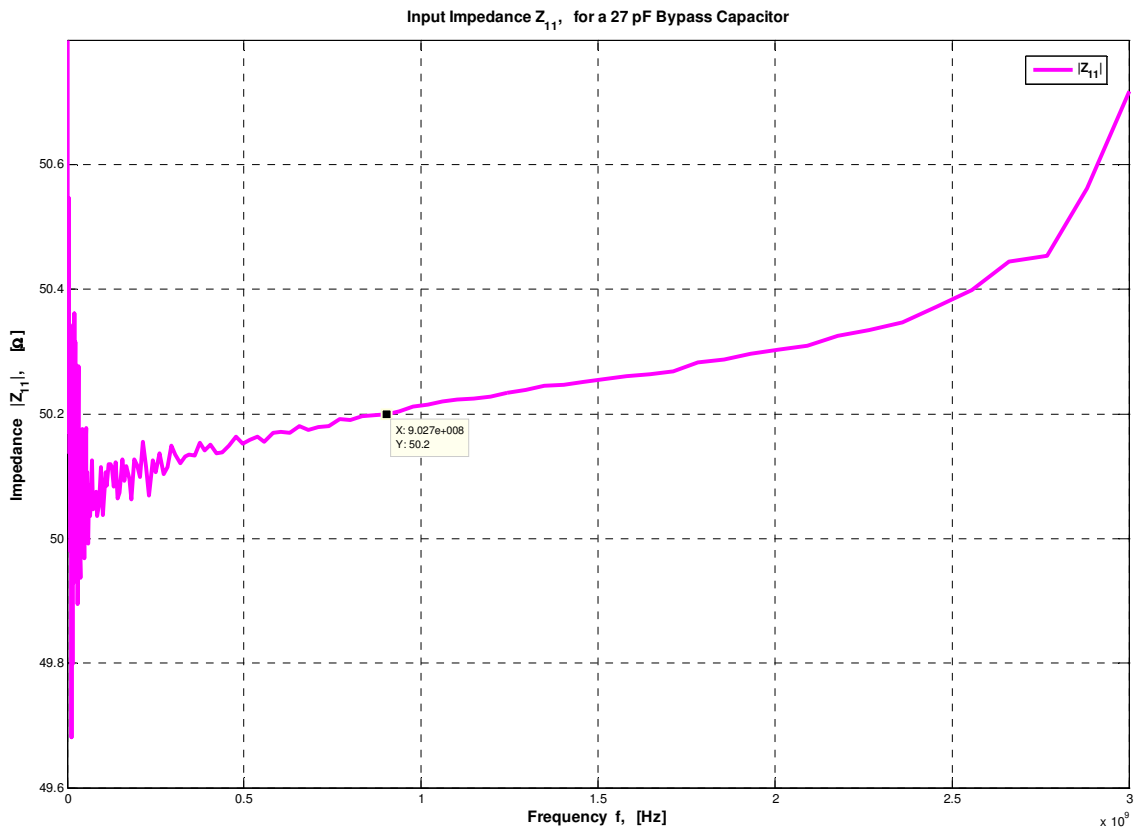


Figure 4.20: Representation of Z_{11} , the Impedance of the 27 pF capacitor, at port 1.

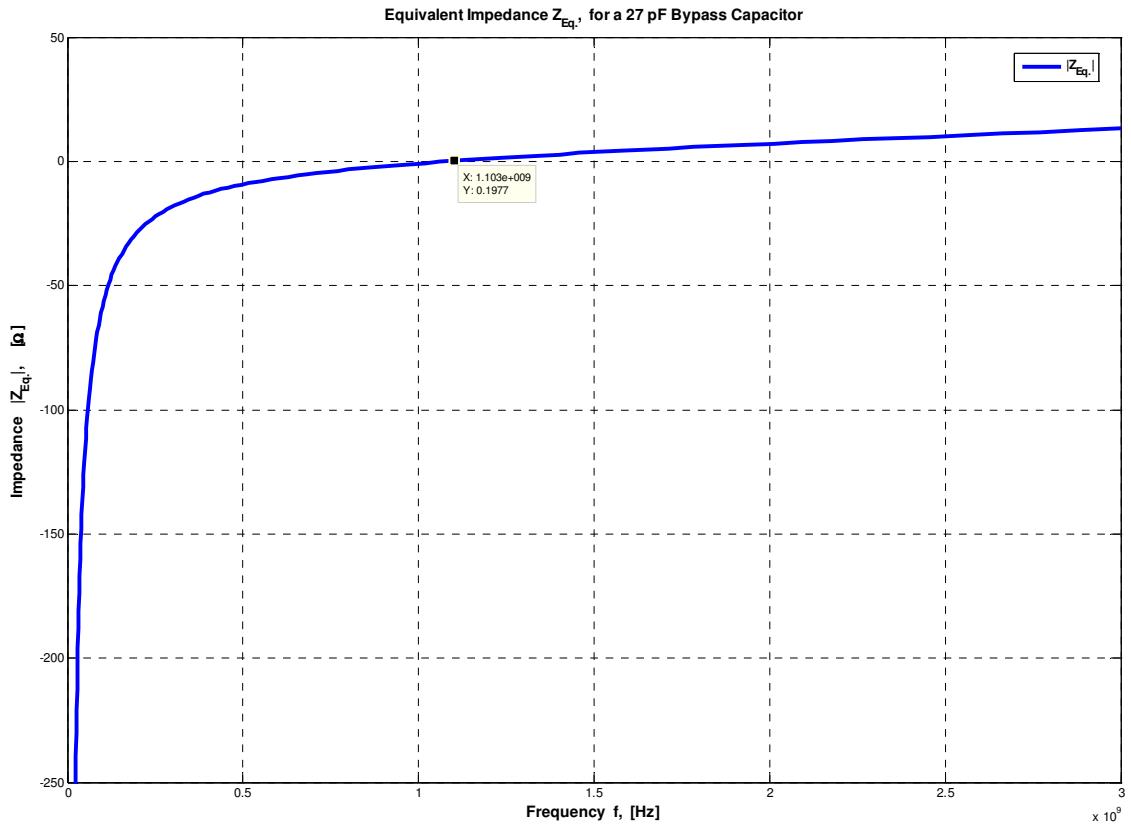


Figure 4.21: Equivalent Impedance Z_{eq} of the 27 pF capacitor, plotted against f .

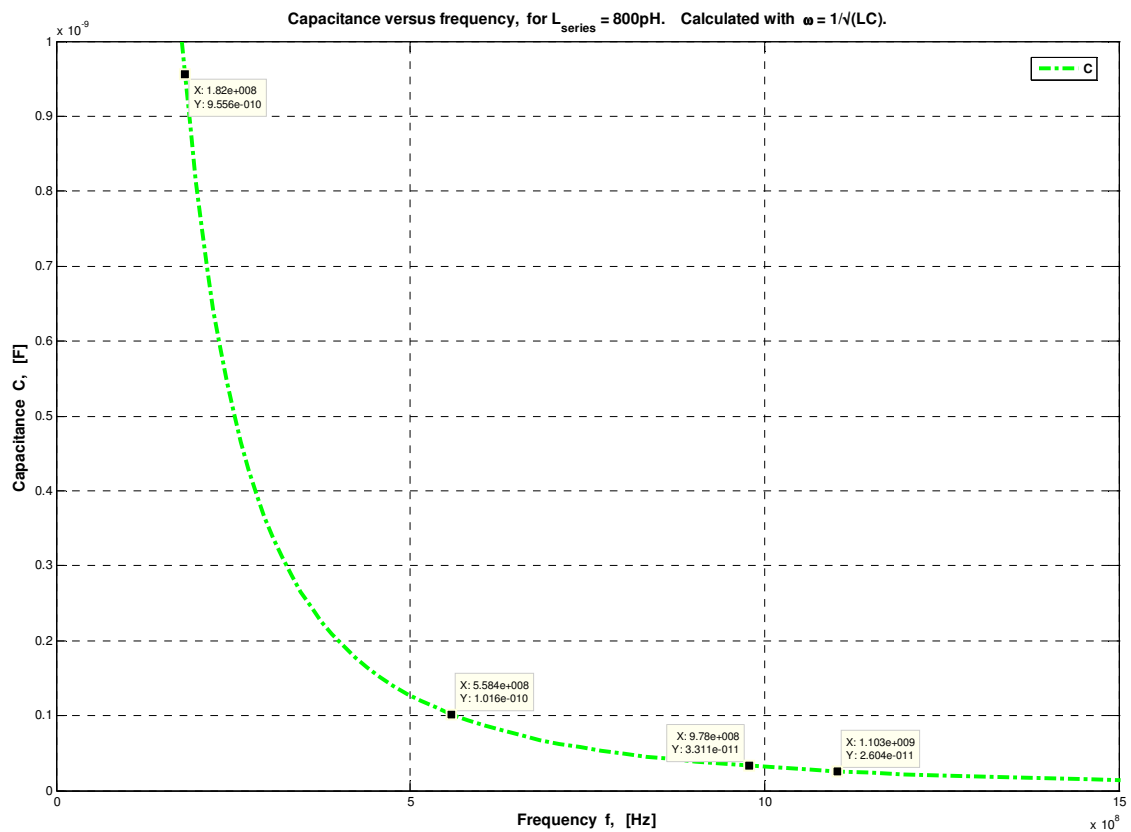


Figure 4.22: Capacitance versus frequency for $L_S = 800\text{ pH}$.

4.1.5 The PCB layout Design

The PCB layout was designed in AUTOCAD. The following figure is a representation of the layout of the varactor diodes with their bypass capacitors.

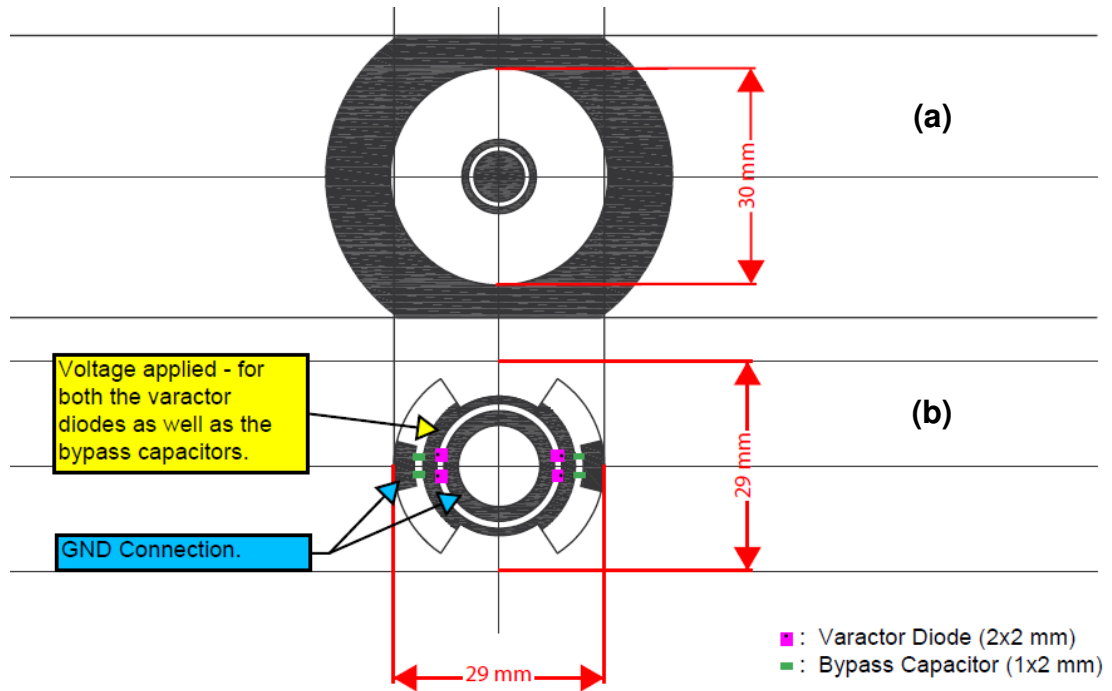


Figure 4.23: Proposed Varactor Diode and Bypass Capacitor layout, with (a) the Resonator, and (b) the PCB.

The layout illustrated in Fig. 4.23 was designed in the software tool **AutoCAD**. In Fig. 4.23 (a) a top view of the resonator and its conductors are shown. The cavity into which the designed PCB will be dropped is also visible. In Fig. 4.23 (b) the proposed PCB layout is shown. To provide a good ground for both the diodes as well as the capacitors, the tracks for the ground connections were designed quite big. As a result the most inner circle, as well as the two pads on the outer diameter serves as the ground connections respectively. The inner circle represents the track where the tuning voltage V_{tune} is connected. When viewing the PCB, pieces has been cut out at its north and south ends. This was necessary because by coincidence, the height at which there was decided to couple the varactor diodes (discussed in Section 4.1.3), was exactly the same height at which the SMA connectors were fixed. Therefore, to leave room for the coupling loops to be tuned, one had to cut away some of the PCB.

By referring back to Fig. 3.27 (page 120), where the magnetic field inside the cavity is illustrated, a symmetry plane is visible. The latter is in the YZ plane, since that is the plane in which the SMA connectors were fixed (see Fig. 3.29 on page 122). Consequently to keep to the cavity symmetric, it was decided to layout the diodes and their bypass capacitors on opposite sides in the cavity, as illustrated in Fig. 4.23 (b).

Something quite interesting that was also observed [23], was the order in which the diode to the bypass capacitor was laid out. In the following figure, Fig. 4.24 two different ways of laying out the diode to the capacitor is shown.

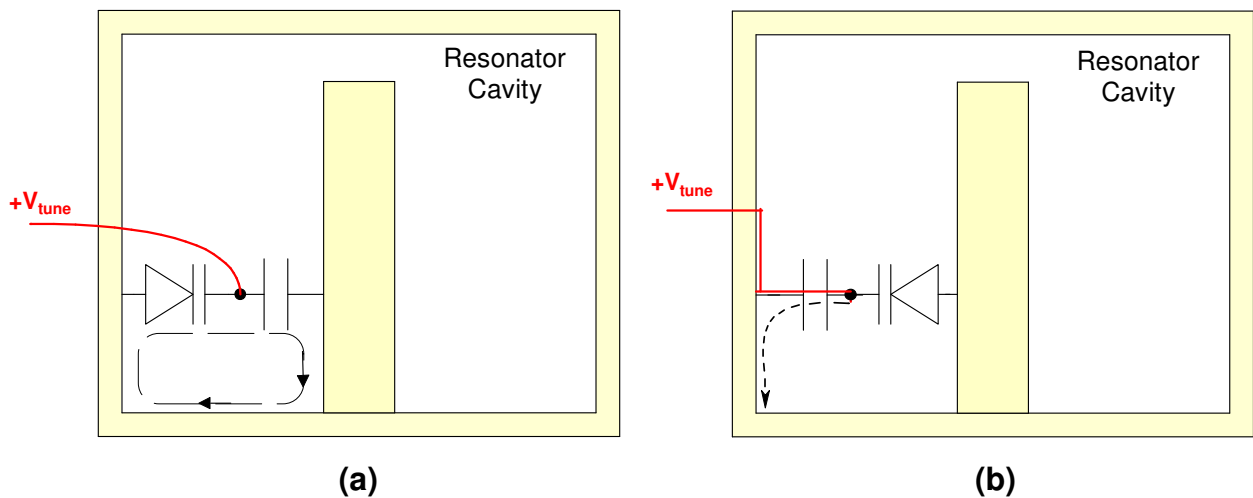


Figure 4.24: Layout Topologies for the Varactor Diode and its Bypass Capacitor (a) illustrating the problems experienced, and (b) giving the proposed solution.

In Fig. 4.24 (a), the varactor diode is connected on the outside of the PCB, while the bypass capacitor is connected on the inside. Consequently the ‘filtered’ AC forms a ground loop, which could indicate that the bypass capacitor is not effectively executing its duty. Where, as in Fig. 4.24 (b) the AC is directly ‘filtered’ to ground, cancelling any possibility of developing a loop.

Another important technique is represented by the red V_{tune} wire, also illustrated in Fig. 4.24. It was suggested that first of all, to arrange the V_{tune} wire as close to the PCB and boundaries of the cavity as possible, in order to keep it from making any loop to which the magnetic field inside the cavity could couple. Secondly it was also decided to make use of thinner wire.

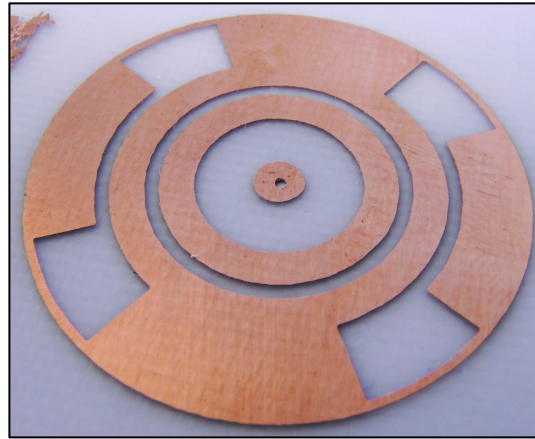
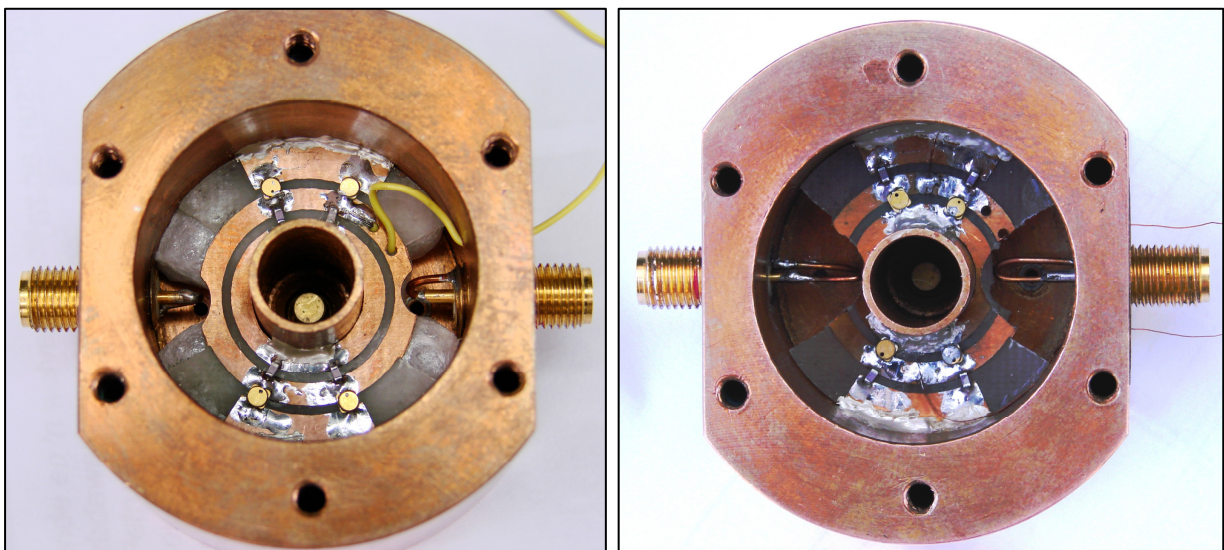


Figure 4.25: Photograph of the designed Printed Circuit Board.

The designed PCB is illustrated in Fig. 4.25. This photograph was taken before the PCB was cut to fit into the cavity. The PCB was made out of the thinnest possible sheet of **FR-4**, measuring as 0.2 mm thick. The reason for the latter was to minimise the dielectric losses present. The sheet used, had a loss factor of $\tan(\delta) = 0.025$, $\epsilon_r = 4.9$, and $\mu = 1$.



(a)

(b)

Figure 4.26: Photographs of the Varactor Diodes and their Bypass Capacitors soldered onto the PCB. (a) Illustrate the problems experienced, while (b) demonstrate the proposed solutions.

The system shown in Fig. 4.26 (a) were build and measured as illustrated, before the improvements were applied, producing the system in Fig. 4.26 (b). Fig. 4.26 closely represents that illustrated in Fig. 4.24.

4.2 MEASUREMENTS AND RESULTS

4.2.1 SA Confirmation of Oscillation

A measurement to confirm the oscillation of the VCO system before its phase noise was measured, were done at *Reutech Radar Systems (RRS)* just outside Stellenbosch. It was made on a **Hewlett Packard – Agilent HP E4407B 9 kHz – 26.5 GHz, ESA-E Series Spectrum Analyser**. The latter is illustrated in the following figure.



Figure 4.27: Photograph of the HP Spectrum Analyser at RRS.

It is always important to know exactly what power level one is connecting to expensive measuring equipment. Therefore, performing the latter measurement is essential. In Fig. 4.28, the confirmed oscillation is illustrated. This was done with a 1 dB attenuator in the feedback loop of the system. A +5V DC power supply voltage was connected to the ZX60-2522M amplifier, while a +22V DC power supply voltage was connected as V_{tune} to the varactor diodes.

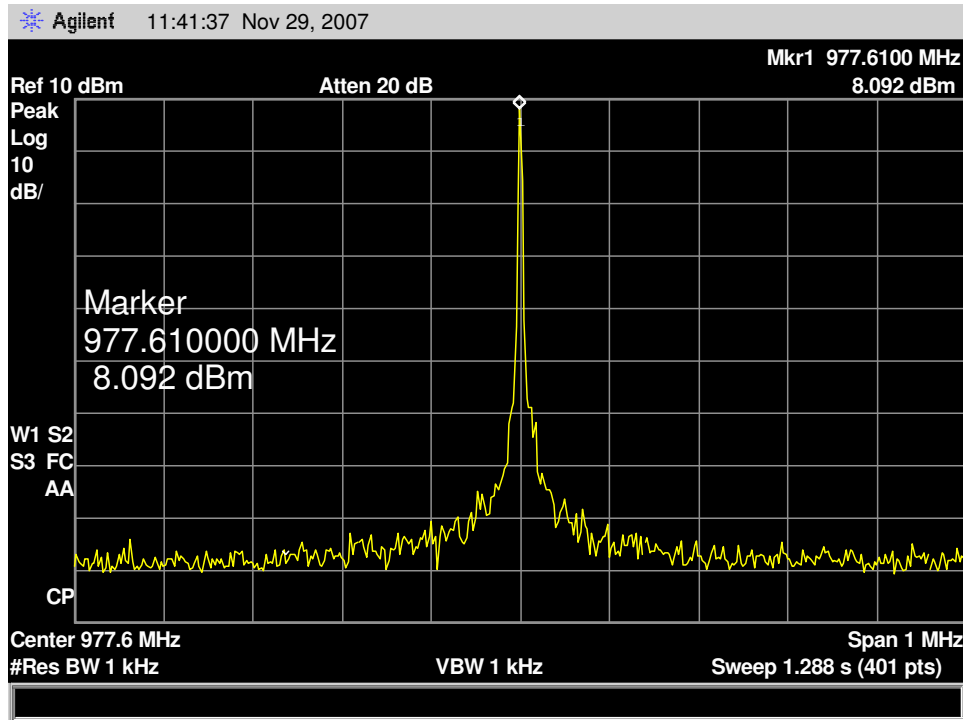


Figure 4.28: Confirmed oscillation of the VCO system before its PN measurement.

4.2.2 Loaded and Unloaded Q-values

The Q-value of the resonator, loaded by the presence of the varactor diodes is calculated by the 3 dB BW in Fig. 4.29. The same is done for the unloaded Q-value of the resonator, illustrated in Fig. 4.30. The measured values are summarised in the following table:

Table 4.4: Measured Q-values for the VCO system.

	Unloaded Q-value, Q_U	Loaded Q-value, Q_L
VCO	362.44	195

The plot for the unloaded S-parameters illustrated in Fig. 4.30, is non-symmetric. Therefore a wide-band (1.5 GHz) measurement, shown in Fig. 4.31 was conducted, to confirm the possibility of another resonant point present, which could explain the non-symmetric plot for the unloaded resonator. The latter is found to be at least 10 dB lower than the fundamental, which indicates that it should have little, if not zero effect.

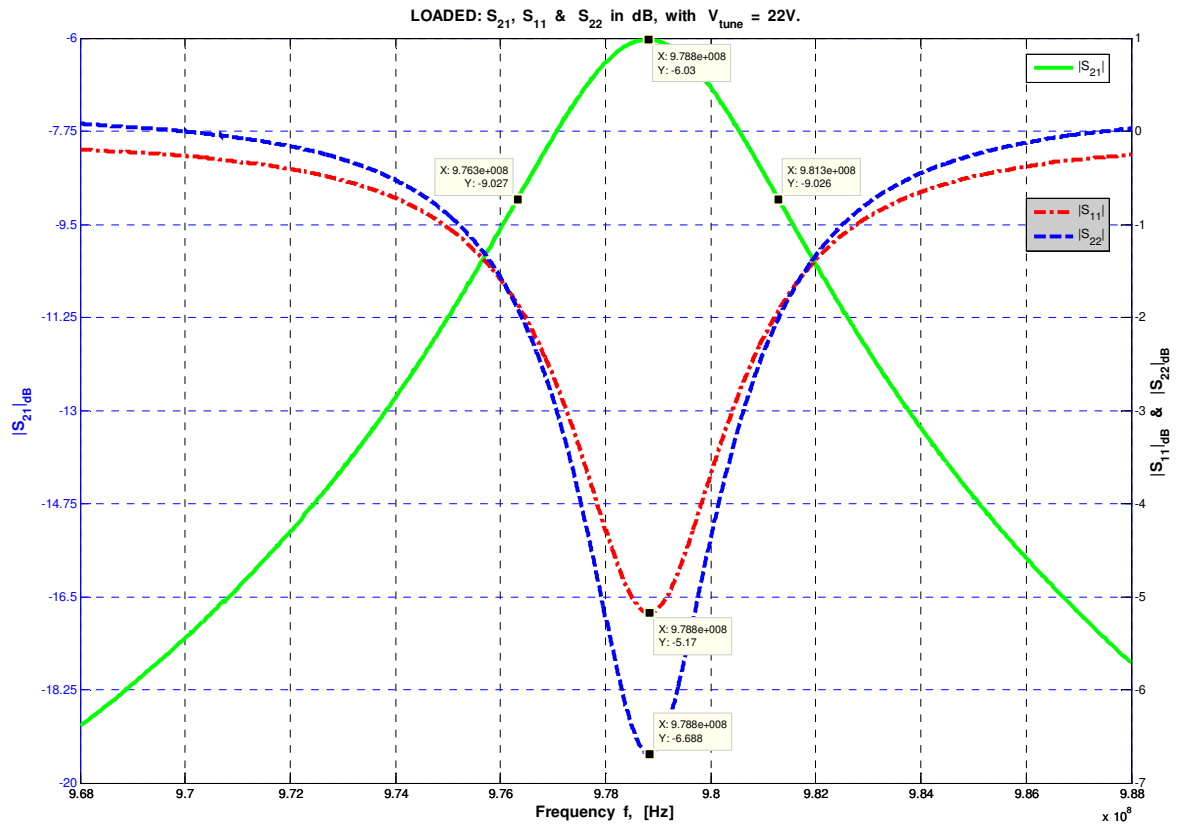


Figure 4.29: S-parameters of the Resonator loaded by the Varactor Diodes.

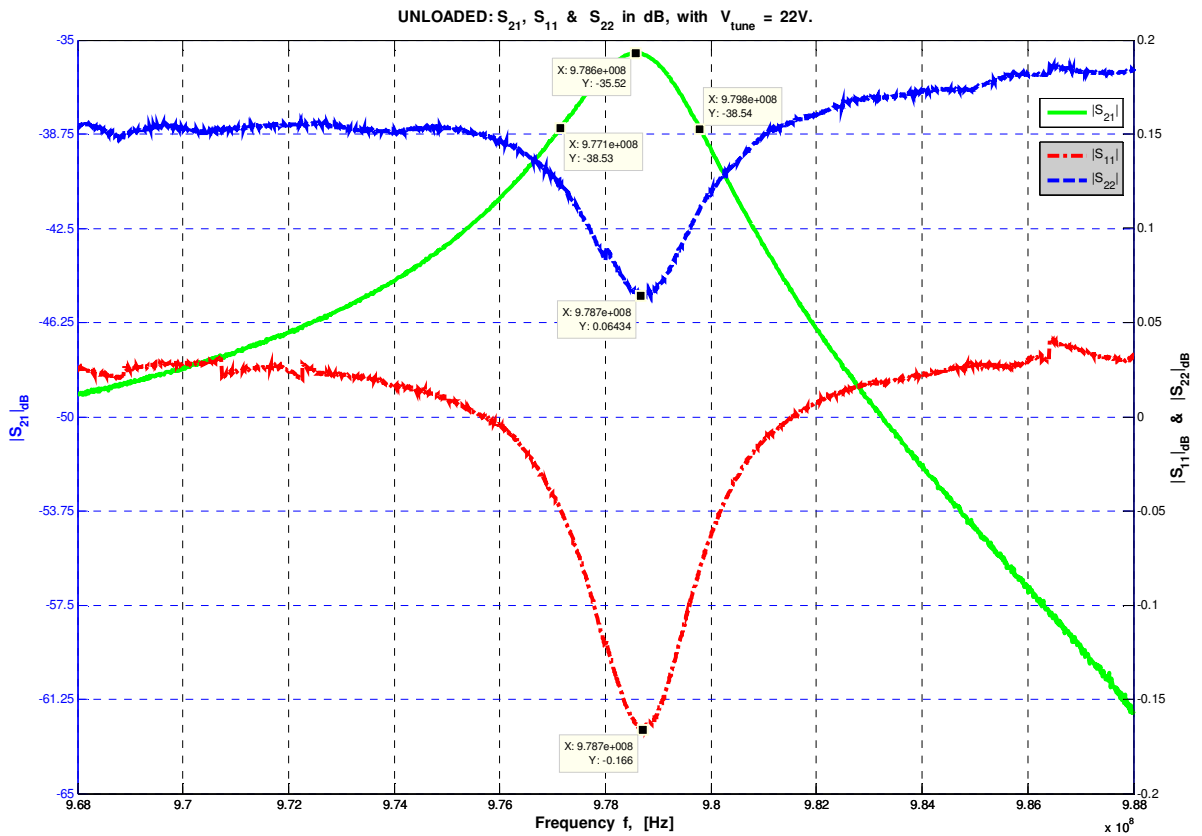


Figure 4.30: S-parameters of the unloaded Resonator.

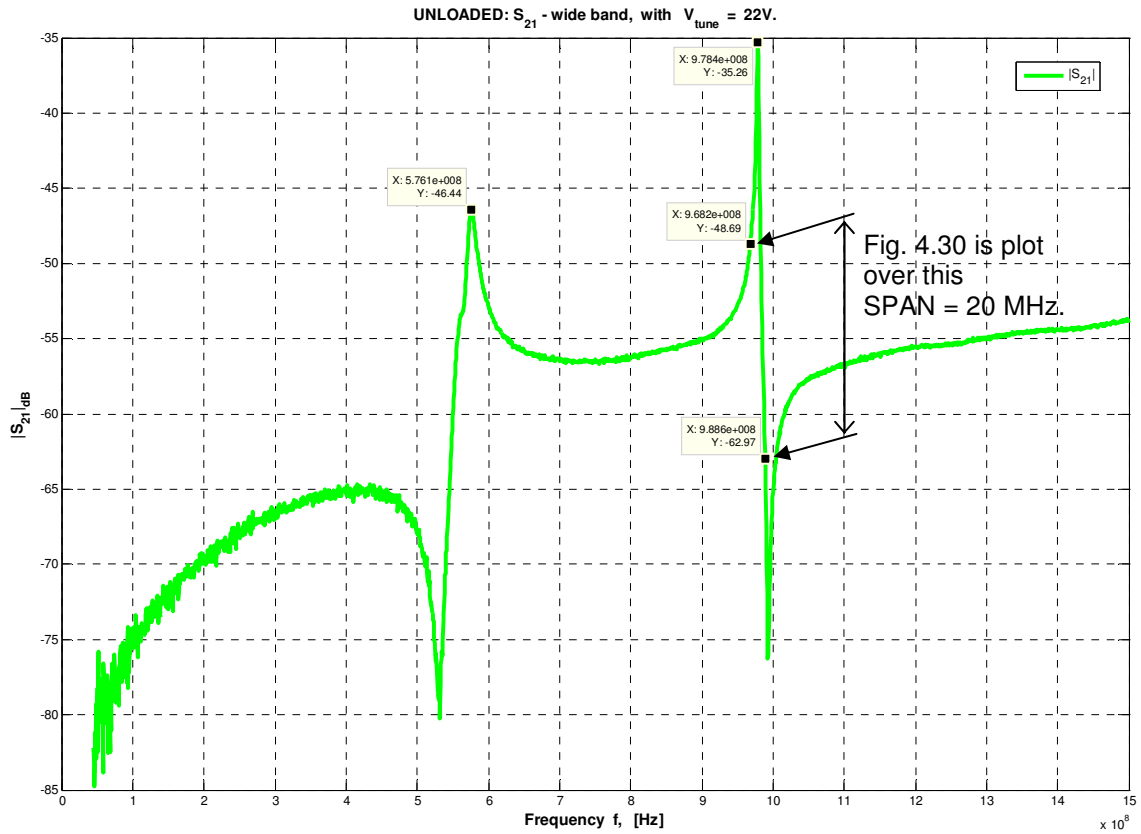


Figure 4.31: Wide-band plot of the S-parameters of the unloaded Resonator.

4.2.3 Tuning bandwidth, Δf

In the following figures, the frequency response of the variable tuning diodes is illustrated. The plot would have been linear if the Q of the diodes stayed constant. The tuning voltage applied to the varactor diodes is set from +22 V to +4 V. The latter was measured on three different occasions, confirming the tuning bandwidth (Δf) obtained for the designed VCO system. It is summarised in the following table.

Table 4.5: Summary of the Tuning Bandwidth (Δf) measurements.

Measurement	$V_{\text{tune}} = +22 \text{ V}$		$V_{\text{tune}} = +4 \text{ V}$		Δf [MHz]
	f [MHz]	dB	f [MHz]	dB	
SA (Univ.STB, RF Lab)	977.60	+ 8.316	947.40	- 33.05	30.20
VNA (Univ.STB, RF Lab)	978.84	- 5.921	939.92	- 10.72	38.92
HP SA (RRS)	977.28	+ 8.729	948.03	- 24.57	29.25

From Table 4.5 the average tuning bandwidth is calculated as: $\Delta f = 32.79 \text{ MHz}$.

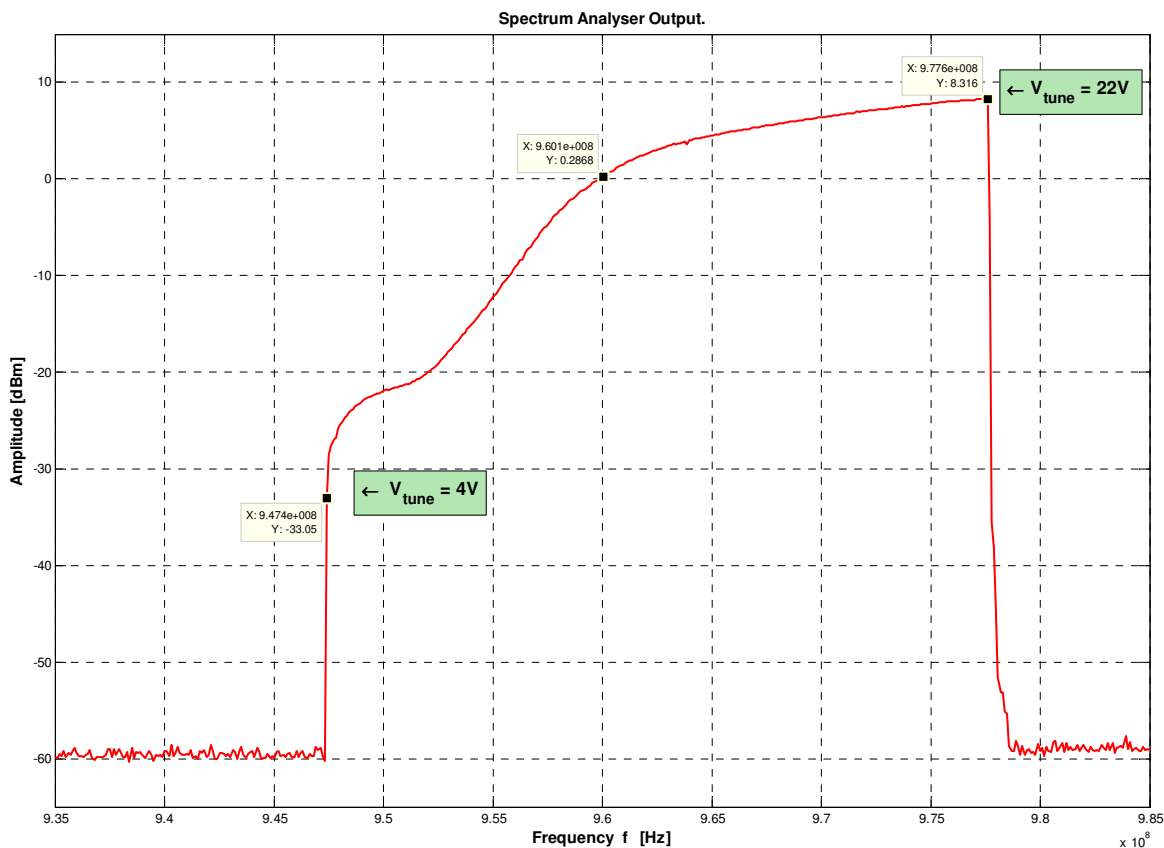


Figure 4.32: Tuning bandwidth Δf measured on the Spectrum Analyser.

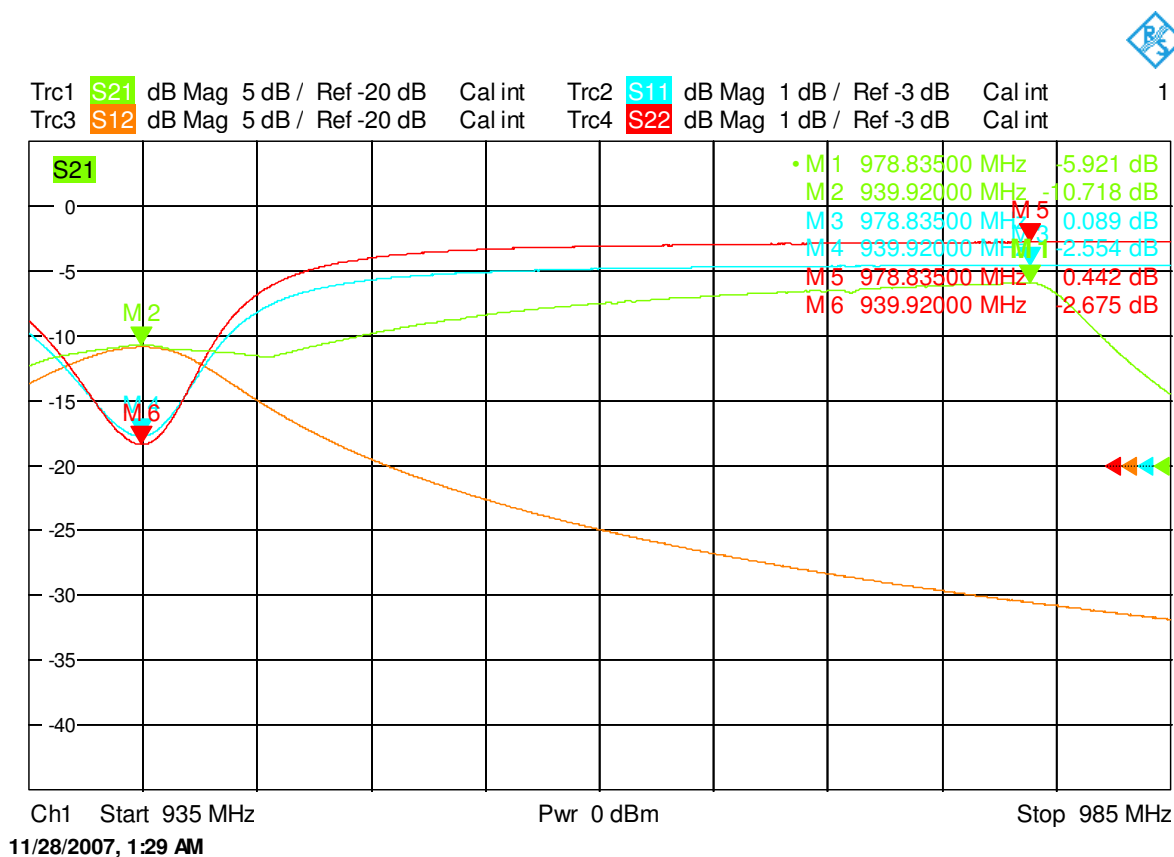


Figure 4.33: Tuning bandwidth Δf measured on the Vector Network Analyser.

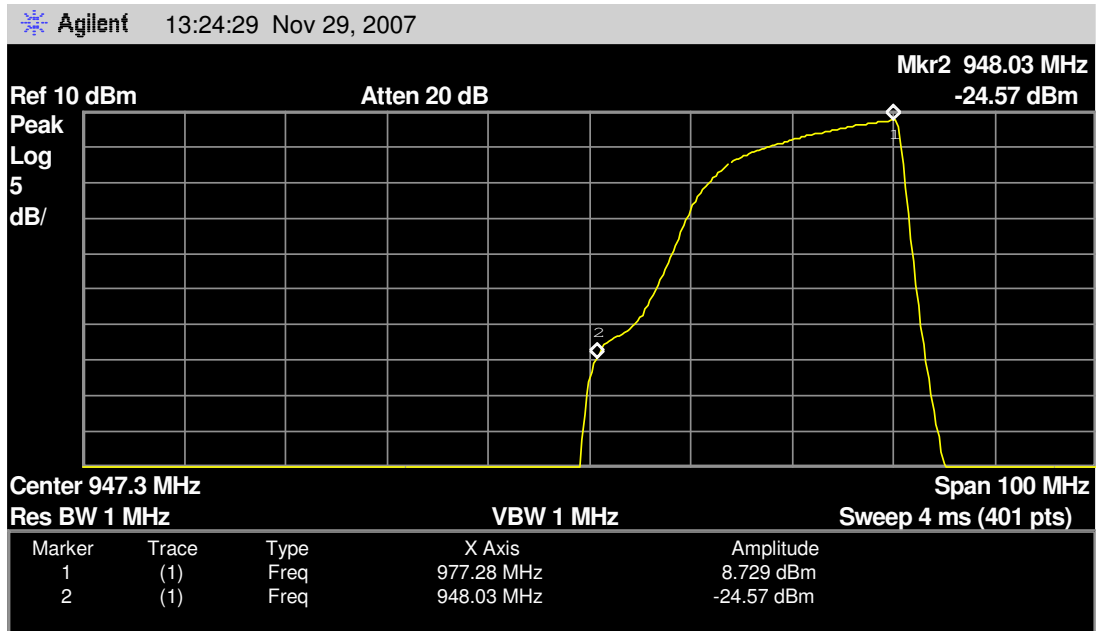


Figure 4.34: Tuning bandwidth Δf measured on the HP SA at RRS.

In comparing the expected values in Table 4.3 (p.174) to that measured in Table 4.4 (p.187) and Table 4.5 (p.189), a vast difference is clearly visible. In the following table the result is summarised for better comparison; i.e. for Q_U , Q_L and Δf .

Table 4.6: Comparison of the Expected values to that Measured for Q_U , Q_L and Δf .

Diodes @ L = 6 mm		Expected Value	Measured Value
Tailored, $Q_{R\&D}$	(= Q_U)	≈ 750	362.44
Loaded, $Q_{R\&D\&C}$	(= Q_L)	≈ 370	195
Tuning BW, Δf	[MHz]	≈ 27	32.79

The measured Q-values shown in Table 4.6 are approximately half of the expected values. As a result, it was decided that the wire connected to the PCB supplying the V_{tune} voltage, the bypass capacitors, the varactor diodes and then lastly the PCB itself had to be removed systematically, measuring Q_U and Q_L after every component removed. These measurements are referred to as the '**Destructive Measurements**', and are conducted to precisely confirm what component causes the discrepancy between the expected and measured results. See Section 4.2.5.

Firstly the phase noise of the VCO system as it is, was measured on the Aeroflex Phase Noise Test System. This is discussed in the following section.

4.2.4 PN9000B – Automatic Phase Noise Test System

In the case of measuring the phase noise of the VCO system, the exact same procedure to that discussed in Chapter 3 (p.155) were followed to setup the software of the Phase Noise Test System.

- **Theory of Operation (*Delay Line FM Discrimination Method*)**

When measuring a free running source, the '*Delay Line*' method is the ideal solution. The VCO (SUT) usually has a phase noise higher than that of a PLL VCO close-in to the carrier. But at frequency offsets of 100 kHz and beyond its phase noise is lower. This is particularly true for offset frequencies far from the carrier, where it is difficult to find a reference source with a noise floor below -160 dBc/Hz.

The *Delay Line* module provides higher phase noise detection sensitivity and lower noise floor, up to:

- 130 dBc/Hz at 20 kHz offset, with the 100 ns delay, and

- 170 dBc/Hz at 20 MHz offset, with the 20 ns delay option.

Since a linear phase shift as a function of frequency is provided by a delay line, the latter operates as a frequency discriminator. The demodulated signal, or noise voltage, is then given by the following formula (see Appendix **M**):

$$V_{noise}(f_m) = K_\phi \cdot 2\pi\tau \cdot \frac{\sin(2\pi\tau \cdot f_m)}{2\pi\tau \cdot f_m} \cdot \Delta f(f_m) \quad (4.5)$$

where

K_ϕ – depends on the phase detector characteristics and input levels, in [V/rad]

τ – is the delay of the line, in [ns]

$\sin(x)/(x)$ – limits the offset analysis.

A block-diagram showing the principle of operation is illustrated in Fig. 4.35 on the following page.

The frequency drift and phase/frequency fluctuation of free running sources such as VCOs are generally too high, to allow phase locking to a DC FM reference source. As a result, their phase noise are difficult to measure using the *reference phase locking method*, as described in Section 3.5.2.2 (p.152) for the Oscillator system. Therefore, the method just described on the previous page – *the delay line FM discrimination method* – is used to obtain phase quadrature between RF and LO inputs of the RF phase detector. The latter is situated on the PN9000B base system.

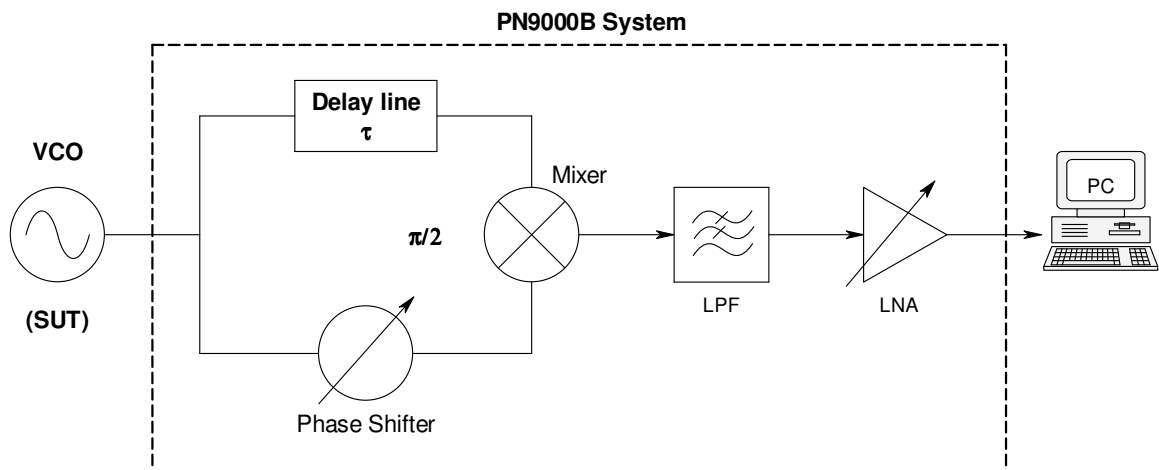


Figure 4.35: Block diagram of the VCO measurement setup in Fig. 4.36.

- **Setup for the VCO Phase Noise Measurement**

Appendix **M** provides all relevant pages taken from the PN9000 reference manual, for a description of exactly where to connect the device to be measured, and the necessary cabling for the system itself [35]. Alternatively the cabling illustrated in the following photograph (Fig. 4.36), could also be used as a guideline. The ‘Delay Line’ module present on the PN9000B base system is the PN9715 delay line. When studying Appendix **M**, keep in mind to make use of the PN9715’s values provided for the residual phase noise (noise floor).

In the following section, the phase noise was measured for three different attenuators in the feedback loop, respectively. Oscillations were observed for both the 1 dB and 6 dB attenuators, but no oscillation occurred for the case in which the 10 dB attenuator was present in the feedback loop. The latter indicates that the power in the feedback loop was too little to overcome the losses in the circuit, and sustain an oscillation.

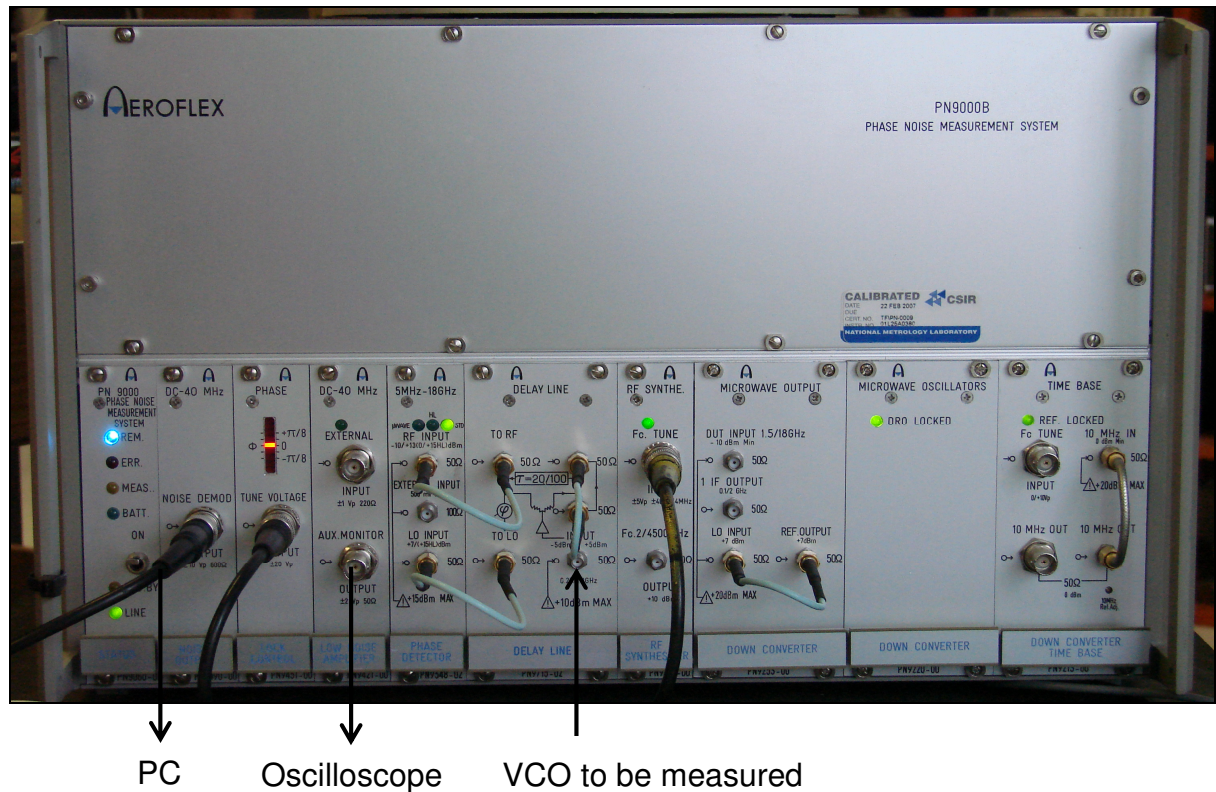


Figure 4.36: Photograph of the cabling done on the Aeroflex Phase Noise Measurement System, for the VCO phase noise measurement setup.

▪ Measured Results

All phase noise measurements captured on the *Aeroflex Automatic Phase Noise Test System* for the VCO, are illustrated on pages 196 to 199.

Measurements were done for both delay lines available, i.e. the 20 ns as well as the 100 ns lines. Fig. 4.37 illustrates the case in which the 20 ns line was utilized, with a 1 dB and 6 dB attenuator present in the feedback loop, respectively. The phase noise of the system obtained for the different attenuations, are weighed against each other. The latter confirms the theory that a higher feedback attenuation causes a more linearly operation of the active element (amplifier) present in the loop, which undoubtedly provides a reason for the phase noise to drop. The same can be said for the measurement illustrated in Fig. 4.38 where the 100 ns delay line was employed.

Take note that the residual phase noise (noise floor) of the *Delay Line* module present in the PN9000B base system, is specified in the manual (Appendix **M**) only at offset frequencies from 1 kHz to 10 MHz for the 20 ns line, and from 1 kHz to 4 MHz for the 100 ns line. As a result, a predicted noise floor for offset frequencies below 1 kHz is introduced in the figures. The latter is indicated by a dashed line.

Consider for instance Fig. 4.40, with the 6 dB attenuator in the feedback loop. It would be recommended to rather make use of the 100 ns delay line when measuring the phase noise of the designed VCO system. The latter statement is made, since the measured SSB phase noise is still above the specified residual phase noise for offset frequencies up to about 200 kHz. Thereafter the measurement becomes unreliable as the noise floor grows to be dominant. For the 20 ns delay line, the noise floor already becomes dominant at an offset frequency of 40 kHz. The latter is suggested, to get the most accurate measurement at as high an offset frequency as possible.

Up and until the offset frequency where the residual phase noise becomes dominant, are all plots portraying a noise power decrease of -30 dB/decade. The latter represents the up-converted $1/f$ -noise, as discussed in Chapter 2.

For both delay lines, i.e. the 20 ns as well as the 100 ns, no reliable measured results for the SSB phase noise of the VCO were obtained for offset frequencies beyond 200 kHz. That is because the residual phase noise grows to be dominant at those offset frequencies.

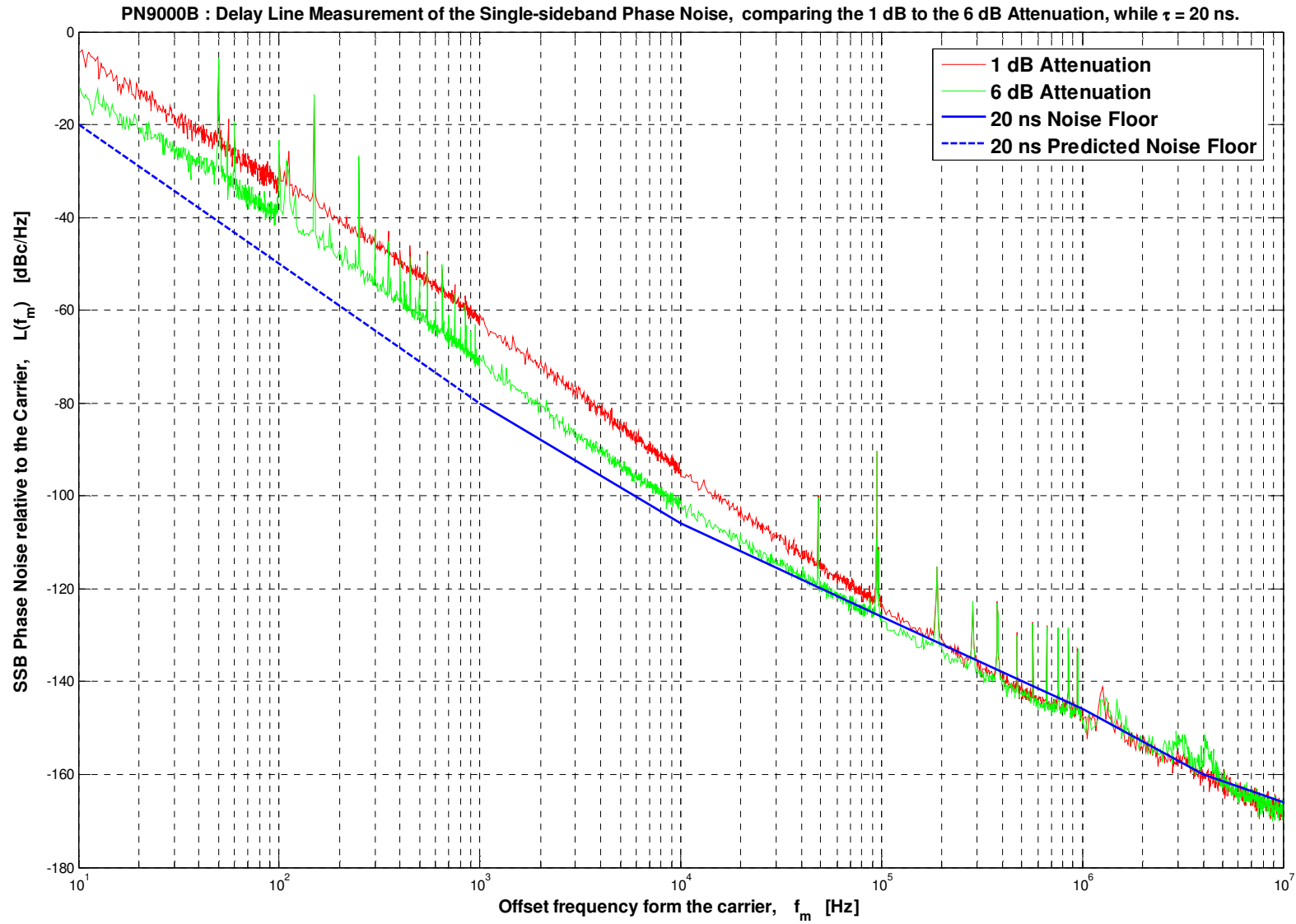


Figure 4.37: Delay Line Measurement of the SSB Phase Noise, comparing the 1 dB to the 6 dB Attenuation, while $\tau = 20$ ns.

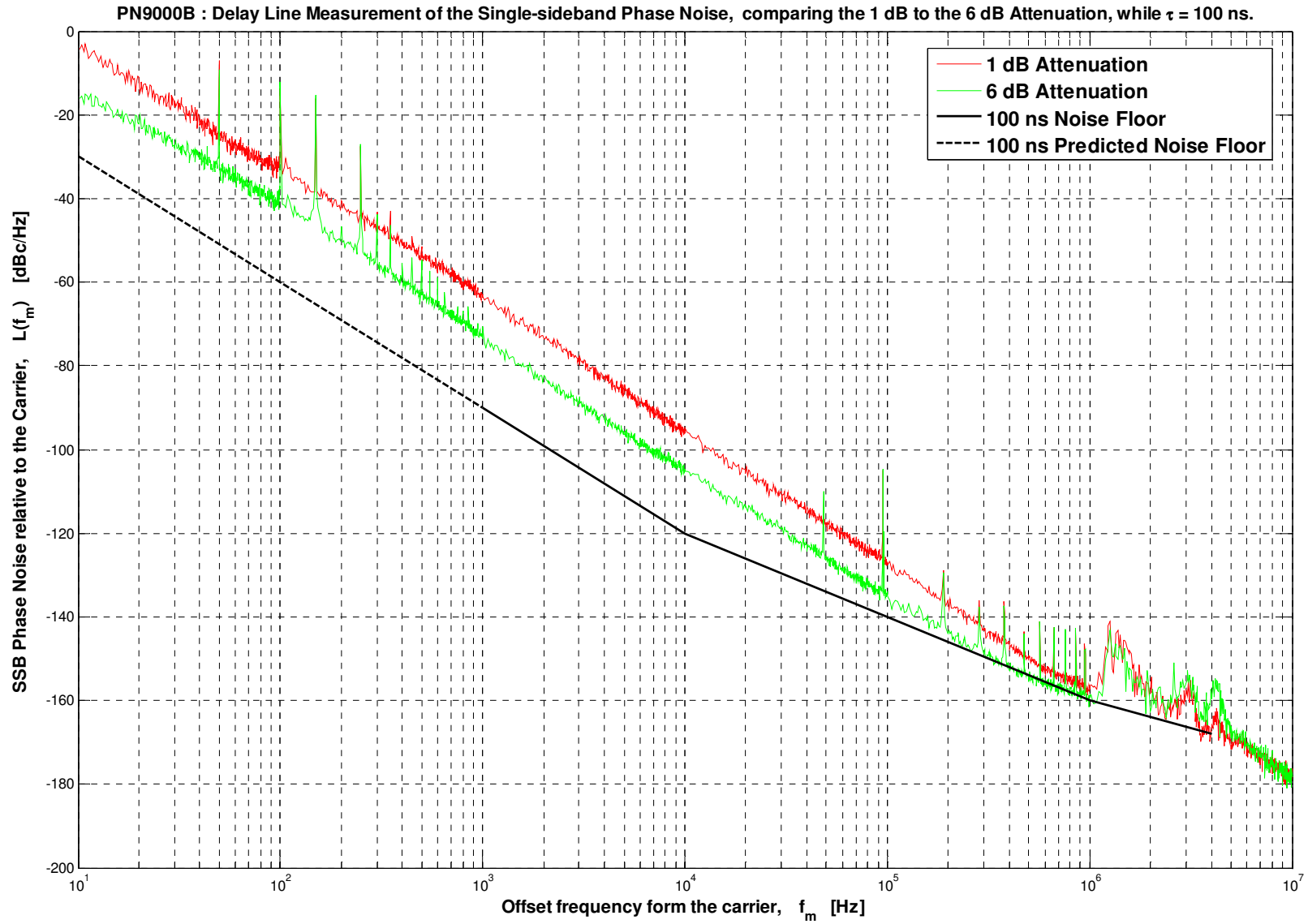


Figure 4.38: Delay Line Measurement of the SSB Phase Noise, comparing the 1 dB to the 6 dB Attenuation, while $\tau = 100$ ns.

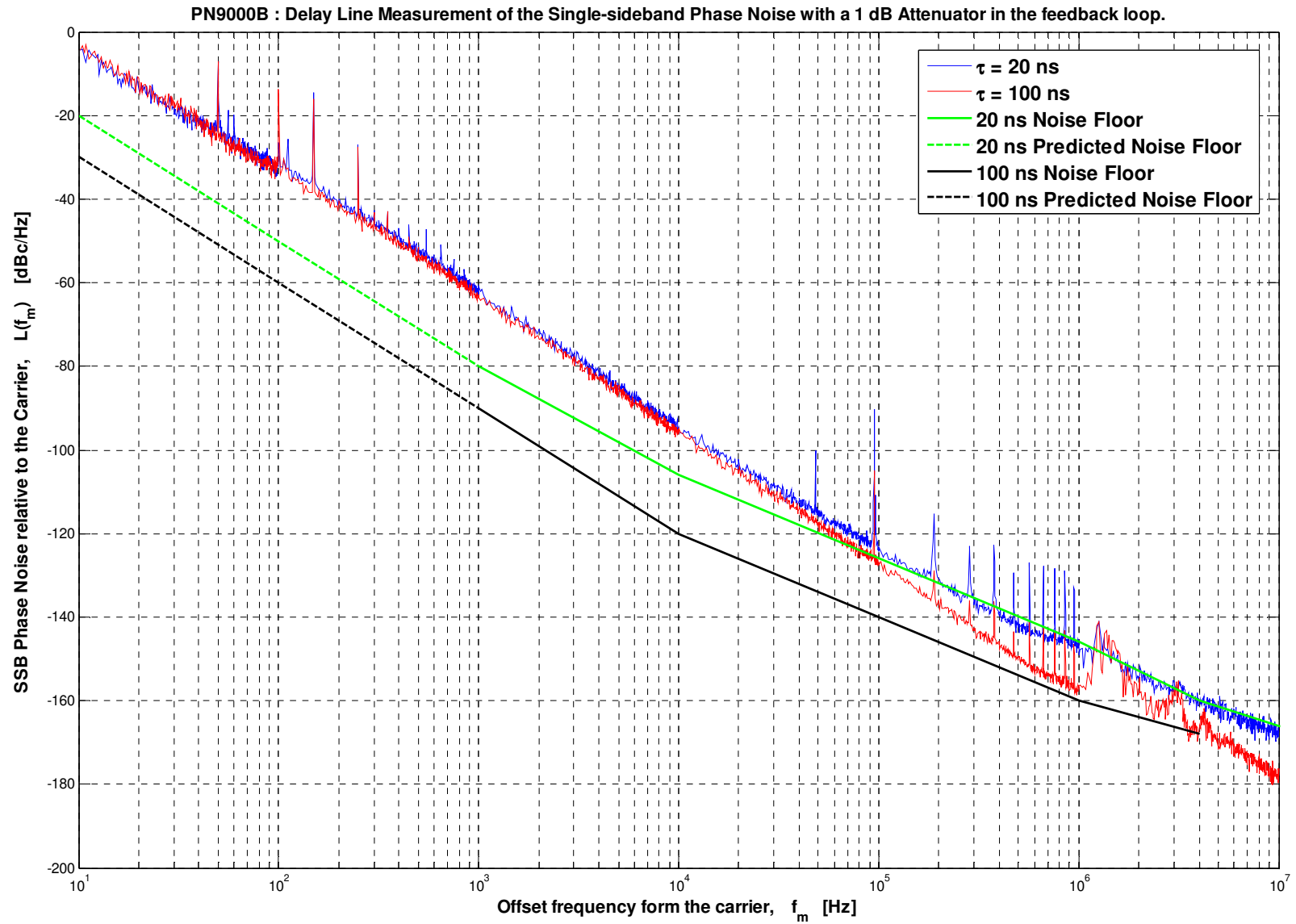


Figure 4.39: Delay Line Measurement of the SSB Phase Noise with a 1 dB Attenuator in the feedback loop.

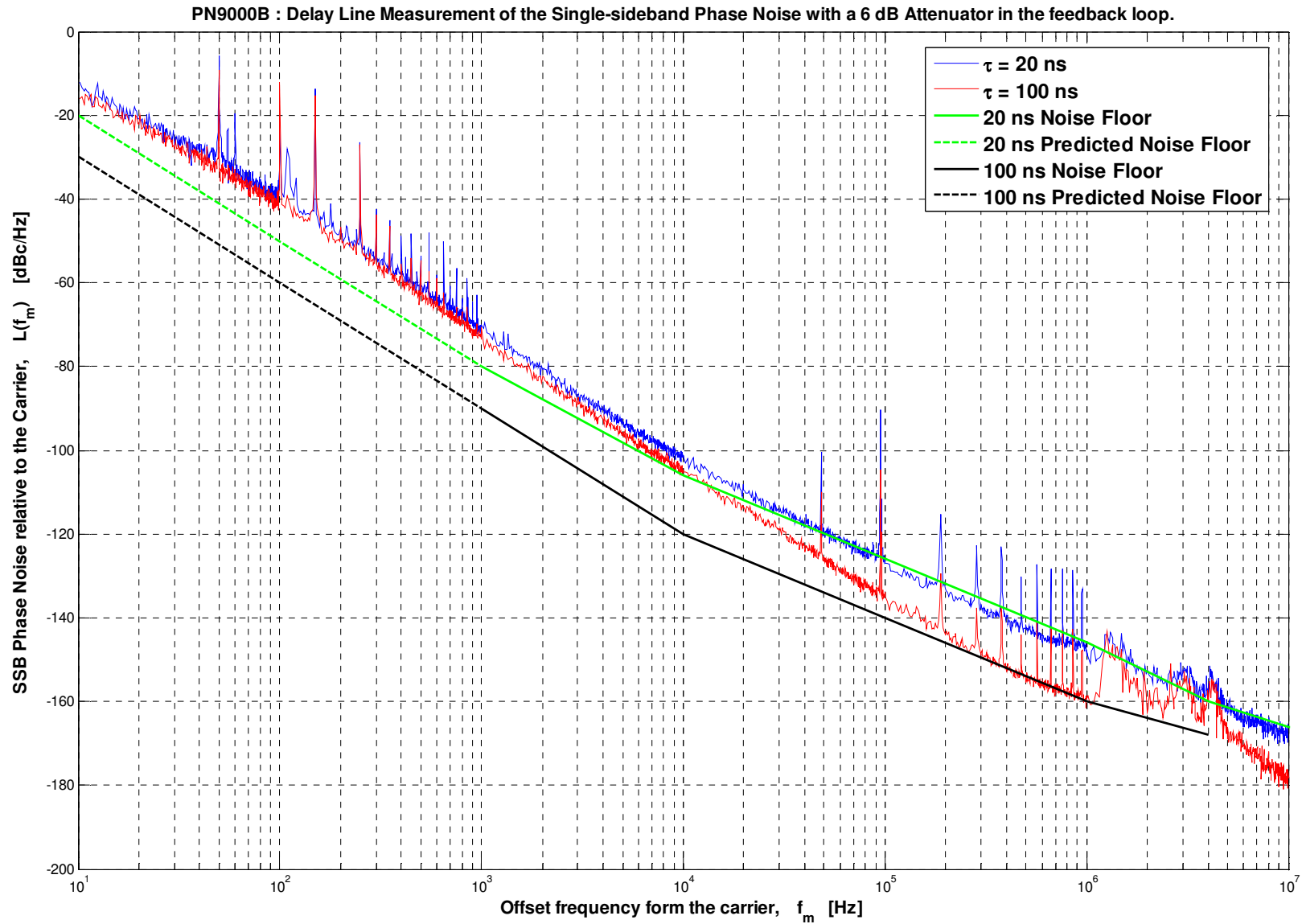


Figure 4.40: Delay Line Measurement of the SSB Phase Noise with a 6 dB Attenuator in the feedback loop.

4.2.5 ‘Destructive’ Measurements

As shown in Table 4.6 on page 191 in Section 4.2.3, a discrepancy exists between the expected values and the measured values for Q_U and Q_L . As a result, it was decided to take the VCO system apart – therefore conducting the ‘destructive measurements’ – to precisely confirm which component is causing this vast difference.

The process involved removing a set of components at one time e.g. all four of the varactor diodes, while the unloaded as well as the loaded Q-values were measured before and after removing the components. After removing the varactor diodes, this process was repeated for the bypass capacitors, the V_{tune} wires as well as the PCB, respectively. Until only the resonator with its SMA connectors were left.

It was decided to, instead of showing all the Q_U and Q_L S-parameter plots, to rather report on these measurements by summarising all relevant values in the table below, and then discussing it afterwards.

Table 4.7: Q-values measured during the ‘Destructive’ Measurements.

Measurement		Q_U	Q_L
0	Resonator – Table 4.2 (p.172)	1427.40	713.71
1	Resonator Alone	1426.29	747.67
2	Put the PCB in...	542.37	273.54
3	+ V_{tune} wires	407.03	200.01
4	+ Bypass Capacitors	482.42	260.48
5	+ Varactor Diodes*	372.11	200.59

* Complete system reached: Resonator and PCB (with Diodes, Capacitors and V_{tune}).

A few comments on the measurements taken above:

- All of the above measurements were taken at $V_{\text{tune}} = 22 \text{ V}$.
- *Measurement 1 to 2:* When the **PCB** is added to the resonator, the loaded Q-value decreases with about **63 %**:

$$\text{Decrease}_{\%} = \frac{Q_{L_{\text{Resonator}}} - Q_{L_{\text{Res\&PCB}}}}{Q_{L_{\text{Resonator}}}} \% = \frac{(747.67 - 273.54)}{747.67} \% = 63.414\%$$

- *Measurement 3*: Adding the V_{tune} wires causes Q_L to decrease further with another **10 %**:

$$\text{Decrease}_{\%} = \frac{Q_{L_{\text{Res\&PCB}}} - Q_{L_{\text{Res\&PCB\&Vtune}}}}{Q_{L_{\text{Resonator}}}} \% = \frac{(273.54 - 200.01)}{747.67} \% = 9.8359\% .$$

- *Measurement 4*: Next, the bypass capacitors were added. As a result the loaded Q-value increased again, with **10 %**. The reason for the latter is probably because; the V_{tune} -biasing track on the PCB is now dynamically defined as GND.
- *Measurement 5*: By adding the varactor diodes, the latter increase of 10 % cancels again due to the loaded Q-value decreasing by **10 %**.
- Thus, while measurements **4** and **5** cancels each other, a total decrease in the loaded Q-value, of 550 occurred when the PCB and all its components (V_{tune} wires, variable tuning diodes and their bypass capacitors) are added. The latter value represents about a total of **73 %** decrease in Q_L .

The obvious question then is: ‘What is causing the PCB to have such an unwanted effect on the Q-value of the resonator?’ Probable answers to this question are explained in the following section.

4.2.6 Theoretical Explanation for the adverse effect of the PCB on the Q-value

The reason for choosing to make use of FR-4 as the dielectric material for the PCB, was due to the availability of a very thin sheet of FR-4, i.e. 200 μm thick. The thinnest possible piece of FR-4 was chosen, in order to keep the dielectric losses to a minimum.

There are three possible explanations for this unwanted effect that the PCB has on the Q-value of the resonator. The first two reasons will only be mentioned lightly, while the third will be explained in more detail.

Firstly, refer back to Fig. 4.26 (b) on page 185. The latter illustrates the exact, final PCB that was removed from the resonator in the ‘Destructive’ measurements.

The PCB illustrated in Fig. 4.26 (b) has been produced by cutting the PCB depicted in Fig. 4.26 (a). When the PCB was added to the cavity, bigger coupling loops were required to still get the desired amount of coupling. As a result, the PCB had to be cut. The problem is more likely to occur for the PCB in Fig. 4.26 (b) since the possibility exists that one of the tracks present on the PCB, could be resonating at some frequency point. This would cause the loss in the resonator to increase, which will result in a decreased Q-value.

Secondly, by referring back to the illustrated magnetic field inside the cavity of the resonator (Fig. 3.27 on page 120), it is clearly visible that the H-field is parallel to the floor of the resonator. For that specific reason it was decided to add the PCB, also level to the floor of the resonator. That is, parallel to the magnetic field, in the belief that the PCB would have no effect. But according to the ‘Destructive’ measurements done in the previous section, the PCB itself is the main reason for the poor Q-value. It was thought that, since the PCB sheet is so thin, and due to the already many adjustments made to the PCB itself, that it is no longer level to the resonator floor, and perhaps appear a bit ‘wobbly’. As a result, it could be possible that the magnetic field couple to the tracks on the PCB, causing unnecessary currents to arise and as a result, redundant dielectric losses.

Finally, the last explanation for the adverse effect that the PCB has on the Q-value of the resonator has to do with the electric field present inside the cavity [23, 38]. From the theory of electromagnetism, $\Phi(\mathbf{r})$ is defined as the electric potential of the point \mathbf{r} with respect to the reference point (usually the GND potential). Therefore the potential difference is equal to the *voltage* at \mathbf{r} relative to that at the GND potential (reference). The equation for the potential difference is:

$$\Phi(\vec{r}) - \Phi(\vec{r}_{ref}) = \int_{\vec{r}}^{\vec{r}_{ref}} \vec{E} \cdot d\vec{s} . \quad (4.6)$$

For the electric field always perpendicular to Φ , it can also be written that, for

$$\vec{E} = -\nabla\Phi , \quad (4.7)$$

$$\int_{\vec{r}_{ref}}^{\vec{r}} \nabla\Phi \cdot d\vec{s} = \Phi(\vec{r}) - \Phi(\vec{r}_{ref}) = \int_{\vec{r}}^{\vec{r}_{ref}} \vec{E} \cdot d\vec{s} . \quad (4.8)$$

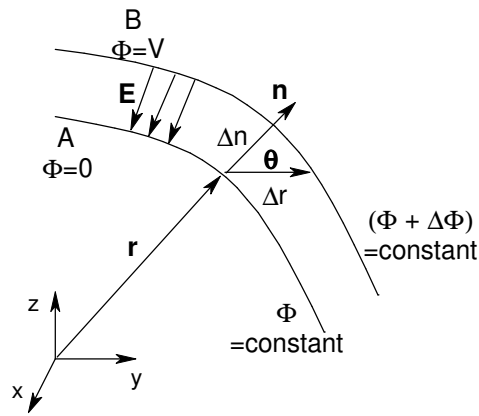


Figure 4.41: Two equipotential surfaces shown.

In Fig. 4.41 are the cross-sections of two equipotential surfaces. The one is passing through the point \mathbf{r} , while the other is passing through the point $(\mathbf{r} + \Delta\mathbf{r})$. The potential at these different points differs by the differential amount $\Delta\Phi$.

The source of the electric field is the charge density, ρ . Relating the \mathbf{E} -field to its source is done by means of Gauss' law:

$$\oint_S \epsilon_0 \bar{E} \cdot d\bar{a} = \int_V \rho dv \quad (4.9)$$

$$\bar{\nabla} \cdot \epsilon_0 \bar{E} = \rho \quad (4.10)$$

The electric flux density ($\epsilon_0 \bar{E}$) passing through a surface S is described by the net charge within an arbitrary volume V , that is enclosed S . The \mathbf{E} -field is always perpendicular to the surface, and it is null inside a conductor since the voltage on the inside, $V = 0$.

Consider the PCB designed in this project, as illustrated in Fig. 4.42 on the next page. As mentioned earlier, the electric field lines are perpendicular to the conductors (outwards, in a radial direction), and are demonstrated in Fig. 4.42 by means of the dashed lines. The pink (GND) and green (V_{tune}) blocks represents the Cu-tracks present on the PCB, while 'g' represents the 'air-gaps' between the Cu-tracks.

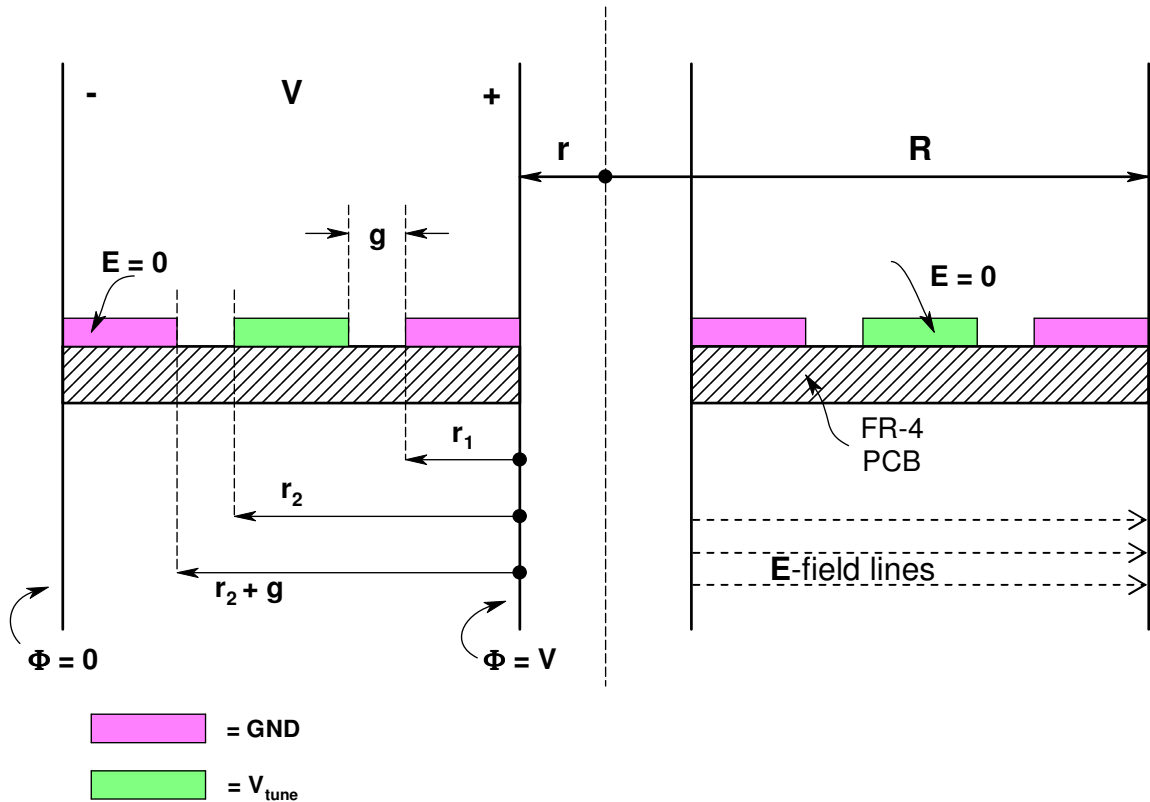


Figure 4.42: Representation of the designed PCB, situated inside the cavity of the resonator.

Therefore, when applying (4.6) to the above figure, the following equation can be written for the potential difference between the inner and outer conductors (point \mathbf{r} and \mathbf{R}) of the resonator:

$$\Phi(\bar{r}) - \Phi(\bar{R}) = (V - 0) = V. \quad (4.11)$$

Therefore, from (4.6) and (4.11) the following can be written:

$$\Phi(\bar{r}) - \Phi(\bar{R}) = \int_{\bar{r}}^{\bar{R}} \bar{E} \cdot d\bar{r}. \quad (4.12)$$

So that,

$$V = \int_{r_1}^{r_1+g} \bar{E} \cdot d\bar{r} + \int_{r_2}^{r_2+g} \bar{E} \cdot d\bar{r}. \quad (4.13)$$

From (4.11) the potential difference between point \mathbf{r} and \mathbf{R} is given as V [volts]. From the latter, the following explanation is given for the distribution of the electric field between the same points on the PCB.

Suppose there are no Cu-tracks present on the PCB, then the electric field would be uniformly distributed from point r to point R , portraying Fig. 4.43 (a). A decline in E is visible, since the field line density is less at point R than at point r .

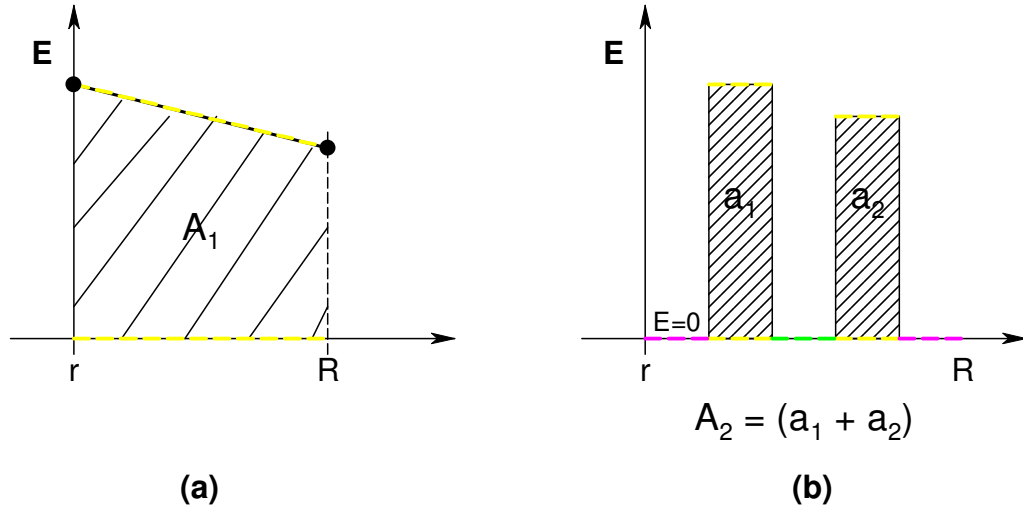


Figure 4.43: Electric Field distribution for the PCB (a) without Cu-tracks, and (b) with Cu-tracks.

Consider Fig. 4.43 (a). The E-field is uniformly distributed from r to R . The area underneath the E-field curve is equal to the integral of the E-field, which is equal to the potential difference between point r and R .

Consider Fig. 4.43 (b). Keep in mind that the potential difference ($=V$) stays the same between points r and R . Since the presence of the Cu-tracks influences the existence of the E-field, and the area underneath the E-field curve should still be sufficiently large to keep the potential difference constant, the only way to achieve the latter would be if the E-field strength increases tremendously in the areas where it is not zero (thus, where there are no conductors present).

Thus for both cases (with or without the Cu-tracks present), it is important that the potential difference stays the same. Therefore, the E-field strength – illustrated by the areas in Fig. 4.43 – need to be sufficiently large, so that $A_2 = A_1$.

But, how does one connect the latter information to the Q-value decreasing as the E-field strength increases?

Consider Example 7.2.1 given by *Haus & Melcher* [38]. For any parallel plate (conducting electrodes constraining the potential) representation of a resistor, with a cross-section area A , length d (between the electrodes) and a conductivity of $\sigma(y)$; the equivalent conductance is defined by:

$$G = A \int_0^d \frac{dy}{\sigma} \quad (4.14)$$

For a constant, uniform conductivity (4.14) becomes:

$$G = \frac{A\sigma}{d} \quad (4.15)$$

Representing (4.15) in terms of the equivalent resistance, it can be written that:

$$R = \rho \cdot \frac{d}{A} \quad (4.16)$$

Thus substituting the latter resistance into the power equation,

$$P \propto \frac{V^2}{R} \quad (4.17)$$

the dissipated power could be calculated for any given resistance, R .

From (4.17) it can be said that for the case in which the Cu-tracks are present, d will be a smaller value, than when no Cu-tracks are present. Therefore, the piece of FR-4 (depicted in Fig. 4.44) will be represented by a smaller resistance, R .

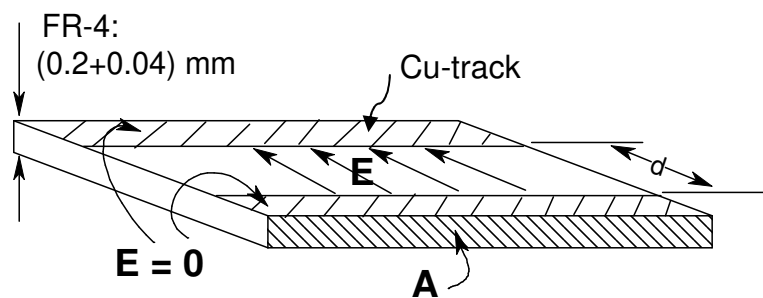


Figure 4.44: A piece of the FR-4 PCB, illustrating the Electric Field present.

Consequently, from (4.17) it is clear that the dissipated power will increase, as R decreases, which results in the Q -value decreasing as well, since $Q \propto (1/P)$.

To summarise – the E-field is concentrated in the regions where no Cu-tracks are present (i.e. between the tracks). This is causing unnecessary losses inside the cavity of the resonator, which finally causes the Q-value to drop below expectation.

In the following section the additional simulations done in **CST**, to confirm the recently gained information, as well as those effects noticed through the ‘destructive’ measurements are discussed.

4.3 ADDITIONAL CST SIMULATIONS

In this section four main simulations were done on the resonator and the PCB. All of the simulations were conducted by utilizing **CSTs Frequency Domain Solver**. For each one of the simulations done the following system parameters were determined:

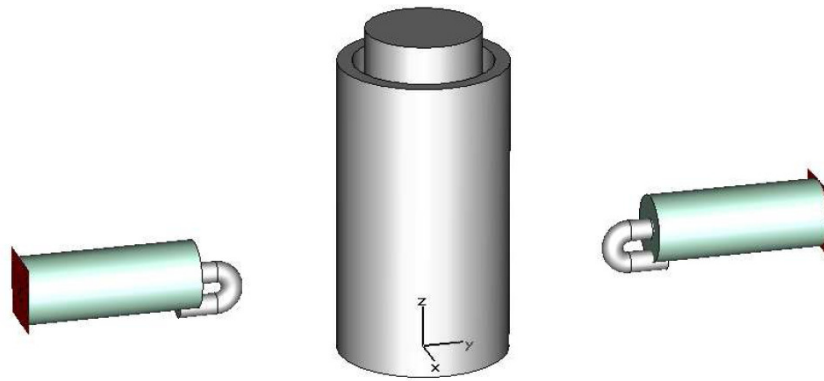
- The resonant frequency,
- S-parameters,
- Internal Q-value (Q_U), as well as the
- Loaded Q-value, (Q_L).

The following simulations were done respectively:

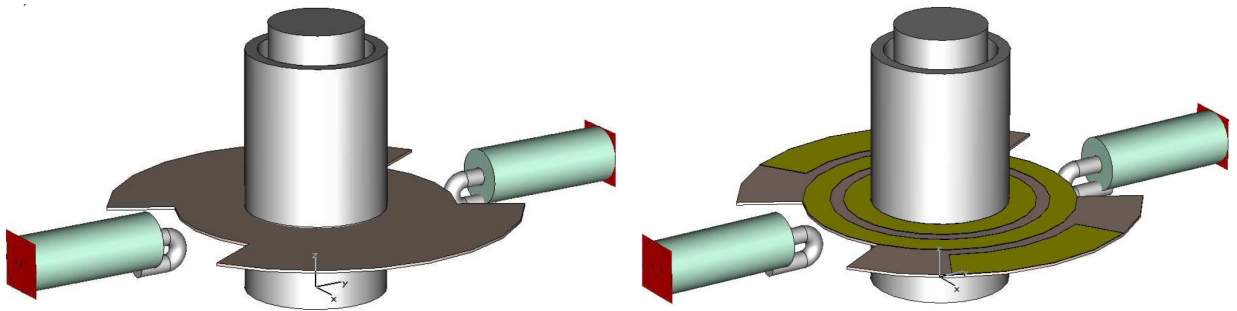
- Resonator Alone, no PCB,
- Resonator and the designed PCB,
- Resonator and the practical adjusted PCB, (*‘practical adjusted’* refers to the PCB that was cut to fit the coupling loops; see Fig. 4.26 (b), p.185),
- Resonator and the proposed ‘key-hole’ solution PCB.

For the last three simulations with the PCB present in the cavity, the above mentioned parameters were determined for the PCB without Cu-tracks as well as for the instance where the Cu-tracks were added.

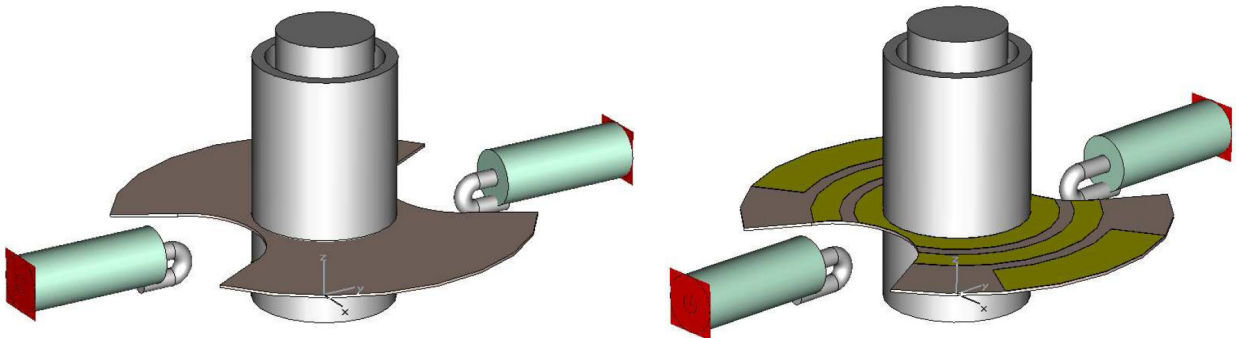
It was decided not to add all of the simulated graphs, but rather to summarise all the results obtained, in Table 4.8 (p.209). On the following page, images are shown of exactly how the simulated systems appeared.



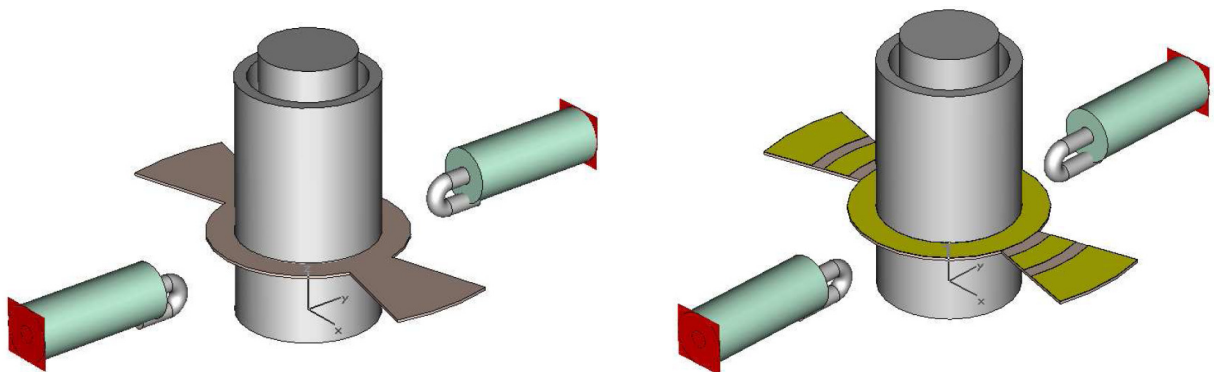
(a) Resonator alone



(b) Resonator and the designed PCB



(c) Resonator and the practical adjusted PCB



(d) Resonator and the proposed 'key-hole' solution PCB

Figure 4.45: Simulations done on the Resonator for different PCB solutions.

Table 4.8: Resonator S-parameters and Q-values obtained for different PCB solutions simulated.

RESONATOR:	FR-4 – without the Cu-tracks					FR-4 – with the Cu-tracks				
	f_0 [MHz]	S_{21}^* [dB]	S_{11}^* [dB]	Q_{intern}^1	Q_{Loaded}^2	f_0 [MHz]	S_{21}^* [dB]	S_{11}^* [dB]	Q_{intern}^1	Q_{Loaded}^2
Alone	979.6458 ³	-6.174	-5.891	2133.7	1671.92	-	-	-	-	-
with the designed PCB[#]	979.7025 ³	-6.147	-5.934	2053.9	1579.76	975.65 ⁴	-5.995	-6.078	1663.4	1136.20
with the practical adjusted PCB	980.052 ⁵	-5.916	-6.164	1972.3	1512.24	967.112 ⁵	-5.857	-6.182	1457.9	959.98
with the proposed 'key-hole' solution PCB	977.97	-6.1	-6.016	1707.0	1365.78	-	-	-	-	-

The PCB material used was: FR-4 – 0.2 mm, with its *Electrical loss factor*, $\tan(\delta) = 0.025$ (**CST**).

* $S_{21} \approx S_{12}$ and $S_{11} \approx S_{22}$.

For the same size coupling loops, S_{21} drops with about 3.5 dB as soon as the Cu-tracks are added to the PCB.

¹ Calculate the internal Q-value ($\approx Q_U$) by means of an H-field Monitor at f_0 : 'Results – Loss and Q Calculation – H-field data'.

² Calculate the loaded Q-value: $Q_L = f_0 / (3\text{dB BW})$, as measured from the S_{21} curve.

³ Simulated over a 700 kHz frequency band. Accuracy = $1e^{-4}$.

⁴ Simulated over a 5 MHz frequency band. Accuracy = $1e^{-5}$.

⁵ Simulated over a 4 MHz frequency band. Accuracy = $1e^{-5}$.

PS. For every single one of the above mentioned simulations, the coupling loop's length (**condel**) was adjusted. See Chapter 3, p.121.

This was done to ensure that the value for S_{21} is as close to -6 dB as possible.

To conclude the results summarised in Table 4.8 a brief discussion is given on the effect of the different PCB solutions:

All 'decrease in percentage' mentioned in the following paragraphs, were determined by comparing the new simulated result to that previously obtained for the resonator itself, where no PCB was present in the cavity.

When adding the *designed* PCB (without the Cu-tracks present) to the resonator's cavity, the loaded Q-value decreases by 5.512 %. When the Cu-tracks are added to the simulation, it results in a reduction of the loaded Q-value by 32 %.

When the *practical adjusted* PCB was added to the cavity of the resonator, the loaded Q-value decreased by 9.551 %; i.e. for the PCB without the Cu-tracks. When the Cu-tracks are added to the PCB, the loaded Q-value reduces by **42.58 %**.

The proposed 'key-hole' solution PCB (without the Cu-tracks) causes the loaded Q-value to decrease by 18.31 %.

In all of these results it is clear that the Cu-tracks are the main reason for the reduction in the loaded Q-value of the resonator. These results confirm the 'destructive' measurements executed and reported on in Section 4.2.5 on page 200.

The concluding results underline the fact that one has to take tremendous care when trying to manage the loss in a system. The only way out would be to investigate alternative ways in coupling the variable tuning diodes to the resonator.

This concludes the design and measurements done for the *Voltage Controlled Oscillator* (VCO) System. In the following chapter, the most significant results of the oscillator system are compared to that obtained for the VCO. A phase noise plot is also provided, in which the measured phase noise result for the oscillator is compared to that of the VCO.

CHAPTER 5

SUMMATION OF THE OSCILLATOR VS. VCO RESULTS

5.1 SUMMARY OF ALL RELEVANT OUTCOMES

Table 5.1: Summation of the Oscillator vs. VCO results.

		$Q_{\text{Simulated}}$	Q_{Measured}	Reference	
UNLOADED	Chapter 3: Oscillator	2133.7	1427.9	Table 3.12	p. 130
	Chapter 4: VCO	1457.9	362.44	Table 4.6 Table 4.8	p. 191 p. 209
LOADED	Chapter 3: Oscillator	1668.2	713.71	Table 3.12	p. 130
	Chapter 4: VCO	959.98	195.01	Table 4.6 Table 4.8	p. 191 p. 209

5.2 COMPARED SSB PHASE NOISE MEASUREMENT

On the following page, the single-sideband phase noise measurement for the *Oscillator* system is compared to the single-sideband phase noise measurement for the *Voltage Controlled Oscillator* system. It is also summarised in Table 5.2.

Table 5.2: SSB phase noise values for the measurement in Fig. 5.1.

	Oscillator	VCO
Offset frequency, f_m [Hz]	$L(f_m)$ [dBc/Hz]	$L(f_m)$ [dBc/Hz]
10	≈ -32	≈ -15
100	- 62.89	- 42.75
1k	- 90	- 73.42
10k	- 121.6	- 105.1
30k	≈ -132	≈ -119
100k	--	-135

PN9000B : Comparing the Single-sideband Phase Noise measurement of the Oscillator to that of the VCO, with a 6 dB Attenuator in the feedback loop.

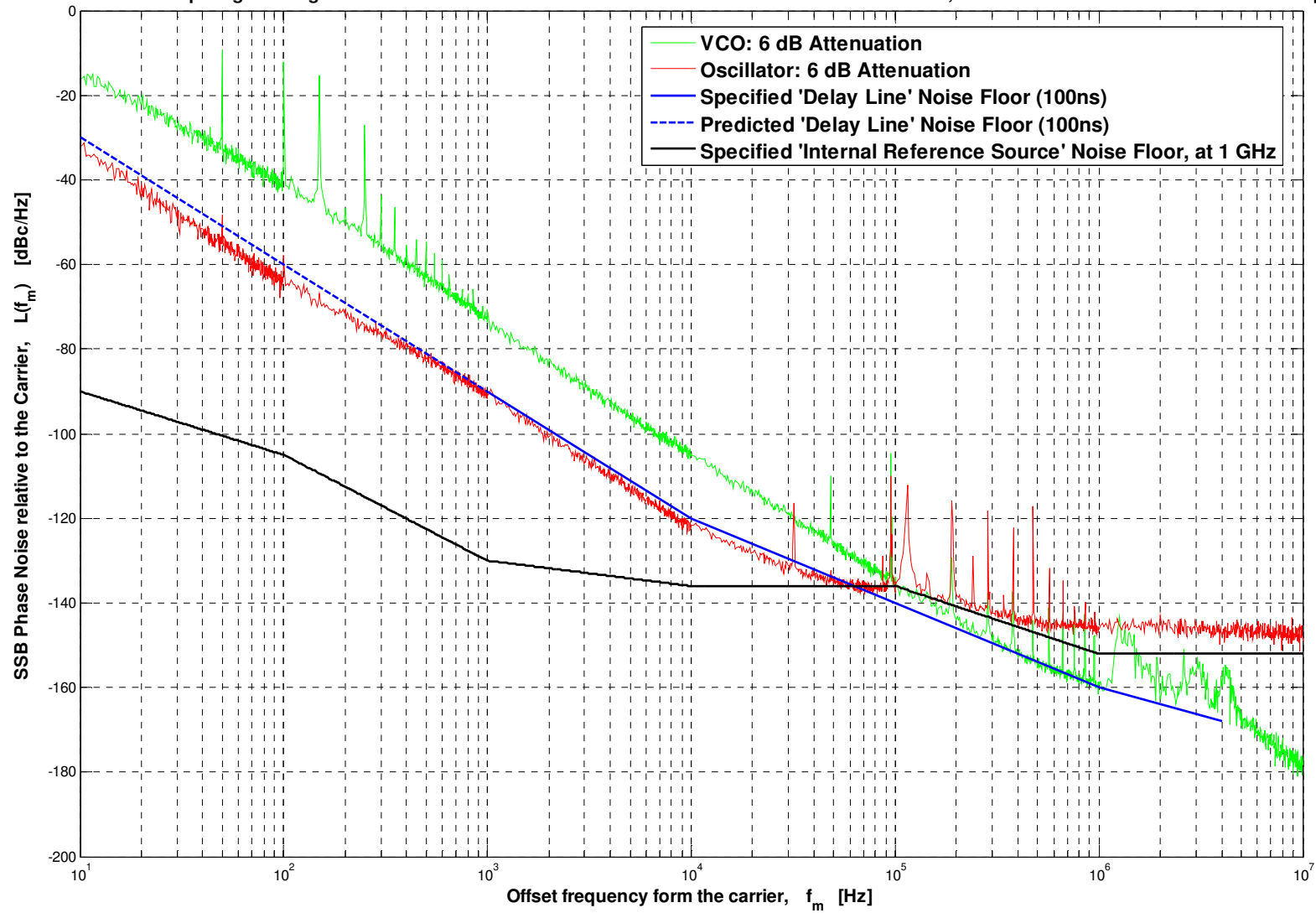


Figure 5.1: Comparison between the SSB phase noise measurements for the Oscillator and the VCO Systems.

CHAPTER 6

CONCLUSIONS AND RECOMMENDATIONS

This thesis was started by thoroughly investigating the literature on the requirements, design, simulation and measurement of oscillator systems. A simulation example was also included for a Colpitts oscillator, in which some light was shed on linear- vs. non-linear simulation techniques. This study was augmented with a detailed review of exactly what noise and in particular, phase noise is. The study on phase noise involved the consideration of how phase noise is specified (Leeson's Phase Noise Model), where it originates from, and how it could be controlled and minimised in systems sensitive to phase noise.

Subsequently, the specification for a high Q-value, low phase noise Voltage Controlled Oscillator was received. It wasn't sure beforehand if the specifications would even be reachable, but with no less effort the task was attempted.

The project started off with the design of a low phase noise, high Q-value *Oscillator* system. It was learnt from the recently completed study of oscillators, that one of the primary factors that determine the overall Q-value of the oscillator system is the Q-factor of the frequency selective component; the resonator present in the design. As a result, a major focus of this Master Study was to design a high-Q resonator. Several software packages were utilized and considerably detailed transmission line theory was studied for proper design. After the successful design of the resonator, all necessary measurements were done to be able to exactly describe the resonator's behaviour. With regard to the resonator, the only problem experienced, was that its simulated Q-value did not concur with that which was measured. Several techniques were tried to establish a reason for this observation; but no apparent explanation could be found. Consequently, all simulated values were adjusted to those measured, in order for further design to take place. The various parts constituting the oscillator design were compiled, respectively measured

and discussed. Finally the oscillator system was constructed, which was followed by several distinct measurements taken of the system to accurately describe its performance. The final measurement done was that of the oscillators' single-sideband phase noise relative to the carrier. The predicted (by Leeson's Phase Noise Model) result for the SSB phase noise accurately described that which was measured. The only problem that was experienced at this stage was that the measurement equipment used to ascertain the SSB phase noise of the oscillator was not sufficient to perform the measurement, especially at offset frequencies of 40 kHz and beyond. Therefore it would be advised for future development, to make use of another external reference oscillator when utilizing the *Aeroflex PN9000B Automatic Phase Noise Test System*. A reference oscillator with a phase noise lower than that of the internal reference oscillator of the PN9000B is suggested. As mentioned previously, a good example of such an oscillator would be an identical replica to the one designed in this project. To conclude the oscillator design, it can be said that the oscillator system performed particularly well, and subsequently the phase noise meter could not establish the oscillator's noise floor.

Following the oscillator design, the latter was modified to a Voltage Controlled Oscillator. This is where the other primary factor in the overall Q-value of the system comes in, the variable tuning diodes. As a result, high-Q varactor diodes were obtained for this design. Unfortunately the disadvantage of these diodes is that they limit the maximum frequency tuning bandwidth that could be reached. Thus, an optimum had to be reached where the loaded Q-value was not permitted to reduce below a certain (chosen) value, while the maximum tuning bandwidth was required. This optimum point was the indication of where to couple the diodes to the resonator. A printed-circuit board was designed onto which the diodes were soldered, before the former was connected to the resonator. All necessary measurements were done to confirm the Q-values of the VCO, as well as the tuning bandwidth achieved. The only problem that occurred was that the PCB had a much greater effect on the Q-value of the resonator, than was expected. Additional simulations were done to confirm this behaviour. Finally, the phase noise of the VCO was also measured on the Aeroflex system. Unfortunately, due to the residual phase noise of the meter, no accurate measurements could be made at offset frequencies beyond 200 kHz. To

conclude, it would be advised to consider alternative methods of coupling the varactor diodes to the resonator.

Overall, both systems performed extremely well, and for the problems experienced during the project, one can only declare that valuable knowledge was gained in the end, which ends this Mater study on a high note.

LITERATURE REFERENCES

- [1] Merrill. I. Skolnik (Editor-in-Chief), *Radar Handbook*, McGraw-Hill Book Company, Inc., New York, 1970.
- [2] Robert Buder, *The Invention That Changed The World: How a Small Group of Radar Pioneers Won the Second World War and Launched a Technological Revolution*, Simon & Schuster, New York, 1997.
- [3] P.H. Young, *Electronic Communication Techniques*, 3rd ed., New York: Maxwell Macmillan, 1993, Chapter 2.
- [4] U.L. Rohde (ulr@synergymwave.com), "Voltage controlled oscillators," May 2007, <http://www.synergymwave.com/articles/PDF/Voltage-Controlled-Oscillators.pdf>.
- [5] Donald A. Neamen, *Electronic Circuit Analysis and Design*, 2nd ed., McGraw-Hill International Edition, 2001.
- [6] *AWR Microwave Office 2004 (MWO-225)*, Simulation Program, "MWO/AO User Guide, Linear and Steady State Nonlinear Analysis", <http://appwave.com/>.
- [7] "Appendix C: Linear analysis of oscillator circuit," class notes for MWE 813 – JBdeS, Department of Electrical and Electronic Engineering, University of Stellenbosch, 2006.
- [8] Simon Haykin, "Fourier Transform," in *An Introduction to Analog and Digital Communications*, John Wiley & Sons, Inc., 1989, pp. 20-24, 32.
- [9] *The IEEE Standard Dictionary of Electrical and Electronics Terms*, 6th ed. (IEEE Standard 100-1996), Authored by the 10th Standards Coordinating Committee for Terms and Definitions, April 1997.
- [10] David M. Pozar, *Microwave and RF Design of Wireless Systems*, John Wiley & Sons, Inc., 2001, pp. 68, 73-75.

- [11] Aeroflex, "PN9000 Automated Phase Noise Measurement System," Application note # 1, 2003.
- [12] Mini-Circuits, *VCO Designer's Handbook*, VCO/HB-01, 2001.
- [13] Roger E. Ziemer and William H. Tranter, *Principles of Communication – Systems, Modulation and Noise*, 5th ed., John Wiley & Sons, Inc., 2002.
- [14] David M. Pozar, *Microwave Engineering*, 3rd ed., John Wiley & Sons, Inc., 2005.
- [15] Applied Radio Labs, "Phase Noise Reference," March 2003, <http://www.radiolab.com.au/DesignFile/PNRef/PNRef.htm>.
- [16] Mini-Circuits, "Characterising Phase Noise," pp. 58-59, January 2003, <http://www.rfdesign.com>.
- [17] Ulrich L. Rohde, "A new and efficient method of designing low noise microwave oscillators," Ph.D. dissertation, University of Berlin, Berlin, Germany, 2004.
- [18] Hewlett Packard, "Phase Noise Characterization of Microwave Oscillators – Phase Detector Method," Product Note # 11729B-1, date not available.
- [19] Anderson Electronics, Inc., "Phase Noise," March 2007, <http://www.aextal.com/tutorial-phase-noise.htm>.
- [20] Robert E. Collin, *Foundations for Microwave Engineering*, 2nd ed., McGraw-Hill International Editions, 1992, pp. 481-516.
- [21] RF, RFIC & Microwave Theory, Design, "Phase Noise," February 2007, <http://www.rfic.co.uk/Systems And Devices Page.htm>.
- [22] D.B. Leeson, "A simple Model of Feedback Oscillator Noise Spectrum," *Proceedings of the IEEE*, vol. 54, no. 2, pp. 329-330, February 1966.
- [23] Prof. P.W. van der Walt (private conversation), December 2006.
- [24] Simon Ramo, John R Whinnery, Theodore van Duzer, *Fields & Waves in Communication Electronics*, 2nd ed., John Wiley & Sons, Inc., 1984.

- [25] *Reference Data for Radio Engineers*, 6th ed., Howard W. Sams & Co., Inc., 1975.
- [26] H.A. Wheeler, "Transmission-Line Properties of a Strip on a Dielectric Sheet on a Plane," *IEEE Transactions on Microwave Theory and Techniques*, vol. 25, no. 8, pp. 631-647, August 1977.
- [27] H.A. Wheeler, "Formulas for the Skin Effect," *Proceedings of the IRE*, vol. 30, pp. 412-424, September 1942.
- [28] G. Matthaei, L. Young, and E.M.T. Jones, *Microwave Filters, Impedance-Matching Networks, and Coupling Structures*, reprinted 1st ed. Massachusetts: Artech House, Inc., 1980, pp. 214-217, 430.
- [29] Simon Ramo, John R Whinnery, Theodore van Duzer, *Fields & Waves in Communication Electronics*, 2nd ed., John Wiley & Sons, Inc., 1984, pp. 153, 250-252.
- [30] Robert E. Collin, *Foundations for Microwave Engineering*, 2nd ed., McGraw-Hill International Editions, 1992, p. 89, 523.
- [31] Temex, "Microwave Tuning Elements," pp. 112-113, April 2007, <http://www.temex.com>.
- [32] California Fine Wire, "Copper Alloy," September 2007, <http://www.calfinewire.com>.
- [33] Copper Organisation, "Properties of Wrought and Cast Copper Alloys," September 2007, <http://www.copper.org>.
- [34] Metal Mart International, Inc., "Copper Alloy Guide," September 2007, http://www.metal-mart.com/Guides/Copper_Alloy_Guide.htm.
- [35] High Frequency Laboratory, Dept. of Electronic & Electrical Engineering, University of Stellenbosch, "High Frequency Lab/Equipment", October 2007, http://services.ee.sun.ac.za/wiki/index.php/High_Frequency_Lab/Equipment/
- [36] Seattly Robotics, "Basic Circuits - Bypass Capacitors," October 2005, <http://www.seattlerobotics.org/encoder/jun97/basics.html>.

- [37] Electronic Parts and Components, "Design Tools, Ceramic Capacitors, Impedance Data for simulation, S-Parameters, 0603," November 2007, <http://www.epcos.com>.
- [38] Hermann A Haus, James R Melcher, *Electromagnetic Fields and Energy Vol 1*, Prentice-Hall Inc., 1989, pp. 12, 90, 256.

Appendix A

'Incremental-Inductance Rule'

```

1 % =====
2 % MATLAB code for: The 'Incremental-Inductance Rule' - H.A. Wheeler.
3 % Thesis: Paragraph 3.1.2.2
4 % Aim: Determine typical starting values for the resonator's dimensions
5 % =====
6
7 format long;
8
9 % Constants:
10 % -----
11 u = 1e-6;
12 m = 1e-3;
13 M = 1e6;
14
15 % Variables:
16 % -----
17 f0 = 900*M;
18 c = 2.99792e8;
19 lambda = c/f0;
20 delta = 3.81*sqrt(lambda)*u;
21
22 % =====
23
24 % Line 2: Short-circuit Line:
25 % -----
26 D2 = 30*m;
27 d2 = [0.005 : 0.00001 : 0.01];
28 Z02 = 60*log(D2./d2);
29
30 % Determine the value for d2, where Z02 = 70 ohm:
31 % -----
32 index = find((Z02 > 69.9) & (Z02 < 70.1));
33 a = (Z02(index));
34 for i = 1:length(a)
35     b(i) = abs(a(i)-70);
36 end
37 index_min_b = find(b == min(b));
38 index_closest_to_70ohm = find(Z02 == a(index_min_b));
39 d2_70ohm = d2(index_closest_to_70ohm);
40 Z02_70ohm = Z02(index_closest_to_70ohm);
41

```

```

% resonant frequency, [Hz]
% speed of light, [m/s]
% wavelength at f0, [m]
% skin effect, 2.2e-06 [m], at f0

% Resonator's outer diameter, [m]
% Vector for d2 values...
% We want Z02 = 70 [ohm] - chosen!

```



```

42 % 'Incremental-Inductance Rule':
43 % -----
44 %Z02_delta = 60*log((D2 + delta)./(d2 - delta));
45 Z02_delta = 60*log((D2 + delta)./(d2_70ohm - delta));
46 p2 = (Z02_delta - Z02)./(Z02_delta);
47 Q2 = 1./p2;
48 Q2_70ohm = Q2(index_closest_to_70ohm);
49
50 % =====
51
52 % Line 1: Open-circuit Line:
53 % -----
54 %d2_70ohm = 0.00934;
55 cond = 1*m;
56 D1 = d2_70ohm - cond;
57 d1 = [0.002 : 0.00001 : 0.008];
58 Z01 = 60*log(D1./d1);
59
60 % Determine the value for d1, where Z01 = 10.99 ohm:
61 % -----
62 index1 = find((Z01 > 10.89) & (Z01 < 11.09));
63 a1 = (Z01(index1));
64 for i = 1:length(a1)
65     b1(i) = abs(a1(i)-10.99);
66 end
67 index_min_b1 = find(b1 == min(b1));
68 index_closest_to_10_99ohm = find(Z01 == a1(index_min_b1));
69 d1_10_99ohm = d1(index_closest_to_10_99ohm);
70 Z01_10_99ohm = Z01(index_closest_to_10_99ohm);
71
72 % 'Incremental-Inductance Rule':
73 % -----
74 %Z01_delta = 60*log((D1 + delta)./(d1 - delta));
75 Z01_delta = 60*log((D1 + delta)./(d1_10_99ohm - delta));
76 p1 = (Z01_delta - Z01)./(Z01_delta);
77 Q1 = 1./p1;
78 Q1_10_99ohm = Q1(index_closest_to_10_99ohm);
79
80 % =====
81
82

```

```

% loss PF of the magnetic field
% unloaded Q-value

```

```

% Conductor thickness = 0.5 [mm]

% We want Z01 = 10.99 [ohm] - calculated!

```

```

83 % Plot figures:
84 % -----
85
86 % Line 2: Short-circuit line.
87 % -----
88 figure(1);
89 plot(d2, Z02, 'Linewidth', 3);
90 title('\bfCharacteristic Impedance (Z_{02}) versus the inner-conductor diameter (d_2) of the Short-circuit Line.',
'FontSize', 16);
91 ylabel('\bfZ_{02} - Characteristic Impedance - [\Omega]', 'FontSize', 16);
92 xlabel('\bfd_2 - The inner-conductor diameter of Line 2 - [m]', 'FontSize', 16);
93 grid on;
94 hold on;
95 plot(d2, Z02_70ohm, '-r');
96 plot(d2_70ohm, Z02_70ohm, 'ko', 'Linewidth', 3);
97 plot([d2_70ohm d2_70ohm], [Z02_70ohm (Z02_70ohm + 5)], 'k-', 'Linewidth', 2);
98 text((d2_70ohm - 0.3e-3), (Z02_70ohm + 6), strcat('\bfd_2 = ', num2str(d2_70ohm)), 'FontSize', 16);
99
100 figure(2);
101 plot(d2, Q2, 'Linewidth', 3);
102 title('\bfUnloaded Q-value versus the inner-conductor diameter (d_2) of the Short-circuit Line.', 'FontSize', 16);
103 ylabel('\bfUnloaded Q-value', 'FontSize', 16);
104 xlabel('\bfd_2 - The inner-conductor diameter of Line 2 - [m]', 'FontSize', 16);
105 grid on;
106 hold on;
107 plot(d2_70ohm, Q2_70ohm, 'ko', 'Linewidth', 3);
108 plot([d2_70ohm - 0.3e-3 d2_70ohm], [Q2_70ohm Q2_70ohm], 'k-', 'Linewidth', 2);
109 text((d2_70ohm - 0.95e-3), (Q2_70ohm), strcat('\bfQ_2 = ', num2str(Q2_70ohm)), 'FontSize', 16);
110
111
112
113
114 % -----
115
116
117
118
119
120
121
122

```

```

123 % Plot figures:
124 % -----
125
126 % Line 1: Open-circuit line.
127 % -----
128 figure(3);
129 plot(d1, Z01, 'Linewidth', 3);
130 title('\bfCharacteristic Impedance (Z_{01}) versus the inner-conductor diameter (d_1) of the Open-circuit Line.',
'FontSize', 16);
131 ylabel('\bfZ_{01} - Characteristic Impedance - [\Omega]', 'FontSize', 16);
132 xlabel('\bfd_1 - The inner-conductor diameter of Line 1 - [m]', 'FontSize', 16);
133 grid on;
134 hold on;
135 plot(d1, Z01_10_99ohm, '.-r');
136 plot(d1_10_99ohm, Z01_10_99ohm, 'ko', 'Linewidth', 3);
137 plot([d1_10_99ohm d1_10_99ohm], [Z01_10_99ohm (Z01_10_99ohm + 10)], 'k-', 'Linewidth', 2);
138 text((d1_10_99ohm - 0.3e-3), (Z01_10_99ohm + 11), strcat('\bfd_1 = ', num2str(d1_10_99ohm)), 'FontSize', 16);
139
140 figure(4);
141 plot(d1, Q1, 'Linewidth', 3);
142 title('\bfUnloaded Q-value versus the inner-conductor diameter (d_1) of the Open-circuit Line.', 'FontSize', 16);
143 ylabel('\bfUnloaded Q-value', 'FontSize', 16);
144 xlabel('\bfd_1 - The inner-conductor diameter of Line 1 - [m]', 'FontSize', 16);
145 grid on;
146 hold on;
147 plot(d1_10_99ohm, Q1_10_99ohm, 'ko', 'Linewidth', 3);
148 plot((d1_10_99ohm - 0.3e-3) d1_10_99ohm, [Q1_10_99ohm Q1_10_99ohm], 'k-', 'Linewidth', 2);
149 text((d1_10_99ohm - 1.1e-3), (Q1_10_99ohm), strcat('\bfQ_1 = ', num2str(Q1_10_99ohm)), 'FontSize', 16);
150
151 % -----

```

Appendix B

'Susceptance Slope Parameter'

```

1 % =====
2 % MATLAB code for: The Susceptance Slope Parameter.
3 % Thesis: Paragraph 3.1.2.3
4 % Aim: Determine the unloaded Q-value of the resonator by means of the susceptance slope parameter.
5 % =====
6
7 format long;
8
9 % Constants:
10 % -----
11 p = 1e-12;
12 n = 1e-9;
13 u = 1e-6;
14 m = 1e-3;
15 M = 1e6;
16
17 % Variables:
18 % -----
19 c = 2.99792e8;
20 f0 = 900*M;
21 w0 = (2*pi*f0);
22 lambda = c/f0;
23 beta0 = (2*pi)/lambda;
24
25 f = [500e6 : 1e6 : 1000e6];
26 w = 2*pi*f;
27 lam = c./f;
28 %beta = (2*pi)./lam;
29
30 eps0 = 8.854e-12;
31 epsilon = eps0;
32 j = sqrt(-1);
33 N = length(f);
34 f0_pos = find(f == 900e6);
35
36 % Coper constants:
37 % -----
38 sigma = 5.80e07;
39 mu = (4*pi)*1e-07;
40 delta = 0.066./sqrt(f);
41 Rs = (2.61e-07)*sqrt(f);

```

```

42 % =====
43
44 % Line 2: Short-circuit Line (Z02 = 70.0 [ohm]):
45 % -----
46
47 len = 0.02; % specified line length
48
49 % Starting Values [Wheeler]:
50 % -----
51 D2 = 30*m; % resonator's outer diameter, [m]
52 d2 = 9.34*m; % inner diameter of line 2, [m]
53
54 % Line Characteristics:
55 % -----
56 C2 = (2*pi*epsilon)/log(D2/d2); % capacitance, [F/m]
57 L2 = (mu/(2*pi))*log(D2/d2); % inductance, [H/m]
58 G2 = 0; % conductance, [S/m]; dielect. losses in air = 0
59 R2 = (Rs/(2*pi))*((1/(D2/2))+1/(d2/2)); % resistance, [ohm/m]
60 Li2 = R2./w; % internal inductance, [H/m]
61
62 Z02 = 60*log(D2/d2);
63 alfa2 = (0.5)*sqrt(L2*C2)*((R2/L2) + (G2/C2)); % for, a low-loss transmission line
64 beta2 = w*sqrt(L2*C2); % for, a low-loss transmission line
65 gamma2 = alfa2 + j*beta2; % propagation constant
66
67 % Line Impedance Values, calculated for the whole f vector:
68 % -----
69 ZL2 = 0;
70 Z02_k = sqrt((R2 + j*w*L2)./(j*w*C2)); % load impedance, short-circuit line, [ohm]
71 for i = 1:N % complex impedance, due to loss, [ohm]
72 term1(i) = ZL2*cosh(gamma2(i)*len);
73 term2(i) = Z02_k(i)*sinh(gamma2(i)*len);
74 term3(i) = Z02_k(i)*cosh(gamma2(i)*len);
75 term4(i) = ZL2*sinh(gamma2(i)*len);
76 Zin2(i) = Z02_k(i)*((term1(i) + term2(i)) / (term3(i) + term4(i)));
77 end
78 Zin2; % input impedance of line 2, [ohm]
79 Yin2 = 1./Zin2; % input admittance of line 2, [siemens]
80
81 % =====
82

```

```

83 % =====
84
85 % Line 1: Open-circuit Line (Z01 = 10.99 [ohm]):
86 % -----
87
88 % Starting Values [Wheeler]:
89 % -----
90 thickness = 0.5*m;
91 D1 = d2 - 2*thickness;
92 d1 = 6.94*m;
93
94 % Line Characteristics:
95 % -----
96 C1 = (2*pi*epsilon)/log(D1/d1);
97 L1 = (mu/(2*pi))*log(D1/d1);
98 G1 = 0;
99 R1 = (Rs/(2*pi))*((1/(D1/2))+(1/(d1/2)));
100 Li1 = R1./w;
101
102 Z01 = 60*log(D1./d1);
103 alfa1 = (0.5)*sqrt(L1*C1)*((R1/L1) + (G1/C1));
104 beta1 = w*sqrt(L1*C1);
105 gamma1 = alfa1 + j*beta1;
106
107 % Line Impedance Values:
108 % -----
109 ZL1 = Zin2;
110 Z01_k = sqrt((R1 + j*w*L1)./(j*w*C1));
111 for i = 1:N
112     term1_1(i) = ZL1(i)*cosh(gamma1(i)*len);
113     term1_2(i) = Z01_k(i)*sinh(gamma1(i)*len);
114     term1_3(i) = Z01_k(i)*cosh(gamma1(i)*len);
115     term1_4(i) = ZL1(i)*sinh(gamma1(i)*len);
116     Zin1(i) = Z01_k(i)*((term1_1(i) + term1_2(i)) / (term1_3(i) + term1_4(i)));
117 end
118
119 Zin1;
120 Yin1 = 1./Zin1;
121
122 % =====
123

```

```

124 % =====
125
126 % Determine the Susceptance Slope Parameter, bn; and the unloaded Q-value:
127 % -----
128
129 % Input Admittance:
130 % -----
131 % conductance = Re{Yin1}, [S]
132 % susceptance = Im{Yin1}, [S]
133
134 % Determine the gradient/slope around the resonant point:
135 % -----
136 delta_Bin = Bin(411) - Bin(391);
137 delta_f = f(411) - f(391);
138 gradient = delta_Bin/delta_f;
139
140 % Susceptance Slope Parameter, and the corresponding Q-value:
141 % -----
142 bn = (f0/2)*(gradient);
143 Q = (bn./Gin);
144 % susceptance slope parameter
145 % unloaded Q-value of the resonator
146 % =====
147 % Relevant Figures:
148 % -----
149
150 % Confirm the resonant point:
151 % -----
152 figure(1);
153 ABS = abs(Zin1);
154 maks = max(ABS);
155 m_pos = find(ABS == max(ABS));
156 plot(f, ABS, 'Linewidth', 4);
157 grid on;
158 hold on;
159 plot(f(m_pos), ABS(m_pos), 'ro', 'Linewidth', 4);
160 x = f(m_pos);
161 y = 0;
162 plot([f(m_pos) (x-50e6)], [ABS(m_pos) ABS(m_pos)], 'r-', 'Linewidth', 4);
163 text((x-150e6), (y+maks+100), strcat('\bf|z_{in}| = ', num2str(ABS(m_pos))), ' \Omega' ), 'FontSize', 16);
164 text((x-150e6), (y+maks-3e3), strcat('\bff_0 = ', num2str(f(m_pos)/1e6), ' MHz' ), 'FontSize', 16);

```



```

165 title('\bfResonator Input Impedance, Z_{in} versus Frequency.', 'FontSize', 16);
166 ylabel('\bf|Z_{in}|', 'FontSize', 16);
167 xlabel('\bfFrequency f, [Hz]', 'FontSize', 16);
168
169
170 % Input Susceptance, Bin versus the frequency:
171 % -----
172 figure(2);
173 plot(f, Bin, 'Linewidth', 4);
174 grid on;
175 hold on;
176 plot(f(m_pos), Bin(m_pos), 'ro', 'Linewidth', 4);
177 plot([f(m_pos) (x-20e6)], [Bin(m_pos) (y+0.003)], 'r-', 'Linewidth', 4);
178 text((x-80e6), (y+0.005), strcat('\bfB_{in} = ', num2str(Bin(m_pos)/1e-6), ' \muS' ), 'FontSize', 16);
179 text((x-80e6), (y+0.002), strcat('\bff_0 = ', num2str(f(m_pos)/1e6), ' MHz' ), 'FontSize', 16);
180 title('\bfResonator Input Susceptance, B_{in} versus Frequency.', 'FontSize', 16);
181 ylabel('\bfB_{in}, [S]', 'FontSize', 16);
182 xlabel('\bfFrequency f, [Hz]', 'FontSize', 16);
183
184
185 % Input Susceptance, Bin versus the frequency:
186 % -----
187 figure(3);
188 plot(w, Bin, 'Linewidth', 4);
189 grid on;
190 hold on;
191 plot(w(m_pos), Bin(m_pos), 'ro', 'Linewidth', 4);
192 plot([w(m_pos) (w(m_pos)-0.2e9)], [Bin(m_pos) (Bin(m_pos)+0.004)], 'r-', 'Linewidth', 4);
193 text((w(m_pos)-0.8e9), (y+0.005), strcat('\bfB_{in} = ', num2str(Bin(m_pos)/1e-6), ' \muS' ), 'FontSize', 16);
194 text((w(m_pos)-0.8e9), (y+1.5*m), strcat('\bf\omega_0 = ', num2str(w(m_pos)/1e9), 'e9', ' rad/s' ), 'FontSize', 16);
195 title('\bfResonator Input Susceptance, B_{in} versus Angular Velocity, \omega.', 'FontSize', 16);
196 ylabel('\bfB_{in}, [S]', 'FontSize', 16);
197 xlabel('\bfAngular Velocity \omega, [rad/s]', 'FontSize', 16);
198
199
200
201
202
203
204
205

```

```

206 % Input Conductance, Gin versus the frequency:
207 % -----
208 figure(4);
209 plot(f, Gin, 'Linewidth', 4);
210 grid on;
211 hold on;
212 plot(f(m_pos), Gin(m_pos), 'ro', 'Linewidth', 4);
213 plot([f(m_pos) (x)], [Gin(m_pos) (Gin(m_pos)+0.7e-5)], 'r-', 'Linewidth', 4);
214 text((x-80e6), (Gin(m_pos)+0.75e-5), strcat('\bfg_{in} = ', num2str(Gin(m_pos)/1e-6), ' \muS' ), 'FontSize', 16);
215 text((x-80e6), (Gin(m_pos)+0.5e-5), strcat('\bff_0 = ', num2str(f(m_pos)/1e6), ' MHz' ), 'FontSize', 16);
216 title('\bfResonator Input Conductance, G_{in} versus Frequency.', 'FontSize', 16)
217 ylabel('\bfg_{in}, [S]', 'FontSize', 16);
218 xlabel('\bffFrequency f, [Hz]', 'FontSize', 16);
219
220
221 % Unloaded Q-value versus the frequency:
222 % -----
223 figure(5);
224 line = plot(f, Q, 'Linewidth', 4);
225 grid on;
226 hold on;
227 plot(f(m_pos), Q(m_pos), 'ro', 'Linewidth', 4);
228 plot([f(m_pos) (x-50e6)], [Q(m_pos) Q(m_pos)], 'r-', 'Linewidth', 4);
229 text((x-120e6), (Q(m_pos)+100), strcat('\bfQ_u = ', num2str(Q(m_pos)) ), 'FontSize', 16 );
230 text((x-120e6), (Q(m_pos)-100), strcat('\bff_0 = ', num2str(f(m_pos)/1e6), ' MHz' ), 'FontSize', 16);
231 title('\bfUnloaded Q-value versus Frequency.', 'FontSize', 16);
232 ylabel('\bfQ_{unloaded}', 'FontSize', 16);
233 xlabel('\bffFrequency f, [Hz]', 'FontSize', 16);
234
235 % -----
236
237
238
239
240
241
242
243
244
245
246

```

```

247 % *****
248 %
249 % SUMMARY of all the values calculated for Line 2, at f0:
250 % -----
251
252 f_f0 = f(m_pos) % 901 [MHz]
253 lambda [mm]
254 beta0 [rad/m]
255 delta_f0 = delta(m_pos) [um]
256 Rs_f0 = Rs(m_pos) [ohm]
257 len [mm]
258 D2 [mm]
259 d2 [mm]
260
261 C2 % 47.674818 [pF/m]
262 L2 % 233.37823 [nH/m]
263 G2 % 0 [S/m]
264 R2_f0 = R2(m_pos) % 0.350122 [ohm/m]
265 Li2_f0 = Li2(m_pos) % 61.84642 [pH/m]
266
267 alfa2_f0 = alfa2(m_pos) % 0.0025021
268 beta2_f0 = beta1(m_pos) % 18.88336
269 gamma2_f0 = gamma2(m_pos) % (0.0025021) + j(18.88336)
270
271 Z02 [ohm]
272 ZL2 [ohm]
273 Z02_k_f0 = Z02_k(m_pos) % (69.96577) - j(9.27064m) [ohm]
274 Zin2_f0 = Zin2(m_pos) % (7.72999m) + j(27.75615) [ohm]
275 Yin2_f0 = Yin2(m_pos) % (10.03369u) - j(36.0281m) [S]
276
277 % *****
278
279
280
281
282
283
284
285
286
287

```

```

288 % *****
289
290 % SUMMARY of all the values calculated for Line 1, at f0:
291 % -----
292
293 len                % 20                [mm]
294 D1                 % 8.34              [mm]
295 d1                 % 6.94              [mm]
296
297 C1                 % 302.73665        [pF/m]
298 L1                 % 36.75229         [nH/m]
299 G1                 % 0                [S/m]
300 R1_f0 = R1(m_pos) % 0.658341        [ohm/m]
301 L11_f0 = L11(m_pos) % 116.29103       [pH/m]
302
303 alfa1_f0 = alfa1(m_pos) % 0.029875
304 beta1_f0 = beta1(m_pos) % 18.88336
305 gamma1_f0 = gamma1(m_pos) + j(18.88336)
306
307 Z01                % 11.02569         [ohm]
308 ZL1_f0 = ZL1(m_pos) % (7.72999m) + j(27.75615) [ohm]
309 Z01_k_f0 = Z01_k(m_pos) % (11.01819) - j(17.43175m) [ohm]
310 Zin1_f0 = Zin1(m_pos) % (23.49494) + j(34.12418) [kohm]
311 Yin1_f0 = Yin1(m_pos) % (13.68793) - j(19.88042) [uS]
312
313 % *****
314
315 % SUMMARY of the final values calculated for the Resonator, at f0:
316 % -----
317
318 Yin1_f0 = Yin1(m_pos) % (13.68793) - j(19.88042) [uS]
319 Gin_f0 = Gin(m_pos) % 13.68793 [uS]
320 Bin_f0 = Bin(m_pos) % -19.88042 [uS]
321 delta_Bin         % 1.523528e-3
322 delta_f           % 20.0 [MHz]
323 gradient          % 76.17641e-12
324 bn               % 0.034279
325 Q_unloaded = Q(m_pos) % 2504.3515
326
327 % *****

```

Appendix C

'Resonator, Measured S-parameters'

```

1 % ===== [Resonator Measurements]
2 % MATLAB code for: The Measured S-parameters of the Cavity Resonator.
3 % Thesis: Paragraph 3.1.4.1
4 % Aim: Plot the measured S-parameters against frequency, by processing the measured ZVB Network Analyser Data.
5 % Consequently, from the S21 plot; the corresponding Q-value is calculated.
6 % =====
7
8 % Resoneerder Alone:
9 % -----
10 % Q_Loaded :
11 [S_Res_B f_Res_B] = ldstone('C:\~\S_parameters.s2p', 979e6, 1011e6, 0);
12 S21_dB_Res_B = 20*log10(abs(S_Res_B(:,2))); % S21
13 S11_dB_Res_B = 20*log10(abs(S_Res_B(:,1))); % S11
14 S22_dB_Res_B = 20*log10(abs(S_Res_B(:,4))); % S22
15
16 % Q_Unloaded :
17 [S_Res_O f_Res_O] = ldstone('C:\~\S_parameters.s2p', 979e6, 1011e6, 0);
18 S21_dB_Res_O = 20*log10(abs(S_Res_O(:,2))); % S21
19 S11_dB_Res_O = 20*log10(abs(S_Res_O(:,1))); % S11
20 S22_dB_Res_O = 20*log10(abs(S_Res_O(:,4))); % S22
21
22 % -----
23
24 figure(1);
25 % Plot the S-parameters of the Resonator:
26 % Loaded:
27 % -----
28 plot(f_Res_B, S21_dB_Res_B, '-g', 'Linewidth', 3);
29 hold on;
30 grid on;
31 plot(f_Res_B, S11_dB_Res_B, '-.r', 'Linewidth', 3);
32 plot(f_Res_B, S22_dB_Res_B, '--b', 'Linewidth', 3);
33 str1(1) = {'\bfLoaded Resonator'};
34 text(990.7e6, -19, str1, 'FontSize', 12, ...
35 'BackgroundColor', [.7 .9 .7], ...
36 'EdgeColor', 'black', ...
37 'Margin', 5.5);
38 title('\bfS-parameters of the Cavity Resonator.', 'FontSize', 12);
39 xlabel('\bfFrequency, f, [Hz]', 'FontSize', 12);
40 ylabel('\bf|S_{21}|_{dB}', |S_{11}|_{dB} & |S_{22}|_{dB}', 'FontSize', 12);
41 legend('|S_{21}|', '|S_{11}|', '|S_{22}|');

```

```

42 % Unloaded:
43 % -----
44 plot(f_Res_O, S21_dB_Res_O, '-g', 'Linewidth', 3);
45 %plot(f_Res_O, S11_dB_Res_O, '-.r', 'Linewidth', 3);
46 %plot(f_Res_O, S22_dB_Res_O, '--b', 'Linewidth', 3);
47 str2(1) = {'\bfUnloaded Resonator'};
48 text(990.7e6, -60, str2, 'FontSize', 12, ...
49 'BackgroundColor', [.7 .9 .7], ...
50 'EdgeColor', 'black', ...
51 'Margin', 5.5);
52
53 % -----
54 figure(2);
55 % Plot the Zoomed S-parameters of the Resonator:
56 % Loaded:
57 % -----
58 plot(f_Res_B, S21_dB_Res_B, '-g', 'Linewidth', 3);
59 hold on;
60 grid on;
61 plot(f_Res_B, S11_dB_Res_B, '-.r', 'Linewidth', 3);
62 plot(f_Res_B, S22_dB_Res_B, '--b', 'Linewidth', 3);
63 axis([0.997e9 1.002e9 -60 10]);
64 str1(1) = {'\bfLoaded Resonator'};
65 text(997.25e6, -10, str1, 'FontSize', 12, ...
66 'BackgroundColor', [.7 .9 .7], ...
67 'EdgeColor', 'black', ...
68 'Margin', 5.5);
69 title('\bfs-parameters of the Cavity Resonator.', 'FontSize', 12);
70 xlabel('\bfFrequency, f, [Hz]', 'FontSize', 12);
71 ylabel('\bf|S_{21}|_{dB}', |S_{11}|_{dB} & |S_{22}|_{dB}', 'FontSize', 12);
72 legend(' |S_{21}|', '|S_{11}|', '|S_{22}|');
73
74 % Unloaded:
75 % -----
76 plot(f_Res_O, S21_dB_Res_O, '-g', 'Linewidth', 3);
77 str2(1) = {'\bfUnloaded Resonator'};
78 text(997.25e6, -45, str2, 'FontSize', 12, ...
79 'BackgroundColor', [.7 .9 .7], ...
80 'EdgeColor', 'black', ...
81 'Margin', 5.5);
82 % -----

```

Appendix D

**‘Mini-Circuits Amplifier
ZX60-2522M+
Datasheets & Measured S-parameters’**

Coaxial Amplifier

ZX60-2522M+ ZX60-2522M

50Ω High Isolation 0.5 to 2.5 GHz



CASE STYLE: GC957

Connectors	Model	Price	Qty.
SMA	ZX60-2522M-S(+)	\$59.95 ea.	(1-9)

+ RoHS compliant in accordance with EU Directive (2002/95/EC)

The +Suffix identifies RoHS Compliance. See our web site for RoHS Compliance methodologies and qualifications.

Features

- from 2.8V to 5V operation
- wide bandwidth, 0.5 to 2.5 GHz
- high active directivity, 20 dB typ.
- output power, up to 18.0 dBm typ.
- protected by US patent 6,790,049

Applications

- buffer amplifier
- LO amplifiers for mixers
- cellular
- PCN

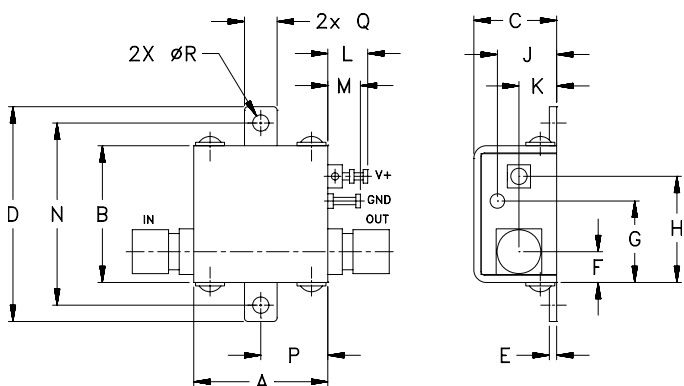
Electrical Specifications T_{AMB}=25°C

MODEL NO.	FREQ. (GHz)		DC VOLTS (V)	GAIN, dB Typical						MAXIMUM POWER (dBm)			DYNAMIC RANGE			VSWR (:1) Typ.		ACTIVE DIRECTIVITY (dB) (Isolation-Gain) Typ.	DC OPERATING CURRENT @ Pin V+ (mA)				
				over frequency, GHz						Output (1 dB Comp.) Typ.		Input (no damage)	NF (dB) Typ.	IP3 (dBm) Typ.	at 1 GHz	at 1 GHz	at 2 GHz		In	Out	Typ.	Typ.	Max.
				0.5	1.0	1.5	2.0	2.5	Min. at 2 GHz	f _L	f _U												
ZX60-2522M(+)	f _L	f _U	5.0 2.8	18.7	22.5	23.5	23.3	21.7	21.5	18.0	15.8	10	3.0	30.6	28.8	1.5	1.7	17	86	95			
				17.2	20.2	20.6	20.6	20.0	—	14.4	14.2	10	3.0	25.7	25.6	1.4	1.8	20	80	—			

Maximum Ratings

Operating Temperature	-40°C to 85°C case
Storage Temperature	-55°C to 100°C
DC Voltage	7V
Input Power(no damage)	10 dBm
Power	500mW

Outline Drawing



Outline Dimensions (inch/mm)

A	B	C	D	E	F	G	H	J	K	L	M	N	P	Q	R	wt
.74	.75	.46	1.18	.04	.17	.45	.59	.33	.21	.22	.18	1.00	.37	.18	.09	grams
18.80	19.05	11.68	29.97	1.02	4.32	11.43	14.99	8.38	5.33	5.59	4.57	25.40	9.40	4.57	2.29	23.0



P.O. Box 350166, Brooklyn, New York 11235-0003 (718) 934-4500 Fax (718) 332-4661 For detailed performance specs & shopping online see Mini-Circuits web site



The Design Engineers Search Engine Provides ACTUAL Data Instantly From MINI-CIRCUITS At: www.minicircuits.com

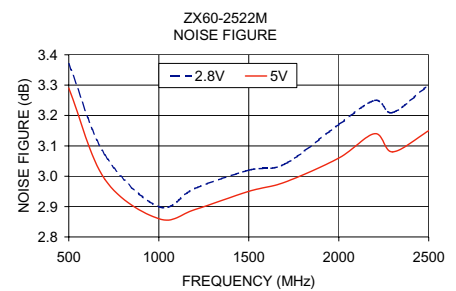
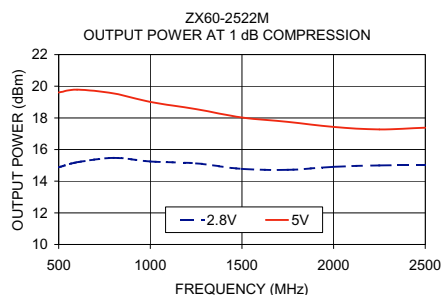
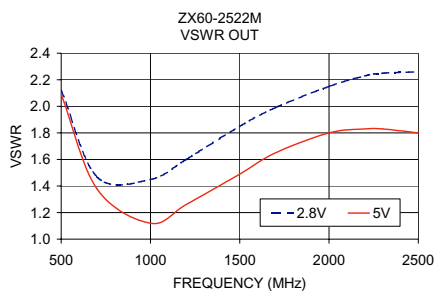
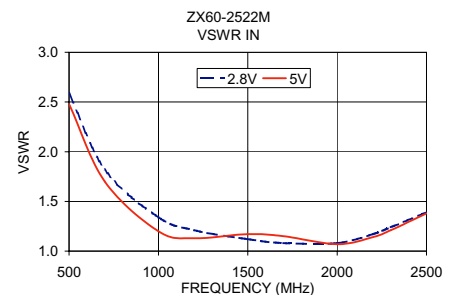
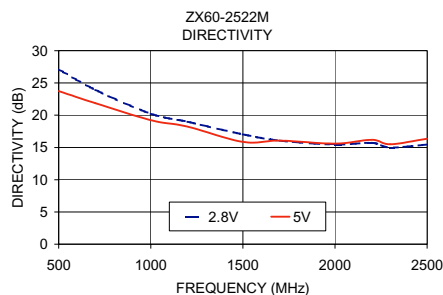
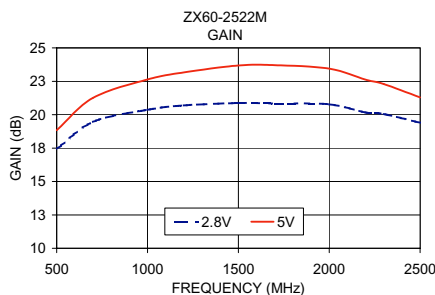
RF/IF MICROWAVE COMPONENTS

REV. B
M98898
ZX60-2522M
EDR-6127
RVN/TD/CP/AM
070330
Page 1 of 2

Typical Performance Data/Curves

ZX60-2522M+ ZX60-2522M

FREQUENCY (MHz)	GAIN (dB)		DIRECTIVITY (dB)		VSWR IN (:1)		VSWR OUT (:1)		NOISE FIGURE (dB)		POUT at 1 dB COMPR. (dBm)	
	2.8V	5V	2.8V	5V	2.8V	5V	2.8V	5V	2.8V	5V	2.8V	5V
500.00	17.44	18.83	27.10	23.74	2.59	2.48	2.12	2.09	3.37	3.29	14.88	19.61
700.00	19.46	21.26	23.93	21.85	1.82	1.70	1.47	1.38	3.07	2.99	15.20	19.78
1000.00	20.37	22.64	20.23	19.23	1.34	1.20	1.45	1.12	2.90	2.86	15.47	19.55
1200.00	20.69	23.17	18.98	18.22	1.21	1.13	1.60	1.26	2.96	2.89	15.25	19.01
1500.00	20.87	23.68	17.04	15.87	1.12	1.17	1.85	1.49	3.02	2.95	15.13	18.55
1700.00	20.84	23.71	16.06	16.05	1.08	1.15	1.99	1.65	3.04	2.98	14.78	18.03
2000.00	20.78	23.45	15.45	15.60	1.08	1.07	2.15	1.80	3.17	3.06	14.72	17.75
2200.00	20.17	22.62	15.71	16.17	1.17	1.14	2.23	1.83	3.25	3.14	14.91	17.43
2300.00	20.05	22.29	15.00	15.51	1.24	1.21	2.25	1.83	3.21	3.08	15.00	17.27
2500.00	19.40	21.29	15.46	16.36	1.39	1.38	2.26	1.80	3.30	3.15	15.02	17.38



P.O. Box 350166, Brooklyn, New York 11235-0003 (718) 934-4500 Fax (718) 332-4661 For detailed performance specs & shopping online see Mini-Circuits web site



The Design Engineers Search Engine Provides ACTUAL Data Instantly From MINI-CIRCUITS At: www.minicircuits.com

RF/IF MICROWAVE COMPONENTS

High Directivity

Monolithic Amplifier

0.5-2.5 GHz

Product Features

- 2.8V & 5V operation
- Micro-miniature size .120"X.120"
- Internal DC blocking at RF input and output
- High directivity, 17 dB typ.
- Low noise figure, 2.9 dB typ.
- Output power, up to +18 dBm typ.
- Excellent repeatability
- Low cost
- Aqueous washable

Typical Applications

- Buffer amplifier
- Cellular
- PCN
- Communications satellite
- Defense



MNA-6+

CASE STYLE: DQ849
PRICE: \$2.25 ea. QTY. (30)

+ RoHS compliant in accordance with EU Directive (2002/95/EC)

The +Suffix has been added in order to identify RoHS Compliance. See our web site for RoHS Compliance methodologies and qualifications.

General Description

MNA-6+ is a wideband amplifier offering high dynamic range. It has repeatable performance from lot to lot. It is enclosed in a 3x3 mm MCLP plastic package. MNA-6+ is fabricated using GaAs MESFET technology. Expected MTBF at 85°C case temperature is 45,000 years at 2.8V; 7,000 years at 5V.

Function	Pin Number	Description
RF IN	2	RF input pin
RF-OUT	5	RF output pin
DC	7, with 1000 pF bypass to ground; connect pin 8 via 33 ohms to pin 7 externally	Bias pins
GND	3,4 and paddle in center of bottom	Connections to ground
OPTIONAL	1,6	No internal connection; recommended use: per PCB Layout PL-078



P.O. Box 350166, Brooklyn, New York 11235-0003 (718) 934-4500 Fax (718) 332-4661 For detailed performance specs & shopping online see Mini-Circuits web site



The Design Engineers Search Engine Provides ACTUAL Data Instantly From MINI-CIRCUITS At: www.minicircuits.com

RF/IF MICROWAVE COMPONENTS

REV. L
M108520
MNA-6+
070522
Page 1 of 4

Electrical Specifications at 25°C

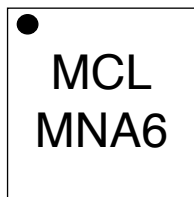
Parameter	Min.	Typ.		Max.	Units	
Frequency Range	0.5			2.5	GHz	
at DC Volts	5.0	5.0	2.8	5.0	V	
Gain					dB	
	f=0.5 GHz	19.4	18.6			
	f=1.0 GHz	23.5	21.5			
	f=1.5 GHz	23.6	21.2			
	f=2.0 GHz	23.0	21.0			
	f=2.5 GHz	20.2	19.0			
Input Return Loss	f=0.75-2.5 GHz		14	14	dB	
Output Return Loss	f=0.75-2.5 GHz		12.5	10	dB	
Output Power @ 1 dB compression	f=0.5 GHz f=2.5GHz		18.0 15.8	14.1 13.2	dBm	
Output IP3	f=1 GHz f=2 GHz		27.1 28.0	23.4 25.0	dBm	
Noise Figure	f=1 GHz		2.9		dB	
Directivity (Isolation - Gain)			17			
DC Current			81	65	95	mA
Thermal Resistance, junction-to-case			78		°C/W	

Absolute Maximum Ratings

Parameter	Ratings
Operating Temperature	-40°C to 85°C
Storage Temperature	-55°C to 100°C
DC Voltage	7V at pin 7 10V at pins 2 & 5
Power Dissipation	500mW
Input Power	10dBm

Note: Permanent damage may occur if any of these limits are exceeded. These ratings are not intended for continuous normal operation.

Product Marking



Additional Detailed Technical Information

Additional information is available on our web site. To access this information enter the model number on our web site home page.

Performance data, graphs, s-parameter data set (.zip file)

Case Style: DQ849

MNA-6+: Plastic package, exposed paddle, lead finish: tin/silver/nickel

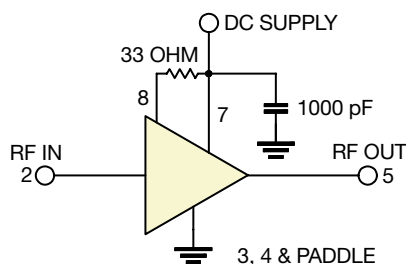
Tape & Reel: F66

Suggested Layout for PCB Design: PL-078

Evaluation Board: TB-186+

Environmental Ratings: ENV08T1

Recommended Application Circuit



ESD Rating

Human Body Model (HBM): Class 1A (250v to < 500v) in accordance with ANSI/ESD STM 5.1 - 2001

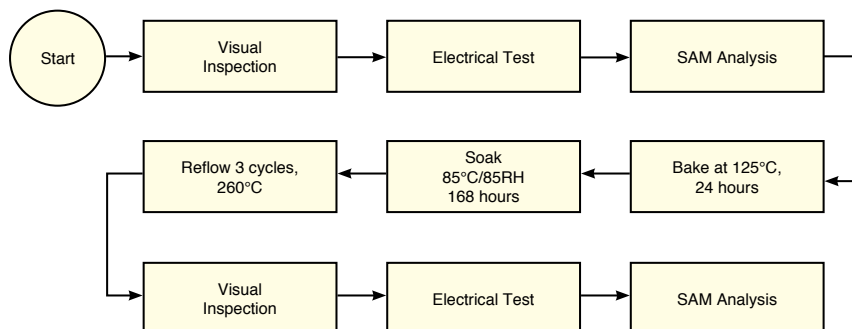
Charged Device Model (CDM): Class III (500 to 1000v) in accordance with JESD22-C101A

MSL Rating

Moisture Sensitivity: MSL1 in accordance with IPC/JEDEC J-STD-020C

No.	Test Required	Condition	Standard	Quantity
1	Visual Inspection	Low Power Microscope Magnification 40x	MIP-IN-0003 (MCT spec)	45 units
2	Electrical Test	Room Temperature	SCD (MCL spec)	45 units
3	SAM Analysis	Less than 10% growth in term of delamination	J-Std-020C (Jedec Standard)	45 units
4	Moisture Sensitivity Level 1	Bake at 125°C for 24 hours Soak at 85°C/85%RH for 168 hours Reflow 3 cycles at 260°C peak	J-Std-020C (Jedec Standard)	45 units

MSL Test Flow Chart



```

1 % ===== [Amplifier Measurements]
2 % MATLAB code for: The Measured S-parameters of the Amplifier, ZX60-2522M+.
3 % Thesis: Paragraph 3.2.2.1
4 % Aim: Plot the measured S-parameters against frequency, by processing the measured ZVB Network Analyser Data.
5 % =====
6
7 % Amplifier Alone:
8 % -----
9 [S_Amp freq_Amp] = ldstone('C:\~\S_parameters.s2p', 449e6, 2551e6, 0);
10
11 % -----
12
13 figure(1);
14 % Plot the S-parameters of the Amplifier:
15 % -----
16 S11_dB_Amp = 20*log10(abs(S_Amp(:,1)));
17 S21_dB_Amp = 20*log10(abs(S_Amp(:,2)));
18 S12_dB_Amp = 20*log10(abs(S_Amp(:,3)));
19 S22_dB_Amp = 20*log10(abs(S_Amp(:,4)));
20
21 plot(freq_Amp, S11_dB_Amp, '-g', 'Linewidth', 3);
22 hold on;
23 grid on;
24 x1 = freq_Amp(1);
25 xn = max(freq_Amp);
26 axis([x1 xn -50 30]);
27 set(gca, 'XTick', [450e6 1150e6 1850e6 2550e6]);
28 plot(freq_Amp, S21_dB_Amp, '-b', 'Linewidth', 3);
29 plot(freq_Amp, S12_dB_Amp, '-r', 'Linewidth', 3);
30 plot(freq_Amp, S22_dB_Amp, '-k', 'Linewidth', 3);
31
32 title('\bfs-parameters of Amplifier ZX60-2522M, in dB.', 'FontSize', 12);
33 xlabel('\bFrequency, f [Hz]', 'FontSize', 12);
34 ylabel('\bf|S|_dB', 'FontSize', 12);
35 legend('S_{11}', 'S_{21}', 'S_{12}', 'S_{22}');
36
37 % -----
38
39
40
41

```

```

42 figure(2);
43 % Plot only S21 of the Amplifier:
44 % -----
45 plot(freq_Amp, S21_dB_Amp, '-b', 'Linewidth', 3);
46 hold on;
47 grid on;
48 ylims = get(gca, 'YLim');
49 axis([450e6 2550e6 ylims(1) ylims(2)]);
50 set(gca, 'XTick', [450e6 1150e6 1850e6 2550e6]);
51
52 title('\bfForward Transmission Coefficient of the Amplifier - S_{21} in dB.', 'FontSize', 12);
53 xlabel('\bfFrequency, f [Hz]', 'FontSize', 12);
54 ylabel('\bf|S_{21}|_{-} dB', 'FontSize', 12);
55 legend('S_{21}');
56
57 f_pos = find((freq_Amp >= 0.999e9) & (freq_Amp <= 1.001e9));
58 x = freq_Amp(f_pos);
59 y = S21_dB_Amp(f_pos);
60 plot(freq_Amp(f_pos), S21_dB_Amp(f_pos), 'ro', 'Linewidth', 3);
61 plot([x x], [y (y + 0.5)], 'r-', 'Linewidth', 3);
62 text((x - 250e6), (y + 0.7), strcat('\bfs_{21} = ', num2str(y), '\bf dB'), 'FontSize', 12);
63 text((x - 250e6), (y + 0.4), strcat('\bff = ', num2str(x/1e9), '\bf GHz'), 'FontSize', 12);
64
65 % =====

```


Appendix E

**'Power Splitter – ZFSC-2-5+
Datasheet'**

Coaxial Power Splitter/Combiner

ZFSC-2-5+ ZFSC-2-5

2 Way-0° 50Ω 10 to 1500 MHz



BNC version shown
CASE STYLE: K18

Maximum Ratings

Operating Temperature	-55°C to 100°C
Storage Temperature	-55°C to 100°C
Power Input (as a splitter)	1W max.
Internal Dissipation	0.125W max.

Coaxial Connections

SUM PORT	3
PORT 1	1
PORT 2	2

Features

- wideband, 10 to 1500 MHz
- high insertion loss, 0.5 dB typ.
- high isolation, 30 dB typ.
- excellent amplitude unbalance, 0.1 dB typ.
- excellent phase unbalance, 0.5 deg. typ.
- rugged shielded case

Applications

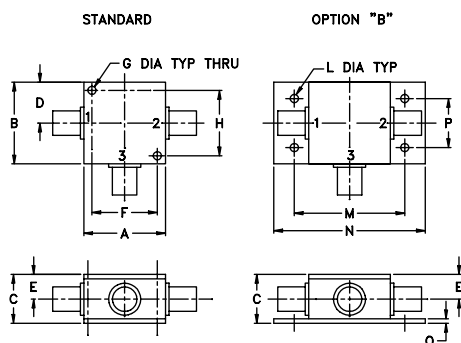
- cellular
- satellite distribution
- VHF/UHF

Connectors	Model	Price	Qty.
BNC	ZFSC-2-5(+)	\$59.95	(1-9)
SMA	ZFSC-2-5-S(+)	\$64.95	(1-9)
N-TYPE	ZFSC-2-5-N(+)	\$64.95	(1-9)
BRACKET (OPTION "B")		\$2.50	(1+)

+ RoHS compliant in accordance with EU Directive (2002/95/EC)

The +Suffix identifies RoHS Compliance. See our web site for RoHS Compliance methodologies and qualifications.

Outline Drawing



Outline Dimensions (inch/mm)

A	B	C	D	E	F	G	H
1.25	1.25	.75	.63	.38	1.00	.125	1.000
31.75	31.75	19.05	16.00	9.65	25.40	3.18	25.40

J	K	L	M	N	P	Q	wt
--	--	.125	1.688	2.18	.75	.07	grams
--	--	3.18	42.88	55.37	19.05	1.78	70.0

For option B with N-type connectors, dimension "C" increases to 0.94 inches.

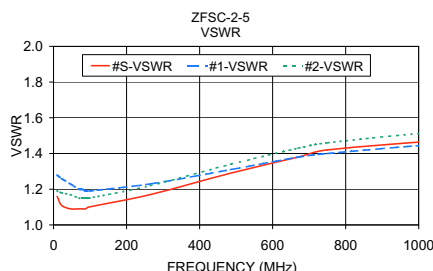
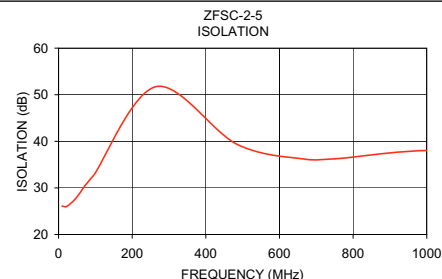
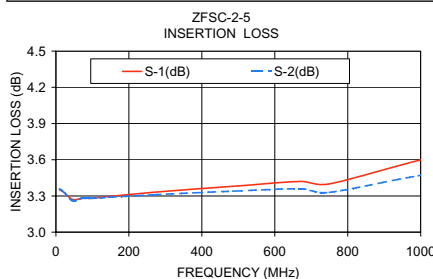
Electrical Specifications

FREQ. RANGE (MHz)	ISOLATION (dB)			INSERTION LOSS (dB) ABOVE 3.0 dB			PHASE UNBALANCE (Degrees)			AMPLITUDE UNBALANCE (dB)								
	L	M	U	L	M	U	L	M	U	L	M	U						
10-1500	25	15	30	20	25	18	0.25	0.6	0.5	1.0	0.8	1.5	2	3	4	0.15	0.20	0.50

L = low range [f_L to 10 f_L] M = mid range [$10 f_L$ to $f_U/2$] U = upper range [$f_U/2$ to f_U]

Typical Performance Data

Frequency (MHz)	Insertion Loss (dB)		Amplitude Unbalance (dB)	Isolation (dB)	Phase Unbalance (deg.)	VSWR S	VSWR 1	VSWR 2
	S-1	S-2						
10.00	3.35	3.36	0.00	26.11	0.04	1.16	1.28	1.19
22.00	3.33	3.33	0.00	26.02	0.02	1.11	1.26	1.18
46.00	3.27	3.26	0.01	27.66	0.01	1.09	1.23	1.17
70.00	3.28	3.28	0.00	30.29	0.07	1.09	1.20	1.15
79.00	3.28	3.28	0.01	31.18	0.10	1.09	1.20	1.15
88.00	3.28	3.28	0.00	32.04	0.02	1.09	1.19	1.15
97.00	3.28	3.28	0.00	32.89	0.08	1.10	1.19	1.15
265.00	3.33	3.31	0.02	51.74	0.16	1.17	1.23	1.22
485.00	3.38	3.34	0.03	39.34	0.22	1.29	1.31	1.34
670.00	3.42	3.36	0.06	36.17	0.13	1.38	1.38	1.43
750.00	3.40	3.33	0.07	36.25	0.21	1.42	1.40	1.46
1050.00	3.63	3.49	0.14	37.77	0.23	1.47	1.45	1.52
1200.00	3.62	3.43	0.19	30.23	0.15	1.47	1.44	1.52
1350.00	3.92	3.67	0.25	24.72	0.09	1.54	1.40	1.51
1500.00	4.12	3.83	0.29	20.60	0.48	1.82	1.33	1.49



electrical schematic



Mini-Circuits®
ISO 9001 ISO 14001 CERTIFIED

ALL NEW
minicircuits.com

P.O. Box 350166, Brooklyn, New York 11235-0003 (718) 934-4500 Fax (718) 332-4661 For detailed performance specs & shopping online see Mini-Circuits web site



The Design Engineers Search Engine Provides ACTUAL Data Instantly From MINI-CIRCUITS At: www.minicircuits.com

RF/IF MICROWAVE COMPONENTS

REV. A
M108014
ZFSC-2-5
HY/TD/CP/AM
070424

Appendix F

**'Fixed Attenuator – VAT-2+
Datasheet'**

Coaxial SMA Fixed Attenuator

50Ω 1W 2dB DC to 6000 MHz

VAT-2+
VAT-2



Maximum Ratings

Operating Temperature	-45°C to 100°C
Storage Temperature	-55°C to 100°C

Features

- wideband coverage, DC to 6000 MHz
- 1 watt rating
- rugged unibody construction
- off-the-shelf availability
- very low cost

Applications

- impedance matching
- signal level adjustment

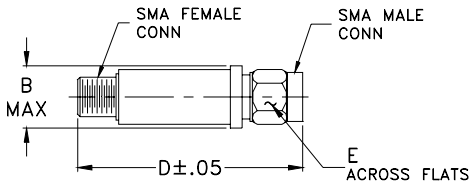
CASE STYLE: FF704

Connectors	Model	Price	Qty.
SMA	VAT-2(+)	\$11.95 ea.	(1-9)

+ RoHS compliant in accordance with EU Directive (2002/95/EC)

The +Suffix identifies RoHS Compliance. See our web site for RoHS Compliance methodologies and qualifications.

Outline Drawing



Electrical Specifications

FREQ. RANGE (MHz)	ATTENUATION * (dB)					VSWR (:1)					MAX. INPUT POWER (W)
	Flatness **										
	DC-3 GHz	3-5 GHz	5-6 GHz	DC-6 GHz		DC-3 GHz	3-5 GHz	5-6 GHz			
f_L - f_U	Nom.	Typ.	Typ.	Typ.	Typ.	Typ.	Max.	Typ.	Max.	Typ.	
DC-6000	2±0.3	0.20	0.20	0.25	0.65	1.05	1.20	1.20	1.50	1.50	1.0

* Attenuation varies by 0.3 dB max. over temperature.

** Flatness= variation over band divided by 2.

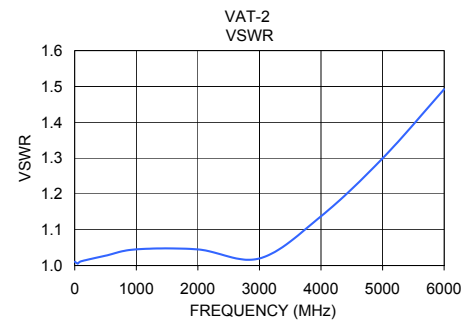
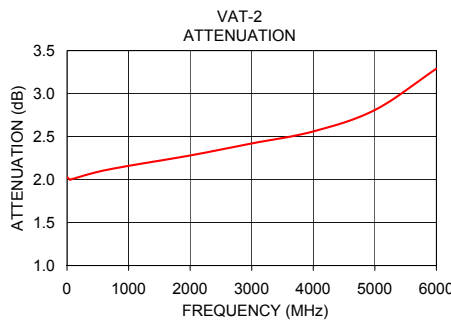
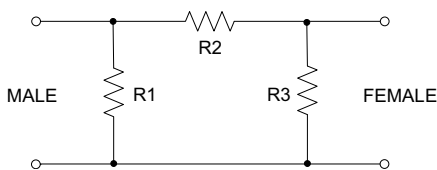
Outline Dimensions (inch/mm)

B	D	E	wt
.410	1.43	.312	grams
10.41	36.32	7.92	10.0

Typical Performance Data

Frequency (MHz)	Attenuation (dB)	VSWR (:1)
0.03	2.03	1.01
50.00	2.00	1.01
100.00	2.01	1.01
500.00	2.09	1.03
1000.00	2.16	1.05
2000.00	2.28	1.05
3000.00	2.42	1.02
4000.00	2.56	1.14
5000.00	2.81	1.30
6000.00	3.29	1.49

Electrical Schematic



Mini-Circuits®
ISO 9001 ISO 14001 CERTIFIED

ALL NEW
minicircuits.com

P.O. Box 350166, Brooklyn, New York 11235-0003 (718) 934-4500 Fax (718) 332-4661 For detailed performance specs & shopping online see Mini-Circuits web site



The Design Engineers Search Engine Provides ACTUAL Data Instantly From MINI-CIRCUITS At: www.minicircuits.com

RF/IF MICROWAVE COMPONENTS

REV. E
ED-105218
VAT-2
LC/TD/CP/AM
070423

Appendix G

**‘Leeson’s Phase Noise Model -
Oscillator Phase Noise
Prediction’**

```

1 % =====
2 % MATLAB code for: Implement LEESON's Phase Noise Model to theoretically predict the SSB Phase Noise of the Oscillator.
3 % Thesis: Paragraph 3.5.1.1
4 % Aim: Plot the predicted SSB phase noise relative to the carrier in [dBc/Hz].
5 % =====
6
7 % See Leeson's Model in Chapter 2 - pp. 60-67.
8 % -----
9
10 % Constant accounting for the strength of the 1/f-noise.
11 % Boltzmann's constant.
12 K = 1;
13 k = 1.380658e-23;
14 T = 290;
15 F = 1.927525;
16 Pin = 4.07e-03;
17 QU = 1427.9;
18 QL = 713.71;
19 f0 = 1e9;
20 fh = f0/(2*QL);
21 fm = [1 : 100 : 10e6];
22 fc = 5e6;
23
24 % Amplifier, noise factor (abs). NF = 2.85 dB.
25 % Input power to the amplifier = 6.1 dBm.
26 % measured, unloaded Q-value..
27 % = QU/2;
28 % Fundamental frequency of oscillation.
29 % Half-power 3dB BW of the resonator, 700.565 kHz.
30 % Offset frequency vector.
31 % 1/f-noise cut-off frequency for GaAs MESFETs (typ), Chapter 2, p.63.
32
33 % Implement the different terms of Leeson's Model: (See Chapter 2, p. 64)
34 % =====
35
36 % Fourth term: Thermal Noise Floor
37 -----
38 Thermal_Noise_Floor = (k*T*F)/(Pin);
39 Noise_Floor_dBm = 10*log10(Thermal_Noise_Floor);
40 % 1.8962e-018 (abs)
41 % -177.2211 dBm
42
43 % First term: Upconverted 1/f Noise
44 -----
45 Flicker_FM = (K*fc*(f0^2))./(4*(QL^2)*(fm^3));
46 mult1 = K*fc*(fh^2);
47 for n = 1:length(fm)
48     mult2(n) = (fm(n)^(-3));
49     Flicker_FM(n) = mult1*mult2(n);
50 end
51 Flicker_FM_dB = 10*log10(Flicker_FM);
52
53
54
55
56
57
58
59
60
61
62
63
64
65
66
67
68
69
70
71
72
73
74
75
76
77
78
79
80
81
82
83
84
85
86
87
88
89
90
91
92
93
94
95
96
97
98
99
100

```

```

42 % Implement the different terms ...
43 % =====
44 % Second term: Thermal FM Noise
45 % -----
46 % White_FM = (f0^2)./(4*(QL^2)*(fm^2));
47 mull = fh^2;
48 for n = 1:length(fm)
49     mul2(n) = (fm(n)^(-2));
50     White_FM(n) = mull*mul2(n);
51 end
52 White_FM_dB = 10*log10(White_FM);
53
54 % Third term: Flicker Phase Noise
55 % -----
56 Flicker_PM = (K*fc)./(fm);
57 Flicker_PM_dB = 10*log10(Flicker_PM);
58
59 % =====
60 % Output Power Spectral Density (PSD):
61 % -----
62 for n = 1:length(fm)
63     S_fm(n) = Thermal_Noise_Floor*(Flicker_FM(n) + White_FM(n) + Flicker_PM(n) + 1);
64 end
65
66 % Single-sideband (SSB) Phase Noise:
67 % -----
68 L_fm = (0.5)*S_fm;
69
70 % Single-sideband (SSB) Phase Noise relative to the Carrier, in [dBc/Hz]s
71 % -----
72 L_fm_dBc = 10*log10(L_fm);
73
74 % =====
75
76
77
78
79
80
81
82

```

```

83 % =====
84 % Figures:
85 % =====
86
87 figure(1)
88 % Plot the different noise contributions towards the system phase noise:
89 semilogx(fm, Noise_Floor_dB, 'bo', 'LineWidth', 2);
90 semilogx(fm, Flicker_FM_dB, 'g-', 'LineWidth', 3);
91 hold on;
92 grid on;
93 semilogx(fm, Flicker_FM_dB, 'g-', 'LineWidth', 3);
94 semilogx(fm, White_FM_dB, 'm-', 'LineWidth', 3);
95 semilogx(fm, Flicker_PM_dB, 'r-', 'LineWidth', 3);
96 xlabel('\bfoffset frequency from the carrier, f_m [Hz]', 'FontSize', 12);
97 ylabel('\bfSSB Oscillator Noise contributions, in [dB]', 'FontSize', 12);
98 title('\bfDifferent Phase Contributions to the SSB Phase Noise of the Oscillator, according to Leeson.', 'FontSize', 12);
99
100 %legend('Noise Floor', 'Flicker FM', 'White FM', 'Flicker PM');
101 legend('\fontsize{14}\bfFlicker FM', '\fontsize{14}\bfWhite FM', '\fontsize{14}\bfFlicker PM');
102
103 figure(2)
104 % K = 1 of K = 0:
105 semilogx(fm, L_fm_dBc, 'r-', 'LineWidth', 3);
106 grid on;
107 hold on;
108 xlabel('\bfoffset frequency from the carrier, f_m [Hz]', 'FontSize', 12);
109 ylabel('\bfSSB Phase Noise relative to the Carrier, L(f_m) [dBc/Hz]', 'FontSize', 12);
110 title('\bfPhase Noise of the Oscillator as predicted by Leeson's Phase Noise Model.', 'FontSize', 12);
111 legend('\fontsize{14}\bfSSB Phase Noise');
112 axis([10^0 10^7 -185 20]);
113
114 str1(1) = {'\fontsize{14}\bfLeeson's Parameters:'};
115 str1(2) = {'-----'};
116 str1(3) = {' '};
117 str1(3) = {' K = 1'};
118 str1(3) = {' K = 0'};
119 str1(3) = {' K = 0.5'};
120 str1(3) = {' K = 0.0005'};
121 str1(4) = {' P_{in} = 6.1 dBm'};
122 str1(5) = {' NF = 2.85 dB'};

```



```

123 str1(6) = { ' Q_U = 1427.9' };
124 str1(7) = { ' Q_L = 713.71' };
125 str1(8) = { ' f_0 = 1 GHz' };
126 str1(9) = { ' f_c = 5 MHz' };
127 str1(10) = { ' f_h = f_0/2Q_L = 700.57 kHz.' };
128 text(150e3, -50, str1, 'HorizontalAlignment', 'left', ...,
129 'BackgroundColor', 'black', ...,
130 'EdgeColor', 'black', ...,
131 'Margin', 5);
132
133 str2(1) = {'\fontsize{14}\bfK = 1'};
134 text(10, -20, str2, 'HorizontalAlignment', 'left', ...,
135 'BackgroundColor', [.9 .1 .5], ...,
136 'EdgeColor', 'black', ...,
137 'Margin', 5);
138
139 str3(1) = {'\fontsize{14}\bfK = 0.5'};
140 text(4, -35, str3, 'HorizontalAlignment', 'left', ...,
141 'BackgroundColor', [.2 .9 .1], ...,
142 'EdgeColor', 'black', ...,
143 'Margin', 5);
144
145 str4(1) = {'\fontsize{14}\bfK = 0.0005'};
146 text(5, -60, str4, 'HorizontalAlignment', 'left', ...,
147 'BackgroundColor', [.5 .5 .5], ...,
148 'EdgeColor', 'black', ...,
149 'Margin', 5);
150
151 str5(1) = {'\fontsize{14}\bfK = 0'};
152 text(7, -80, str5, 'HorizontalAlignment', 'left', ...,
153 'BackgroundColor', [.1 .4 .9], ...,
154 'EdgeColor', 'black', ...,
155 'Margin', 5);
156
157 % =====
158
159
160
161

```

Appendix H

**'Spectrum Analyser
Phase Noise Measurement
of the
Oscillator
&
ERA-51SM Datasheet'**

```

1 % =====
2 % MATLAB code for: Measure the Phase Noise of the closed-loop Oscillator on the Spectrum Analyser.
3 % Thesis: Paragraph 3.5.2.1
4 % Aim: Plot the measured oscillation as well as the calculated SSB phase noise relative to the carrier in [dBc/Hz].
5 % =====
6
7
8 load('C:\~\02 RBW = 1 kHz; VBW = 50 Hz\matlab.mat')
9
10 figure(1);
11 % Plot the Spectrum Analyser Output:
12 plot(f, data, '-r', 'Linewidth', 2);
13 hold on;
14 grid on;
15 title('\bfSpectrum Analyser Output', 'FontSize', 12);
16 xlabel('\bfFrequency, f [Hz]', 'FontSize', 12);
17 ylabel('\bfAmplitude [dBm]', 'FontSize', 12);
18
19 str1(1) = {'\fontsize{12}\bfSA Settings :'};
20 str1(2) = {' RBW = 1 kHz;'};
21 str1(3) = {' VBW = 50 Hz;'};
22 str1(4) = {' SPAN = 100 kHz.'};
23 text(999.993e6, -10, str1, 'HorizontalAlignment', 'left', ...
24 'BackgroundColor', [.7 .9 .7], ...
25 'EdgeColor', 'black', ...
26 'Margin', 5);
27
28 x = 0.003e6;
29 index = find(data == max(data)); % 250
30 data_f0 = data(index); % 7.9703 dBm
31 f0 = f(index); % 1.000041989029599 GHz
32 plot(f0, data_f0, 'ob', 'Linewidth', 2);
33 plot([f0 (f0 - 2*x)], [data_f0 data_f0], '-b', 'Linewidth', 2);
34 text((f0 - 10*x), data_f0, strcat('\bfAmplitude = ', num2str(data_f0), ' dBm'), 'FontSize', 14);
35 text((f0 - 10*x), (data_f0 - 4), strcat('\bff = ', num2str(f0/1e6), ' MHz'), 'FontSize', 14);
36
37
38
39
40
41

```

```

42 % ... figure(1) ...
43 x1 = 0.019e6;
44 x2 = 0.01e6;
45 ylimits = get(gca, 'YLim');
46 plot([(f0 + 10e3) (f0 + 10e3)], [ylimits(1) ylimits(2)], '--b', 'Linewidth', 2);
47 plot([(f0 + 1e3) (f0 + 1e3)], [-20, 'ob', 'Linewidth', 2]);
48 plot([(f0 + 1e3) (f0 + 1e3 + x1)], [-20 -20], '-b', 'Linewidth', 2);
49 text((f0 + 1e3 + x1), -19, '\bfFrequency Offset = 1 kHz.', 'FontSize', 14);
50 text((f0 + 1e3 + x1), -22, strcat('\bf ', num2str(0.4882), ' dBm'), 'FontSize', 14);
51 plot([(f0 + 1e3) (f0 + 1e3)], [ylimits(1) ylimits(2)], '--b', 'Linewidth', 2);
52 plot([(f0 + 10e3), -30, 'ob', 'Linewidth', 2);
53 plot([(f0 + 10e3) (f0 + 10e3 + x2)], [-30 -30], '-b', 'Linewidth', 2);
54 text((f0 + 10e3 + x2), -29, '\bfFrequency Offset = 10 kHz', 'FontSize', 14);
55 text((f0 + 1e3 + x1), -32, strcat('\bf ', num2str(-74.49), ' dBm'), 'FontSize', 14);
56
57
58
59 figure(2);
60 % Plot the SSB Phase Noise relative to the Carrier, L(fm) [dBc/Hz] :
61 % -----
62 % Theory :
63 % Measured in a 1 Hz bandwidth, filter : RBW = 1 Hz;
64 % Sc_f = Pssb/Ps;
65 % OR : Sc_f = Pssb - Ps;
66 % data_dBc_Hz = 10*log10(Sc_f);
67 % semi_logx(f_offset, data_dBc_Hz, '-r', 'Linewidth', 2);
68 % -----
69
70 index = find(data == max(data));
71 data_f0 = data(index);
72 index_f = find(f == max(f));
73
74 ESB_data(1) = data_f0;
75 for n = 2 : index
76     ESB_data(n) = data(index + n - 1) - data_f0;
77     ESB_f(n) = f(index + n - 1) - f0;
78 end
79
80
81
82

```

```

83 % ... figure(2) ...
84 % Test...
85 ESB_data(1);
86 ESB_data(2);
87 ESB_data(250);
88 ESB_f(1);
89 ESB_f(2);
90 ESB_f(250);
91
92 RBW = 1e3;
93 RBW_dB = 10*log10(RBW);
94
95 L_fm_dBc_Hz(1) = ESB_data(1);
96 for n = 2 : index
97     L_fm_dBc_Hz(n) = ESB_data(n) - RBW_dB;
98 end
99 L_fm_dBc_Hz(1);
100 L_fm_dBc_Hz(2);
101 L_fm_dBc_Hz(250);
102
103 semilogx(ESB_f, ESB_data, '--b', 'Linewidth', 3);
104 hold on;
105 grid on;
106 semilogx(ESB_f, L_fm_dBc_Hz, '-r', 'Linewidth', 3);
107 title('\bfPhase Noise Measurement done on the Spectrum Analyser', 'FontSize', 12);
108 xlabel('\bfOffset Frequency from the Carrier, [Hz]', 'FontSize', 12);
109 ylabel('\bfSingle Sideband Phase Noise relative to the Carrier, L(f_m) [dBc/Hz]', 'FontSize', 12);
110 legend('\bfdBc/1kHz', '\bfdBc/Hz');
111
112 plot([ (20e3) (20e3)], [-115 -105], '--g', 'Linewidth', 3);
113 text((15e3), -102, '\bfThermal Noise of the Oscillator.', 'FontSize', 14);
114
115 % =====
116
117 f(250);
118 f(251);
119 delta_f = f(251) - f(250);
120 (f0 + delta_f) - f(251);
121
122 % =====
123

```

Surface Mount

Monolithic Amplifier

DC-4 GHz

Product Features

- DC-4 GHz
- Single Voltage Supply
- Internally Matched to 50 Ohm
- Unconditionally Stable
- Low Performance Variation Over Temperature
- Transient Protected
- Aqueous washable
- Protected By US Patent 6,943,629

Typical Applications

- Cellular/ PCS/ 3G Base Station
- CATV, Cable Modem & DBS
- Fixed Wireless & WLAN
- Microwave Radio & Test Equipment



ERA-51SM+

CASE STYLE: WW107
PRICE: \$3.90 ea. QTY. (30)

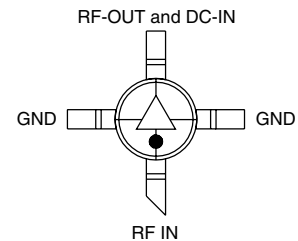
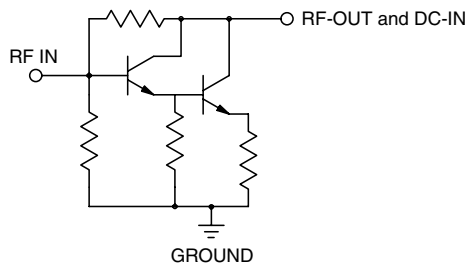
+ RoHS compliant in accordance with EU Directive (2002/95/EC)

The +Suffix has been added in order to identify RoHS Compliance. See our web site for RoHS Compliance methodologies and qualifications.

General Description

ERA-51SM+ (RoHS compliant) is a wideband amplifier offering high dynamic range. It has repeatable performance from lot to lot. It is enclosed in an Micro-X package. ERA-51SM+ uses Darlington configuration and is fabricated using InGaP HBT technology. Expected MTBF is 450 years at 85°C case temperature.

simplified schematic and pin description



Function	Pin Number	Description
RF IN	1	RF input pin. This pin requires the use of an external DC blocking capacitor chosen for the frequency of operation.
RF-OUT and DC-IN	3	RF output and bias pin. DC voltage is present on this pin; therefore a DC blocking capacitor is necessary for proper operation. An RF choke is needed to feed DC bias without loss of RF signal due to the bias connection, as shown in "Recommended Application Circuit".
GND	2,4	Connections to ground. Use via holes as shown in "Suggested Layout for PCB Design" to reduce ground path inductance for best performance.

Mini-Circuits®
ISO 9001 ISO 14001 CERTIFIED

ALL-NEW
minicircuits.com

P.O. Box 350166, Brooklyn, New York 11235-0003 (718) 934-4500 Fax (718) 332-4661 For detailed performance specs & shopping online see Mini-Circuits web site



Provides ACTUAL Data Instantly From MINI-CIRCUITS At: www.minicircuits.com

RF/IF MICROWAVE COMPONENTS

REV. L
M108520
ERA-51SM+
070122
Page 1 of 4

Electrical Specifications at 25°C and 65mA, unless noted

Parameter	Min.	Typ.	Max.	Units	Cpk	
Frequency Range*	DC		4	GHz		
Gain	f=0.1 GHz	17	18	19	dB	≥ 1.5
	f=1 GHz		17.4			
	f=2 GHz	14	16.1	17.2		
	f=3 GHz		14.8			
	f=4 GHz	11.5	12.5	14.5		
Magnitude of Gain Variation versus Temperature (values are negative)	f=0.1 GHz		.0012	.0024	dB/°C	
	f=1 GHz		.002	.004		
	f=2 GHz		.0027	.0054		
	f=3 GHz		.0033	.0066		
	f=4 GHz		.0043	.0086		
Input Return Loss	f=0.1 GHz		26		dB	
	f=1 GHz		29			
	f=2 GHz		32			
	f=3 GHz		28			
	f=4 GHz		25			
Output Return Loss	f=0.1 GHz		28		dB	
	f=1 GHz		24			
	f=2 GHz		21			
	f=3 GHz		24			
	f=4 GHz		21			
Reverse Isolation	f=1.0 GHz	19	22		dB	
Output Power @ 1 dB compression	f=0.1 GHz		18.3		dBm	≥ 1.33
	f=1 GHz	16.5	18.1			
	f=2 GHz		17.8			
	f=3 GHz		16.9			
	f=4 GHz		14.8			
Saturated Output Power (at 3dB compression)	f=0.1 GHz		18		dBm	
	f=1 GHz		18			
	f=2 GHz		18			
	f=3 GHz		17			
	f=4 GHz		16			
Output IP3	f=0.1 GHz	33.5	35.1		dBm	≥ 1.33
	f=1 GHz		35.4			
	f=2 GHz	31	33.9			
	f=3 GHz		31			
	f=4 GHz	25	27.8			
Noise Figure	f=0.1 GHz		3.6	4.2	dB	≥ 1.33
	f=1GHz		3.7			
	f=2 GHz		3.7	4.5		
	f=3 GHz		3.9			
	f=4 GHz		4	5		
Group Delay	f=1 GHz		100		psec	
Recommended Device Operating Current			65		mA	
Device Operating Voltage		4.2	4.5	4.8	V	≥ 1.5
Device Voltage Variation vs. Temperature at 65mA			-3.2		mV/°C	
Device Voltage Variation vs. Current at 25°C			5.8		mV/mA	
Thermal Resistance, junction-to-case ¹			154		°C/W	

*Guaranteed specification DC-4 GHz. Low frequency cut off determined by external coupling capacitors.

Absolute Maximum Ratings

Parameter	Ratings
Operating Temperature*	-45°C to 85°C
Storage Temperature	-65°C to 150°C
Operating Current	120mA
Power Dissipation	650mW
Input Power	13dBm

Note: Permanent damage may occur if any of these limits are exceeded. These ratings are not intended for continuous normal operation.
¹Case is defined as ground leads.
 *Based on typical case temperature rise 5°C above ambient.



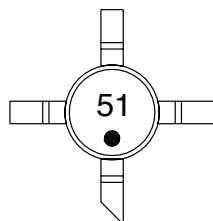
P.O. Box 350166, Brooklyn, New York 11235-0003 (718) 934-4500 Fax (718) 332-4661 For detailed performance specs & shopping online see Mini-Circuits web site



The Design Engineers Search Engine Provides ACTUAL Data Instantly From MINI-CIRCUITS At: www.minicircuits.com

RF/IF MICROWAVE COMPONENTS

Product Marking



Additional Detailed Technical Information

Additional information is available on our web site. To access this information enter the model number on our web site home page.

Performance data, graphs, s-parameter data set (.zip file)

Case Style: WW107

Plastic micro-x, .085 body diameter, lead finish: tin/silver/nickel

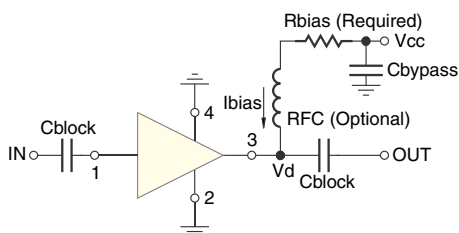
Tape & Reel: F4

Suggested Layout for PCB Design: PL-075

Evaluation Board: TB-408-51+

Environmental Ratings: ENV08T2

Recommended Application Circuit



Test Board includes case, connectors, and components (in bold) soldered to PCB

R BIAS	
Vcc	"1%" Res. Values (ohms) for Optimum Biasing
7	40.2
8	53.6
9	68.1
10	82.5
11	97.6
12	113
13	127
14	143
15	158
16	174
17	191
18	205
19	221
20	237

ESD Rating

Human Body Model (HBM): Class 1B (500 v to < 1000 v) in accordance with ANSI/ESD STM 5.1 - 2001

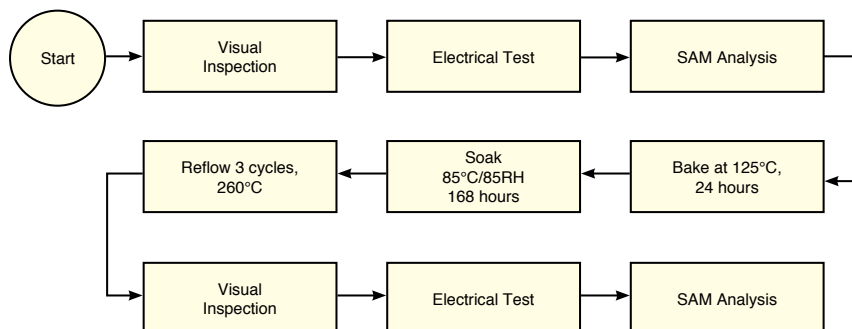
Machine Model (MM): Class M1 (< 100 v) in accordance with ANSI/ESD STM 5.2 - 1999

MSL Rating

Moisture Sensitivity: MSL1 in accordance with IPC/JEDECJ-STD-020C

No.	Test Required	Condition	Standard	Quantity
1	Visual Inspection	Low Power Microscope Magnification 40x	MIP-IN-0003 (MCT spec)	45 units
2	Electrical Test	Room Temperature	SCD (MCL spec)	45 units
3	SAM Analysis	Less than 10% growth in term of delamination	J-Std-020C (Jedec Standard)	45 units
4	Moisture Sensitivity Level 1	Bake at 125°C for 24 hours Soak at 85°C/85%RH for 168 hours Reflow 3 cycles at 260°C peak	J-Std-020C (Jedec Standard)	45 units

MSL Test Flow Chart



P.O. Box 350166, Brooklyn, New York 11235-0003 (718) 934-4500 Fax (718) 332-4661 For detailed performance specs & shopping online see Mini-Circuits web site



The Design Engineers Search Engine Provides ACTUAL Data Instantly From MINI-CIRCUITS At: www.minicircuits.com

RF/IF MICROWAVE COMPONENTS

Appendix I

'Spectrum Analyser – FSEK30 Specifications'

-- only relevant pages --



Spectrum Analyzers FSEx

20 Hz to 40 GHz

- ◆ Spectrum analysis with ultra-wide dynamic range
Noise figure = 18 dB/TOI = 20 dBm typ. (FSEB)
- ◆ Universal analysis of digital and analog modulated signals (option) such as
BPSK, QPSK, $\pi/4$ -DQPSK, 8PSK, QAM, MSK, GMSK, 2FSK, AM, FM, PM
- ◆ High-speed synthesizer
5 ms for full span (FSEA, FSEB)
- ◆ Refresh rate, quasi-analog
25 sweeps/s
- ◆ Large LC TFT display
24 cm/9.5", active
- ◆ Future-proof modular design
Customized solutions through wide variety of options



ROHDE & SCHWARZ

Getting down to analysis

Specifications in brief

- ◆ Resolution bandwidths
1 Hz to 10 MHz,
adjustable in steps of 1/2/3/5/10
- ◆ Displayed noise floor –150 dBm (typ.)
in 10 Hz bandwidth
- ◆ 3rd-order intercept point
+20 dBm typ.

- ◆ 1 dB compression point of RF input
+10 dBm
- ◆ Phase noise at 10 kHz from carrier:
–123 dBc (Hz) (typ.) (FSEA 30)
- ◆ Total level measurement uncertainty
up to 1 GHz <1 dB, up to 7 GHz 1.5 dB
- ◆ AM/FM audio demodulator (with
built-in loudspeaker and headphones
connector)
- ◆ Internal RF trigger (trigger threshold
approx. –20 dBm)
- ◆ 5 ms full-span sweep time with fully
synchronized sweep (FSEA, FSEB),
150 ms with FSEM, 230 ms with FSEK
- ◆ 1 μs zero-span sweep time
- ◆ Pretrigger and trigger delay
- ◆ Gated sweep

Vector analysis for digital communication

The analyzers of the FSE family combine the capabilities of high-end RF or microwave spectrum analysis with those of universal digital-signal demodulation and analysis. This becomes possible with the vector signal analyzer option. The spectrum analyzer function offers the wide dynamic range necessary for many measurements on digitally modulated signals (e.g. burst measurements), and the vector signal analyzer option adds demodulation capability to bit stream level for signals such as

- BPSK, QPSK, $\pi/4$ -DQPSK
- 16QAM, (G)MSK, (G)FSK

All this is backed up by a variety of display types:

- ◆ Eye diagram
- ◆ Vector and constellation diagram
- ◆ Frequency and phase error
- ◆ Vector error

With a spectrum analyzer of the FSE family, you are perfectly equipped for the future of digital communication.

● Required ○ Recommended

Modularity safeguards investments

Series FSE analyzers are of modular design throughout. From the wide variety of options, you can choose exactly those needed for your particular application (see also fold-in page).

You thus get an instrument tailor-made to your requirements and pay for no more

than what you actually need. At the same time, you can feel sure that FSE will grow with your tasks and requirements as virtually all options can be retrofitted. Even extending the frequency range from 3.5 GHz to 7 GHz is no problem with option FSE-B2.

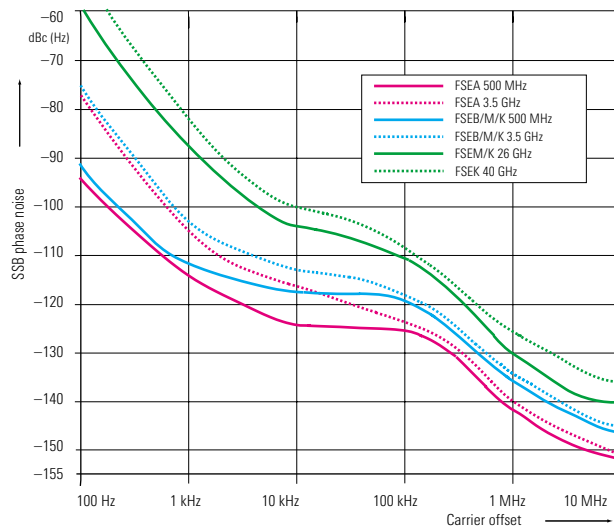
Your decision for Spectrum Analyzer FSE is a decision for a safe investment.

FSE options and their applications

Digital mobile radio systems	Analog mobile radio systems	TV and CATV	AM and FM sound broadcasting	General-purpose RF measurements		
○				○	FSE-B2	7 GHz Frequency Extension
●	○		●		FSE-B7	Vector Signal Analyzer
		○		○	FSE-B8/-B9/-B10/-B11	Tracking Generator
○					FSE-B13	1 dB Attenuator
○				○	FSE-B15	Controller
				○	FSE-B21	External Mixing
				○	FSE-B23	Broadband Output 741.4 MHz
○	○	○		○	FS-K3	Noise Measurement Software
○	○			○	FS-K4	Phase Noise Measurement Software
○					FSE-K10/-K11	GSM Application Firmware
○					FSE-K20/-K21	EDGE Application Firmware

Specifications

	FSEA30	FSEB30	FSEM30	FSEK30
Specifications are guaranteed under the following conditions: 30 minutes warmup time at ambient temperature, specified environmental conditions met, calibration cycle adhered to, and total calibration performed. Data without tolerances: typical values only. Data designated "nominal" apply to design parameters and are not tested.				
Frequency				
Frequency range	20 Hz to 3.5 GHz	20 Hz to 7 GHz	20 Hz to 26.5 GHz	20 Hz to 40 GHz
Frequency resolution	0.01 Hz			
Internal reference frequency, nominal				
Aging per day ¹⁾	1 x 10 ⁻⁹			
Aging per year ¹⁾	2 x 10 ⁻⁷			
Temperature drift (0°C to +50°C)	5 x 10 ⁻⁸			
Total error limit (per year)	2.5 x 10 ⁻⁷			
External reference frequency				
Frequency display	10 MHz or n x 1 MHz, n = 1 to 16 with marker			
Resolution	0.1 Hz to 10 kHz (as a function of span)			
Error limit (sweep time > 3 x auto sweep time)	±(marker frequency x reference error + 0.5 % x span + 10 % x resolution bandwidth + 1/2 (last digit))			
Frequency counter				
Resolution	measures the marker frequency 0.1 Hz to 10 kHz (selectable)			
Count accuracy (S/N > 25 dB)	±(frequency x reference error + 1/2 (last digit))			
Display range for frequency axis				
Resolution/error limit of display range	0 Hz, 10 Hz to full span 0.1 Hz/1%			
Spectral purity (dBc (Hz))				
SSB phase noise, f ≤ 500 MHz for f > 500 MHz see diagram below				
Carrier offset	100 Hz	<-87		<-81
	1 kHz	<-107		<-100
	10 kHz	<-120		<-114
	100 kHz ²⁾	<-119		<-113
	1 MHz ²⁾	<-138		<-132
Sweep time				
Span = 0 Hz	1 μs to 2500 s in 5% steps			
Span ≥ 10 Hz	5 ms to 16 000 s in steps ≤ 10%			
Error limit	< 1%			
Picture refresh rate (span ≤ 7 GHz)	> 20 updates/s with 1 trace, > 15 updates/s with 2 traces			
Sampling rate	50 ns (20 MHz A/D converter)			
Number of pixels	500			
Time measurement	with marker and cursor lines			
Resolution	50 ns			
Sweep trigger	free run, single, line, video, gated, delayed, external			
Zero span	additionally pretrigger, posttrigger, trigger delay			
Resolution bandwidths				
3 dB bandwidths (in 1/2/3/5 steps)	1 Hz to 10 MHz			
FFT filter (in 1/2/3/5 steps) (see also page 16)	1 Hz to 1 kHz			



SSB phase noise (typical values)

Specifications

	FSEA30	FSEB30	FSEM30	FSEK30
Bandwidth error	≤3 MHz		<10%	
	5 MHz		<15%	
	10 MHz		+25%, -10%	
Shape factor 60:3 dB	<1 kHz		<6	
	1 kHz to 2 MHz		<12	
	>2 MHz		<7	
Video bandwidths			1 Hz to 10 MHz, 1/2/3/5 steps	
Level				
Display range				noise floor displayed to 30 dBm
Maximum input level				
RF attenuation 0 dB				
DC voltage			0 V	
CW RF power			20 dBm (=0.1 W)	
Pulse spectral density			97 dBμV (MHz)	
RF attenuation ≥10 dB				
DC voltage			0 V	
CW RF power			30 dBm (=1 W)	
Max. pulse voltage		150 V		50 V
Max. pulse energy (10 μs)		1 mWs		0.5 mWs
1 dB compression of input mixer (0 dB RF attenuation)				+10 dBm nominal
Displayed average noise floor	in dBm (0 dB RF attenuation, RBW 10 Hz, VBW 1 Hz, 20 averages, trace average, span 0 Hz, termination 50 Ω)			
Frequency	20 Hz	<-80		<-74
	1 kHz	<-110		<-104
	10 kHz	<-125		<-119
	100 kHz	<-135		<-129
	1 MHz	<-145, -150 typ.		<-142, typ. -145
	10 MHz to 3.5/6 GHz	<-145, -150 typ.	<-142, -147 typ.	<-138, -140 typ.
	6 GHz to 7 GHz	-	<-139	<-135, -138 typ.
	7 GHz to 18 GHz	-	-	<-138, -140 typ. <-134, -139 typ.
	18 GHz to 26.5 GHz	-	-	<-135, -138 typ. <-131, -136 typ.
	26.5 GHz to 30 GHz	-	-	- <-120, -125 typ.
	30 GHz to 40 GHz	-	-	- <-116, -122 typ.
Max. dynamic range, bandwidth 1 Hz				
Displayed noise floor to 1 dB compression	165 dB	162 dB		160 dB
Max. harmonics suppression, f >50 MHz				>90 dB
Max. intermodulation-free range				
50 MHz to 3.5 GHz (nominal)	115 dB	-		-
150 MHz to 7/26.5 GHz (nominal)	-	115 dB		112 dB
Intermodulation				
TOI, intermodulation-free dynamic range, level 2 × -30 dBm, Δf >5 × RBW or >10 kHz	>84 dBc for f >50 MHz (TOI >12 dBm, 18 dBm typ.)	>90 dBc for f >150 MHz (TOI >15 dBm, 20 dBm typ.)		>94 dBc for f >100 MHz >80 dBc for f >7 GHz, (TOI >17 dBm, 22 dBm typ.; >10 dBm for f >7 GHz)
Intermodulation-free range at -40 dBm mixer level				105 dB
Intercept point k2 (dBm)	>25, >40 typ. for f <50 MHz, >45, >50 typ. for f >50 MHz			>25 for f <150 MHz, >35 typ., >40 for f >150 MHz, >45 typ.
Immunity to interference				
Image frequency (dB)		>80, >90 typ.		>80, >90 typ. for f <22 GHz >75, >80 typ. for f >22 GHz
Intermediate frequency (dB)	>100 dB			>75 dB
Spurious response (f >1 MHz, without input signal, 0 dB attenuation)				
Span <30 MHz				<-110 dBm
Span ≥30 MHz				<-100 dBm
f _{in} = 25.06 MHz, 25.175 MHz, 5.7172 GHz				<-100 dBm
f _{in} = 60 MHz	<-110 dBm			<-100 dBm
f _{in} = 14.1894 GHz, 15.6722 GHz				
Span >10 MHz				-90 dBm
Other interfering signals (mixer level <-10 dBm)	<-80 dB ³⁾			<-75 dB ³⁾

Specifications

	FSEA30	FSEB30	FSEM30	FSEK30
Level display				
Measurement display	500 × 400 pixels (with one diagram displayed); max. 2 diagrams with independent settings			
Logarithmic level range	10 dB to 200 dB, in steps of 10 dB			
Linear level range	10% of reference level per division (10 divisions) or logarithmic scaling			
Traces	max. 4 per diagram (max. 2 if 2 diagrams are displayed) quasi-analog display of all results			
Trace detector	max peak, min peak, auto peak (normal), sample, rms, average			
Trace functions	clear/write, max hold, min hold, average			
Setting range of reference level				
Logarithmic level display	−130 dBm to 30 dBm, in steps of 0.1 dB			
Linear level range	7.0 nV to 7.07 V in steps of 1%			
Units of level axis	dBm, dBμV, dBmV, dBμA, dBpW (logarithmic and linear level display); mV, μV, mA, μA, pW, nW (linear level display)			
Level measurement uncertainty (−40 dBm, RF attenuation 20 dB, reference level −15 dB, RBW 5 kHz)	The values are guaranteed for bandwidths from 10 Hz to 30 kHz and 100 kHz to 10 MHz.			
Absolute error limit at 120 MHz	<0.3 dB			
Frequency response (10 dB RF attenuation)				
<1 GHz			<0.5 dB	
1 GHz to 3.5/7 GHz			<1 dB	
7 GHz to 18 GHz	–			<2 dB ⁴⁾
18 GHz to 26.5 GHz	–			<2.5 dB ⁴⁾
26.5 GHz to 40 GHz	–		–	<3 dB ⁴⁾
Attenuator error limit	<0.3 dB			
IF gain error	<0.2 dB (0.1 dB typ.)			
Display nonlinearity				
Logarithmic level display (RBW ≥1 kHz, analog)				
0 dB to −50 dB			<0.3 dB	
−50 dB to −70 dB			<0.5 dB	
−70 dB to −80 dB			–	
−70 dB to −95 dB			<1 dB	
Linear level display			5% of reference level	
Bandwidth switching error				
1 Hz to 30 kHz/100 to 500 kHz			<0.2 dB	
1 MHz to 10 MHz			<0.3 dB	
Total measurement uncertainty (0 dB to 50 dB below reference level, span/RBW <100, rss 95% reliability)				
<1 GHz			<1 dB	
1 GHz to 3.5/7 GHz			<1.5 dB	
7 GHz to 18 GHz	–			<2.5 dB ⁴⁾
18 GHz to 26.5 GHz	–			<3 dB ⁴⁾
26.5 GHz to 40 GHz	–		–	<3.5 dB ⁴⁾
Pulse amplitude error (single pulses)				
Bandwidth <1 MHz/≥1 MHz			<0.5 dB, nominal/<2 dB, nominal	
Trigger functions				
Trigger			free run, line, video, RF, external	
Delayed sweep				
Trigger source			free run, line, video, RF, external	
Delay time			100 ns to 10 s, resolution 1 μs min. or 1% of delay time	
Error of delay time			±(1 μs + (0.1% × delay time))	
Delayed sweep time			2 μs to 1000 s	
Gated sweep				
Trigger source			external, RF level	
Gate delay			1 μs to 100 s	
Gate length			1 μs to 100 s, resolution min. 1 μs or 1% of gate length	
Error of gate length			±(1 μs + (0.05% × gate length))	
Gap sweep (span = 0 Hz)				
Trigger source			free run, line, video, RF, external	
Pretrigger			1 μs to 100 s, 50 ns resolution, dependent on sweep time	
Trigger to gap time			1 μs to 100 s, 50 ns resolution, dependent on sweep time	
Gap length			1 μs to 100 s, 50 ns resolution	

Specifications

	FSEA30	FSEB30	FSEM30	FSEK30
Audio demodulation				
AF demodulation types	AM and FM			
Audio output	loudspeaker and headphones output			
Marker stop time	100 ms to 60 s			
Inputs and outputs (front panel)				
RF input	N female, 50 Ω		adapter system, 50 Ω , N male and female, 3.5 mm male and female	adapter system, 50 Ω , N male and female, K male and female, 2.4 mm female
VSWR (RF attenuation ≥ 10 dB)				
f < 3.5 GHz	< 1.5			
f < 7 GHz	–		< 2.0	
f < 26.5 GHz	–	–	< 3	< 2.5
f < 37 GHz	–	–	–	< 2.5
f < 40 GHz	–	–	–	2.5 typ.
Attenuator	0 dB to 70 dB, selectable in 10 dB steps			
Probe power	+15 V DC, –12.6 V DC and ground, max. 150 mA			
Power supply and coding connector for antennas etc (antenna code)	12-contact Tuchel			
Supply voltages	± 10 V, max. 100 mA, ground			
AF output	$Z_{out} = 10 \Omega$, jack plug			
Open-circuit voltage	adjustable up to 1.5 V			
Inputs and outputs (rear panel)				
IF 21.4 MHz	$Z_{out} = 50 \Omega$, BNC female, bandwidth > 1 kHz or resolution bandwidth			
Level	0 dBm at reference level, mixer level > –60 dBm			
Video output	$Z_{out} = 50 \Omega$, BNC female			
Voltage (resolution bandwidth ≥ 1 kHz)	0 V to 1 V, full scale (open-circuit voltage); logarithmic scaling			
Reference frequency				
Output, usable as input	BNC female			
Output frequency	10 MHz			
Level	10 dBm nominal			
Input	1 MHz to 16 MHz, integer MHz			
Required level	> 0 dBm into 50 Ω			
Sweep output	BNC female, 0 V to 10 V in sweep range			
Power supply connector for noise source	BNC female, 0 V and 28 V, selectable			
External trigger/gate input	BNC female, > 10 k Ω			
Voltage	–5 V to +5 V, adjustable			
IEC/IEEE-bus control	interface to IEC625-2 (IEEE 488.2), command set: SCPI 1994.0			
Connector	24-contact Amphenol female			
Interface functions	SH1, AH1, T6, L4, SR1, RL1, PP1, DC1, DT1, C11			
Serial interface	RS-232-C (COM 1 and COM 2), 9-contact female connectors			
Mouse interface	PS/2 mouse compatible			
Plotter⁵⁾	via IEC/IEEE bus or RS-232-C; plotter language: HP-GL			
Printer interface	parallel (Centronics compatible) or serial (RS-232-C)			
Keyboard connector	5-contact DIN female for MF-2 keyboard			
User interface	25-contact Cannon female			
Connector for external monitor (VGA)	15-contact female			
General data				
Display	24 cm LC TFT colour display (9.5")			
Resolution	640 \times 480 pixels (VGA resolution)			
Pixel failure rate	< 2 $\times 10^{-5}$			
Mass memory	1.44 Mbyte 3 1/2" diskette drive, hard disk			
Operating temperature range				
Nominal temperature range	+5 $^{\circ}$ C to +40 $^{\circ}$ C			
Limit temperature range	0 $^{\circ}$ C to +50 $^{\circ}$ C			
Storage temperature range	–40 $^{\circ}$ C to +70 $^{\circ}$ C			
Humidity	+40 $^{\circ}$ C at 95 % relative humidity (IEC 68-2-3)			
Mechanical resistance				
Vibration, sinusoidal	5 Hz to 150 Hz, max. 2 g at 55 Hz; 55 Hz to 150 Hz, 0.5 g const. to IEC 68-2-6, IEC 68-2-3, IEC 1010-1, MIL-T-28800D, class 5			
Vibration, random	10 Hz to 300 Hz, acceleration 1.2 g (rms)			

Appendix J

'Aeroflex PN9000 Phase Noise Test System Manual

-

Oscillator Measurement'

-- only relevant pages --

PN9100

Built-in Low Noise DC/FM Frequency Synthesizer 2 MHz to 4.5/18 GHz

The reference frequency source is the keystone of easy phase noise measurements with low residual noise and high dynamic range. As a matter of fact, the residual system noise will be that of the reference source, in FM mode, since the base system residual noise is much lower (at least 20 and 30 dB).

Most of commercial DC/FM signal generators can be used as the external reference source, controlled from the PN9000 software (more than 20 drivers are included in the software). However, the appropriate signal generator will depend on the expected noise of the DUT. Should DUT noise is low close in or far away from the carrier, the reference synthesizer noise will have to be clean close in or far away accordingly. Unfortunately, most of commercial RF signal generators do not provide both, close-in and far away low noise. Thus, depending on the DUT applications, two sources will have to be used, which is not convenient. It takes too much space and immobilize an instrument with many functions which are not used for phase noise measurements.

The PN9100 is designed to provide simultaneously low phase noise, close-in and far away from the carrier.

Housed in the PN9000 mainframe, it makes the system smaller, lighter and easier to move.

Optional doublers extend the base frequency range to 9 and 18 GHz.

Lower frequency ranges are obtained dividing the upper range, improving the output signal noise up to the residual noise of the dividers, which is better than many crystal oscillators.

CW and DC FM Range 1 - SSB Noise (dBc/Hz),

Frequency Range, MHz	Slope Hz/V	1 Hz	10 Hz	100 Hz	1 kHz	10 kHz	100 kHz	1 MHz	10 MHz
9000 - 18000	3200	- 36	- 66	- 81	- 106	- 112	- 112	- 134	- 150
4500 - 9000	1600	- 42	- 72	- 87	- 112	- 118	- 118	- 140	- 156
2048 - 4500	800	- 48	- 78	- 93	- 118	- 124	- 124	- 146	- 162
1024 - 2048	400	- 54	- 84	- 99	- 124	- 130	- 130	- 152	- 152
512 - 1024	200	- 60	- 90	- 105	- 130	- 136	- 136	- 152	- 152
256 - 512	100	- 66	- 96	- 111	- 136	- 142	- 142	- 152	- 152
128 - 256	50	- 72	- 102	- 117	- 142	- 148	- 148	- 152	- 152
64 - 128	25	- 78	- 108	- 123	- 148	- 152	- 152	- 152	- 152
32 - 64	12.5	- 84	- 114	- 129	- 152	- 152	- 152	- 152	- 152
16 - 32	6.25	- 90	- 120	- 135	- 152	- 152	- 152	- 152	- 152
8 - 16	3.12	- 96	- 126	- 141	- 155	- 155	- 155	- 155	- 155
4 - 8	1.56	- 102	- 132	- 147	- 155	- 155	- 155	- 155	- 155
2 - 4	0.78	- 108	- 138	- 153	- 155	- 155	- 155	- 155	- 155

AEROFLEX - EUROPTEST

35 South Service Road - New York - USA Tel: 1 516 694 6700 Fax: 1 516 694 6771
5 place du general de Gaulle - 78990 Elancourt - France tel: 33 1 3051 3399 Fax: 33 1 3482 0575

PN9100 Specifications (page 2)

Frequency range	: 2.0 MHz to 4.5 GHz : 2.0 MHz to 9.0 GHz with PN9151 option : 2.0 MHz to 18 GHz with PN9151 + PN9152 options
Output level	: + 13 dBm \pm 2 dB
Frequency resolution	: 1 Hz up to 1024 MHz : 2 Hz from 1024 to 2048 MHz : 4 Hz from 2048 to 4500 MHz : 8 Hz from 4.5 to 9.0 GHz : 16 Hz from 9.0 to 18 GHz
Harmonics	: - 20 dBc up to 512 MHz : - 10 dBc above 512 MHz
Sub-Harmonics	: - 90 dBc up to 1024 MHz : - 30 dBc above 1024 MHz
Non Harmonics	: - 90 dBc up to 1024 MHz : Increases by 6 dB for each above range.

FM Mode : The DC FM oscillator is designed to bring the lowest contribution to the noise of the output signal. For FM range 1, used for clean stable sources, there is no contribution at all. For the other ranges, it increases with the selected FM deviation, specifically close-in the carrier.

FM deviation : 4 FM deviation ranges can be selected, to comply with noise and phase/frequency fluctuation of the DUT. FM range 1 provides the same residual noise as the CW mode, making the PN9100 the ideal reference source for any kind of stable source phase noise measurements.

Tables of page 1, 2, 3 & 4 show for each frequency range tune slope and SSB phase noise. Values are for 1 V peak. Input voltage range is \pm 10 V, then for each frequency range full FM deviation is 10 times the slope/V. Ranges 2, 3 and 4 add 10 times more each. FM deviation value is automatically set when selecting FM range and transferred to the loop parameters.

DC FM Range 2 , SSB Noise (dBc/Hz)

Frequency Range, MHz	Slope Hz/V	1 Hz	10 Hz	100 Hz	1 kHz	10 KHz	100 kHz	1 MHz	10 MHz
9000 - 18000	32000	- 12	- 42	- 72	- 106	- 112	- 112	- 134	- 150
4500 - 9000	16000	- 18	- 48	- 78	- 112	- 118	- 118	- 140	- 156
2048 - 4500	8000	- 24	- 54	- 84	- 118	- 124	- 124	- 146	- 162
1024 - 2048	4000	- 30	- 60	- 90	- 124	- 130	- 130	- 152	- 152
512 - 1024	2000	- 36	- 66	- 96	- 130	- 136	- 136	- 152	- 152
256 - 512	1000	- 42	- 72	- 102	- 136	- 142	- 142	- 152	- 152
128 - 256	500	- 48	- 78	- 108	- 142	- 148	- 148	- 152	- 152
64 - 128	250	- 54	- 84	- 114	- 148	- 152	- 152	- 152	- 152
32 - 64	125	- 60	- 90	- 120	- 148	- 152	- 152	- 152	- 152
16 - 32	62.5	- 66	- 96	- 126	- 152	- 152	- 152	- 152	- 152
8 - 16	31.2	- 72	- 102	- 132	- 155	- 155	- 155	- 155	- 155
4 - 8	15.6	- 78	- 108	- 138	- 155	- 155	- 155	- 155	- 155
2 - 4	7.8	- 84	- 114	- 144	- 155	- 155	- 155	- 155	- 155

It must be remarked that phase noise below 100 Hz offset increases with FM deviation (or tune slope).

DC FM Range 3 - SSB Noise (dBc/Hz)

Frequency Range, MHz	Slope Hz/V	1 Hz	10 Hz	100 Hz	1 kHz	10 kHz	100 kHz	1 MHz	10 MHz
9000 - 18000	320000	- 6	- 36	- 66	- 111	- 108	- 112	- 134	- 150
4500 - 9000	160000	- 12	- 42	- 72	- 97	- 114	- 118	- 140	- 156
2048 - 4500	80000	- 18	- 48	- 78	- 103	- 120	- 124	- 146	- 162
1024 - 2048	40000	- 24	- 54	- 84	- 109	- 126	- 130	- 152	- 152
512 - 1024	20000	- 30	- 60	- 90	- 115	- 132	- 136	- 152	- 152
256 - 512	10000	- 36	- 66	- 96	- 121	- 138	- 142	- 152	- 152
128 - 256	5000	- 42	- 72	- 102	- 127	- 144	- 148	- 152	- 152
64 - 128	2500	- 48	- 78	- 108	- 133	- 152	- 152	- 152	- 152
32 - 64	1250	- 54	- 84	- 114	- 140	- 152	- 152	- 152	- 152
16 - 32	625	- 60	- 90	- 120	- 146	- 152	- 152	- 152	- 152
8 - 16	312	- 66	- 96	- 126	- 152	- 155	- 155	- 155	- 155
4 - 8	156	- 72	- 102	- 132	- 155	- 155	- 155	- 155	- 155
2 - 4	78	- 78	- 108	- 138	- 155	- 155	- 155	- 155	- 155

DC FM Range 4 , SSB Noise (dBc/Hz)

Frequency Range, MHz	Slope kHz/V	1 Hz	10 Hz	100 Hz	1 kHz	10 kHz	100 kHz	1 MHz	10 MHz
9000 - 18000	3200.0		26	56	- 81	- 102	- 102	- 134	- 150
4500 - 9000	1600.0	2	32	62	- 87	- 107	- 118	- 140	- 156
2048 - 4500	800.0	8	38	68	- 93	- 113	- 124	- 146	- 162
1024 - 2048	400.0	14	44	74	- 99	- 119	- 130	- 152	- 152
512 - 1024	200.0	20	50	80	- 105	- 125	- 136	- 152	- 152
256 - 512	100.0	26	56	86	- 111	- 131	- 142	- 152	- 152
128 - 256	50.0	32	62	92	- 117	- 137	- 148	- 152	- 152
64 - 128	25.0	38	68	98	- 123	- 143	- 152	- 152	- 152
32 - 64	12.5	44	74	104	- 129	- 149	- 152	- 152	- 152
16 - 32	6.25	50	80	110	- 135	- 152	- 152	- 152	- 152
8 - 16	3.12	56	86	116	- 141	- 155	- 155	- 155	- 155
4 - 8	1.56	62	92	122	- 147	- 155	- 155	- 155	- 155
2 - 4	0.78	68	98	128	- 153	- 155	- 155	- 155	- 155

NB : FM Range 3 and 4 are used for highly drifting and noisy sources only.

The PN9100 is made of three screened modules housed in the back of the PN9000 mainframe, a one slot output front end module and the PN9211 reference time base, a two slot module also plugged in the front.

When the configuration includes the PN9253/54 MW downconverter, the PN9211 is removed and replaced by the PN9210, one of the three modules of the PN9253/54.

Appendix K

**'Oscillator Phase Noise Measurements
-
PN9000B'**

```

1 % =====
2 % MATLAB code for: Phase Noise Measurements taken of the Oscillator System on the Aeroflex PN9000B Measurement System.
3 % Thesis: Paragraph 3.5.2.2
4 % Aim: Plot the measured SSB phase noise relative to the carrier in [dBc/Hz].
5 % =====
6
7 % The phase noise were measured for three different attenuators in the feedback loop, respectively.
8
9 % Noise floor of the PN9000B Phase Noise Meter, at 1 GHz:
10 % -----
11 load -ascii 'C:\~\freq_Ruismeter_Ruivvloer.txt';
12 load -ascii 'C:\~\dBc_Ruismeter_Ruivvloer.txt';
13 figure(1);
14 semilogx(freq_Ruismeter_Ruivvloer, dBc_Ruismeter_Ruivvloer, '-k', 'Linewidth', 2);
15 hold on;
16 grid on;
17
18 % -----
19 % 1 dB Attenuation:
20 % -----
21 % Power Supply:
22 load -ascii 'C:\~\freq_ldBAtt_Kragbron.txt';
23 load -ascii 'C:\~\dBc_ldBAtt_Kragbron.txt';
24 semilogx(freq_ldBAtt_Kragbron, dBc_ldBAtt_Kragbron);
25
26 % Battery Power:
27 load -ascii 'C:\~\freq_ldBAtt_Batterye.txt';
28 load -ascii 'C:\~\dBc_ldBAtt_Batterye.txt';
29 semilogx(freq_ldBAtt_Batterye, dBc_ldBAtt_Batterye, '-r');
30
31 % 1dB - Testing... Same measurement, taken the following day...
32 load -ascii 'C:\~\freq_ldBAtt_Kragbron_2deMeting.txt';
33 load -ascii 'C:\~\dBc_ldBAtt_Kragbron_2deMeting.txt';
34 semilogx(freq_ldBAtt_Kragbron_2deMeting, dBc_ldBAtt_Kragbron_2deMeting, '-g');
35
36 title('\bfPN9000B : Single-sideband Phase Noise Measurement with a 1 dB Attenuator in the feedback loop.',
37 'FontSize', 12);
38 xlabel('\bfOffset frequency form the carrier, f_m [Hz]', 'FontSize', 12);
39 ylabel('\bfSSB Phase Noise relative to the Carrier, L(f_m) [dBc/Hz]', 'FontSize', 12);
40 legend('\fontsize{14}\bfPN9000B Noise floor at 1 GHz', '\fontsize{14}\bfDay 1 : Power Supply',
41 '\fontsize{14}\bfDay 1 : Battery Power', '\fontsize{14}\bfDay 2 : Power Supply');

```

```

42 % -----
43 % 6 dB Attenuation:
44 % -----
45 %
46 load -ascii 'C:\~\freq_6dBAtt_Kragbron.txt';
47 load -ascii 'C:\~\dBC_6dBAtt_Kragbron.txt';
48
49 figure(2);
50 semilogx(freq_Ruismeter_Ruisvloer, dBc_Ruismeter_Ruisvloer, '-k', 'Linewidth', 2);
51 hold on;
52 grid on;
53 semilogx(freq_1dBAtt_Kragbron_2deMeting, dBc_1dBAtt_Kragbron_2deMeting, '-g');
54 %semilogx(freq_1dBAtt_Kragbron, dBc_1dBAtt_Kragbron, '-g');
55 semilogx(freq_6dBAtt_Kragbron, dBc_6dBAtt_Kragbron, '-r');
56
57 % -----
58 % 7 dB Attenuation:
59 % -----
60 load -ascii 'C:\~\freq_7dBAtt_Kragbron.txt';
61 load -ascii 'C:\~\dBC_7dBAtt_Kragbron.txt';
62 semilogx(freq_7dBAtt_Kragbron, dBc_7dBAtt_Kragbron, 'k');
63
64 title('\bFPN9000B : Single-sideband Phase Noise Measurement with different Attenuators in the feedback loop.',
65 'FontSize', 12);
66 xlabel('\bOffset frequency form the carrier, f_m [Hz]', 'FontSize', 12);
67 ylabel('\bSSB Phase Noise relative to the Carrier, L(f_m) [dBc/Hz]', 'FontSize', 12);
68 legend('\fontsize{14}\bFPN9000B Noise floor at 1 GHz', '\fontsize{14}\bDay 2 : 1 dB', '\fontsize{14}\bDay 2 : 6 dB',
69 '\fontsize{14}\bDay 2 : 7 dB');
70
71
72 % =====
73
74

```

Appendix L

**'M/A-COM
Surface Mount Tuning Varactors
-
MA46H201'**

Features

- Constant Gamma Abrupt Junction: 0.5
Hyperabrupt Junctions: 0.75, 1.25 and 1.5
- Low Cost
- Surface Mount Packages
- Very High Quality Factor
- Capacitance Ratio to 10:1
- Case Style 1056 is Hermetic and may be Screened to JANTX levels
- Tape and Reel Packaging Available

Description Applications

M/A-COM offers four families of low cost surface mount gallium arsenide tuning varactors. All families have silicon nitride protected junctions for low leakage current and high reliability.

The **MA46H500 through MA46H504** family has hyperabrupt junctions with constant gamma of 1.5 from 2 to 12 volts and high quality factor.

The **MA46H200 through MA46H206** family has hyperabrupt junctions with constant gamma of 1.25 from 2 to 20 volts and higher quality factor.

The **MA46H070 through MA46H073** family has hyperabrupt junctions with constant gamma of 0.75 from 0 to 20 volts and very high quality factor.

The **MA46504 through MA46506** family has abrupt junctions with constant gamma of 0.5 from 0 to 30 volts and the highest quality factor.

Applications

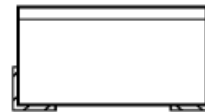
The **MA46H500 through MA46H504 (gamma 1.5)** family of constant gamma hyperabrupt GaAs tuning varactors is designed for wide bandwidth VCOs and voltage tuned filters where limited bias voltage is available. These varactors have lower quality factor than the other families of GaAs varactors.

The **MA46H200 through MA46H206 (gamma 1.25)** family of constant gamma hyperabrupt GaAs tuning varactors has the largest capacitance ratio of the families of GaAs varactors and high quality factor. These diodes are very well suited for wide bandwidth VCOs and VTFs where the optimum combination of very wide tuning range and high quality

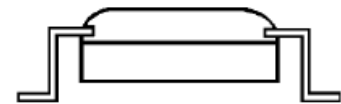
Absolute Maximum Ratings @ $T_A=+25^\circ\text{C}$

Parameter	Absolute Maximum	
	Case 1056	Case 1088
Operating Temperature	-65°C to +150°C	-65°C to +125°C
Storage Temperature	-65°C to +200°C	-65°C to +125°C
Reverse Voltage	Breakdown Voltage	
Forward Current	50mA @ 25°C	
Power Dissipation	50mW @ 25°C, derate linearly to 0mW at maximum operating temperature	

Common Case styles

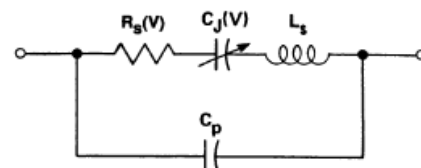


1056



1088

PACKAGED TUNING VARACTOR EQUIVALENT CIRCUIT



The **MA46H070 through MA46H073 (gamma 0.75)** family of constant gamma hyperabrupt GaAs tuning varactors has quality factor approaching that of abrupt junction varactors, but higher capacitance change versus tuning voltage. These diodes are very well suited for narrower bandwidth VCOs and VTFs where wide tuning range and very high quality factor are required.

The **MA46504 through MA46506 (gamma 0.5)** family of constant gamma abrupt GaAs tuning varactors has the highest quality factor. These diodes are very well suited for narrower bandwidth VCOs and VTFs where highest quality factor is of paramount concern

Electrical Specifications @ T_A = +25 °C

Gamma 0.5 Abrupt Tuning Varactors

Breakdown Voltage @ 10 μA = 30 V minimum
Reverse Current @ 24 V = 100 nA maximum
Gamma = 0.48 - 0.50, VR = 0 to 30 V

Part Number	Total Capacitance ^{2,3,5,7} +/-10%	Total Capacitance Ratio	Q Minimum
	Vr=4V	$\frac{Vr=0V}{Vr=30V}$	Vr=4V f=50MHz
	(pF)	-	-
MA46504	0.5 - 0.7	2.1	6000
MA46505	0.9 - 1.1	2.8	5700

Electrical Specifications @ T_A = +25 °C

Gamma 0.75 Hyperabrupt Tuning Varactors

Breakdown Voltage @ 10 μA = 20 V minimum
Reverse Current @ 16 V = 100 nA maximum
Gamma = 0.68 - 0.83, VR = 0 to 20 V

Part Number	Total Capacitance ^{2,3,5,7} +/-10%	Total Capacitance Ratio	Q Minimum
	Vr=4V	$\frac{Vr=0V}{Vr=20V}$	Vr=4V f=50MHz
	(pF)	-	-
MA46H070	0.5 - 0.7	5.5	4500
MA46H071	0.9 - 1.1	6.4	4500
MA46H072	2.7 - 3.3	7.5	3000
MA46H073	4.5 - 5.5	7.5	2200

Electrical Specifications @ T_A = +25 °C

Gamma 1.25 Hyperabrupt Tuning Varactors

Breakdown Voltage @ 10 μA = 22 V minimum
Reverse Current @ 16 V = 100 nA maximum
Gamma = 1.13 - 1.38, VR = 2 to 20 V

Part Number	Total Capacitance ^{2,3,5,7} +/-10%	Total Capacitance Ratio	Q Minimum
	Vr=4V	$\frac{Vr=2V}{Vr=20V}$	Vr=4V f=50MHz
	(pF)	-	-
MA46H200	0.5-0.7	3	3000
MA46H201	0.9-1.1	4.1	3000
MA46H202	2.7-3.3	5.6	2000
MA46H203	4.5-5.5	10	1500
MA46H204	9-11	10	1500
MA46H205	10.8-13.2	10	1500

Electrical Specifications @ T_A = +25 °C

Gamma 1.5 Hyperabrupt Tuning Varactors

Breakdown Voltage @ 10μA = 18 V minimum
Reverse Current @ 14 V = 100 nA maximum
Gamma = 1.4 - 1.6, VR = 2 to 12 V

Part Number	Total Capacitance ^{2,3,5,7} +/-10%	Total Capacitance Ratio	Q Minimum
	Vr=4V	$\frac{Vr=2V}{Vr=12V}$	Vr=4V f=50MHz
	(pF)	-	-
MA46H500	0.5-0.7	2.8	2500
MA46H501	0.9-1.1	3.9	2500
MA46H503	4.5-5.5	8.1	1200
MA46H504	9-11	8.1	1200

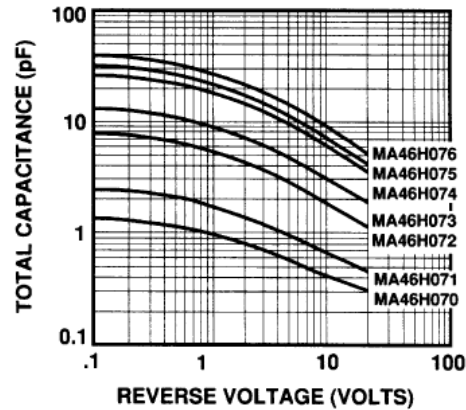
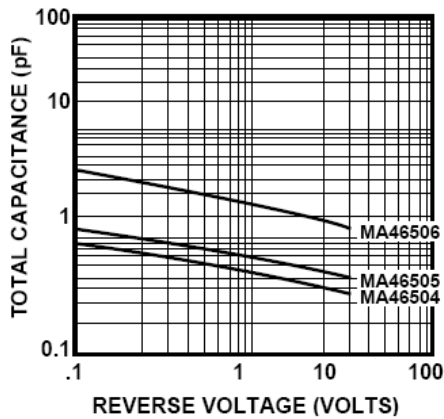
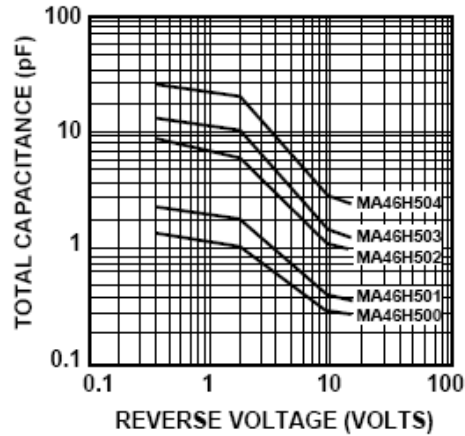
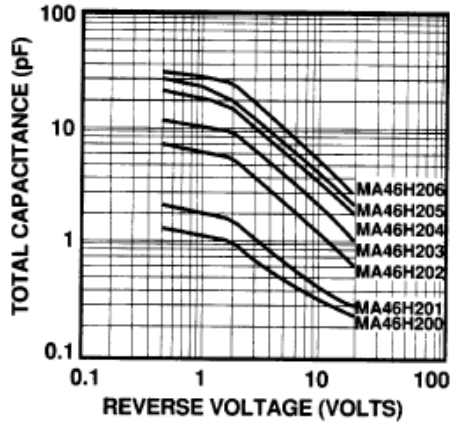
Notes:

1. Case parasitics (Cp and Ls) are given for most case styles along with case outlines in the appendix. The Cp values listed typically have tolerances of ±0.02 pF.
2. The values guaranteed for gamma are measured on unpackaged chips. The total capacitance versus bias voltage curve will deviate slightly from the chip capacitance versus bias voltage curve due to the package parasitic capacitance (Cp).
3. Capacitance is measured at 1 MHz.
4. Reverse voltage (VB) is measured at 10 microamps.
5. The total capacitance and capacitance ratios shown are for diodes housed in case style 30. Other case styles will result in different values.

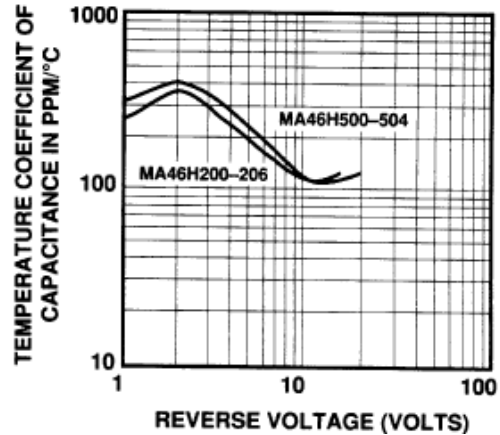
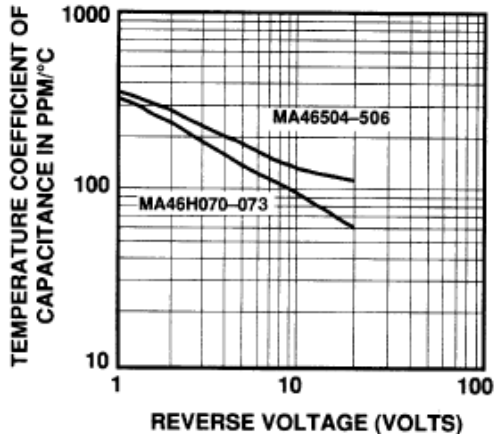
Specifications Subject to Change Without Notice.

Typical Performance Curves

Capacitance vs Reverse Voltage

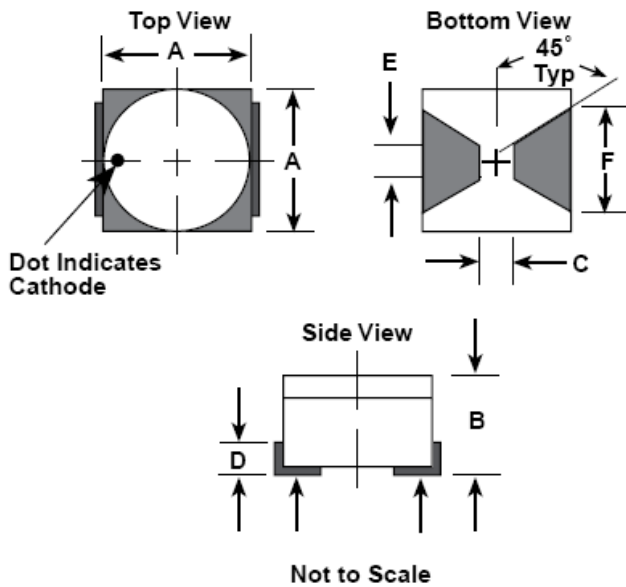


Temperature Coefficient of Capacitance vs Reverse Voltage



Case Styles

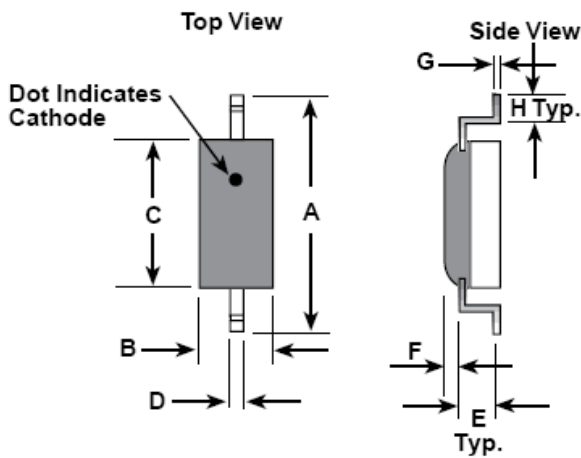
ODS-1056



DIM.	INCHES		MILLIMETERS	
	MIN.	MAX.	MIN.	MAX.
A	0.065	0.075	1.72	1.90
B	0.034	0.041	0.86	1.04
C	0.030	0.036	0.76	0.91
D	0.013	0.017	0.33	0.44
E	0.010	0.014	0.25	0.36
F	0.043	0.053	1.09	1.35

Package Capacitance: 0.15 pF Typical
Package Inductance: 0.45 nH Typical

ODS-1088



DIM.	INCHES		MILLIMETERS	
	MIN.	MAX.	MIN.	MAX.
A	0.175	0.195	4.44	4.95
B	0.040	0.050	1.02	1.27
C	0.085	0.095	2.16	2.41
D	0.015	0.025	0.38	0.64
E	0.010	0.015	0.25	0.38
F	0.015	0.020	0.38	0.51
G	0.004	0.006	0.10	0.15
H	0.020	0.030	0.51	0.76
J	0.013	0.033	0.33	0.84
K	0.003	0.005	0.08	0.13

Package Capacitance: 0.13 pF Typical
Package Inductance: 0.50 nH Typical

Ordering Information

These GaAs tuning varactors are available in either case style as shown. When ordering, specify the desired case style by adding the case designation as a suffix to the model number. For example, a MA46H200-1088 specifies a 1.25 gamma hyperabrupt tuning diode in case style 1088.

Appendix M

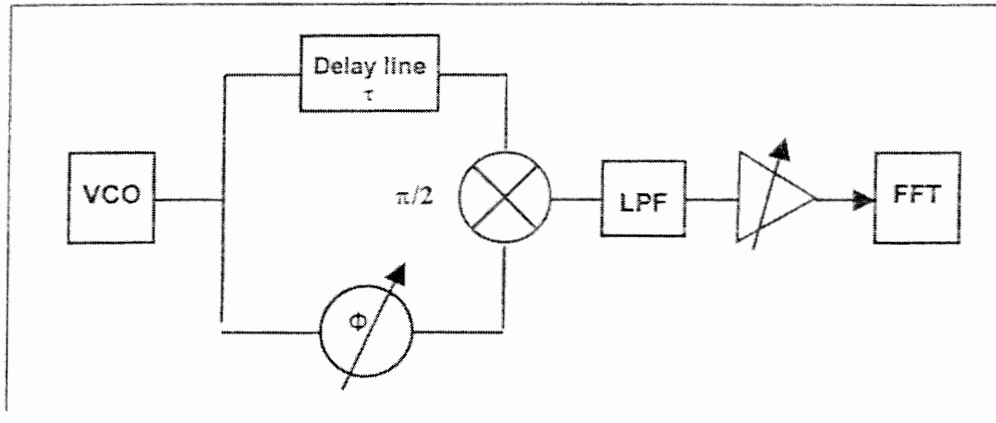
'Aeroflex PN9000 Phase Noise Test System Manual

-

VCO Measurement'

-- only relevant pages --

Delay Line FM Discrimination Method



$$V(t) = K\Phi \frac{2\pi\tau \sin(\pi f\tau) \Delta f(t)}{(\pi f\tau)}$$

This formula shows that the level of the detected noise is proportional to :

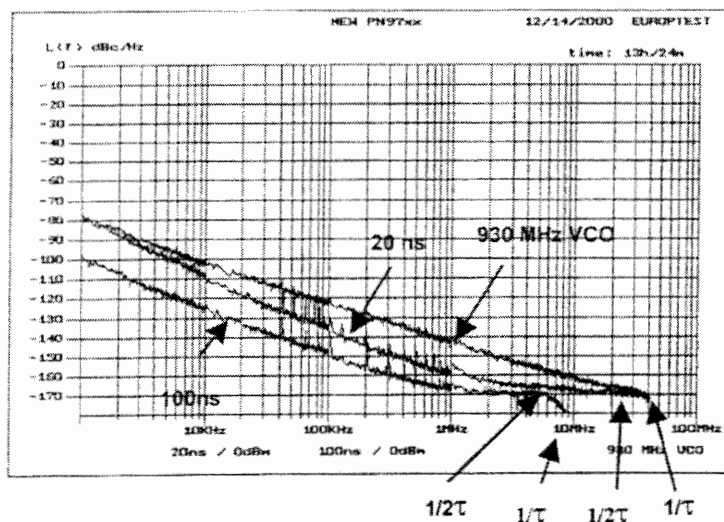
- The constant factor $K\Phi$, which depends on the phase detector characteristics and the input levels.
- The delay (τ) of the line, usually expressed in nanoseconds.
- The term $\sin x/x$, which limits the offset analysis. As a matter of fact :

For $f < 1/2\pi\tau$, $\sin(\pi f\tau) / (\pi f\tau) \cong 1$ and $V(t) = K\Phi 2\pi\tau \Delta f(t)$

Up to $f = 1/2\tau$ measurements are possible with software correction.

The first null of the magnitude transfer function is at $1/\tau$, which, for a 100 ns delay line is at : $1/100 \cdot 10^{-9} \text{ Hz} = 10 \text{ MHz}$. With software correction measurements remain calibrated up to 5 MHz.

The simple formula $1000 / 2\tau$ (ns) provides the maximum measurement offset of a delay line in MHz.



These graphs show the actual residual noise of two delay lines, 20 ns for 25 MHz offset measurements and 100 ns for 5 MHz offset, since they are measurements of a lower noise resonator source.

The noise of the VCO shows that a single 20 ns delay line can measure a GSM 900 MHz VCO from 1 KHz to 25 MHz offset.

Delay line method is the ideal solution to measure free running sources, with phase noise usually higher than that of a PLL VCO close-in to the carrier, but lower for 100 KHz offset and beyond, where it is difficult to find a reference source with noise floor below -160 dBc/Hz .

With a residual noise of -170 dBc/Hz the delay line method can also be used to measure very low noise PLL sources from 100 KHz offset.

PN9000

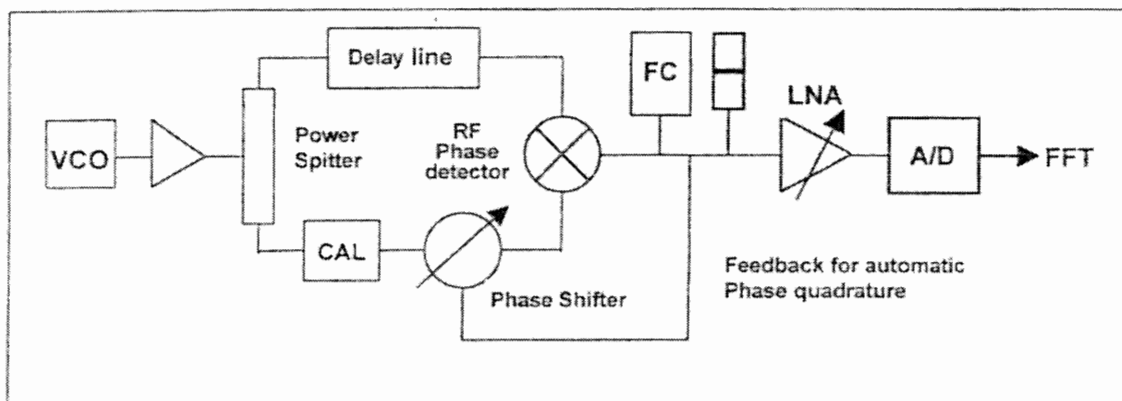
RF and MW Free-run Source
Phase Noise Measurements

(From 100 MHz to 100 GHz)

Phase noise of Free-run frequency sources, such as VCO, DRO or YIG oscillators cannot be easily measured using the reference phase locking method. Their frequency drift and phase/frequency fluctuation are generally too high to allow phase locking a DC FM reference source.

Fortunately, an other method can be used to obtain phase quadrature between RF and LO inputs of the RF phase detector of the PN9000 base system. Its principle of operation is shown below.

PN9000 Delay Line Operating Diagram



The DUT signal is connected to the power splitter through the input amplifier-conformer, to compensate insertion loss of the delay line and the phase shifter. One power splitter output is connected, through the delay line to the RF input of the phase detector. The other output goes to LO input through the calibrator and the phase shifter, which allows to adjust fine phase quadrature.

Feedback from the phase detector output to the phase shifter allows automatic phase quadrature adjust. the same routine controls the built-in calibrator. One button launches a complete measurement sequence.

Operating frequency range is 250 MHz to 2 GHz (need the RF and MW phase detector).

A family of VCO U/D converters extend frequency range from 2GHz to 18GHz. From 18GHz to 100GHz, Harmonic mixers driven by MW LO source downconvert mmW free-run sources to the operating range of the delay lines. (see mmW note)

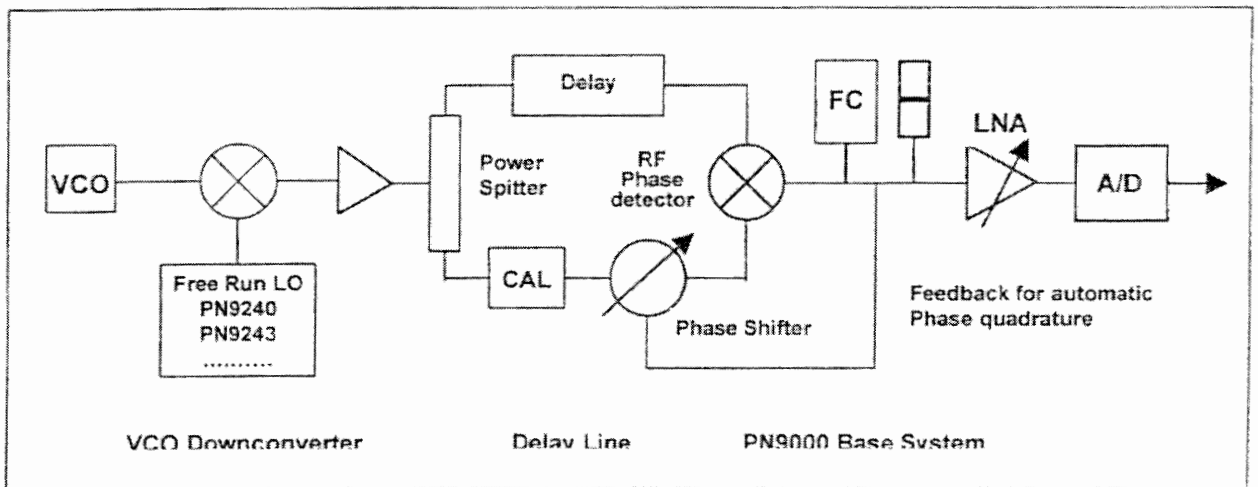
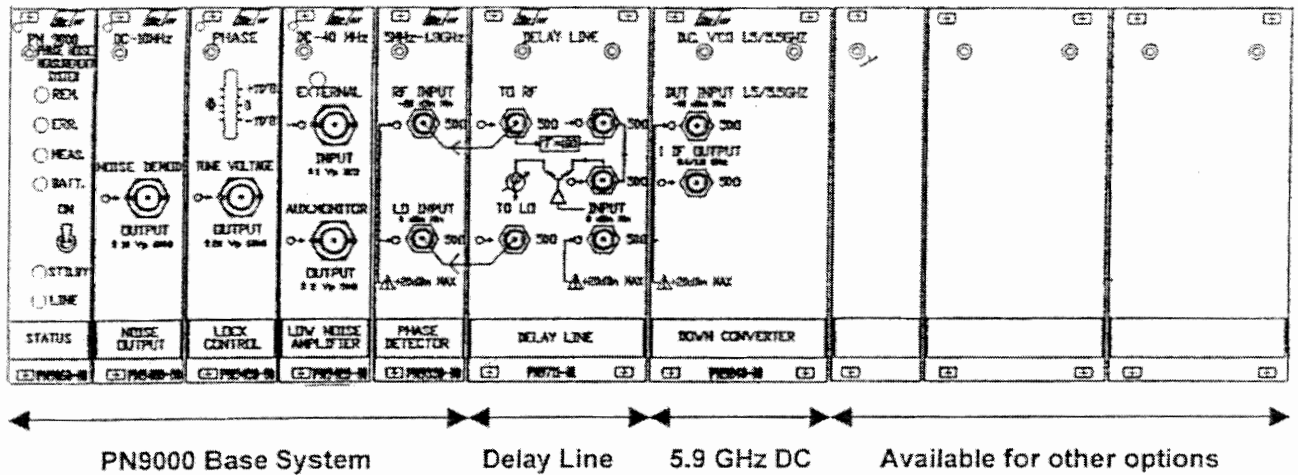
Due to $\sin(x)/x$ response of a delay line, appropriate delay must be selected depending on the desired offset analysis , taking into account the residual noise is depending of length of the delay line (see table below) . Null energy transfer through the delay line can be calculated as follows:

$1000/\text{delay in ns} = \text{Null offset in MHz}$. The PN9000 software compensates the $\sin(x)/x$ response up to half of the null offset. The PN9715 delay line provides 20 and 100 ns delay. 20 ns delay allows measurements up to 25 MHz offset, and 100 ns up to 5 MHz with lower residual noise. The PN9716, 10 & 100 ns, measurement offset is extended to 40 MHz.

AEROFLEX – EUROPTTEST

35 South Service Road – New York 11803 – USA – Tel 1 516 694 6700 Fax 1 516 694 6771
5 place du general de Gaulle– 78990 – Elancourt – France – Tel 33 1 3051 3399 Fax 33 1 3051 0575

PN9000 UP and Downconverters



Free-run Local oscillators are required to downconvert MW free-run sources. As a matter of fact, noise floor of phase locked sources is generally higher than the noise of free run sources far away from the carrier. For example, noise floor of clean PLL or synthesizers is rarely lower than -150 dBc/Hz at 1 MHz, when last VCO generation provides -160 dBc/Hz at 1MHz and lower than -165 dBc/Hz at 10MHz. The residual noise of the PN9240 downconverter, for VCOs from 2 to 5.9 GHz is as low as -168 dBc/Hz at 10 MHz offset, due to the use of free-run DROs.

The family of PN9000 VCO Up/Downconverters includes :

- PN9245, 2 to 2.9 GHz input frequency range
- PN9240, 2 to 5.9 GHz
- PN9242, 2 to 10 GHz
- PN9243, 2 to 18 GHz. See mmW note for devices above 18 GHz.
- PN9908, 100MHz 1GHz up-converter.

All work in their specifications with input level of -10 to 0 dBm/50 Ohm.

Residual System Phase Noise

The residual phase noise of the system will be the combination of the delay line residual noise and the Local oscillators of the downconverters. The table at the next page gives the noise figures of each contributor. The actual residual noise will be the worst case, of course.

PN9000 Delay Line Specifications

Frequency Range	: 250 MHz to 2 GHz (need RF and MW phase detector)
RF Input Level	: - 10 to + 0 dBm/50 Ω
Delay	: 20 and 100 ns for the PN9715 10 and 100 ns for the PN9716 Other values on request
Offset Analysis	: 40 MHz for 10 ns delay 25 MHz for 20 ns delay 5 MHz for 100 ns delay
Residual Phase Noise	: Depends on the selected delay and the noise of the downconverter LO. See table below.



Offset	100 ns	20 ns	10 ns	2-5.9 GHz	5.9-10 GHz	18 GHz
1 KHz	- 90	- 80	- 74	- 90	- 84	- 78
10 KHz	- 120	- 106	- 100	- 120	- 114	- 108
100 KHz	- 140	- 126	- 120	- 140	- 134	- 128
1 MHz	- 160	- 146	- 140	- 160	- 154	- 148
4 MHz	- 168	- 160	- 154	- 166	- 160	- 154
10 MHz	NA	- 166	- 158	- 168	- 162	- 156
20 MHz	NA	- 166	- 160	- 168	- 162	- 156

For the delay lines, figures are typical values at 1 GHz. Delay line residual noise increases as a function of the frequency : $20 \log F_{dut}/1\text{GHz}$. For example for $F_{dut} = 1.5 \text{ GHz}$, residual noise can be 3.5 dB higher. Above 2GHz , the total residual noise is the sum of the delay line and downconverter individual noise .

It is interesting to note that for very clean stable phase locked sources, delay line method provides lower residual noise than most of the phase locked references and MW down-converters.

For other specifications see **PN9000 base system data sheet**.

For more information e-mail to Info@europtest.com

Revision 03 / January / 2001

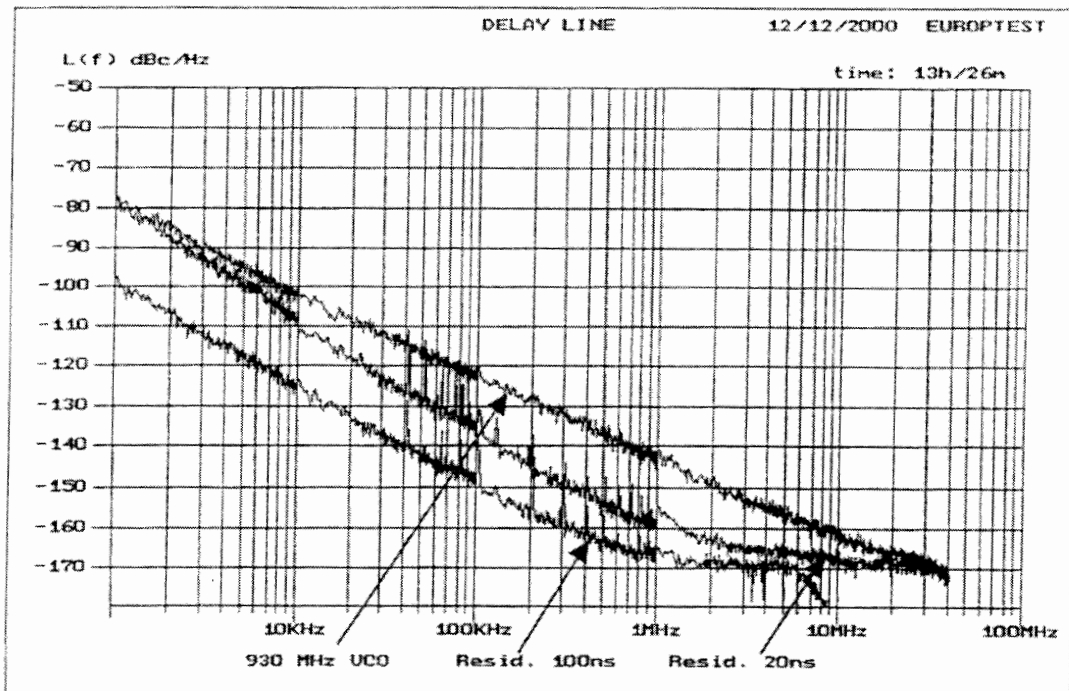
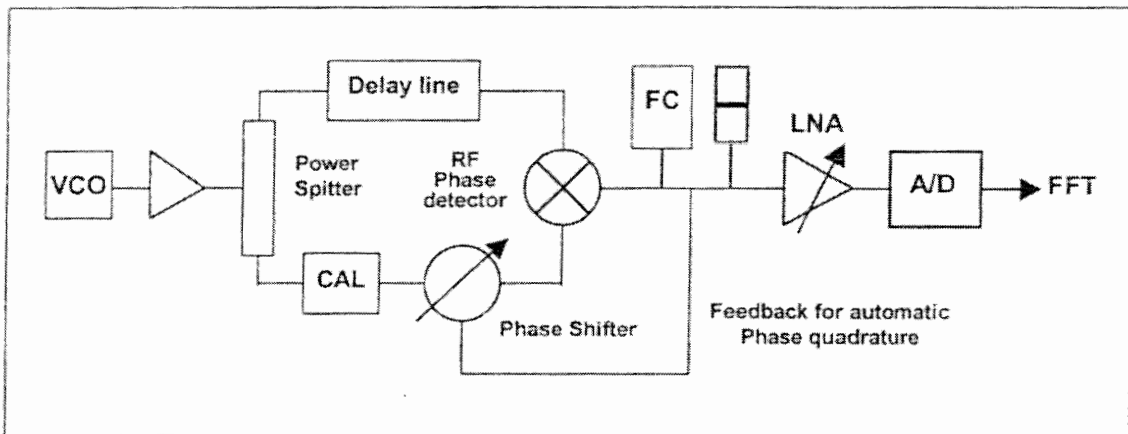
SOLUTIONS FOR UNSTABLE SOURCES

VCO frequency drift and phase/frequency fluctuations are generally too high to achieve phase locking of a DC FM reference source. Then a delay line will be used to make phase quadrature between RF & LO input signals of the phase detector. Diagram of operation is shown below.

Standard PN9000 delay lines with 10 and 100 ns or 20 and 100 ns delay, provide offset measurements up to 5, 25 and 40 MHz.

VCOs from 250 MHz to 2.0 GHz

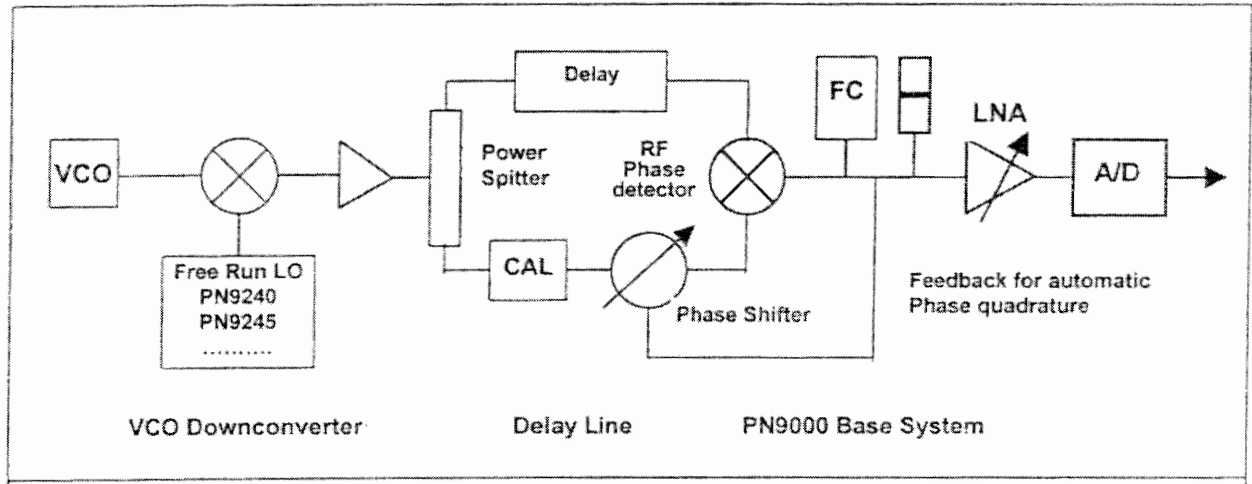
The baseband delay line frequency range is 250 MHz to 2 GHz with the standard RF and MW phase detector.



VCOS from 100 MHz to 250 MHz and from 2 GHz to 5.9, 10, 18 GHz

A family of up and downconverter extend the baseband delay line frequency range from 100 MHz to 18 GHz. For details and specifications see unstable source measurement data sheet.

The DRO used in stable source downconverters are phase locked to provide low phase noise close-in the carrier, like the stable DUTs. Those used for unstable source downconverters are not phase locked to provide low phase noise far away from the carrier (100 KHz and beyond).

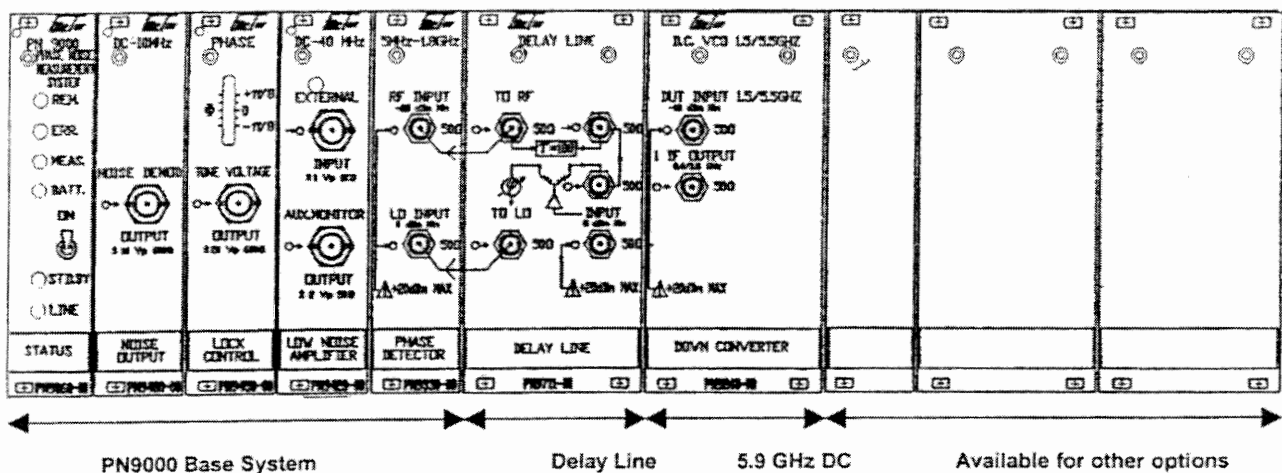


The table below shows residual noise figures according to DUT frequency and offset analysis from the carrier. Table page 14 shows residual noise comparison between Stable source, unstable source downconverters and the PN9100. The free run LO downconverter provides the lowest residual noise from 100 kHz and beyond.

Offset from carrier

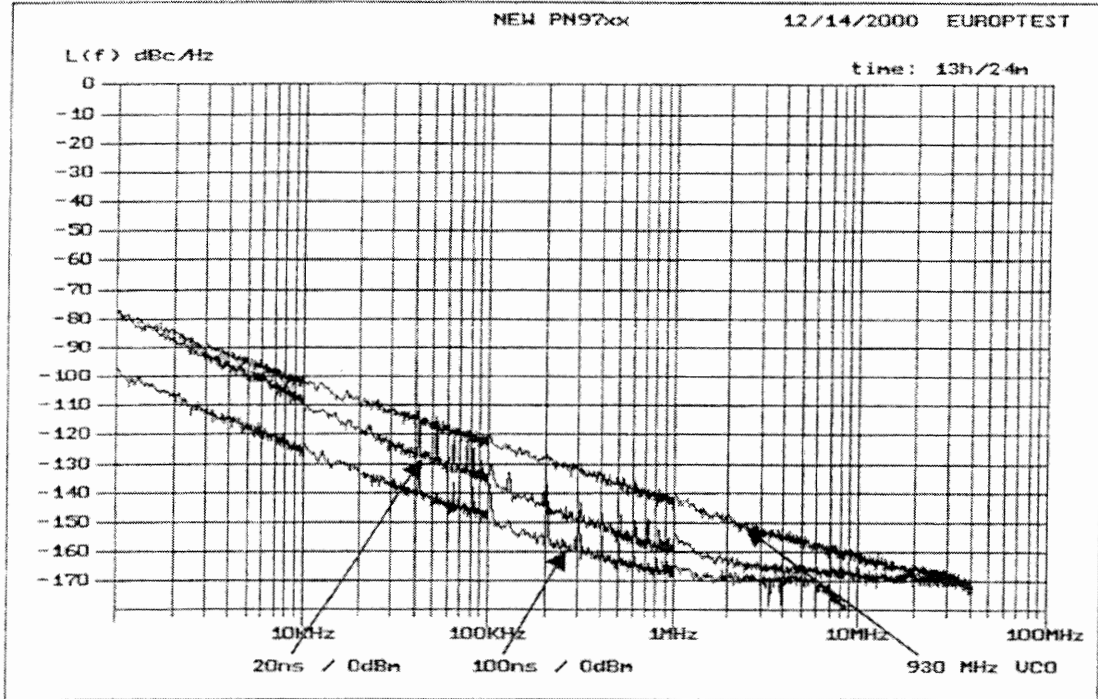
DUT frequency	1 kHz	10 kHz	100 kHz	1 MHz	4 MHz	10 MHz
2 – 5 GHz	- 90	- 120	- 140	- 160	- 166	- 168
5 – 10 GHz	- 84	- 114	- 134	- 154	- 160	- 162
18 GHz	- 78	- 108	- 128	- 148	- 154	- 156

Layout of a PN9000 delay line set-up for 250 MHz to 5.9 GHz



The New PN97xx Delay Line For Very Low Noise VCO Measurements

(Preliminary information)



To make easy measurements of the new generation of GSM, DCS and UTMS VCOs Europtest has designed this new delay line with higher phase noise detection sensitivity and lower noise floor.

The above plots show the measurement of a 1 GHz very low noise SAW oscillator. They show the actual residual noise of the delay line since the phase noise of this oscillator, measured against a second similar unit using the reference phase locking method, is lower. **Measurement of a real 930 MHz VCO shows that the residual noise of the 20 ns delay is low enough to measure GSM and DCS VCOs.**

Offset	SAW Osc.	100 ns	20 ns	GSM	DCS
1 KHz	- 112	- 100	- 80		
10 KHz	- 135	- 125	- 110		
100 KHz	- 160	- 148	- 135		
150 KHz	- 162	- 153	- 136	- 120	- 115
1 MHz	- 168	- 167	- 159		
5 MHz	- 168	- 169	- 167		
10 MHz	- 168	NA	- 168		
20 MHz	- 168	NA	- 168	- 166	- 155

Label, price and specs of the PN97xx will be available in January. First shipments are forecasted in March-April 2001. Then the PN9715/16 will likely be discontinued.

For more information e-mail to Info@europtest.com

Revision 03 / January / 2001

PN 9000 DELAY LINE METHOD

See figure VIII bis : For Hardware configuration .

Automatic Software measurement procedure is installed in Window F7 .

Select Delay Line .

To initialize the Menu Configuration use the program : RECALL CONFIG .

To make a measurement use either :

- Automeasure = full automatic process
- Program = step by step process .

- * For "quadrature adjust" press key "↑" or "↓" to command the electronic phase shifter .

PN9000 DELAY LINE METHOD

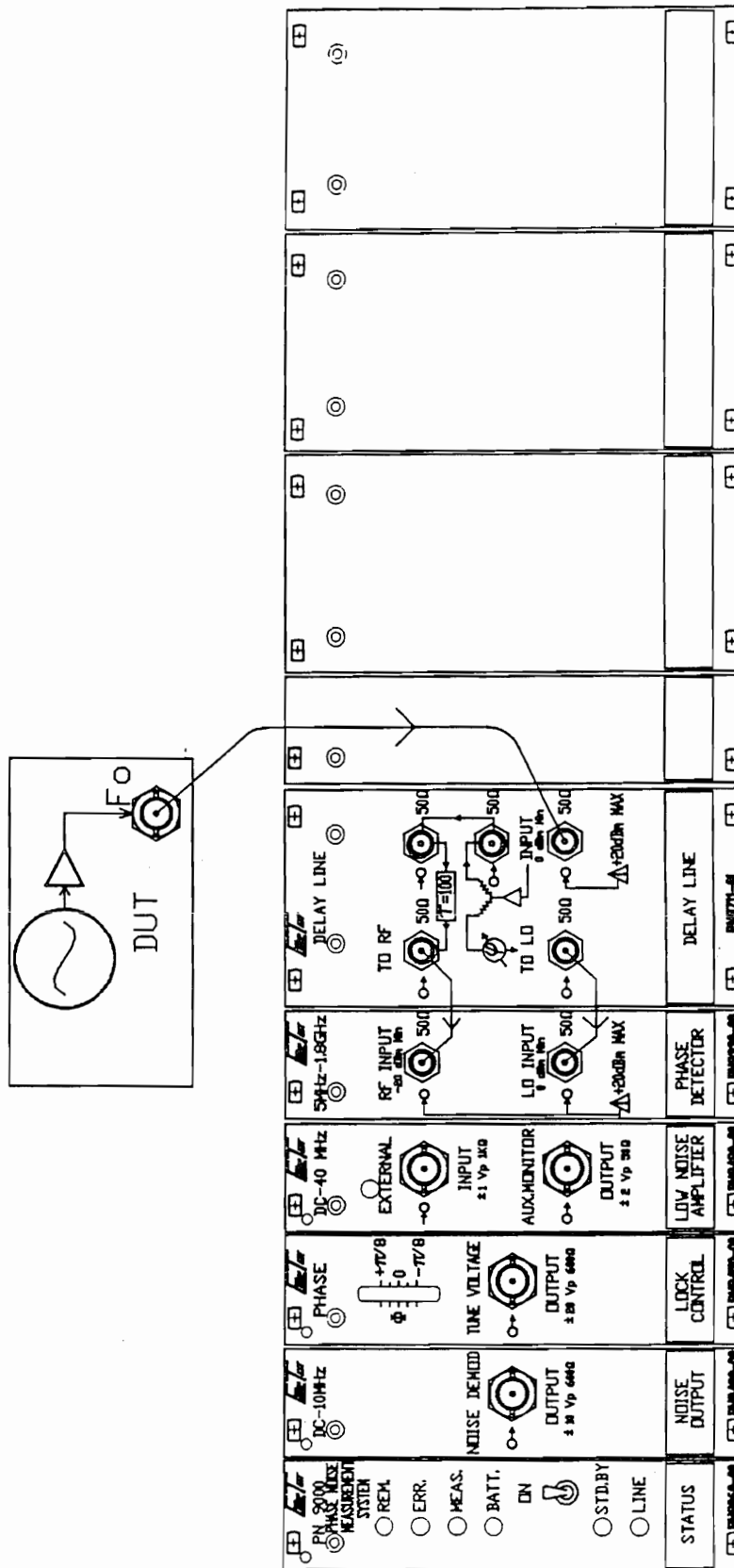


FIGURE VIII BIS